The role played by quasi-elastic and inelastic break-up of the ^{12}C and ^{16}O projectiles in the production of Intermediate Mass Fragments at 14-35 MeV/u

by

Joele Paulus Mira

Dissertation presented for the degree of Doctor of Philosophy
in the Faculty of Science at Stellenbosch University

Department of Physics,
University of Stellenbosch,
Private Bag X1, Matieland 7602,
South Africa.

Promoters:

Prof. P. Papka
Dept. Physics

Dr. S. V. Förtsch
Dept. of Nuclear Physics, iThemba LABS

November 2013

Declaration

By submitting this dissertation electronically, I declare that the entirety of the work contained therein is my own, original work, that I am the sole author thereof (save to the extent explicitly otherwise stated), that reproduction and publication thereof by Stellenbosch University will not infringe any third party rights and that I have not previously in its entirety or in part submitted it for obtaining any qualification.

Date: ....

Abstract

The role played by quasi-elastic and inelastic break-up of the ^{12}C and ^{16}O projectiles in the production of Intermediate Mass Fragments at 14-35 MeV/u

J.P. Mira

Department of Physics,
University of Stellenbosch,
Private Bag X1, Matieland 7602,
South Africa.

Dissertation: PhD (Physics)

November 2013

Two experiments were performed to investigate the role played by quasi-elastic (QE) and inelastic break-up of ^{12}C and ^{16}O in the production of Intermediate Mass Fragments (IMFs) in the interaction with light to heavy target nuclei. Two detector telescopes were used to measure emitted fragments in both experiments. The standard ΔE-E technique was implemented in both experiments for particle identification and isotope separation.

In the first experiment the correlation of ^{8}Be$_{g.s.}$ and α-particle was measured in coincidence in the interaction of ^{12}C with ^{12}C, ^{93}Nb and ^{197}Au targets at an incident energy of $E_{lab} = 400$ MeV. Coincident data were measured at six angle pairs with the ^{8}Be$_{g.s.}$ detector telescope fixed at $\theta_{lab} = 9°$ while the α-particles were measured over an angular range between $\theta_{lab} = 16°$ to $26°$ on the opposite side with respect to the beam axis. Good energy resolution allowed clear separation of the QE break-up events from the inelastic break-up events. Apart from the QE component at the highest emission energy, a further contribution was observed in the coincidence spectra at energies below about 30 MeV for forward emission angles from $\theta_{\alpha} = 16°$ to $22°$. It was found that, due to the presence of hydrogen (H) on the target, a competing mechanism of a fusion-like process between the ^{12}C projectile and the H nucleus followed by a sequential break-up of the compound system contributed to the QE, as well as to the inelastic break-up regions of the coincidence spectra. These contributions were identified and corrected for to extract the QE angular distributions which showed a smooth and decreasing trend as function of target mass and the α-particle emission angle. While the GEANT4 code was unable to model the QE break-up and in the absence of a formal theory, the Monte Carlo SimSort simulation code was implemented to qualitatively reproduce the features of the experimental coincidence data.

In the second experiment the reaction mechanisms involved in the inclusive production of Intermediate Mass Fragments (IMFs) were studied. The energy spectra of the IMFs ranging from Li to Ne isotopes were measured in the interaction of ^{16}O and ^{12}C beams with a ^{12}C target at an incident energy of E_{lab} = 235 MeV and 400 MeV, respectively. The double differential cross-sections of these IMFs were measured over an angular range between $\theta_{lab} = 8°$ and 50° with two detector telescopes. A Monte-Carlo code FLUKA was used to simulate the spectra of fragments heavier than the target in the interaction of ^{16}O with ^{12}C at an incident energy of E_{lab} = 235 MeV. The Boltzmann Master Equations (BME) were incorporated into FLUKA to evaluate time evolution of nucleon-nucleon scattering during the complete and incomplete fusion reactions, while the projectile and target fragmentations were modelled by folding the Local Plane Wave Born Approximation (LPWBA) with the exponential survival probability of the projectile.

The production of fragments lighter than both the projectile and target nuclei mainly originates from a nucleon coalescence mechanism and shows a maximum at intermediate emission energies at all emission angles. The production of projectile-like fragments (PLF) emitted at most forward angles with higher energy is mainly due to nucleon transfer mechanisms. This is exhibited by the angular distributions of these PLF which show an exponential decreasing curve as function of emission angle.

The theoretical calculations show reasonable agreement with the experimental data for all the simulated fragments except for the highest energy part of the spectator fragments which are mainly produced via multi-nucleon transfer from the projectile or target nucleus.

Results of both experiments have shown that at these energies the binary break-up plays an important role in the emission of particles at the most forward angles with energies corresponding to the beam velocity. To an extent it was shown that both QE and inelastic break-up can lead to direct emission or can also be followed by the complete or incomplete fusion of one of the fragments with the target.

The present results will add to a much needed experimental database to further investigate theories that are able to interpret the reaction mechanisms involved in the production of IMFs at incident energies of a few tens of MeV/u. In addition, these data will also provide information that will help to predict the production of positron emitters (^{11}C, ^{13}N, ^{15}O and ^{18}F) which are essential in medicine for locating tumour during hadron irradiation therapy.

Uittreksel

Die rol vervul deur die kwasie-elastiese en onelastiese opbreek van ^{12}C en ^{16}O in die vervaardiging van Intermediêre Massa Fragmente teen 14-35 MeV/u

("The role played by quasi-elastic and inelastic break-up of the ^{12}C and ^{16}O projectiles in the production of Intermediate Mass Fragments at 14-35 MeV/u")

J.P. Mira
Departement Fisika,
Universiteit van Stellenbosch,
Privaatsak X1, Matieland 7602,
Suid-Afrika.

Proefskrif: PhD (Fisika)
November 2013

Twee eksperimente is uitgevoer om die interaksies van ^{12}C en ^{16}O met ligte en swaar teikenkerne te ondersoek, en spesifiek om die rol te bepaal wat gespeel word deur kwasie-elastiese (KE) en onelastiese opbreek van ^{12}C en ^{16}O in die produksie van Intermediêre Massa Fragmente (IMF). Twee detektorteleskope is gebruik in beide eksperimente om die vrygestelde fragmente waar te neem. Die standaard ΔE-E tegniek is geïmplimenteer tydens albei eksperimente vir deeltjie en isotoopidentifikasie.

In die eerste eksperiment is die korrelasie van $^{8}\mathrm{Be}_{g.s.}$ en α-deeltjies gemeet in die interaksie van ^{12}C met teikens van ^{12}C, ^{93}Nb en ^{197}Au teen 'n invalsenergie van $E_{lab} = 400$ MeV. Koinsidensdata is gemeet by ses hoekpare. Die $^{8}\mathrm{Be}_{g.s.}$ detektorteleskoop is opgestel by $\theta_{lab} = 9°$ terwyl die α-deeltjie gemeet is by hoeke vanaf $\theta_{lab} = 16°$ tot $26°$ aan die teenoorgestelde kant ten opsigte van die bundelas. Duidelike onderskeiding tussen KE opbreking en die onelastiese opbreking is moontlik gemaak deur die goeie energieresolusie van die meting. Buiten die KE komponent by die hoogste vrystellingsenergie word 'n verdere bydrae waargeneem, 30 MeV laer, in die koinsidensie spektra vir voorwaarste hoeke van $\theta_{\alpha} = 16°$ tot $22°$. Hierdie kompeterende meganisme, veroorsaak as gevolg van die teenwoordigheid van waterstof (H) op die teiken, word beskou as die gevolg van 'n fusieproses tussen die ^{12}C bundeldeeltjies en vrye waterstofkerne in die teiken, wat gevolg word deur 'n opbreekproses van die saamgestelde stelsel. Hierdie opbreekproses vertoon as ekstra sterkte in die KE gebied asook in die gebied van onelastiese opbreking. Die identifikasie van hierdie proses was baie belangrik ten einde suiwer KE hoekverdelings te kan produseer. Finale, gekorrigeerde KE hoekverdelings vertoon 'n gladde afwaartse gedrag as ‘n funksie van teikenmassa en α-deeltjie vrystellingshoek. In die afwesigheid van 'n formele teorie om die KE opbreek te simuleer is die GEANT4 kode getoets maar dit kon nie die KE-data besfryf nie. 'n Monte Carlo program, genaamd SimSort, is egter suksesvol aangewend om eienskappe van die eksperimentele data kwalitatief te reproduseer.

Die reaksiemeganismes wat lei tot die produksie van IMF's, soos waargeneem in inklusiewe metings, is tydens die tweede eksperiment ondersoek. Die energiespektra van verskeie IMFs, vanaf Li tot Ne isotope, is waargeneem tydens die interaksie van onderskeidelik 'n E_{lab} = 235 MeV ^{16}O bundel en 'n E_{lab} = 400 MeV ^{12}C bundel met 'n ^{12}C teiken. Dubbel differensiële kansvlakke is gemeet vir die hoekgebeid van θ_{lab} = 8° tot 50°.

Die Monte Carlo program FLUKA isgebruik om spektra te genereer van IMFs wat swaarder is as ^{12}C. Die Boltzmann Master vergelykings (BMV) is in FLUKA geïmplimenteer en gebruik om nukleon-nukleon verstrooiing tydens volledige of onvolledige fusiereaksies te modeleer. Die fragmentasieprosesse van die projektiel en teikenkerne is gemodelleer met behulp van die Lokale Vlakgolf Born benadering.

Fragmente, ligter as die projektiel of teiken, word geproduseer deur middel van 'n nukleoonsamesmeltingsmeganisme. 'n Maksimum is waargeneem vir gemiddelde emissie energië, maar is onafhanklik van emissiehoek. Fragmente soortgelyk aan die invallende deeltjie, oftewel projektiele ekwivalente fragmente (PEF), word meestal waargeneem by voorwaartse hoeke by energieë wat in ooreenstemming is met die bundelenergie. 'n Kernoordragsmeganisme is verantwoordelik vir die vervaardiging van PEFs, wat eksponensieel afneem as 'n funksie van emissiehoek.

Teoretiese berekeninge toon 'n redelike ooreenkoms tussen die eksperimentele data en al die gesimuleerde fragmente, met die uitsondering van die hoogste energie gedeelte van die toeskouerfragmente. Hierdie fragmente word geproduseer deur middel van 'n multi-nukleon oordragsmeganisme vanaf die projektiel na die teikenkern.

Beide eksperimente bevestig dat die binêre opbreekproses 'n belangrike rol vervul tydens die emissie van kerne by voorwaartse hoeke en teen hoë energië. Verder is aangetoon dat beide die KE en onelastiese opbreekmeganismes 'n direkte emissieproses tot gevolg kan hê, of opgevolg kan word deur volledige of onvolledige fusieprosesse van een van die fragmente met die teikenkern.

Die data wat versamel is met hierdie navorsing, verteenwoordig 'n belangrike toevoeging tot die wêreldwye eksperimentele databasis wat gebruik word om teorië te toets wat handel oor die reaksiemeganismes wat lei tot die vervaardiging van IMFs. Verder sal hierdie data ook bydra tot akkurater voorspellings van die produksie van positronuitstralers (^{11}C, ^{13}N, ^{15}O en ^{18}F) wat

’n belangrike mediese rol vervul ten opsigte van die lokalisering van gewasse en monitering van die bundel tydens hadronbestralingsterapie.

KETELLA-PELE

Karolo e bapalwang ke karohano ya dibetsetswa tsa ^{12}C le ^{16}O ka mokgwa o otlolohileng le mokgwa osa otlolohang tlhahisong ya dikotwana tse mahareng (IMF) matleng a petsetso pakeng tsa 14-35 MeV/u

("The role played by quasi-elastic and inelastic break-up of the ^{12}C and ^{16}O projectiles in the production of Intermediate Mass Fragments at 14-35 MeV/u")

J.P. Mira
Lefapha la Mahlale,
Unibesiti ya Stellenbosch,
Mokotla wa Poraefete X1, Matieland 7602,
Afrika Borwa.

Dithuto: PhD (Thuto ya Mahlale)
Pudungwana 2013

Diexperimente tse pedi di ile tsa phethwa ho batlisisa ka karolo e bapalwang ke karohano e otlolohileng (quasi-elastic) le karohano e sa otlolohang (inelastic) ya ^{12}C le ^{16}O tlhahisong ya dikotwana tsa boima ba athomo tse bitswang IMF ($Z \geq 3$), ha di thulantshwa le dinutlere tse bobebe le tse boima. Diteleskoupu tse pedi tsa dimethi (detektara) di ile tsa sebediswa ho metha dikotwana tse hlahisitsweng. Tegenike ya ΔE-E e ile ya sebediswa ho kgetha leho arohanya dikotwana tse methilweng.

Ekseperimente ya pele ene e metha tlhahiso ya dikotwana tsa ^{8}Be$_{g.s.}$ le α-particle ha sebetsetswa sa ^{12}C sa matla a petsetso a $E_{lab} = 400$ MeV se thulana le dinutlere tsa ^{12}C, ^{93}Nb le ^{197}Au. Dikotwana tsena di methilwe ka nako ele enngwe dikgutlong tse tsheletseng, teleskoupu ya ^{8}Be$_{g.s.}$ e beilwe sekgutlong sa $\theta_{lab} = 9°$ ka nako tsohle, haele ya α-particle yona e methile pakeng tsa 16° le 26° ka karolong e nngwe. Tharollo e ntle ya matla a dikotwana e ile ya dumella tharollo ya diketsahalo tsa mokgwa wa quasi-elastic (QE) le mokgwa wa inelastic. Diketsahalo tsa QE ke tse fumanwang matleng a mangata, diketsahalo tse ding tsa dikotwana di ile tsa bonwa ho dipektramo matleng a ka bang 30 MeV ka tlasa diketsahalo tsa QE dipakeng tsa dikgutlo tsa $\theta_{\alpha} = 16°$ le 22°. Ho fumanwe hore ka baka la hydrogene (H) e fumanwang dinutlereng tsa dithakethe, hona le mekhaniseme e hlodisanang le tse boletsweng e bakwang

ke kgomarelano pakeng tsa ^{12}C le H mme di be di arohana ka ho kgaoha ka tatellano ho hlahisa dikotwana tse nkang karolo diketsahalong tsa QE le inelastic. Diketsahalo tsena tse tswang kgomarelanong di ile tsa lemohwa mme tsa lokiswa ha ho hlahiswa sepektramo se bontshang diketsahalo tsa QE tse methilweng dikgutlong, mme sepektramo sena se bontsha diketsahalo tse theohang hantle ho latela dikgutlo tsa α-particle. Kaha GEANT4 ha ea kgona ho hlahisa diketsahalo tsa QE, le bosiyong ba theori, Monte Carlo SimSort e ile ya sebediswa ho hlahisa diketsahalo tsena tsa ekseperimente.

Ekseperimente ya bobedi e phethilwe ho ithuta ka ketsahalo (mekhaniseme) e nkang karolo tlhahisong ya dikotwana tse dipakeng (IMF). Disepektramo tsa matla di ile tsa methwa ha dipetsetswa tsa ^{16}O le ^{12}C tse nang le matla a petsetso a $E_{lab} = 235$ MeV le 400 MeV, ka tatellano, di thulana le nutlere ya ^{12}C. Di double-differential cross-section tsa di IMF tsa nutlere tsa Li ho ya ho Ne di ile tsa methwa pakeng tsa dikgutlwana tsa $8°$ le $50°$ tshebedisong ya di teleskoupu tse pedi tsa detektara. Monte Carlo khoutu e bitswang FLUKA e ile ya sebediswa ho etsisa disepektramo tsa dikotwana tsa boima ho feta nutlere ya ^{12}C thulanong ya ^{16}O le ^{12}C, ya matla a petsetso a $E_{lab} = 235$ MeV. Boltzmann Master Equations (BME) e ile ya kenyelletswa ho FLUKA ho batlisisa dikotwana tse hlahisitsweng ka mora hore dinucleone di thulane, mme karohanyo ya sebetsetswa le thakethe tsona di ile tsa batlisiswa ka ho mena Local Plane wave Born Approximation (LPWBA).

Tlhahiso ya dikotwana tse bobebe ho thakethe le sebetsetswa boholo di hlahiswa ke mekhaniseme ya nucleon-coalescence mme di bontsha bongata matleng a mahareng dikgutlong tsohle tse methilweng. Tlhahiso ya dikotwana tse batlileng di lekana ka boima le sebetsetswa (^{16}O), tse methilweng dikgutlong tse ka pele ebile dina le matla a hodimo di hlahiswa ke mekhaniseme wa nucleon-transfer.

Disepektramo tsa dikotwana tse hlahisitsweng ka FLUKA di bontshitse tumellano e ntle le dikotwana tse hlahisitsweng ekseperimenteng, ntle le tseo tse hlahisitsweng ka matla a hodimo ka mekhaniseme wa multi-nucleon transfer ho tloha ho sebetsetswa kapa thakethe.

Diphetho tse fumanweng diekseperimenteng tsena tse pedi di bontsha hore karohano ya koto tse pedi e bapala karolo ya bohlokwa tlhahisong ya dikotwana tse nang le matla a hodimo tse methilweng dikgutlong tse ka pele, tse nang le lebelo le lekanang le la sebetsetswa. Dipheto tsena di bontsha hape hore karohano ya QE le inelastic di ka etella pele tlhahiso e otlolohileng kapa tsa latelwa ke kopano ya dithulani e felletseng kapa kopano ya sekotwana se le seng le thakethe.

Diphetho tsena di tlo thusa ho eketsa tsebo (database) e hlokahalang ya di ekseperimente e tla sebediswa ho batlisisa di diketsahalo tse hlalosang tlhahiso ya di IMF matleng a mahareng a ka bang mashongwana a MeV/n. Hape diphetho tsena di tlo nehelana ka tsebo etla thusa ho utlwisisa tlhahiso ya dinutlere tse hlahisang positron (^{11}C, ^{13}N, ^{15}O le ^{18}F) tse sebediswang ho fumana mofetshe (kankere) e le hore etle e phekolwe ka ho cheswa ka di hadron.

Dedication

This work is dedicated to my late mother, Mrs Puleng Leah Mira. She was my pillar of strength, she was like a glue that held the family together. We will always remember her. May her soul rest in peace.

Acknowledgements

First of all I would like to express my immense gratitude to our Almighty Heavenly Father for protecting me, and giving me power, strength and sound health to complete this thesis.

Secondly I would like to express my sincere gratitude to my promoters, Prof. P. Papka and Dr S. V Förtsch for their invaluable supervision and support towards the completion of this thesis.

I would also like to thank my mentors, Dr G.F. Steyn, Dr R. Neveling, Dr. I. Usman and Dr. F.D. Smit, for the support they gave me during my data analysis and thesis writting. I would also like to express my sincere gratitude to Dr S. Peterson for his invaluable contribution to the GEANT4 simulations. Thank you very much for your assistance. I would also like to thank Mr. Cobus Swartz for helping with the translation of the abstract into Afrikaans. To the rest of the nuclear physics department and everyone who participated in my experiment, I would like to say thank you very much for your contribution. I woulnd't have done all these without your help. I would also like to thank the iThemba LABS and the Accelerator department for the quality beam they delivered during the data taking, as well as for providing me with the necessary support to complete this thesis.

Lastly, I would like to express my sincere gratitude to my family (Thabo, Ntsoaki and Tsietsi, Moeketsi), and my son Chere, friends and everyone who had a positive contribution to my life. To all those that I offended during my stressful days, I apologise from the bottom of my heart.

Contents

List of Figures

List of Tables

Chapter 1

Introduction

1.1 Introduction

The production and emission of clusters of nucleons known as Intermediate Mass Fragments (IMF) in the interaction of two nuclei are governed by different reaction mechanisms. These clusters of nucleons are reffered to as IMFs if they have a nuclear charge Z $\geq$ 3. Many studies have been performed over the past decades with light projectiles such as protons, deuterons and α-particles and were extended to the use of heavy-ion projectiles in heavy ion reactions [Fuc94]. In the early studies of heavy ion reactions the accelerators could only provide projectiles with very low energies ranging from $E_{lab} = 2$ MeV/u to 10 MeV/u. At these energies heavy ion collisions were very useful tools for learning about the bulk properties of nuclei which led to the discovery and exploration of deep inelastic collisions [Sch84]. In these types of reactions the two colliding nuclei slow down upon contact until they come to rest before they re-separate [Fuc94].

The study of heavy ion reactions is still of great interest in basic research as well as in applications such particle therapy and radiation protection of crew and equipment during space missions. Information that could help improve the theory of the reaction mechanisms involved could be obtained from studying heavy ion reactions. These reactions can be divided into two reaction phenomena, direct reactions and compound reactions. The direct reactions typically take place in about 10^{-22} s, with particles being emitted directly upon impact before the projectile fuses with the target nucleus [Hod97]. The compound reactions, on the other hand begin with the capture of the entire projectile by the target nucleus (complete fusion) [Sin11], or the fusion of projectile or target fragments with either of the two nuclei (incomplete fusion) to form an excited compound nucleus. The excitation energy of the compound nucleus is shared among its nucleons due to a sequence of nucleon-nucleon collisions after which nucleons escape as single entities or clusters of nucleons [Sin11].

A number of previous studies have found that a transition in the reaction mechanism responsible for the production of IMFs, takes place at energies around 10 MeV/u [Fuc94, Mag98]. This was observed in different studies of nucleus-nucleus collisions which were performed from the Coulomb barrier to beyond the Fermi energy [Fat85, Chi86]. At low energies, below 10 MeV/u, the spectra are characterised by a sharp and pronounced peak in the energy dependence of the cross-sections. This strongly suggests that the reaction proceeds through a single state, a resonance of the compound nucleus. As the projectile energy increases above 10 MeV/u the cross-sections are forward peaked and can be attributed to one-step direct reactions. It was also observed that at low incident energies below 10 MeV/u the angular distribution cross-sections of fission fragments correspond to a full linear momentum transfer [Gel87] due to the complete fusion. As the incident energies reach 10 MeV/u the distribution of linear momentum transfer is spread over a broad continuum, as the maximum possible contribution from complete fusion decreases. It was also observed by Gadioli *et al.* [Gad02] that the spectra of the emitted fragments at incident energies around 10 MeV/u have a Gaussian shape with a maximum at about beam velocity and do not significantly change as a function of the emission angle as expected for the break-up mechanism. In the energy region below 10 MeV/u, the production of IMFs is dominated by reaction mechanisms such as complete fusion, quasi-elastic transfer and deep-inelastic reactions [Fuc94]. The improvement of Accelerator technologies in subsequent years which provided higher bombarding energies significantly beyond 10 MeV/u, afforded researchers the opportunity to extend the study of nuclear bulk properties to higher energies in order to expose a nucleus to more stress and eventually to breaking up. The energy region above 10 MeV/u is dominated to a large extend by binary break-up and nuclear transfer [Fuc94, Mag98, Chi86], where the projectile might break-up after which one fragment fuses with the target nucleus or can be emitted without further interaction with the target nucleus.

Heavy ion reactions play a significant role in studying the reaction mechanisms involved in the production of IMFs. The experimental studies of IMF can be divided into two categories whereby fragments are measured in an inclusive or a coincident experiment. Coincidence measurements have thus far provided important information about the binary break-up mechanism. Previous coincidence experiments performed by Lynen *et al.* [Lyn82] and Mittig *et al.* [Mit85] showed evidence for coplanarity of the fragments associated with heavy reaction products and the beam axis, and also demonstrated that the IMFs are emitted following the binary break-up. The present study of the correlation between ^{8}Be and α-particles following the break-up of ^{12}C will play a vital role in the analysis to separate the inelastic from quasi-elastic binary break-up. This choice is unique due to the fact that ^{8}Be fragments cannot survive final-state interactions without breaking the correlation between its constituent α-particles, which will simplify the data analysis of the reaction mechanisms leading to inelastic and quasi-elastic break-up.

1.1.1 Resonance Nuclei of ^{8}Be and ^{9}B

The resonant nucleus of ^{8}Be is the most enigmatic member of the beryllium isotopes. This nucleus can be considered as two α-particles in orbit with zero angular momentum [Kha83]. The ^{8}Be system is unbound and lies 92 keV above the α-α threshold and has a lifetime of 0.1 femto seconds. The binding energy in ^{8}Be is 7.06 MeV/u. The lifetime of the resonant ^{8}Be ground state (g.s.) is an important factor in the astrophysical triple-α process. The $^8\text{Be}_{g.s}$ fuses with the α-particle in a stellar environment to form a stable ^{12}C nucleus. The reaction of ^{8}Be + α to produce ^{12}C proceeds through a resonance state called the "Hoyle state" in ^{12}C that lies at the binding energy of 7.04 MeV/u which is very close to that of ^{8}Be. The first excited state of ^{8}Be is at 3.04 MeV and disintegrates with a half life of $T_{1/2} = 3 \times 10^{-22}$ s and a Q-value of 3.13 MeV into two α-particles. Due to the higher Q-value, the two α-particles from this state exhibit larger opening angles [Gon01].

The resonant nucleus of ^{9}B is regarded as the mirror nucleus of ^{9}Be [Ara03]. Since these nuclei are considered as cluster nuclei which decay into $\alpha\alpha p$ and $\alpha\alpha n$, respectively, their structures are expected to be similar [Bar09]. The isotope of ^{9}B is unbound to ^{8}Be + p decay by 185 keV. In their analysis of ^{12}C(p,p'3α) break-up reaction induced by 14, 18 and 26 MeV protons, Harada *et al.* [Har99] studied, amongst other channels, also the break-up of $^9\text{B}_{g.s.}$ into a proton and $^8\text{Be}_{g.s.}$, which also decays into two α-particles.

The following section introduces the reaction mechanisms which were applied to interpret the data obtained in this study.

1.2 Reaction Mechanisms

When two heavy ions collide, several processes such as the emission of γ-rays, protons, neutrons or α-particles may occur, as well as the emission of IMFs. These processes are governed by several different reaction mechanisms which dominate at different projectile energies. There are few reaction mechanisms that are not applicable to the energy range used in the present study, such as fusion reactions and deep inelastic reactions. In the energy range used in this study there are several reaction mechanisms which are applicable, such as nucleon transfer, quasi-elastic and inelastic break-up, sequential break-up, nucleon coalescence and nuclear evaporation, which are discussed in detail in the following subsections. Fig. 1.1 shows a schematic representation of a complete energy spectrum with the contribution from different reaction mechanisms as a function of emission energy and excitation energy.

1.2.1 Direct reactions

According to Hodgson [Hod97], direct reactions typically take place in about 10^{-22} s, which is the time the projectile takes to traverse the target nucleus.

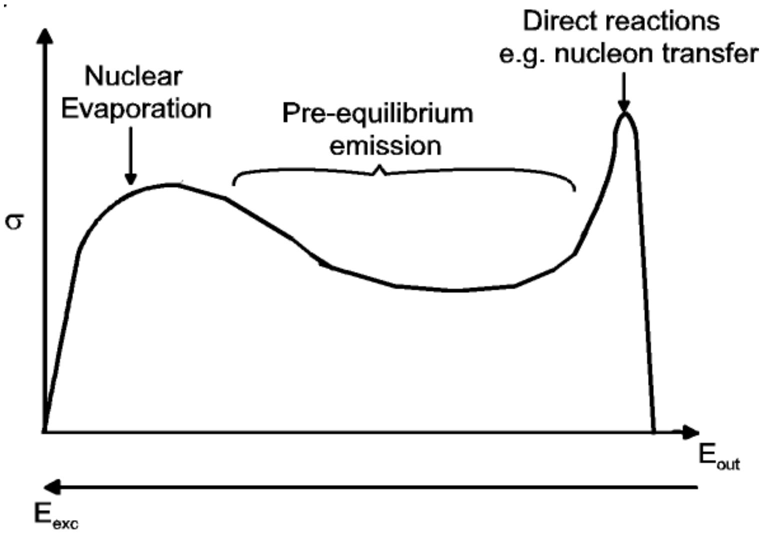

Figure 1.1: Schematic representation of a complete energy spectrum showing the contributions from different reaction mechanisms as a function of emission energy E_{out} and excitation energy E_{exc}.

The projectile may interact either with a single nucleon, a group of nucleons or the whole nucleus leading to immediate emission of charged particles and neutrons. Elastic scattering of the projectile is the simplest direct reaction, in which case the projectile leaves the target nucleus in its ground state.

i **Transfer reactions**
One-nucleon transfer reactions excite single-particle states, while multi nucleon transfer reactions excite cluster states of the target nucleus. The cross-sections of the nuclear transfer are calculated by using a Distorted wave Born Approximation (DWBA) as described in the literature e.g. by Schmittroth *et al.* [Sch70]. In their studies, they examined one nucleon transfer using different reactions such as, $^{10}B(^{14}N,^{13}N)^{11}B$, $^{27}Al(^{16}O,^{15}N)^{28}Si$ and $^{11}B(^{16}O,^{15}N)^{12}C$. In the present work an example of such a process includes the production of ^{15}O in the interaction of ^{16}O with ^{12}C which is produced in the transfer of one neutron from the projectile to the target nucleus, while the transfer of one proton from the target to the projectile could produce ^{17}F. What could also happen is the pick-up of an α-particle by the ^{16}O which leads to the production of ^{20}Ne. As in the case of elastic scattering, the cross-sections for inelastic scattering and nucleon transfer reactions often have compound nucleus components at low kinetic energies.

ii **Quasi-elastic and Inelastic Fragmentation**
The break-up of the projectile or target nucleus can be classified as different break-up mechanisms such as projectile multi-fragmentation, quasi-elastic binary break-up and inelastic break-up and the sequential break-up.

Multi-fragmentation, typically witnessed at much higher incident energies above few 10 MeV/u, is the process whereby both the projectile and target nuclei break-up into more than two fragments upon contact with one another [Gro90, Ogu11]. This reaction mechanism is not applicable with the energies used to perform the measurements in this study.

Binary break-up is assumed to be a peripheral direct reaction by which the projectile divides into two fragments [Gad02]. The focus of this study is based on the QE binary break-up and the inelastic break-up mechanisms. QE binary break-up occurs when the projectile breaks up into two fragments upon colliding with the target without energy transfer between the nuclei leaving the target in its ground state while the fragments are emitted without further interactions with the target [Lil01, För10]. The resulting spectra at small emission angles have a peak at an energy corresponding to the incoming projectile velocity. Fig. 1.2 shows a schematic representation of the quasi-elastic binary break-up of ^{12}C into ^{8}Be observed in the ground state and an α-particle. The inelastic break-up occurs when one of the two fragments interact or fuses with the target nucleus, and spectator fragments fly away without further interaction with the target nucleus [Bue78, Lil01]. In previous studies by the iThemba-Milano collaboration, the double differential cross-section spectra of α-particles and ^{8}Be fragments, produced from the binary break-up of ^{12}C, were evaluated in the Serber approximation [Gad99]. In the model it is assumed that the break-up transition matrix is given by the Fourier transform of the function describing the relative motion of the α-particle and the ^{8}Be fragment in ^{12}C. According to the perturbative Serber approximation [Ser47], the projectile break-up has a maximum probability at the energy corresponding to the beam velocity. The energy spectra of QE break-up components peak at energies very close to the beam velocity. The spectra tend to fall-off rapidly on the high energy side and have long tails of inelastic break-up components on the low energy side [Hus81].

iii **Sequential break-up**

The sequential break-up of an excited nucleus is described as a succession of binary processes that lead to a final mass and charge distribution [Ric90]. After the dynamical formation of a thermalised source, its further evolution depends crucially on the excitation energy and mass number. The compound nucleus exists only at low excitation energy when the sequential evaporation of light particles is the dominant decay channel. The nuclei formed in these reactions decay by emitting γ-rays or particles. Due to the interference between different magnetic substates, the angular correlations between particle-γ-rays and particle-particle depend critically on the magnitude and phases of the transition amplitudes [Rae84]. Sequential break-up of the projectile occurs when the projectile, upon contact with the target, starts to emit fragments one at the time (sequentially) until the remaining part can no longer emit any fragments [Sho81]. Sequential break-up of the projectile takes place at projectile energies below the Coulomb barrier. The projectile may be excited by the electromagnetic fields between the incident channel nuclei, and if the excited states are above the threshold for particle emission, the projectile will most likely break-up sequentially [Gol78]. Harada *et al.* [Har99], studied, amongst others, the sequential decay of ^{13}N into $^{9}B_{g.s.}$ and α-particle. In their study they assumed that the proton induced ^{12}C break-up reaction occurs through sequential break-up via unstable levels excited by (p,p') and (p,α) reactions.

In previous studies conducted by the Milano-iThemba LABS collaborators, the spectra of the break-up fragments were normally evaluated by folding the Local Plane Wave Born Approximation (LPWBA) cross section with an exponential survival probability [Gad00, Gad02]. The exponential survival probability was introduced because of the assumption that the probability of the projectile surviving a break-up or mass transfer reaction decreases exponentially with increasing projectile energy loss [Gad03, Mai07].

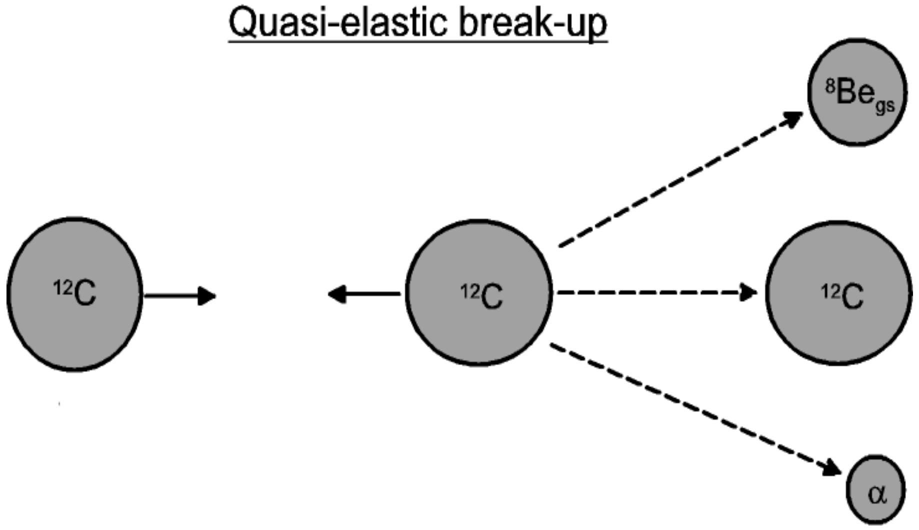

Figure 1.2: Schematic representation of the quasi-elastic binary break-up of ^{12}C into $^{8}Be_{gs}$ and α-particle.

1.2.2 Compound reactions

In nuclear fusion reactions, a non-equilibrated excited nucleus is formed either in the complete fusion of the projectile with the target nucleus, or in the incomplete fusion of the participant fragments with the target nucleus [Gad03]. A complete fusion process is characterised by the transfer of the full amount of energy and momentum from the projectile to the composite nucleus composed of the projectile and target nuclei [Sha04]. The complete fusion between ^{16}O projectile with ^{12}C target form an excited ^{28}Si compound nucleus which will decay mainly by single nucleons or clusters of nucleons and γ-rays until it is in its ground state. Fig. 1.3 shows a schematic representation of the complete fusion between two ^{12}C nuclei in the centre-of-mass system to form an excited compound nucleus of ^{24}Mg.

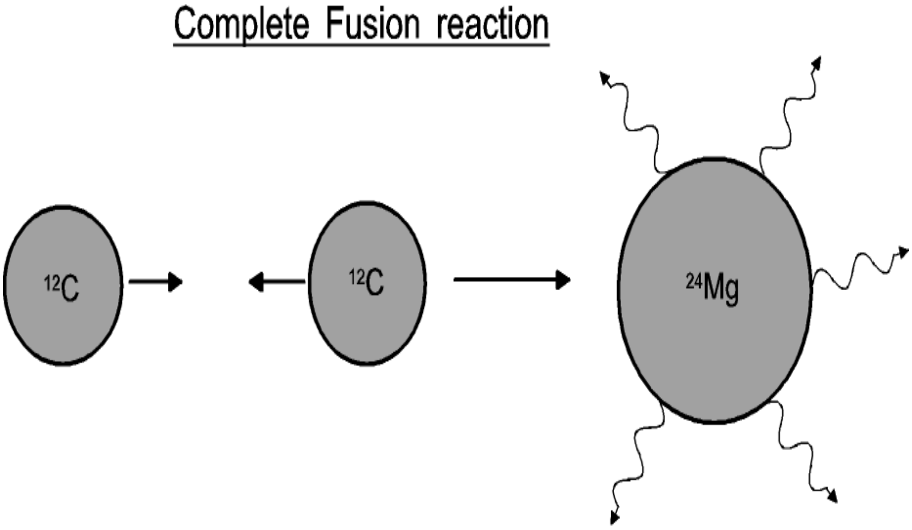

Figure 1.3: Schematic representation of a complete fusion reaction.

In the case of an incomplete fusion process, it is assumed that the projectile breaks up into two fragments (e.g. ^{16}O may break-up into ^{12}C and an α-particle and a ^{12}C may break-up into ^{8}Be and an α-particle), one of which fuses with the target nucleus while the rest moves in the forward direction with almost the same velocity of the incident ion. The energy and momentum of the projectile fragments are also transferred to the composite nucleus [Sha04]. Conversely, the target nucleus can also break-up with part of it fusing with the projectile. Fig. 1.4 shows the schematic representation of the incomplete fusion of ^{16}O breaking up into ^{12}C and α-particle upon contact with the ^{12}C centre-of-mass system, the α-particle acts as a spectator fragment whereas the ^{12}C fuses with the oncoming ^{12}C nucleus to form an excited compound ^{24}Mg.

Both the above processes lead to an excited compound nucleus which will decay by emitting light particles and γ-rays until it reaches its ground state.

Subsections below explain different reaction mechanisms which result from the complete and incomplete fusion reactions.

i Nucleon coalescence mechanisms

In previous studies [Awe81, Awe82], the theory of a coalescence model was first proposed and introduced in heavy-ion reactions to interpret the

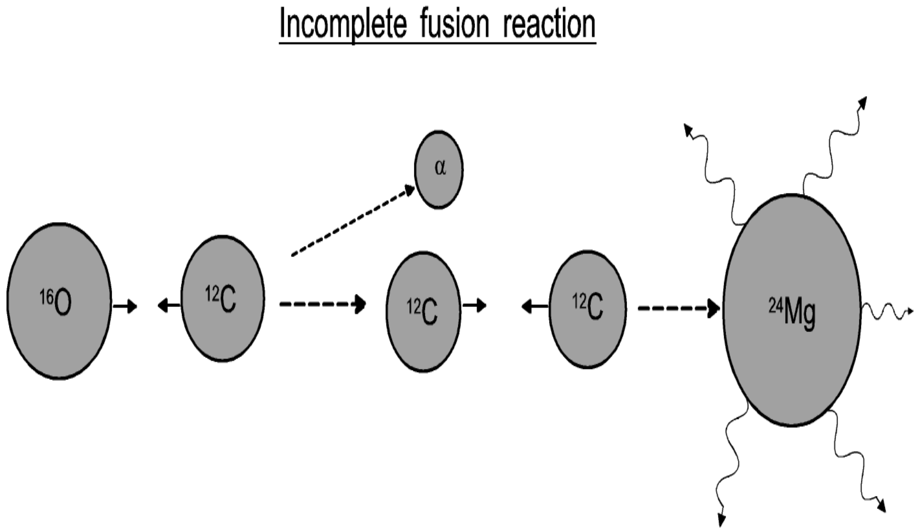

Figure 1.4: Schematic representation of an incomplete fusion reaction.

energy spectra of light composite ejectiles. The nucleon coalescence was introduced to account for the presence of contributions peaking at the emitted fragment Coulomb barrier at incident energies around 15 MeV/u. These contributions become dominant at larger emission angles where the contribution from a pure break-up disappears [Gad02]. This component in the spectra of the fragment was attributed by Hussein *et al.* [Hus81] to a complex pre-compound process unrelated to the break-up of the projectile. This mechanism was also taken into account in the interpretation of low energy components in the spectra of the IMF. It starts with the complete fusion of the projectile with the target nucleus, or the incomplete fusion of a participant fragment with the target nucleus after projectile break-up creating a non-equilibrated excited nucleus [Gad03]. Statistical equilibrium is subsequently reached through a cascade of nucleon-nucleon interactions. The complete fusion process dominates at lower beam energies, in this case the overlapping of the two ions is slowed down by their Coulomb repulsion force. Consequently, the energies of the projectile's nucleons transform into thermal energy while they are still forming a dinuclear system. At the same time, a large part of the Coulomb potential energy is not re-transformed into nucleon kinetic energy [Cav98]. At higher incident energies, the ions overlap rapidly and their nucleons may even increase their energy when they fall into the common potential well because the Fermi energy of the composite nucleus is larger than those of the projectile and target. If the excitation energy is higher than the binding energy, nucleons of the same momentum will escape from the compound nucleus as single entities or clusters of nucleons with higher energies than expected from evaporation of an equilibrated system [Gad03].

In previous studies the theoretical interpretation of the nucleon coalescence was simulated by a set of Boltzmann Master Equations (BME) [Gad02, Cav98].

ii **Nuclear Evaporation mechanisms**
The nuclear evaporation process begins with the capture of the projectile (complete fusion) or the capture of one of the participant fragments (incomplete fusion) by the target nucleus. This capture leads to the formation of an excited compound nucleus [Gad92], of which the energy is shared among all its nucleons. According to the Bohr independent hypothesis, the decay of the compound nucleus is determined by its energy, angular momentum and parity [Gad92]. For this hypothesis to be valid a long time should elapse between the time of its formation and the time it starts to decay, which would only be possible if the average excitation energy of an individual nucleon is less than its binding energy. Mainly light particles are emitted long after the fusion process by a statistical process similar to the evaporation of molecules from a liquid drop until the residual nucleus reaches its ground state by eventually emitting gamma rays. These light particles are emitted with lower energies and populate the lower energy region of the spectra. The usual Weisskopf [Wei37] evaporation model is used to determine the theoretical probabilities of single particles or IMFs emitted by nuclear evaporation.

1.3 Motivation for this study

The emission of intermediate mass fragments (IMFs) is a common feature in heavy ion reactions. Several experimental as well as theoretical studies have been performed by scientists from iThemba LABS in collaboration with the Universities of Milano and the Witwatersrand (WITS) [Gad00, Gad01, Bec03]. These experiments were conducted in order to study the reaction mechanisms involved in the production of IMFs in the interaction ^{12}C, ^{16}O and ^{27}Al ion beams with target nuclei ranging from ^{12}C to ^{197}Au at energies between 10 MeV/u and 33.3 MeV/u [Gad99, Gad00, Gad03, För05, Mud05]. Previous experimental data and theoretical studies showed that the emission of Intermediate Mass Fragments (IMFs) at forward angles is dominated by the direct break-up process. This process was included in several theoretical studies that have been conducted by this collaboration to interpret the experimental spectra. It was also observed that the production of α-particles and lighter IMFs is dominated by a non-evaporative mechanisms at forward as well as at larger emission angles [Gad99, För05]. Studies conducted by this collaboration have shown that in addition to the fragments produced in the binary fragmentation of the projectile at about the beam velocity, the other fragments are produced due to the nucleon coalescence during thermalisation of composite nuclei created in the complete and incomplete fusion of the two colliding ions [Bec03]. In a previous study involving the interaction of ^{12}C + ^{27}Al and ^{27}Al + ^{12}C, it was observed that the production of IMFs with (Z $\geq$ 6) was mainly dominated by the binary projectile and target break-up and nucleon coalescence resulting from complete fusion reactions. The main reason to perform these inverse reactions was to study the underlying reaction mechanisms involved in the production of IMFs and also to separate the fragments produced from the binary fragmentation of the projectile from those of binary target fragmentation [För05].

Two experiments were performed in order to complete the present study.

i **Correlation experiment**
The first experiment was a coincidence measurement which was performed in order to ascertain the relative differences between quasi-elastic (QE) fragmentation and inelastic fragmentation. QE fragmentation is the process in which both fragments do not suffer any further interactions after they are produced, while inelastic fragmentation is a process in which one or both particles interact and even fuse with the target nucleus. The velocity of the fragments produced in QE fragmentation is not too different from the respective beam velocity, only the recoil energy of the target nucleus is involved. This was investigated by measuring the correlations of ^{8}Be fragments and α-particles emitted in the binary break-up of ^{12}C in the interaction with ^{12}C, ^{93}Nb and ^{197}Au at an incident energy of 33.3 MeV/u. By studying the ^{8}Be and α-particle channels, the measurement of QE fragmentation is simplified since the ^{8}Be fragments are unlikely to survive any final state interactions without breaking the correlations between its two constituents α-particles. Only the final state interaction between the α-particles and the target nucleus has therefore to be considered.

The emission of α-particles near Fermi energy has been investigated previously in many studies [Ho80, Ho83, Gon87]. In these studies, the α-particles were measured in coincidence with projectile-like fragments (PLF) like e.g. ^{12}C in the interaction of an ^{16}O beam with a ^{58}Ni target at different energies ranging from 6 MeV/u to 35 MeV/u. It was observed that the α-particle energy spectra measured at the most forward angle on the opposite site of the beam with respect to the projectile like fragments were peaking at energies exceeding the corresponding projectile velocity [Gon87, Fuc94]. This anomalous behaviour of the coincident α-particles was also observed by Schwarz *et al.* in the interaction of ^{32}Sm with ^{197}Au [Sch92]. In order to separate the *pure* quasi-elastic break-up from inelastic break-up and also to further understand the above findings of the unexplained energy distributions of the coincidence α-particles, a similar coincidence experiment, denoted as project PR88, was conducted by the iThemba LABS-Milano-WITS collaboration. In this experiment the correlations of ^{8}Be fragments and α-particles were measured in coincidence in the interaction of a ^{12}C beam with ^{57}Co and ^{93}Nb targets at an incident energy of $E_{lab} = 400$ MeV. In this case the break-up of ^{12}C into ^{8}Be and α-particles simplifies this study due to the fact that ^{8}Be is unbound and cannot survive any final state interactions with the target nucleus without breaking the correlations between its constituent α-particles. Due to the above mentioned reason only the interaction between the α-particle and target nucleus is considered. These measurements of the coincidence cross-sections, as a function of the sum of the kinetic energies of ^{8}Be$_{g.s.}$ and α-particles, showed an unexpected peak that appeared about 28 MeV below the QE peak, see Fig. 1.5. This lower energy peak needed to be further investigated in order to understand its origin. From the SimSort simulations [Pap07] it was suspected that this lower energy peak could be resulting from the interaction of ^{12}C projectile with the hydrogen contaminants on the target foils. Homeyer *et al.* [Hom82] also observed that very small target contaminants can cause serious background problems in such correlation measurements.

Gadioli *et al.* [Gad01] also observed that the energy spectra of ^{8}Be measured in the interaction of ^{12}C with ^{59}Co, ^{93}Nb differed from the spectra when a ^{197}Au target was used. These ^{8}Be energy spectra show broader distributions of the ^{8}Be break-up peak in the case of ^{12}C with ^{59}Co and ^{93}Nb, while the distributions are narrower in the case where a ^{197}Au target was used. This subtle difference in the ^{8}Be energy spectra also needed to be investigated further.

In order to investigate the above mentioned aspects, the PR88 measurement was supplemented by the follow-up coincidence measurement, denoted as PR136, and refered to in this study as the correlation experiment. In this correlation measurement the break-up of ^{12}C into a ^{8}Be fragment and α-particle was further studied in the interaction of ^{12}C with ^{12}C, ^{93}Nb and ^{197}Au at an incident energy of $E_{lab} = 400$ MeV. To test the conjecture that the peak at lower energy is possibly due to a hydrogen contaminant on the target, a polyethylene $(CH_2)_n$ target was also used in the correlation experiment.

ii **IMF experiment**

In the second experiment, another series of measurements were performed to study the production of IMFs using two different ion beams of ^{12}C and ^{16}O, interacting with a ^{12}C target at incident energies of 33.3 MeV/u and 14.7 MeV/u, respectively. These studies are still of great interest not only for basic research and knowledge of the underlying reaction mechanisms, but also in the application of fields such as hadron therapy [Pön04, Mai07]. Double differential cross-sections of IMFs produced in the interactions of these nuclei over a wide range of incident energies are used in the Treatment Planning System (TPS) [Mai07], which compromises complex computer software that helps to design radiation treatments and to compute

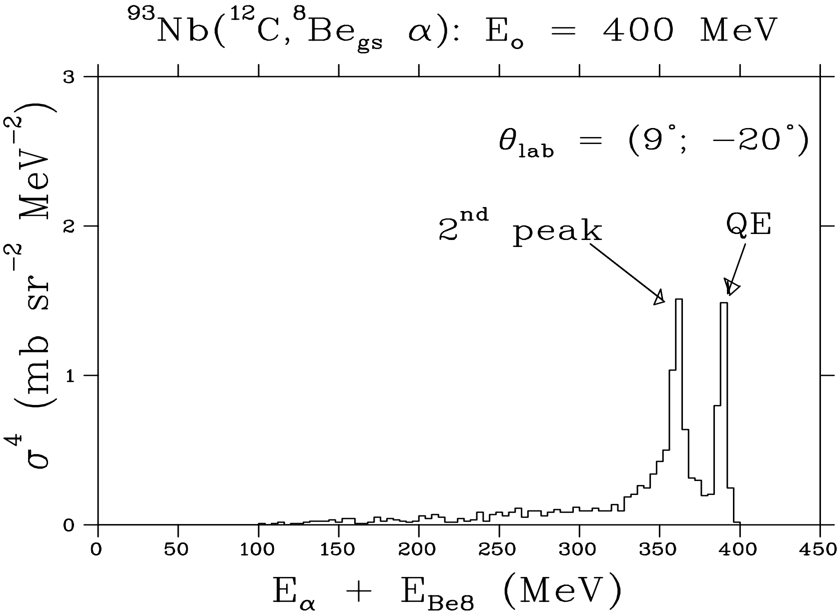

Figure 1.5: The laboratory coincidence cross sections as a function of the sum of the kinetic energies of ^{8}Be detected in the ground state at $\theta_{lab} = 9°$ and α-particles detected at $\theta_{lab} = 20°$ on the opposite side with respect to the beam axis in the interaction of a 400 MeV ^{12}C beam with a ^{93}Nb target showing the second peak under scrutiny.

the absorbed dose and the biological effective dose delivered to the patient. Studies of the production of IMFs provide physicians with information which also allows the estimation of the production of positron emitters such as (^{10,11}C, ^{12,13}N, ^{13,14,15}O, ^{17,18}F and ^{17,18,19}Ne). The positron emitters are useful during tumour irradiation, whereby β^+-radioactive nuclei are produced when the projectile interacts with the nuclei of the irradiated tissue [Pön04]. The spatial distribution of such β^+-activity can be detected and imaged by means of Positron Emission Tomography (PET) [Eng04]. Therapy monitoring is performed by comparing the β^+-activity distributions with an expected pattern which is calculated on the basis of the treatment plan and the duration of the irradiation.

The motivation for the IMF measurement is to further study the underlying reaction mechanisms involved in the production of IMFs emitted in the interaction of light systems such as ^{12}C + ^{12}C and ^{16}O + ^{12}C. The purpose was to extract the complete energy spectra of the following isotopes ^{6,7}Li, ^{7,9}Be, ^{8,10,11}B, ^{11,12,13,14}C, ^{13,14,15}N, ^{15,16,17}O, ^{17,18,19}F and ^{19,20}Ne in the interaction of ^{16}O with ^{12}C at an incident energy of 235 MeV. The double differential cross-sections of these IMFs were measured over an angular range between $\theta_{lab} = 8.5°$ and 50°. At these incident energies above 10 MeV/u different reaction mechanisms to deep-inelastic and fusion reactions such as binary fragmentation and nucleon transfer have to be introduced.

> The experimental advantages of using light projectiles and target nuclei in the entrance channel is that the reaction products are detected with a low energy threshold, good mass and charge separation of the ejectiles as well as good energy resolution.

The historical motivation for undertaking this study is outlined in this chapter of the thesis. Different reaction mechanisms involved in the production of IMFs in the interaction of two nuclei at incident energies of 10 to 35 MeV/u are also re-visited. The experimental setup as well as the technique applied in both the coincidence and the inclusive measurements is explained in Chapter 2.

Chapter 3 deals with the online data taking as well as the offline data analysis. In this chapter, the offline detector calibrations and the extraction of energy spectra are discussed in detail. The correction for the H contamination of the target used in the coincidence measurements which is applied during the extraction of the energy integrated angular distribution, in particular, is described in detail.

In Chapter 4 the theory used to interpret the experimental data is described. This includes the theory used in GEANT4 to interpret the QE break-up mechanism as well as the Boltzmann master equations (BME) used to interpret the energy spectra of the IMFs in the inclusive measurements.

Chapter 5 presents the experimental cross-sections as well as comparisons with the theoretical calculations of these cross-sections measured both in the coincidence and inclusive experiments. The summary and conclusions of this work are presented in Chapter 6. Complete set of the cross-sections of the coincidence measurements can be found in Appendix A, while the cross-sections of the IMF measurements are shown in Appendix B.

Chapter 2

Experiments

2.1 Overview

Two different experiments were performed to test and consolidate our understanding of the interplay of the reaction mechanisms involved in these reactions. The first experiment was a coincidence measurement, while the second experiment was based on inclusive measurements.

The first experiment, as mentioned in Chapter 1, was initially proposed in project PR88, which was conducted at iThemba LABS. The aim of the PR88 was to measure, in a coincident measurement, the correlations of ^{8}Be fragments and α-particles produced in the interaction of ^{12}C with ^{59}Co and ^{93}Nb target nuclei at an incident energy of $E_{lab} = 400$ MeV. The analysis of PR88 revealed a second peak about 28 MeV below the QE break-up peak as mentioned in Chapter 1. As mentioned in Sec. 1.3 PR88 was supplemented by the follow-up experiment PR136. In the measurements of the PR136, the break-up of ^{12}C into ^{8}Be fragments and α-particles was further studied in the interaction of ^{12}C with ^{12}C, ^{93}Nb and ^{197}Au at the same incident energy of $E_{lab} = 400$ MeV. In the analysis of PR88 data the second peak was assumed to be originating from the interaction of the projectile with hydrogen contamination on the target foils. In order to verify this hypothesis the measurements of PR136 were also performed using a $(CH_2)_n$ target. The $(CH_2)_n$ was used due to its hydrogen abundance which would enable the ^{12}C beam to interact more often with the hydrogen nuclei. In this experiment the pre-scaled singles were also measured. These singles were the ^{8}Be fragments and α-particles which were measured individually; only 20% of the actual detected fragments were stored.

The second experiment was based on the study of the reaction mechanisms involved in the production of Intermediate Mass Fragments (IMFs) using two different ion beams of ^{12}C and ^{16}O ions. The first experiment of the inclusive measurements was based on the interaction of a 400 MeV ^{12}C beam with a ^{12}C target. From this measurement complete energy spectra of isotopes ranging from Lithium to Oxygen were extracted. The second experiment of the inclusive measurements was based on the interaction of an $E_{lab} = 235$ MeV ^{16}O beam with ^{12}C target. Complete energy spectra ranging from Lithium to Neon isotopes were extracted from these measurements.

This chapter discusses the experimental set-up for both the correlations measurement and the inclusive measurement. It commences by explaining all the common aspects used in both measurements. The electronic set-up of the correlation measurement is discussed after the discussion of common aspects and is followed by the inclusive measurement. The last part explains the computer system as well as the VME crate.

2.2 Experimental Facility

The study of correlated ^{8}Be and α-particles as well as the inclusive measurements for the study of the production of IMFs were carried out in the A-line scattering chamber situated at iThemba LABS. The A-line scattering chamber is about 1.5 m in diameter and consists of a target ladder at the centre and two rotatable arms to host the detectors. Since both experiments were performed in the A-line scattering chamber at iThemba LABS, they shared several similar techniques and layout. Both the coincidence measurements and the study of production of IMFs made use of the two detector telescopes. This section discusses all common aspects used for both the correlation and inclusive measurements.

2.2.1 iThemba LABS

iThemba LABS is a multi-disciplinary facility operated by two Solid Pole Injector cyclotrons, namely, SPC1 and SPC2, and a Separated Sector Cyclotron (SSC). It provides particle beams for different purposes, such as the production of Radioactive Isotopes mainly for medical purposes, proton and neutron therapy, and also for nuclear physics research. The experimental facilities used in nuclear physics research include the γ-ray spectrometer AFRODITE, the A-line nuclear reaction scattering chamber, the K600 magnetic spectrometer and a neutron detection vault. The layout of the iThemba LABS facility is shown in Fig. 2.1. Table 2.1 shows a list of abbreviations of the facilities shown in the cyclotron figure. This facility is situated near Somerset West in Cape Town, South Africa.

2.2.2 Beams

The SSC is a K200 separated sector cyclotron which is capable of accelerating proton beams up to an energy of 200 MeV. It can also accelerate heavier ions to energies up to 33.3 MeV/nucleon depending on the beam species and charge states. In order to generate the beams of ^{12}C and ^{16}O, an Electron Cyclotron

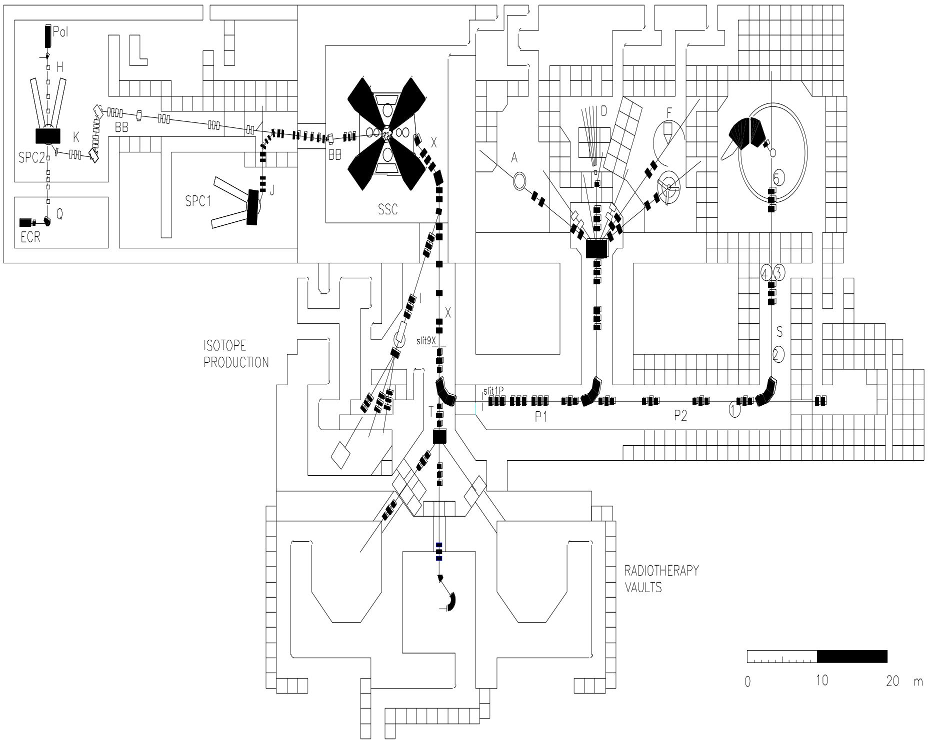

Figure 2.1: The layout of the cyclotron facility at iThemba LABS.

Resonance (ECR) ion source was used. The ECR ion source is based on a plasma, which is held in an open magnetic trap. This ion source makes use of an alternating Radio Frequency (RF) of 14 GHz, which is used to accelerate electrons. Permanent magnets and electromagnets are used to confine the plasma where electrons gain energy by absorbing microwave power resonantly. CO_2 gas was used to generate a ^{12}C beam. The ^{12}C atoms were dissociated from the O_2 atoms when interacting with electrons inside the chamber. After the dissociation process, the ionization was started by stripping electrons from the ^{12}C. In the present study, the ^{12}C with 5+ charge state was used for 400 MeV beam energy. The charge state selection was performed by using a +20 kV which accelerate highly charged ions from the positive polarity inside the chamber and selected the ions by using the bending magnets and injecting into the SPC2.

An ^{16}O gas was used for the $^{16}O_2$ ion beam. A similar process was implemented to dissociate the gas and form ^{16}O ions, which were then ionized and the desired charge state ions were selected and extracted from the ECR ion source and were transmitted to the SPC2 for further acceleration. In the case of the ^{16}O beam measurement a 6+ charge state was used for 235 MeV beam energy. The ECR ion source generated and accelerated those ions to 20

Table 2.1: Abbreviations used on the layout of the cyclotron facility

Abbreviation	Full name
A	A-line Scattering Chamber vault
D	Collimated neutron beam vault
ECR	Electron Cyclotron Resonance ion Source
F	γ-ray detectors (AFRODITE)
IP	Isotope production facility
L	Low-energy experimental vault
Pol	Polarised-ion source
SPC1	Solid-pole injector cyclotron for light-ions
SPC2	Solid-pole injector cyclotron for heavy and polarised ions
SSC	Separated Sector Cyclotron
TC	Isocentric neutron therapy vault
TR	Horizontal proton therapy vault
K	K600 magnetic spectrometer

keV/u and injected the ions into a SPC2, which then accelerated the ions to 5% of the desired beam energy. From the SPC2, the beam was injected into the SSC, which then accelerated the ions to the desired beam energy. The ion beams were delivered to the A-line scattering chamber where the experiments were performed.

2.2.3 Scattering Chamber

The scattering chamber is about 1.5 m in diameter and is situated in the A-line vault at iThemba LABS shown in Fig. 2.4. The chamber is equipped with two rotatable detector arms. These arms can be rotated remotely to the desired angles relative to the beam axis. The aluminium target ladder is mounted at the centre of the scattering chamber and can host five different targets arranged vertically. Both the detector arms and the target ladder can be remotely controlled using a control unit in the data room. The chamber has a viewing window sealed by a lead glass which is situated above the incoming beam pipe. This window is used for a closed-circuit television camera to view the beam spot on the ruby target when aligning and focusing the beam. The chamber is also equipped with other ports which are fitted with feedthroughs for the different detector cables. The cable patch-panel in the vault corresponds to the one in the control room. The patch-panel consists of slots for the high voltage power (SHV) situated at the top part, followed by the 93 Ω at the middle slots and the 50 Ω signal cables at the bottom. The SHV cables are used to supply the high voltage to the detectors, the pre-amplifiers and the target ladder. The cables are wired from the vaults to the data room using the same types of cables. Before the beam is delivered, the chamber must be pumped down and kept under high vacuum. During the experiment, the pressure inside the scattering chamber was kept around 10^{-5} mbar, which was achieved through the following procedure. First a rotary pump was switched on to pump down the chamber to a pressure of 1 mbar, after which a turbo pump was used to reach a pressure of 10^{-3} mbar. At this pressure a cryogenic pump was used to reach a pressure of 10^{-5} mbar. In order to protect the Si detectors while under vacuum, a holding bias of 10% of the operating bias was applied. A typical arrangement of the experimental set-up for the correlation experiment, is shown in Fig. 2.2.

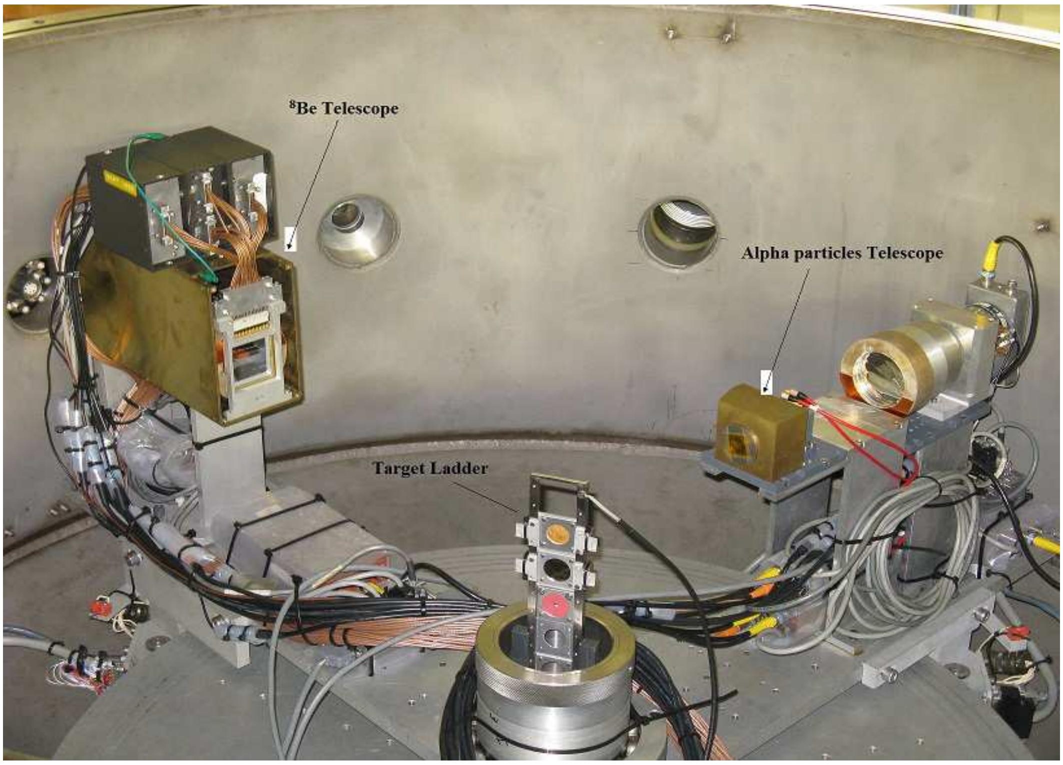

Figure 2.2: The A-line scattering chamber showing the experimental setup with detectors mounted on the rotatable arms and the target ladder at the centre

2.2.4 Targets

The targets were mounted on the ladder, which can house five different targets, as shown in Fig. 2.3. The δ-electrons released from the target are deflected away from reaching the detector by means of high voltage supplied to the target ladder and by permanent magnets mounted on both sides of the target ladder (see Fig. 2.3). The target angle can be changed by rotating the target ladder clockwise or anti-clockwise. The change in the target angle allows the target to be visible to the full solid angle of the detector. The correlations experiment was performed over two weekends, while the inclusive experiment was performed over four weekends, two weekends using the ^{12}C beam and the other two weekends using the ^{16}O beam. During the first weekend, the target ladder for the correlation measurement hosted a ^{197}Au, a ^{93}Nb, a $(CH_2)_n$, an empty target and a ruby target with a 3 mm diameter hole used to align and focus the beam on the centre of the target. During the second weekend, the ^{93}Nb was replaced by the ^{12}C target. During the inclusive measurement a 0.22 mg/cm^2 thick ^{12}C target was used for data taking. A ruby target is a scintillating material which gives off light when interacting with radiation. The ruby target was used to align the beam at the centre of the target by using the 3 mm diameter hole. The beam was directed through the 3 mm ruby hole and monitored for sparks by using a closed-circuit television (CCTV) camera. Table 2.2 shows a list of different targets used for both the correlations and inclusive measurements.

i **Target Uniformity**
A method proposed by Adair was implemented for checking the uniformity of the ^{12}C target used in the inclusive measurements [Ada72]. This was achieved by viewing the change in energy peak position of an 8.78 MeV α-particle emitted from a ^{228}Th source when passing through the target under vacuum. The collimator was used to guide the α-particles to different positions on the target. The measurement was first performed by using an empty target and the α-particle energy spectrum was plotted with an energy peak position corresponding to a 145.5 channels. Then the collimator was placed at five different positions on the target, at the centre, one third and two third below and above the centre of the target. Table 2.3 shows five different positions on the target and their corresponding α-particle peak position on the energy spectrum in channel number. The consistency of the 8.78 MeV α-particle peak position on different target position shows that the target thickness is uniform.

2.2.5 ΔE-E Technique

Both measurements used the ΔE-E technique for particle identification and mass separations. In this technique the energy loss in the ΔE detector is plotted against the energy deposited by a detected particle in the E stopping detector. It is easier to separate the isotopes with this technique due to their different stopping powers which lead to different energy losses when passing through the detector. For the triple element telescope, two sets of ΔE-E PID spectra were generated using the ΔE_1-ΔE_2 and ΔE_2-E stopping detector, two energy spectra were summed together to produce a full energy spectrum.

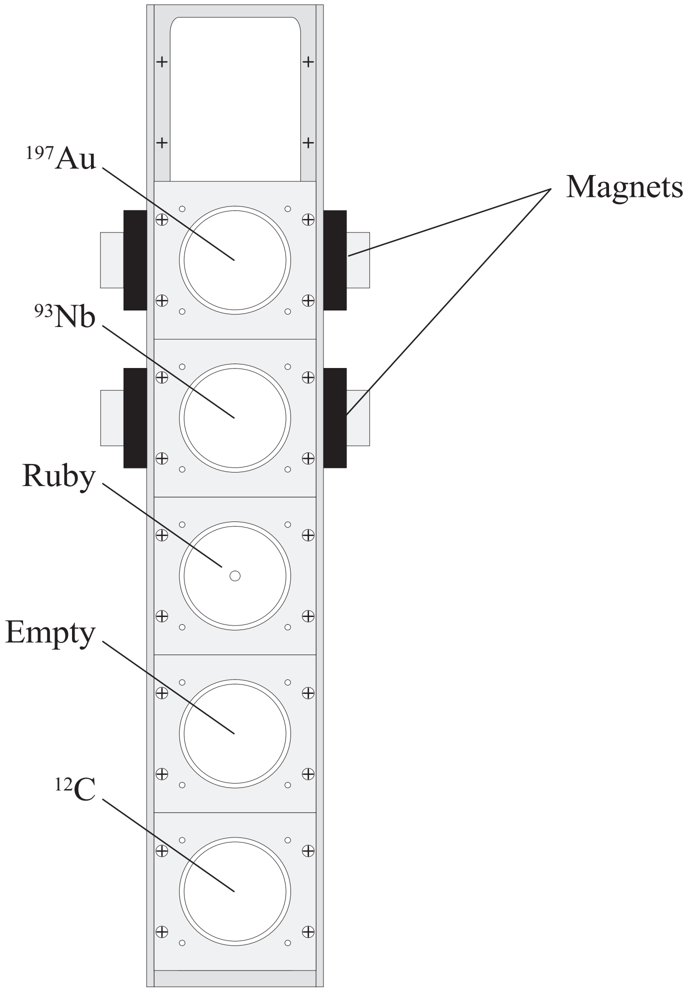

Figure 2.3: A schematic diagram of the target ladder showing five different targets as well as the permanent magnets.

Table 2.2: List of targets and their thicknesses used in both coincidence and inclusive experiments

Target material	Thickness (mg/cm^2)
^{12}C	0.22
^{12}C	1.053
^{93}Nb	1.05
^{197}Au	0.9

2.3 Correlation Experiment

This section describes both the detector and the electronic set-up which was used to process the signals from both the ^{8}Be detector arm and the α-particle detector telescope.

Table 2.3: List of α-particle positions on the target and their corresponding energy peaks on the spectra

Target position	8.78 MeV α-particle peak (channel)
2/3 above	144.1
1/3 above	143.8
Centre	143.9
1/3 below	144.0
2/3 below	144.0

2.3.1 Detectors and pre-amplifiers

The α-particle telescope consisted of two Silicon ΔE detectors followed by a NaI stopping detector, while the ^{8}Be detector telescope consisted of a Double-Sided Silicon Strip Detector (DSSSD) followed by a NaI stopping detector. Ortec Model 142A and 142B preamplifiers were used for the Silicon Surface Barrier (SSB) detector signals. These preamplifiers are low-noise, fast-rise-time, charge-sensitive preamplifiers designed for optimum performance with charged-particle or heavy-ion detectors. The DSSSD used 2×8 channels charge sensitive pre-amplifiers which were developed specifically for reading out the DSSSD [Ste05]. The individual preamplifier boards are based on the design by Bassini *et al.* [Bas91]. Special care was taken when selecting the input Field-Effect Transistors (FETs) to optimise the capacitive matching with the DSSSD [Ste05]. These preamplifiers were mounted inside the scattering chamber in close proximity to the detector in order to reduce the capacitance of the input connections and noise pick-up. Three pre-amplifier boxes were used to connect all 18 outputs from 16 vertical and two signals from horizontal odd and even strips. For the NaI detector, an Ortec 113 light sensitive pre-amplifier, designed for use with dynode or anode signals from photomultiplier tubes was used. The charge in the photomultiplier output pulse was integrated with the input capacitance of the preamplifier to produce a voltage pulse [Ort113]. Short BNC cables were used to connect the detectors to the pre-amplifiers. The purpose of the pre-amplifiers was to convert a charge pulse to a voltage step. The pre-amplifiers for both ^{8}Be and α-particle detector telescopes were mounted on the rotatable detector arms inside the scattering chamber to prevent them from picking up the background.

2.3.2 Detector setup

Since ^{8}Be is unbound and decays into two constituent α-particles, a DSSSD was used to measure the two α-particles in coincidence. The DSSSD has a square surface area of $50 \times 50\ mm^2$ and consists of 16 vertical anode and 16 horizontal cathode strips of 251 μm thickness. The strips are 3 mm wide separated by an inter-strip gap of 100 μm. Instead of wiring each strip to its

Table 2.4: Detector thickness and their conventions used in the correlation experiment

Detector	Thickness [μm]	Convention	Experiment
Si strip	251	DSSSD	Correlation: ^{8}Be telescope
Si	21	ΔE_1	Correlation: α-particle telescope
Si	1017	ΔE_2	Transmission detector for Correlation: α-particle telescope
NaI	6.35×10^4	NaI	Stopping detector on ^{8}B and α-particle telescopes

own output channel of electronics to give 256 pseudo pixels, the experimental set-up was simplified by bussing the odd and even numbers of the horizontal strips together to supply only one odd (O) and one even (E) signal respectively, as described in Ref. [Ste05]. In addition, all vertical strips were read out individually providing 18 channels of ΔE information from the DSSSD. These signals were fed to a 2×8 channel pre-amplifier.

The NaI detector is a cylindrical aluminium casing which houses a crystal, $3''$ diameter and $2''$ in length, and is coupled to a photo multiplier tube. The photo multiplier tube is connected to a base which provides connections for high voltage and BNC signals from the anode and the fifth dynode. Since the NaI detector is hygroscopic, it is equipped with a 63.5 mm diameter entrance window consisting of a 7 μm thick Havar foil to prevent the atmospheric moisture to enter the detector. Another reason for using Havar as entrance window is its strength, which allows the design to be very thin to eliminate particle energy loss. A brass collimator with an opening radius of 31 mm was placed between the DSSSD and NaI detector. The ^{8}Be detector telescope subtended a solid angle of 11.03 ± 0.02 msr. The DSSSD detectors efficiency calibrations were performed using the Monte Carlo Code UNIMONTE described in Chapter 3.

The α-particle detector telescope was mounted on the detector arm on the opposite side with respect to the beam axis inside the scattering chamber. It consisted of a 21 μm thick Si ΔE_1 surface barrier detector, a 1017 μm thick Si ΔE_2 surface barrier detector followed by a $3''$ diameter by $2''$ length NaI stopping E detector. The advantages of using Si detectors include the ability to operate at room temperature without excessive current leakage [Tyk95][Sin68]. They also have a thin dead layer, and have good energy resolution. A 50 mm thick brass collimator was mounted in front of ΔE_1 and was used to protect the α-particle detectors from radiation damage. A 30 mm thick brass collimator insert with a 14 mm diameter opening was fitted into the collimator hole thereby subtending a solid angle of 1.829 ± 0.012 msr.

While the ^{8}Be fragments were measured in their ground state at a fixed lab angle of $\theta_{lab} = 9°$, the coincident α-particles were measured over an angular range between $\theta_{lab} = 16^\circ$ - 26° on the opposite side of the beam.

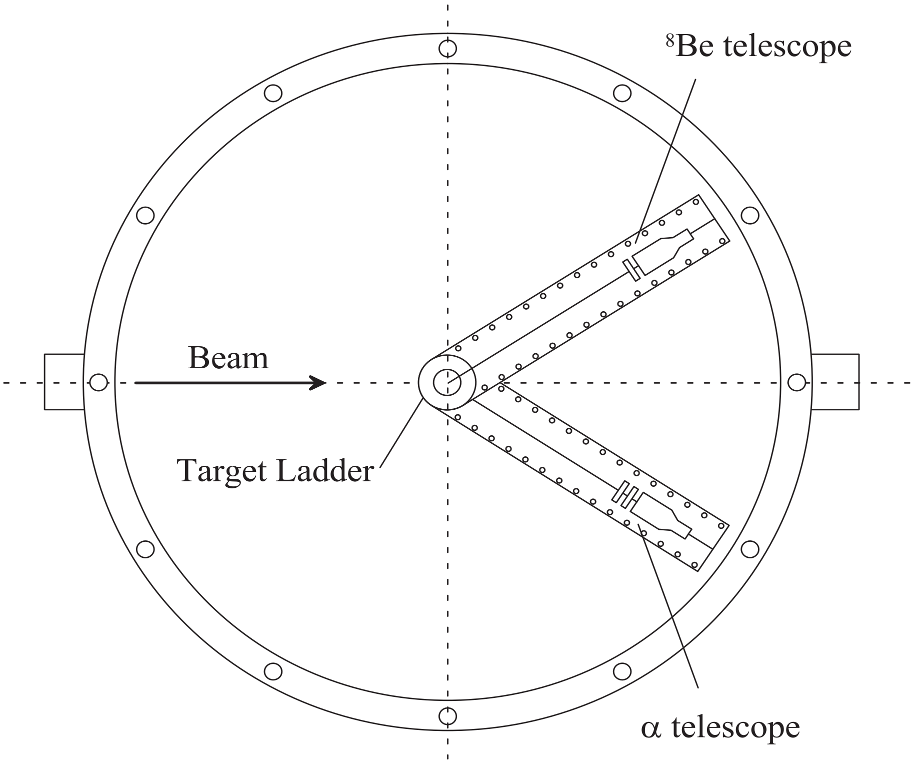

Figure 2.4: A schematic diagram of the A-line scattering chamber showing the beam direction and two rotatable arms hosting the ^{8}Be and α-particle detectors.

2.3.3 Electronic setup

The following sections outline the details of the electronic modules used to process both linear and logic signals of the correlation experiment.

i **Logic signals of the ^{8}Be telescope**
The logic signals have a fixed shape and are used to provide the timing information of detected particles. A 16-channel CAEN amplifier was used to amplify the analog signal from the DSSSD and generate the fast analog signal which was fed into the Constant Fraction Discriminate (CFD). The role of the CFD is to process the fast pulse and produce a logic signal when a constant fraction of the fast pulse peak amplitude is reached [Met04]. From the CFD, the signal was fed into a 2×8 discriminator module which is used to set the threshold. The timing signals from the 2×8 discriminator were fed into the coincidence box in order to search for the coincidence between two strips. The analog signal from the NaI detector's pre-amplifier was fed into a Timing Filter Amplifier (TFA), which amplifies the analog and

transmits the signal to the CFD for delay and setting of the thresholds. For every coincidence between the strips, the signal was fed into a 4-fold logic unit (4FLU) used to search for coincidence between the DSSSD and NaI detector and perform an AND operation. For every coincidence the signal was transmitted to a 4FLU to search for a coincidence between the α-particle and the ^{8}Be telescope, and also fed into a Gate and Delay Generator (GDG) which transmits the signal to the timer to count events and send every 20th event to the pattern register and scaler input. Once a coincident event is established, a gate signal is supplied to the linear gate stretcher (LGS) unit in the linear electronics and this allows the linear signals to be processed by the Analog to Digital Converter (ADC) as shown in Fig. 2.5.

ii **Logic signals of the α telescope**

The α-particle detector telescope logic requirement to process the detector signals for lower and higher energy α-particles was set as follows: $(\Delta E_1 \cap \Delta E_2) \cup (\Delta E_2 \cap E)$. The timing signal for the two Si detectors were transmitted from individual charge sensitive pre-amplifiers to the data room through 50 Ω BNC cables, which were patched to the individual timing filter amplifiers modules. After the amplification, the signals were fed to individual CFDs to set the threshold and for delaying. For every signal that met the CFDs requirement, the signal from CFDs were transmitted to a 4FLU in order to search for coincidence between the ΔE_1 and ΔE_2. The ΔE_2 timing information was used to set the timing reference for the ΔE_1-ΔE_2 subset, because the detector is thicker and the signal is more stable compared to the signal from ΔE_1. The timing signal from the NaI was generated following a process similar to that used by the NaI detector for ^{8}Be telescope. The analog signal from the NaI detector's pre-amplifier was fed into a Timing Filter Amplifier (TFA). After the amplification the signal was transmitted to the CFD to generate the timing signal used for timing information. From the CFD, the timing signal of the NaI detector was fed into a 4FLU in order to search the coincidence for high energy α-particles between ΔE_2 and NaI detectors. For every coincidence between ΔE_1-ΔE_2 and ΔE_2-NaI, the signal was fed into 4FLU to perform the AND operation. For every valid α-particle event, the signal was first fed into a GDG and transmitted to the timer to pre-scale the events, with every 20th event being transmitted to the scalers and pattern register. The signal was also fed into a 4FLU used to search for coincidence between the ^{8}Be and α-particle telescopes. The diagram in Fig. 2.5 shows the trigger logic used to establish the coincidence between the ^{8}Be and α-particle detector arms.

iii **Linear Signal of the ^{8}Be detector telescope**

The linear signals from the preamplifiers contain information about the energy, mass and charge of the detected particles. The DSSSD signals

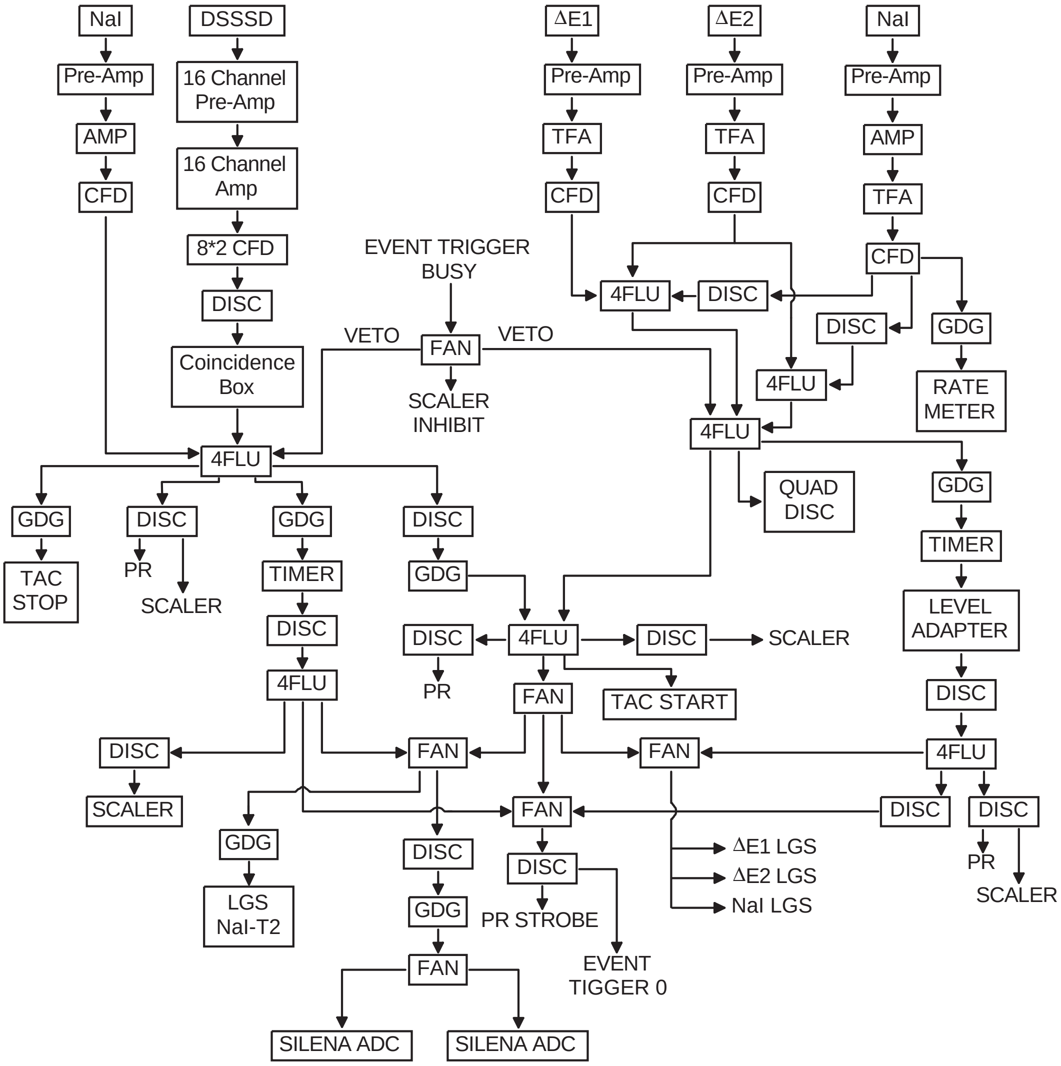

Figure 2.5: Diagram of the trigger logic for both the ^{8}Be and α-particle detector arms.

were transmitted from the 2×8 channel preamplifiers to the 16 channel spectroscopy amplifier in the data room using a 93 Ω cables as shown in Fig. 2.6. After the amplification the output was fed through the Linear Gate and Stretcher (LGS) gate to the SILENA Analog to Digital Converter (ADC) for every detector coincidence obtained using logic information. The linear signal from the NaI detector was also transmitted using a 93 Ω BNC cable from the light sensitive preamplifier to the dataroom. The signal was fed into a spectroscopic amplifier for amplification; from the amplifier the signal was fed into an Ortec (427A) delay amplifier. For every coincidence between strips and NaI, a logic gate is generated and the information is sent to the LGS to open the gate for the linear signal and fed to the Canberra ADC (8077).

iv **Linear Signal of α-particle telescope**

The 93 Ω BNC cables were used for the transmission of linear signals from the individual α-particle telescope Ortec (142) preamplifiers to the data room (see Fig. 2.6). These cables were patched to the individual Canberra (2020) spectroscopy amplifiers in the data room. The NaI detector's linear signal was also transmitted using 93Ω BNC cables from the Ortec 113 preamplifier to the spectroscopic amplifier. After the amplification, the signal was fed to the Ortec (427A) delay amplifier. For every coincidence between the α-particle detectors as well as coincidence between two telescopes, a logic gate was generated and the information was sent to the LGS on the linear side. From the delay amplifiers the signals were transmitted through the linear gates and stretcher (LGS) module to the Canberra (8077) ADCs.

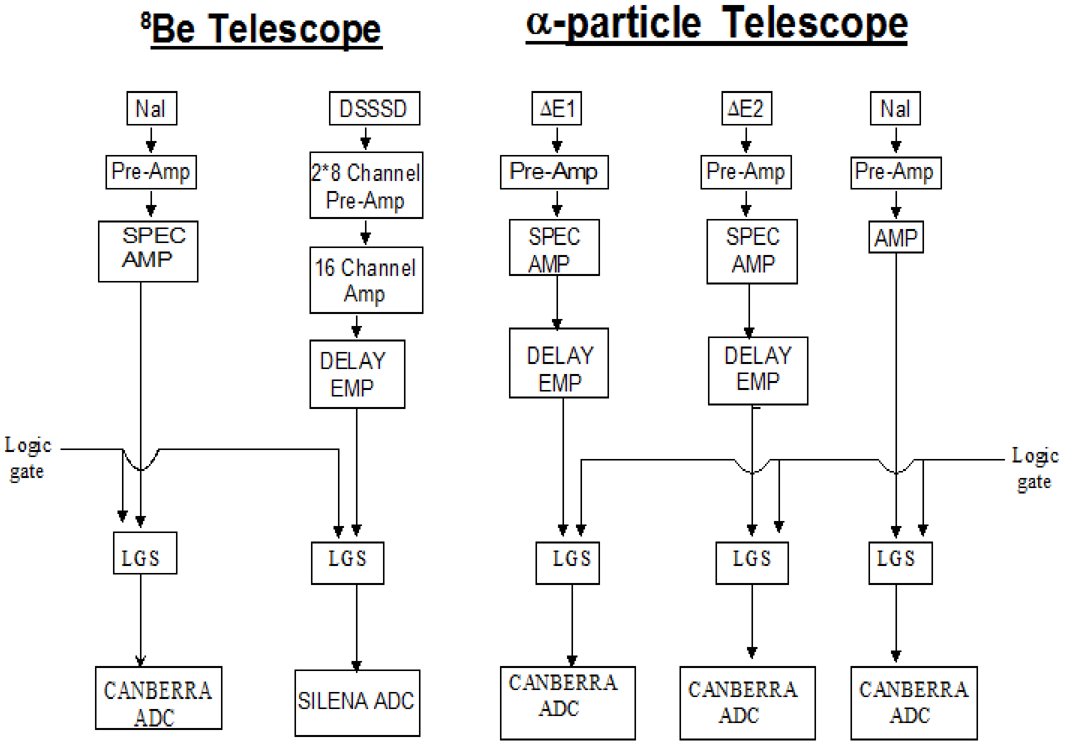

Figure 2.6: Electronic diagram used to process the linear signals for both ^{8}Be and α-particle detector telescopes.

2.4 Inclusive Experiment

This section deals with the detectors and electronic set-up which was used to process the signals for the inclusive measurement in the interaction of 400 MeV

^{12}C ions and 235 MeV ^{16}O ions with a ^{12}C target nucleus.

2.4.1 Detectors and pre-amplifiers

For the inclusive measurements two detector telescopes were used to measure different IMFs. The detector telescope denoted as (T2) was used for lighter fragments ranging from Li to Be isotopes and another telescope denoted as T1 measured IMFs ranging from B to Ne isotopes. T2 consisted of one SSB followed by a NaI stopping detector, while telescope T1 consisted of three SSB detectors. An Ortec 124B charge sensitive pre-amplifier was used for 57 μm thick SSB ΔE used for lighter fragments telescope. Two special charge sensitive pre-amplifiers for high capacitative detectors were manufactured specifically for the two 1017 μm thick SSB detectors by the INFN-MILANO group. These two 1017 μm thick SSB detectors were used as a transmission and stopping detectors to measure heavier fragments on telescope T1. These pre-amplifiers are built with high capacitance in order to avoid the saturation of the detector signal. The pre-amplifier casings were built in-house. The NaI stopping detector used a similar Ortec 113 light sensitive pre-amplifier as explained above in the correlations measurement. Table 2.6 shows the output comparison between the Ortec pre-amplifiers and the high capacitative pre-amplifiers built at INFN-MILANO.

Table 2.5: Detector thickness and their conventions used in the IMF experiment

Detector	Thickness [μm]	Convention	Experiment
Si	57	T1A	IMF $5 \leq Z \leq 10$
Si	93	T2A	IMF ΔE for $3 \leq Z \leq 4$
Si	1017	T1B	Transmission detector for IMF: $5 \leq Z \leq 10$
Si	1017	T1C	IMF stopping detector for $5 \leq Z \leq 10$
NaI	6.35×10^4	NaI	Stopping detector IMF $3 \leq Z \leq 4$

Table 2.6: List of output from preamplifiers showing comparison between different preamps

Preamplifier	Input Voltage	Output Voltage
Ortec 142A	5 mV	200 mV
Canberra 2003BT	5 mV	600 mV
INFN-MILANO Preamp	5 mV	40 mV

2.4.2 Detector set-up

This experiment, as indicated in Sec. 2.1, was performed with two different ion beams of ^{12}C and ^{16}O. The detector set-up for both ion beams was similar. Two different detector telescopes (T1 and T2) were used to detect the emitted fragments.

Telescope T1 was used to measure the Projectile-Like Fragments (PLF) ranging from Boron to Oxygen isotopes in the interaction of ^{12}C with ^{12}C and from Boron to Neon isotopes produced in the interaction of ^{16}O and ^{12}C. This arm consisted of a 57 μm thick Silicon ΔE_1 SSB (T1A) and a 1.017 mm ΔE_2 thick SSB (T1B) detector, followed by a 1.017 mm SSB E (T1C) stopping detector. A 10 mm thick brass collimator block was used to shield the silicon detector telescope from radiation damage. An 8 mm thick brass collimator insert with a 6 mm diameter opening was fitted to the collimator block. The solid angle subtended by Telescope 1 as defined by the rear end of the collimator insert was 0.9081 ± 0.018 msr.

Telescope T2 was used to measure the lighter IMFs ($3 \leq Z \leq 4$) and consisted of a 93 μm thick SSB ΔE detector followed by a $3''$ in diameter and $2.5''$ in length crystal NaI stopping E detector. The NaI was used due to its high stopping power in order to stop all the lighter particles. A 50 mm thick brass collimator block was used to shield detector telescope T2. A 53 mm thick brass collimator insert with an opening of 17.1 mm in diameter was fitted to the collimator block. The solid angle subtended by this detector telescope was calculated to be 1.475 ± 0.024 msr.

The ΔE-E technique was used for particle identification and for mass separation of the various isotopes. Double differential cross-sections were measured as a function of the emission energy and angle of the detected IMF over an angular range between $\theta_{lab} = 8^\circ$ - 60° for both beams used.

2.4.3 Electronic setup

The following sections outline the details of the electronics set-up which was used to process both linear and logic signals of the inclusive experiment.

i **Logic signals**
The timing signals of the Si detectors were transmitted from the preamplifiers to the data room through 50 Ω BNC cables, while the NaI detector's timing signal was transmitted from the light sensitive pre-amplifiers through the 93 Ω BNC cable (see Fig. 2.7). Timing filter amplifiers (TFA) were used to shape and amplify the timing signals and the amplified timing signals were fed to CFDs. The outputs of the CFDs were connected to 4-fold logic units (4FLU). The 4FLU were used to perform the AND operation between T1A and T1B and between T1B and T1C for telescope T1, as well as between T2A and T2B for telescope T2. The timing signals

from the T1B and T1C detectors provided the timing reference for setting up coincidences between T1A-T1B and T1B-T1C detectors, respectively. In the case of telescope T2, the reference for the coincidence timing signal was provided by the timing signal of the T2B detector. For every T1A-T1B or T1B-T1C and T2A-T2B coincidence, the corresponding logic pulse was fanned out to the Gate and Delay Generator (GDG), a rate meter and a discriminator. The Logic Gate and Stretcher (LGS) received a logic signal from the GDG to open the gate for the linear signals to be processed by the Analog to Digital Converter (ADC). For the triple element detectors, the bit patterns were set for each detector event, and for the coincidence events between T1A-T1B and T1B-T1C to avoid particles that punched through the T1B detector contaminating the T1A-T1B particle identification (PID) spectrum. All module names and models used to process the logic signals are listed in Table 2.7.

ii **Linear Signals**

The linear signals from the preamplifiers contain information about the energies and nuclear charges of the detected particles. 93 Ω BNC cables were used to transmit the linear signals from the individual Ortec (142B) preamplifiers and also from preamplifiers for high capacitative detectors manufactured by the INFN-MILANO group, which were situated in the scattering chamber, to the data room. These cables were patched to the individual spectroscopy amplifiers in the data room. From the amplifiers the signals from T1B, T1C and T2A were transmitted to the Ortec (427A) delay amplifiers and their output were connected to the LGS, which transmit the signals to the individual Canberra (8077) Analog-to-Digital Converter (ADC) modules upon receiving a gate signal from the trigger electronics. Fig. 2.8 shows the diagram of the electronic set-up used to process linear signals for the heavier fragments arm and the light IMFs arm, respectively. Table 2.8 presents the different modules used to process the linear signals for both the correlation and IMF measurements.

2.5 CAMAC interface modules

The data acquisition (DAQ) system consists of a VME-based frontend, consisting of a processor module and a CBD-8210 CAMAC branch driver module. The CBD-8210 CAMAC branch driver module reads data from a CAMAC crate that has the following modules: Event trigger module, Pattern register module, Scaler modules and ADC modules. A brief description of these modules is provided below.

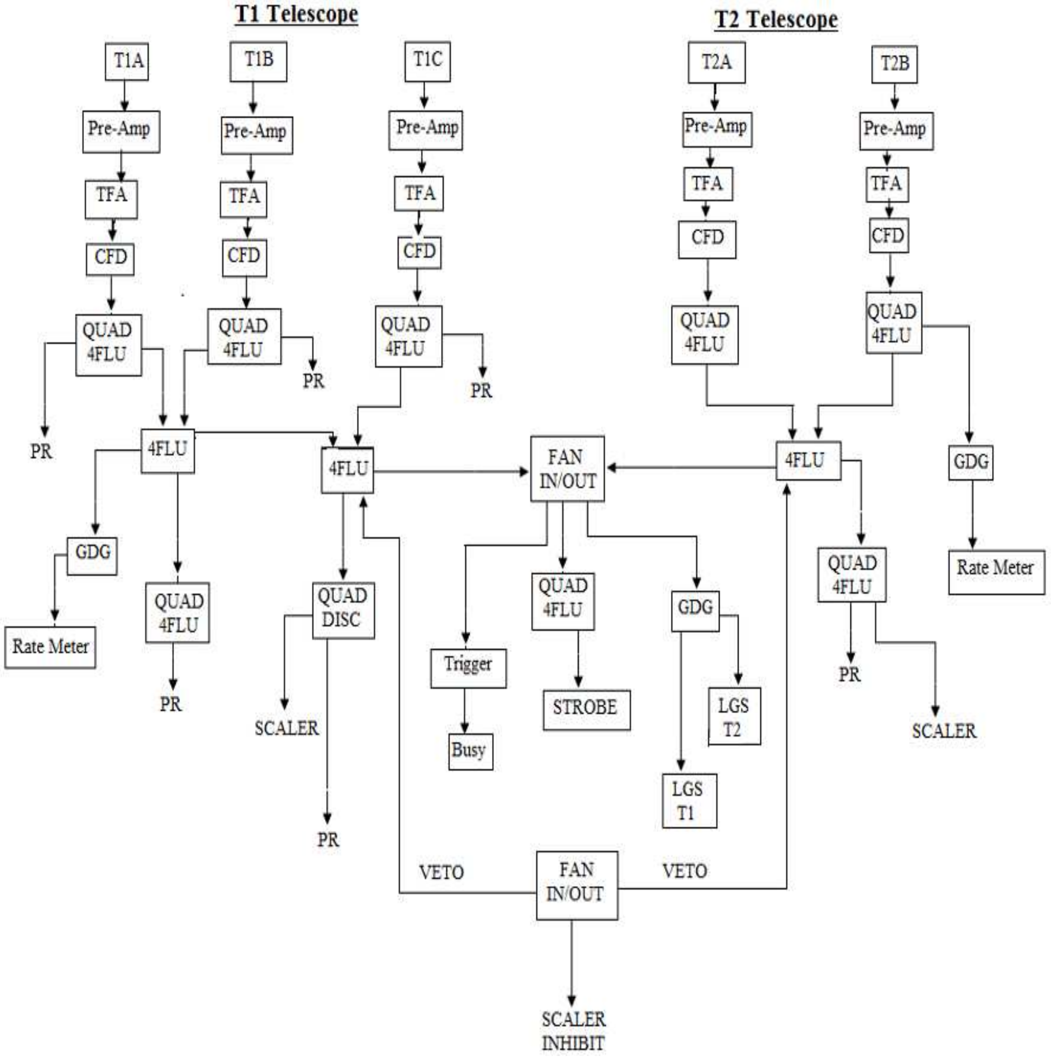

Figure 2.7: Electronic diagram used to process the logic signals of the inclusive experiment.

2.5.1 ADC module

Digitisation of the pulse height of the spectroscopy signals occurs in the NIM Canberra ADCs. The CAMAC ADCs merely hold the digitised information and pass the information to the crate controller and VME frontend when the event trigger signals are received.

2.5.2 Event Trigger module

All detector events that met the logical requirements for a valid event were accepted in a CAMAC event trigger unit module which initiated the data acquisition. For every event-trigger signal accepted by the CAMAC event trigger module, a computer busy signal was generated. This signal was fanned

Table 2.7: NIM modules used to process the logic signals for both the correlation and inclusive experiments

Module	Model
Timing Filter Amplifier (TFA)	ORTEC 474
Constant Fraction Discriminator (CFD)	EG&G ORTEC 934
4-Fold Logic Unit (4FLU)	Le Croy 365AL
Discriminator (DISC)	ORTEC 436
QUAD Discriminator	LeCroy 821
Gate and Delay Generator (GDG)	ORTEC 416
Logic fan-in-out (FAN)	LeCroy 428F
Timer	ORTEC 719
Timing Single Channel Analyser (TSCA)	Ortec 551
Counter	Ortec 875
Ratemeter	Ortec 449-2
Scalers	12-fold LeCroy 2551

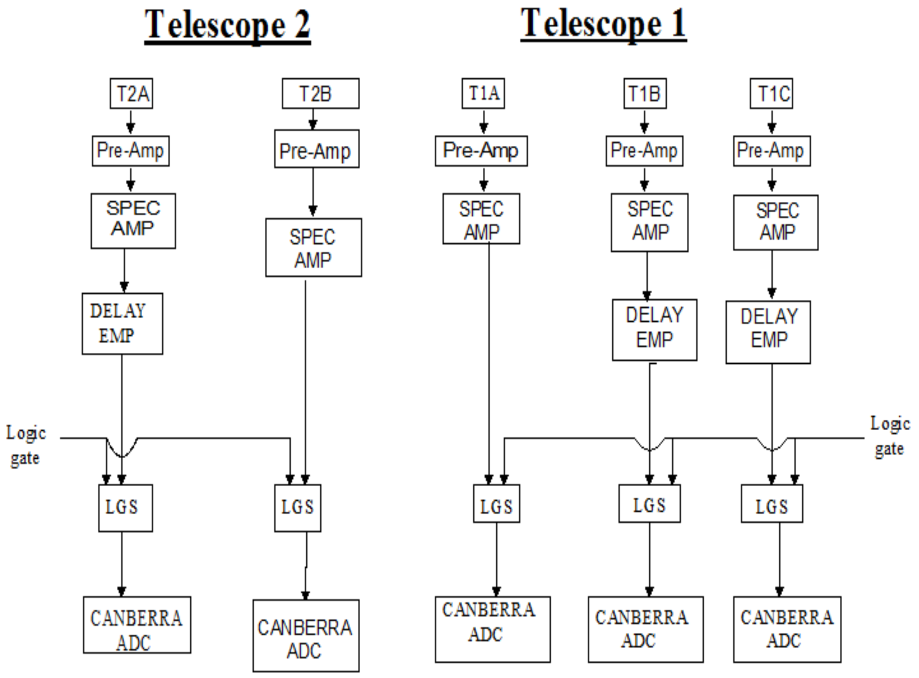

Figure 2.8: Diagram of the electronic set-up used to process the linear signals of the inclusive measurements.

out to veto the trigger electronics and also the inhibited scalers. Table 2.9 consists of all valid events for both the correlation and inclusive measurements.

Table 2.8: NIM modules used to process the linear signals for both the correlation and inclusive experiments.

Module	Model
Charge Sensitive Pre-amplifiers	Ortec 142 (SSB) 2×8-Channel Built in-house (DSSSD)
Light Sensitive Pre-amplifiers	Ortec 113 (NaI)
Spectroscopy Amplifiers	CANBERRA 2020 16-Channel CAEN N5688 (DSSSD)
Analog-to-Digital Converter (ADC)	CANBERRA 8077 SILENA ADC (DSSSD)
Gate and Delay Generator	ORTEC 416 A
Linear Gate and Stretcher (LGS)	ORTEC 542

Table 2.9: Valid events for both the correlation and inclusive measurements

Experiment	Detector coincidence	Valid events
Correlation	DSSSD-NaI	^{8}Be pre-scaled single
	ΔE_1-ΔE_2	α-particle low energy pre-scaled single
	ΔE_2-E	α-particle high energy pre-scaled single
	T1-T2	^{8}Be-α coincidence
Inclusive	T2A-T2B	Light fragment telescope
	T1A-T1B	Low energy for heavier fragment
	T1B-T1C	High energy for heavier fragments

2.5.3 Bit Pattern

The bit patterns were used for all the valid events accepted for both experiments. The prescaled singles events, coincidence and pulser events generated were sent to the pattern register module. The strobe signal was needed for the pattern register to be read out. The pattern register has slots to accept the signal cable for every valid event that satisfied the coincidence between two detectors, as well as coincidence between two telescopes in the case of correlation measurements. The input definitions for the bit patterns used in the correlation experiment are listed in Table 2.10, while Table 2.11 shows the input definitions for the inclusive experiment.

2.5.4 Scalers

All the valid detector events were counted by the two 12-fold LeCroy scalers listed with the electronic modules in Table 2.7. One set of these scalers was inhibited by the computer busy signal. Both scalers counted the total number of events in each detector telescope, the total accumulated charge and the pulser events for both correlations and inclusive measurements.

Table 2.10: Pattern register input definitions for the correlation experiment

Pattern Register	Bit Position
Telescope 1 all events	1
Telescope 2 all events	2
Telescope 1 pre-scaled singles	3
Telescope 2 pre-scaled singles	4
T1-T2 coincidence	5
Pulser	6

Table 2.11: Pattern register input definitions for the inclusive experiment

Pattern Register	Bit Position
Telescope 1 all events	1
Telescope 1 low energy events	2
Telescope 1 high energy events	3
Telescope 2 all events	4
Pulser	5
Telescope 1 element A	6
Telescope 1 element B	7
Telescope 1 element C	8

2.6 Current integrator

The beam stop of the A-line was connected to a Brookhaven Instrument Current integrator (BIC 1000C) in order to measure the amount of current registered at the beam stop. This module allows the current integrator to determine the number of pulses output for every unit of accumulated charge. The BIC 1000C module provides digital output pulses with a width with different ranges in μs.

2.7 Pulser

The output of the BIC 1000C was used to trigger the pulse generators as follows. The BIC digital output was connected to a timing single channel analyzer (TSCA), the positive output of which was connected to a timer module. The pre-scaled signals from this timer module were connected to a gate and delay generator which externally triggered the tail pulse generator as well as the LED pulse generators were used to generate pulses for the NaI detectors. The generated pulser signals for all Si detectors were fed to the test input of the charge sensitive preamplifiers, for the NaI detector the pulser signal was fed to the LED input on the base. The output from the GDG was also connected to a discriminator to feed both the inhibited and uninhibited scalers, as well as a pattern register. In order to determine the electronic dead time the ratio between the number of counts in a pulser spectrum and the measured number of counts from the inhibited scalers was used.

2.8 Clock

A constant running timer was connected to a TSCA to determine the computer dead time. The output of the TSCA was fed to both inhibited and uninhibited scalers. The computer dead time can be obtained from the comparison between inhibited and uninhibited scalers. A dead time of less than 5% was acceptable.

Chapter 3

Data Analysis

3.1 Overview

This chapter describes the experimental data taking and data analysis for both experiments. In the case of the correlation experiment, the data were extracted for all the coincidence events of ^{8}Be and α-particles. The pre-scaled singles events of ^{8}Be and α-particles were also extracted. The double differential cross-sections of IMFs ranging from Li to Ne isotopes were extracted for the inclusive IMF experiment. A brief explanation of the procedure for the online data extractions and signal handling is given, followed by the energy and efficiency calibrations for all the detectors used in both the coincidence and IMF experiments. Finally, the offline data analysis and the error analysis are discussed.

3.2 Online Data Taking

This section discusses the online signal handling and the triggers used to select the events of interest for both the coincidence and IMF measurements.

3.2.1 Signal Handling

Before the measurements were started, the beam was aligned to the centre of the target by using a ruby target with a 3 mm hole, as explained in Section 2.2.4. After the beam had been aligned to the centre of the target the coincidences between all the detector combinations were set up. The timing signal of one of the detectors was widened by using a constant fraction discriminator (CFD) in order for the narrower signal to fall inside the gate while is viewed on the oscilloscope. The CFD thresholds were then set in order to avoid peaking up the noise from the detector signals. The detector signals of interest in the correlation measurements were triggered by both single and coincidence events as mentioned in Chapter 2. The triggers for all the valid events are shown in Table 2.9. In the case of the α-particles detector telescope an event trigger was generated for both the particles emitted with low energies below 50 MeV which stop inside the transmission detector as well as for particle with higher energy that stop inside the NaI detector. The low energy trigger was generated for events between $\Delta E_1 \cap \Delta E_2$ and stopping in E_2 while the high energy trigger covered events fulfilling $\Delta \mathrm{E}_2 \cap E$. In the case of the ^{8}Be detector telescope, two triggers were generated. The first trigger applied to coincidence events between any two strips of the DSSSD and the second trigger was generated for the coincidence between the DSSSD and NaI stopping detector. A further trigger defined the coincidence events between the ^{8}Be and α-particle detector telescopes. The coincidence between the two telescopes was set by using the time signals of these detector telescopes. The ^{8}Be time signal was widened by using a CFD to ensure that the narrow coincident α-particle signal fell inside this gate. To tune the electronics for coincidence between the ^{8}Be and α-particle telescope a $(\mathrm{CH}_2)_n$ target was used. This allowed higher coincidence yield between the elastically scattered ^{12}C beam and recoiling hydrogen. During this procedure the coincidence level between the DSSSD strips was set to one, the elastically scattered ^{12}C ions were measured with the α-particle detector and the coincident protons were measured with the ^{8}Be detector telescope. A nuclear reaction kinematics program (KINMAT) [Che80] was used to determine the geometry of the correlated fragment. From this simulations the coincidence were obtained when the DSSSD is placed at 9° to measure the elastic ^{12}C and the other telescope were placed on the opposite side with respect to the beam axis between $\theta_{lab} = 16°$ and 30°.

The detector signals of the inclusive measurement were handled slightly different. No coincidence between the two telescopes was required for these measurements. In the case of the lighter fragments ($3 \leq \mathrm{Z} \leq 4$) telescope, a trigger was generated for coincidences between Silicon ΔE and NaI stopping detectors for all events stopping inside the NaI detector. The signal was processed as discussed in Sec. 2.4.3 for every light particle that stopped inside the NaI. In the case of heavier fragments ($5 \leq \mathrm{Z} \leq 10$), two triggers were generated for valid events; a first trigger was set for lower energy fragments that stopped inside the Si (T1B) transmission detector, while the higher energy particle trigger was set for particles that stopped inside the Si (T1C) stopping detector, following the logic of $(\Delta \mathrm{E}_1 \cap \Delta \mathrm{E}_2) \cup (\Delta \mathrm{E}_2 \cap \mathrm{E})$ as also discussed in Section 2.4.3.

3.2.2 Data Taking

Before the data could be recorded, some important procedures had to be followed. Both the linearity and zero offsets of all the ADC modules were checked by using a precision pulser. This was done by setting the gain on the precision pulser to maximum and recording the peak position on the spectra. After this, it was set to three quarters, to half and lastly to one quarter for recording all the pulser peak positions. The gain was plotted against the peak position to adjust the DC-offset of the ADC module if necessary; i.e. depending on the zero-intercept of this linear fit.

The count rate of the detectors was monitored by connecting a rate meter to the stopping detector of the telescope placed in the most forward angle. The count rate was used to monitor the beam background. The beam background was monitored by taking the ratio between the count rate without the target and the count rate with the target. A ratio of less than 10% was considered good enough for data taking. The online data taking for both the coincidence and inclusive measurements for accepting beam on target followed similar procedures that were initiated by aligning the beam and focusing through a 3 mm diameter hole on the centre of a viewer target, see Section 2.2.4.

The standard ΔE-E technique was implemented for the extraction of the data on ^{8}Be fragment and α-particle telescopes, as well as on detector telescopes of the inclusive IMF measurements. The PID spectra were monitored to check if all the events were recorded. Once all the detectors were biased, the signals from the detectors were viewed on the oscilloscope.

The correlation experiment ran over two weekends with data collection of two hours for each run and followed by a five-minute empty run to monitor the background. The average beam intensity of 3 nA was used during the data taking. The data for the offline calibration of NaI detector were collected by measuring the elastic peak of ^{12}C ions interacting with ^{197}Au target at different emission angles to be explained in Section 3.4.4. The ^{197}Au target was also used to collect data for the NaI detector offline calibration as explained below under NaI detector calibration. The ^{197}Au target was used because of the low recoil energy of the ^{197}Au which results in a sharp elastic peak.

In the case of the inclusive measurements, a 0.22 mg/cm^2 thick ^{12}C target was used for data taking. The experiment was performed over two weekends using a 400 MeV ^{12}C ion beam and for two weekends using a 235 MeV ^{16}O ion beam. The data were collected during one-hour runs each followed by five minutes runs with the empty target to monitor and record the background. A beam intensity of about 40 nA was used for data taking.

3.3 Data acquisition program

The data acquisition system is made up of two distinct parts, the front-end and the back-end [Mur10]. The front-end communicates with the electronics and builds an event from all the electronic modules. The back-end receives these events from the front-end and performs online sorting for the user with graphical displays for diagnostic purposes [Mur10].

If the desired logic level has been reached from the electronics, and if the vetoes do not cancel the signal, a custom trigger module is triggered. This initiates the read out of the data which is operated via a ferrabus. The ferrabus data is put into a VME dual port memory module. The VME processor then packs the events preceded with a header, detailing what type of event it is into data blocks.

The code executed on the VME computer is user customisable by means of C header files. The header files exist for different steps of the acquisition system, i.e. configuration, initialisation of DAQ, begin run, end run, and event read-out. The user then has the ability to dictate what happens at each of these positions of the acquisition process. These files are compiled and appended to a VME executable image that is then transferred to the VME via trivial file transfer protocol (TFTP) and then become front-end executable code.

The online and offline data analyses were performed via XSYS software. The XSYS system uses a sorting language, called the EVAL code, which is essentially an assembler. The subprocess XSORT needs the COM and the EVAL files to activate the sorting process [Pil96]. All different data areas such as histograms and gates used by the EVAL code are defined inside the COM file. The EVAL file handles the algorithms needed to sort the events and increment the spectra according to the event type.

3.4 Energy Calibration

Different methods were used in order to perform the energy calibrations of the silicon surface barrier (SSB) and NaI detectors used in both the correlation and IMF measurements. These methods included the use of characteristic energies of α-particles from a ^{228}Th source, the use of the kinematics of elastically scattered ^{12}C ions, the use of energy loss of particles as well as the light output of the NaI detector. Tables 2.4 and 2.5 in Chapter 2 show the detectors used in both experiments and their convention. The following sub-sections describe the methods used to calibrate the different detectors that were used.

3.4.1 Silicon ΔE_2, T1B, T1C and T2A detectors

The energy calibration of each of these detectors was performed under vacuum inside the scattering chamber using the discrete spectrum of α-particles emitted from a ^{228}Th source. The ^{228}Th source was placed inside the chamber in front of the detector in the collimator opening which was 6 mm in diameter. The thickness of these detectors was sufficient to stop the high energy α-particles of 8.78 MeV emitted from the ^{228}Th source. All α-particle energy peaks were identified together with their corresponding channel numbers from the energy spectrum. The α-particle energies were plotted against the channel numbers. Both the slope and offset parameters of the energy calibrations were determined by means of a linear fit.

The energy calibration of Si T1C, used as the stopping detector for the IMFs with ($5 \leq Z \leq 10$), was performed in two parts. The low energy calibration was performed by using a ^{228}Th α-particle source as previously described. The high energy calibration was performed during the IMF experiment using the elastic scattered ^{12}C beam off a thin ^{197}Au target. In order to get the calibration points the detector telescope was placed at different emission angles ranging from 8° to 15°. The elastic ^{12}C peaks were identified together with their corresponding channel numbers. Fig. 3.2 shows a typical energy spectrum with the elastic ^{12}C peak. The elastic peak energy parameters were plotted against their corresponding channel numbers. The slope and offset parameters of the energy calibrations were determined by a combined linear fit of both the low and high energy calibration points. Fig. 3.1 shows a typical α-particle energy spectrum. Figs. 3.3(a) to 3.3(d) show the calibration curves for different silicon detectors as indicated in the caption.

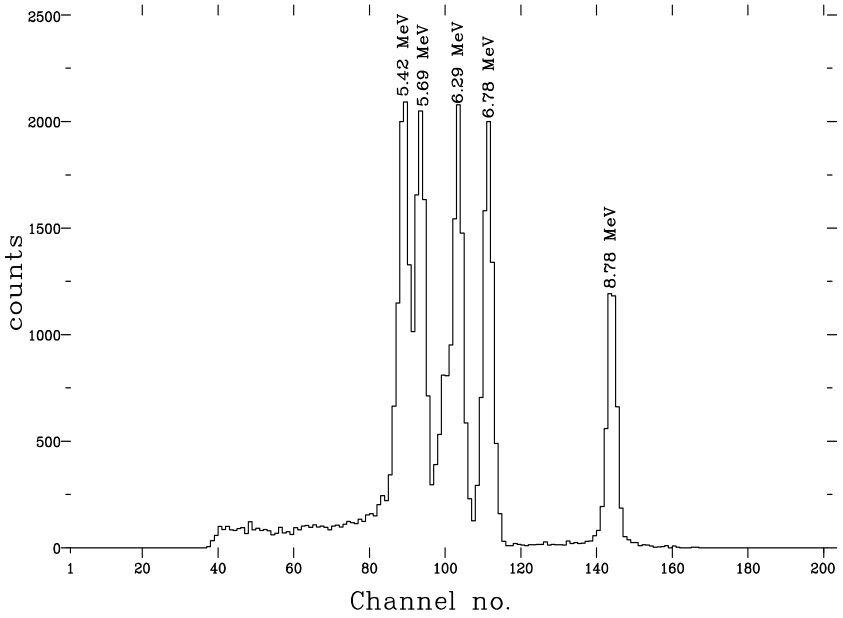

Figure 3.1: Typical energy spectrum of the α-particles from a ^{228}Th source measured with the Si T2A detector showing the discrete energies of the emitted α-particles in MeV.

3.4.2 Silicon ΔE$_1$ and T1A detectors

This section explains the energy calibration of both the 21 μm thick ΔE_1 used for the correlation experiment on the α-particle detector arm as well as the 57 μm thick T1A Silicon detector used to detect the fragments ($5 \leq Z \leq 10$) in the IMF experiment. The calibration was performed in this case by using the calibration parameters of the transmission detectors for both ΔE_2 and T1B. Since these detectors are not thick enough to stop the 8.78 MeV α-particles from the ^{228}Th source, energy loss of the emitted fragments in the ΔE_1 and

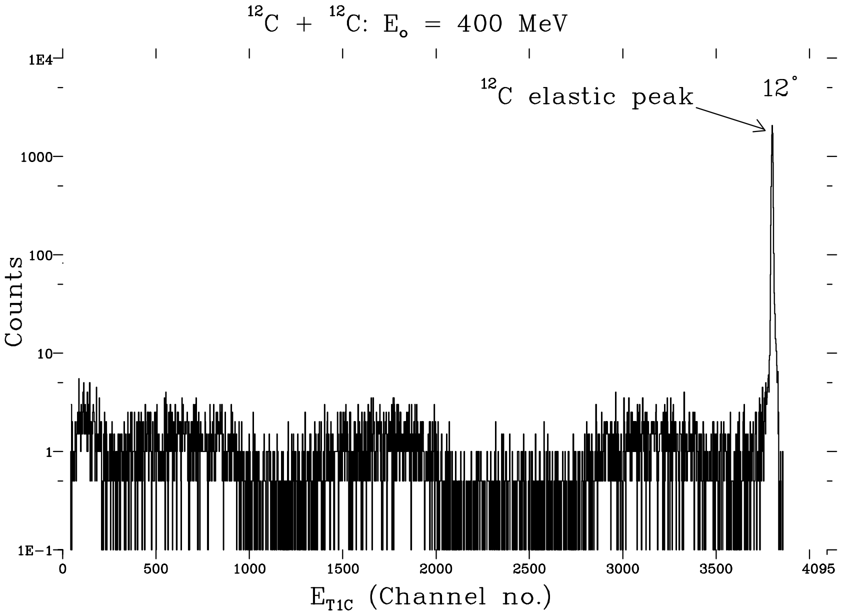

Figure 3.2: Typical energy spectrum of the elastically scattered ^{12}C off a thin ^{197}Au with its elastic peak indicated.

T1A detectors, respectively, were calculated using the ELOSS program [Jip84]. These values of the energy loss were fitted to the calibrated energy deposited by the detected α-particle in the ΔE_2 detector and by ^{6,7}Li, ^{7,9}Be and ^{8,10}B in the T1B Silicon detector. This was done by multiplying the channel numbers of the ΔE_1 and T1A detectors by a factor in order to fit the measured ΔE$_1$ - ΔE$_2$ and T1A-T1B Particle Identification (PID) spectra. These factors were considered to be the slope parameter of the ΔE_1 and T1A detectors. Figs. 3.4(a) and 3.4(b) show the calculated loci fitted to the measured ΔE_1-ΔE_2 and T1A-T1B PID spectra, respectively. Table 3.1 shows the calibration parameters used for all the SSB detectors for both the correlation and IMF experiments.

3.4.3 Silicon DSSSD

The energy calibration of the 251 μm thick DSSSD was performed by following the same procedure as described in section 3.4.2. The calibration was performed for each strip individually.The energy loss of the α-particles passing through the DSSSD was calculated using the ELOSS program [Jip84]. In this case the calibration was performed using the calibration parameters of the NaI stopping detector. The energy loss of the α-particles in each strip of the DSSSD was plotted against the calibrated energy deposited in the NaI detector shown in Fig. 3.5 for strips 2, 8 and 15, respectively. The calculated α-particle locus was fitted to the measured ΔE-E PID spectrum for each strip by multiplying the channel numbers of the DSSSD by a slope parameter. The

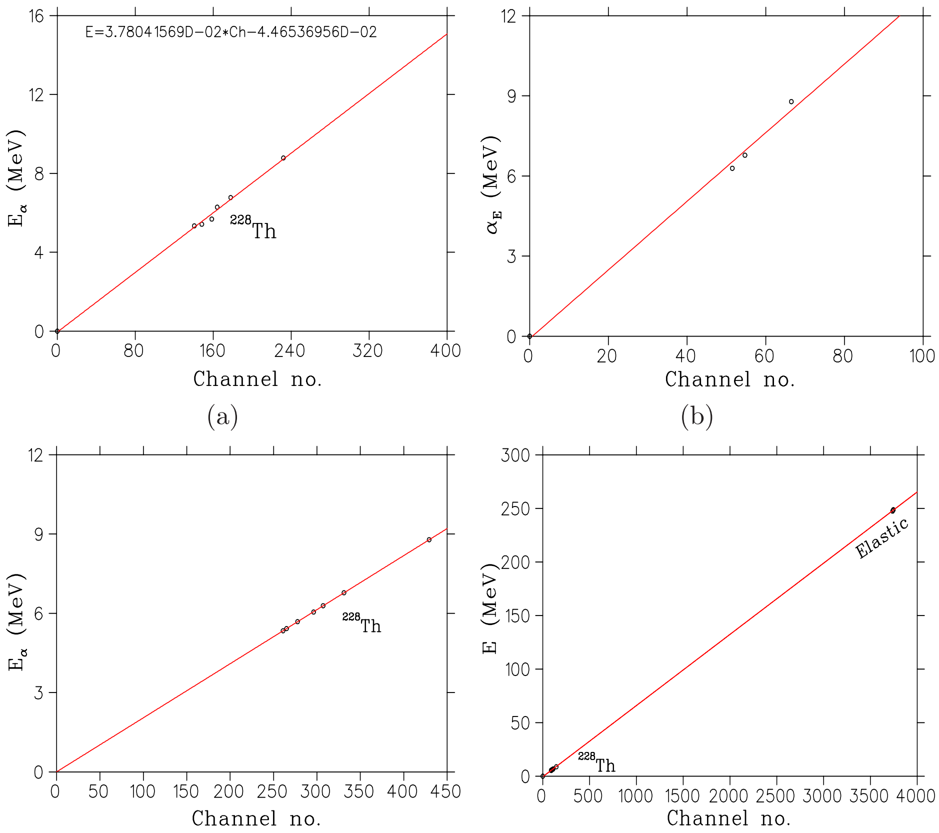

(a) (b)

(c) (d)

Figure 3.3: Calibration curves for the Si ΔE_2 detector (a), the Si T1B detector (b), the Si T2A detector (c) and the Si T1C detector (d) showing the straight line fitted through the energy points of α-particles from the ^{228}Th source, as well from the elastic scattering of the beam.

offset parameter was set to zero in all cases. The slope parameters which were obtained for each strip are tabulated in Table 3.2.

3.4.4 NaI detector

The NaI detectors were calibrated by following the method discussed in Ref. [Ste05]. In this method it is assumed that the light inside the NaI crystal is produced by Coulomb-scattered electrons penetrating to some finite range perpendicular to the incident ion's trajectory as discussed by Michaelian *et al.* [Mic93, Bel93]. The saturation density is determined by comparing a calculated and normalised L *vs* E curve with a few values of (L, E) points from the experimental data for only one ion. The saturation density (ρ_{sat}) is then used to generate the L *vs* E curves for all other ions [Bel93]. In the present measurements the elastic scattered ^{12}C ions were used to generate few representative (L *vs* E) spectra and were used to normalise with respect to

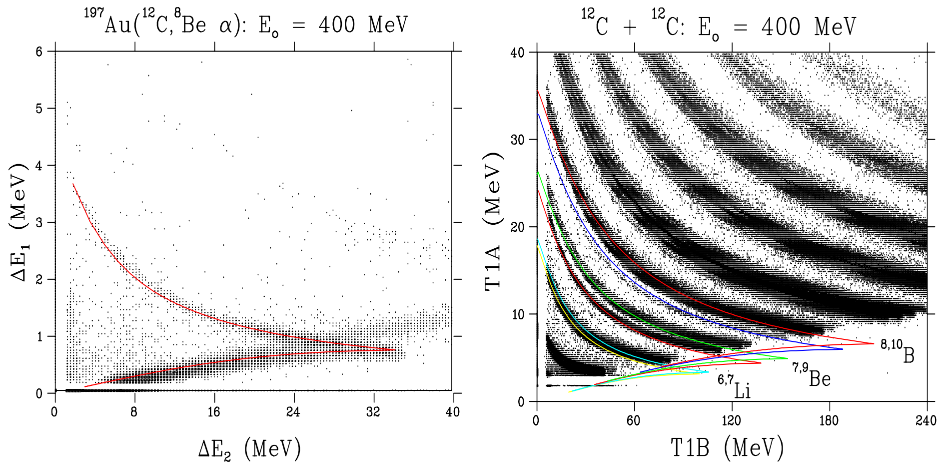

(a) (b)

Figure 3.4: (a) The calibration spectra with the calculated α-particle energy loss overlaid onto the experimental ΔE_1-ΔE_2 spectrum. (b) Loci of the Li, Be and B isotopes calculated with the ELOSS program overlaid onto the experimental T1A-T1B spectrum.

Table 3.1: Calibration parameters of the Silicon detectors

Detector Convention	Slope	Offset
ΔE_1	0.0059	0
T1A	0.11862	0
ΔE_2	0.0378	-0.04465
T1B	0.1241	-0.0205
T1C	0.0665	-0.503
T2A	0.0205	-0.0049

other ions. The method used for the relation between *E vs L* is explained below. In this method the intensity of the scintillation light output in the interaction of an ion of known energy with the crystal, i.e. $L = f(E,Z,A)$ is determined, where *E, Z* and *A* represent the energy, the atomic number and atomic mass of the detected particle, respectively. Experimentally the inverse process is used where the scintillation light output is a measured quantity and the energy has to be deduced, i.e. $E = f(L,Z,A)$. There are different ways to achieve this. One way would be to establish a conventional table for each ion and interpolate the listed values for the energy corresponding to a given pulse-height response. A simple function similar to the approach by Stracener [?] containing one linear and one non-linear term in *L* was considered. For this purpose a TABLECURVE software package [Jan96] was implemented. From more than 600 simple two-term functions with intercept (in this case the intercept set to zero) the following function was chosen because of its high ranking and simplicity [Ste05].

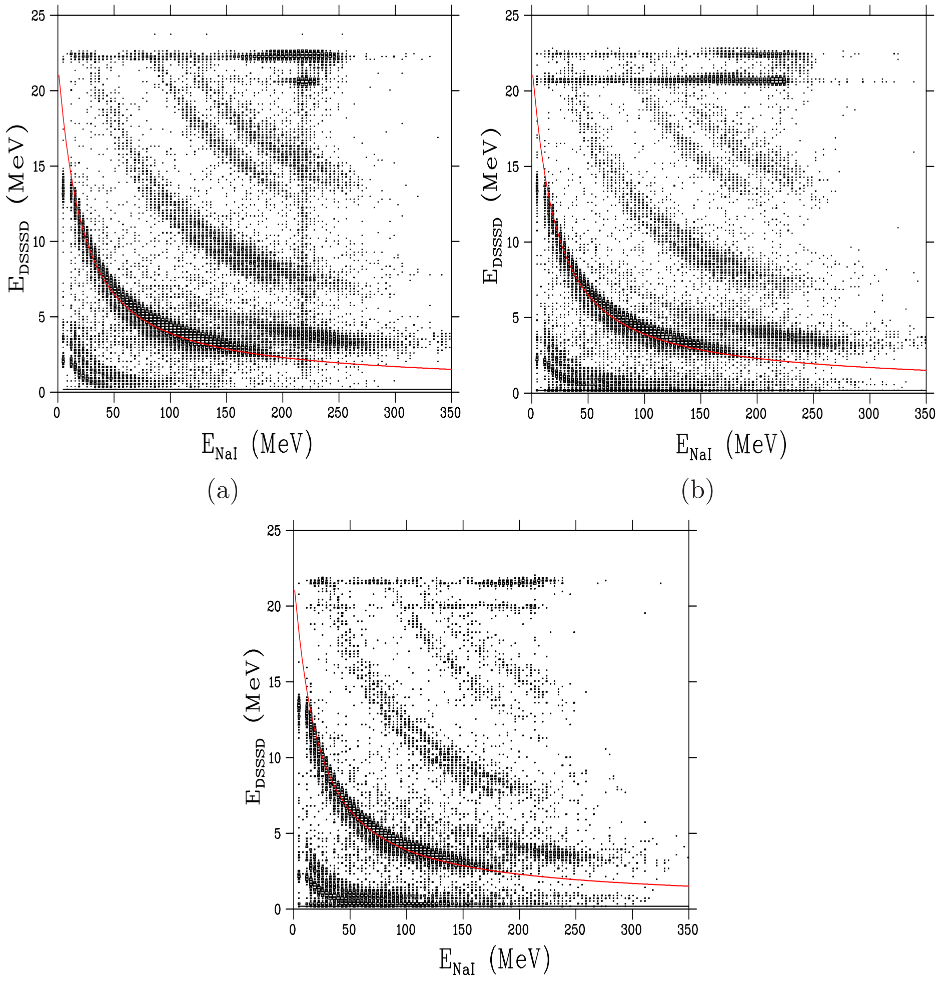

(a) (b) (c)

Figure 3.5: Two-dimensional energy spectra used to calibrate (a) strip 2, (b) strip 8 and (c) strip 15 of the DSSSD.

$$E(L) = a_1 L + a_2 \sqrt{L} \tag{3.1}$$

where the coefficients a_1 and a_2 will generally be the functions of Z and A, but numerical constants for any particular ion. As mentioned above the elastic scattered ^{12}C ion beam was used to obtain the saturation density used to generate the L *vs* E curves for other ions. The simple above mentioned equation fitted the ^{12}C data very well. The light output L of the detector corresponded to the channel number on the energy spectra. Fig. 3.6 shows the (L *vs* E) curve for different particles detected with the NaI detector, as well as the fitted experimental data from elastically scattered ^{12}C ions (open symbols). Table 3.3 shows the parameters used to for the calibration of different ions by using Eq. 3.1. All the detector calibrations were tested during the off-line data analysis to be discussed in the next section.

Table 3.2: DSSSD strips calibration parameters.

Strip no.	Slope	Strip no.	Slope
Strip 1	0.0058	Strip 9	0.0056
Strip 2	0.0058	Strip 10	0.0056
Strip 3	0.0058	Strip 11	0.0056
Strip 4	0.0058	Strip 12	0.0056
Strip 5	0.0058	Strip 13	0.0056
Strip 6	0.0058	Strip 14	0.0056
Strip 7	0.0058	Strip 15	0.0056
Strip 8	0.0058	Strip 16	0.0056

Table 3.3: Calibration parameters used to calibrate the NaI detector for different isotopes in the interaction of ^{16}O with ^{12}C at an incident energy of 235 MeV.

ion	a_1	a_2
^{16}O	0.264	5.761
^{9}Be	0.234	4.213
^{7}Be	0.233	3.744
^{7}Li	0.2204	3.211
^{6}Li	0.2203	2.976
^{4}He	0.2083	1.866

3.5 Correlation Experiment

The offline event-by-event data analysis was performed by making use of the XSYS software architecture which was implemented in the online data acquisition. Both the COM and EVAL files used for the online data extraction were modified to accommodate all the additional two-dimensional gates and energy spectra. The additional spectra that were needed were the two-dimensional summed energy spectrum, the individual QE and inelastic ^{8}Be and α-particle energy spectra. The energy calibration for the NaI was performed by using Eq. 3.1, whereby the light output L was replaced by the channel number and multiplied by the factors (a_1 and a_2).

3.5.1 Coincidence data

This subsection describes the offline data analysis of the correlation experiment. Fig. 3.7 shows a time spectrum used to select the true coincidences from among random coincidences, with the gates used to select true and random coincidences. The random coincidences occur when a coincidence is established between the events originating from different beam bunches. These events were subtracted from the true coincidence events during the data analysis.

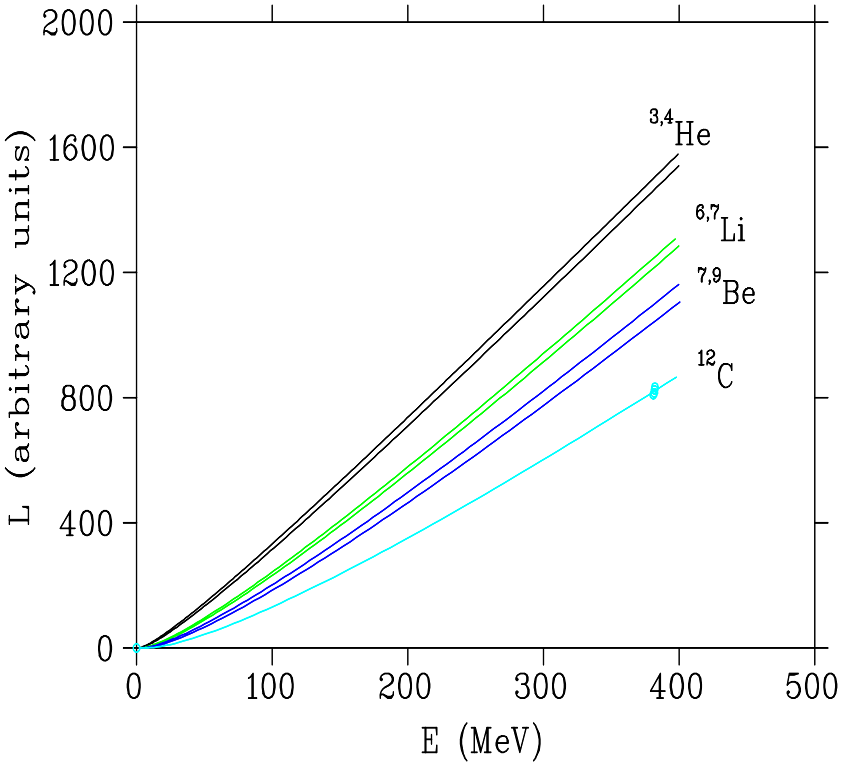

Figure 3.6: Energy calibration curves for ejectile energy versus light output of the NaI detector for ^{3,4}He, ^{6,7}Li, ^{7,9}Be and ^{12}C, as indicated. The lines are calculated predictions based on the Michaelian-Menchaca-Rocha model [Mic93].

3.5.1.1 ^{8}Be fragments

i **Particle Identification**

In order to detect the unbound ^{8}Be fragment made up of its two correlated α-particles, the ΔE-E technique was implemented between each vertical strip and the NaI stopping detector. The PID was populated by various ejectiles ranging from protons to ^{9}Be ions. The ^{8}Be events are identified by a locus with similar ΔE strength as the α-particles but with a higher E strength as indicated by a separate locus which appeared just above the α-particle locus. This is due to the fact that each strip of the DSSSD detects one α-particle but the NaI detector stops both break-up α-particles. A typical ΔE-E PID spectrum for one vertical strip in coincidence with the NaI detector is shown in Fig. 3.8. Similar PID spectra were obtained for each vertical strip. During the off-line replay, and event sorting, gates were set around each locus in the PID spectra for all 16 vertical strips. Two-fold coincidences between strips and NaI were searched using an algorithm in the EVAL file. For every coincidence between two strips the energy of two α-particles were summed up to create a ^{8}Be fragment. Fig. 3.9 shows a two-dimensional ^{8}Be PID spectrum with the gate set around the ground

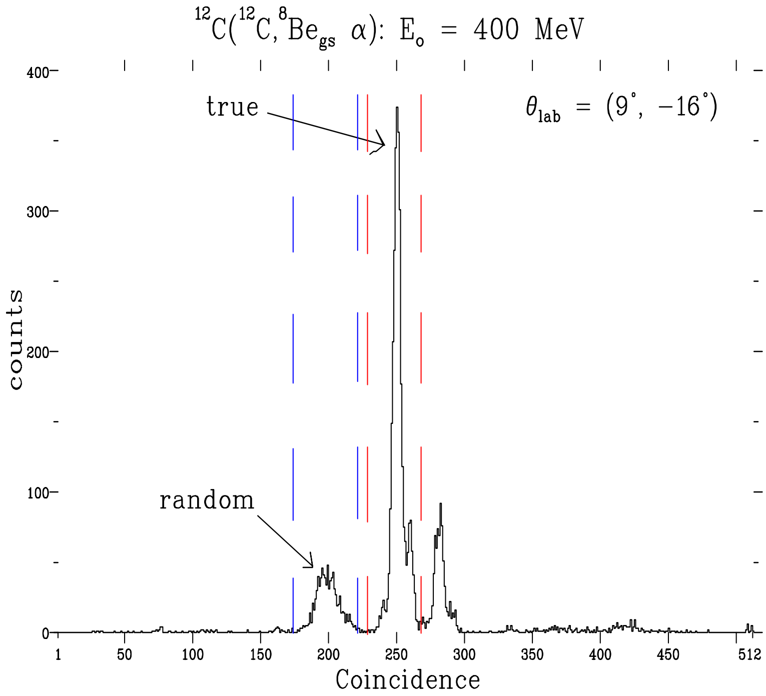

Figure 3.7: A typical TAC spectrum used to select real from random coincidences with gates set around the true coincidences (red) and random coincidences (blue).

0^+ state events.

ii **DSSSD efficiency**
The DSSSD efficiency to detect ^{8}Be fragments was calculated by means of Monte Carlo simulations, as discussed by Steyn *et al.* [Ste05]. This code was developed to simulate break-up reactions followed by the detection of a resonant particle like $^8Be_{g.s.}$ with the DSSSD technology [Mac92]. The DSSSD efficiency is calculated as the ratio from the case where ^{8}Be breaks up to the case where it remains bound. The parameters included in the code are shown in Table 3.4. In this code the collimator geometry which is situated between the DSSSD and NaI is also modelled to account for the cylindrical shape of the NaI detector. These simulations are independent of the target material used. The calculated detector efficiency is expressed as a percentage of the efficiency if it is assumed that a stable and bound ^{8}Be is detected in its ground state and plotted as a function of the ^{8}Be ejectile energy, as shown in Fig. 3.10. This figure shows the case where 16 vertical strips were sorted as well as the case were the strips were reduced by excluding outer strips. It is evident that the detection efficiency increases with the increasing ^{8}Be ejectile energy. This is due to the fact that at low emission energy the separation angle between the two constituent α-particles is larger and one of the α-particles might miss the detector. As discussed in Ref. [Ste05], an α-particle traversing the inter-

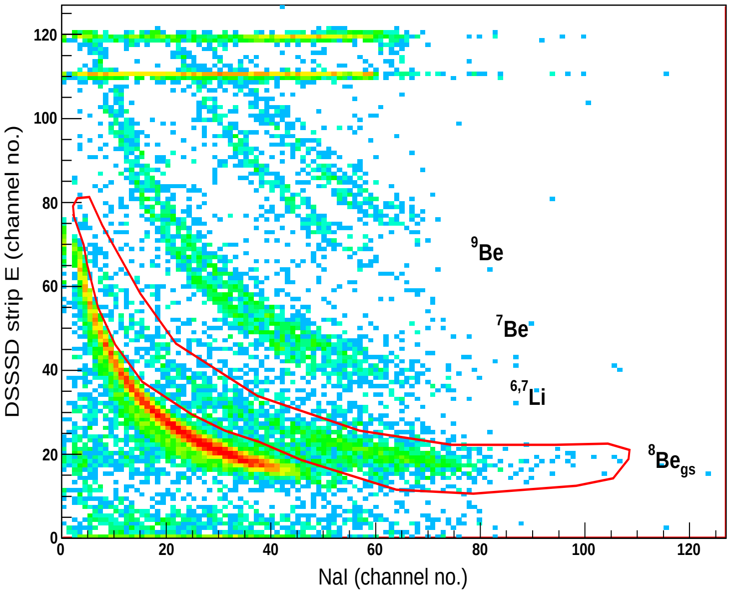

Figure 3.8: A typical ΔE-E particle identification spectrum for one vertical strip (No. 8) in coincidence with the NaI stopping detector.

strip gaps could trigger two adjacent strips. In order to get rid of these intruder events which would mimic ^{8}Be events, data were re-sorted off-line discarding events from adjacent strips and plotted as the effective solid angle of the detector system, as shown in Fig. 3.11. The distance between the centre of the target and the end of the collimator was 469 mm with a subtended solid angle of 11.03 msr which was multiplied by the detector efficiency to give the effective solid angle of the ^{8}Be detector telescope. Fig. 3.12 shows that the DSSSD is more efficient in detecting the ^{8}Be in the ground state denoted by (^{8}Be$_{g.s}$) and less efficient in detecting the ^{8}Be in its first excited 2^+ state. The DSSSD is also less efficient in detecting the ^{8}Be emitted with very low energies due to large separation angle between its two α-particles and one would miss the detector. In the case of a ^{12}C target, it is also probable that the target might break-up into ^{8}Be$_{g.s.}$ and α-particles. In this case, the events from the break-up of the ^{12}C target into the ^{8}Be and α-particles are negligible due to the fact that the separation angle between the two constituent α-particles from ^{8}B$_{g.s.}$ is larger and one of the α-particles will miss the detector.

iii Calibration tests

The prescaled singles energy spectra of the ^{8}Be fragments provided the energy calibration and efficiency test for the ^{8}Be telescope. The ^{8}Be detector was tested by comparing the pre-scaled singles of ^{8}Be cross sections with the published inclusive spectra by Gadioli *et al.* [Gad01]. The pre-

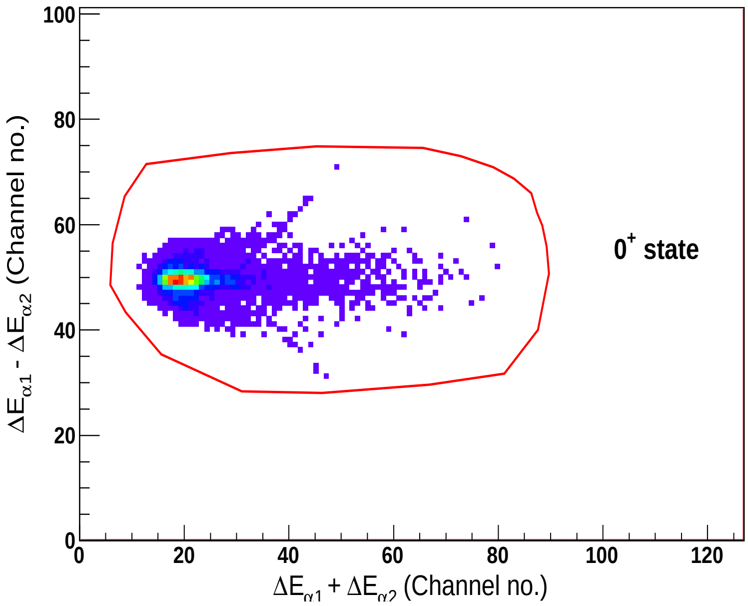

Figure 3.9: A typical two-dimensional spectrum of the sum of ΔE kinetic energy of the detected break-up α-particles plotted against their sum.

Table 3.4: Parameters used in the Monte Carlo simulations

Parameter	value
Detector distance	469 mm
Collimator radius	31 mm
Energy of Recoil state	335 MeV
Strip pitch	3 mm
Strip gap	0.1 mm
Strip length	50 mm

scaled singles data were scaled down to 20, allowing the scalers to count and record every 20^{th} event on the tape. For this reason the ^{8}Be pre-scaled singles data were multiplied by a factor of 20 for normalisation. Fig. 3.13 shows the comparison between the prescaled singles cross sections and the inclusive results for the ^{8}Be detector telescope. The pre-scaled cross sections of the ^{8}Be fragments show good agreement with the published data which confirm that the energy calibration and detector efficiency are reliable.

3.5.1.2 Alpha particles

i **Particle Identification**

The standard ΔE-E technique was also applied to identify the emitted α-particles. The α-particle detector telescope consisted of three detectors. In

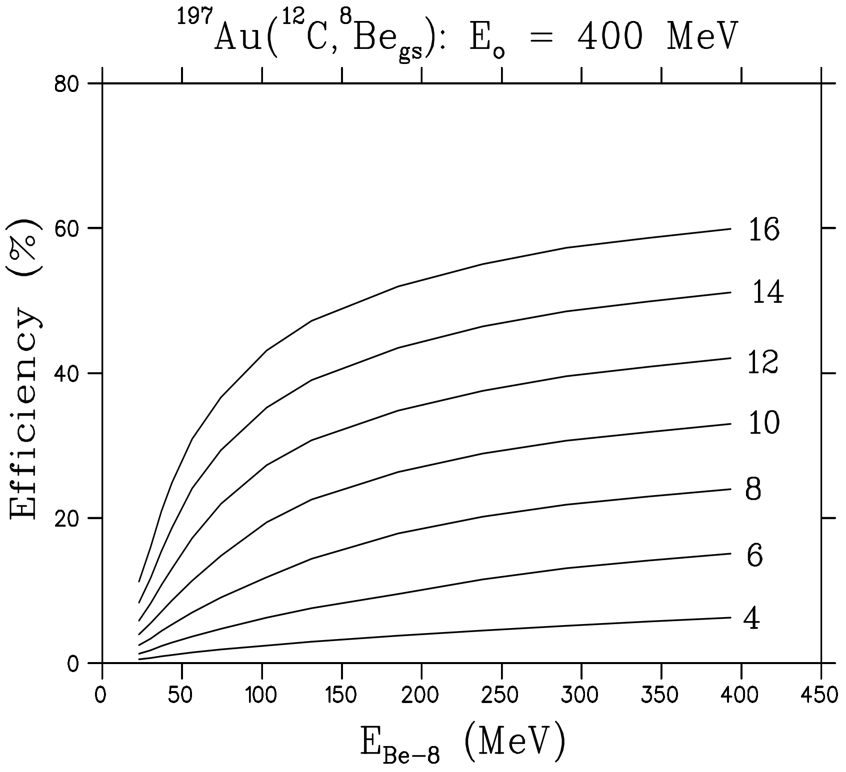

Figure 3.10: The DSSSD efficiency curves for ^{8}Be ejectiles detected in the ground state (0^+) obtained by means of Monte Carlo simulations excluding events from adjacent strips. The curves represent calculations for a different number of central vertical strips, as indicated.

this case two-dimensional PID spectra were generated for events which deposited energy in ΔE_1 and ΔE_2 as shown in Fig. 3.14(a), as well as events in ΔE_2 and the NaI detector, respectively shown in Fig. 3.14(b). Two dimensional gates were set in these spectra to select α-particles as shown in Fig. 3.14(a), and both Helium isotopes as indicated in Fig. 3.14(b). In order to separate α-particles from ^{3}He events, a mass function was generated as discussed below and shown in Fig. 3.15.

ii Mass Function

In order to separate different isotopes, a mass function was generated from the gated loci on the high energy PID spectra of the α-particle. Mass functions were generated by using the following equation [Mud05],

$$MF = [(E_B + E_A)^P - (E_B)^P] \times M_s + M_o \tag{3.2}$$

where, E_B is the energy deposited in the E detector, E_A is the energy lost by the particle passing through the ΔE detector, P is a constant used to optimise the mass function loci, M_s is the slope factor used to optimise the

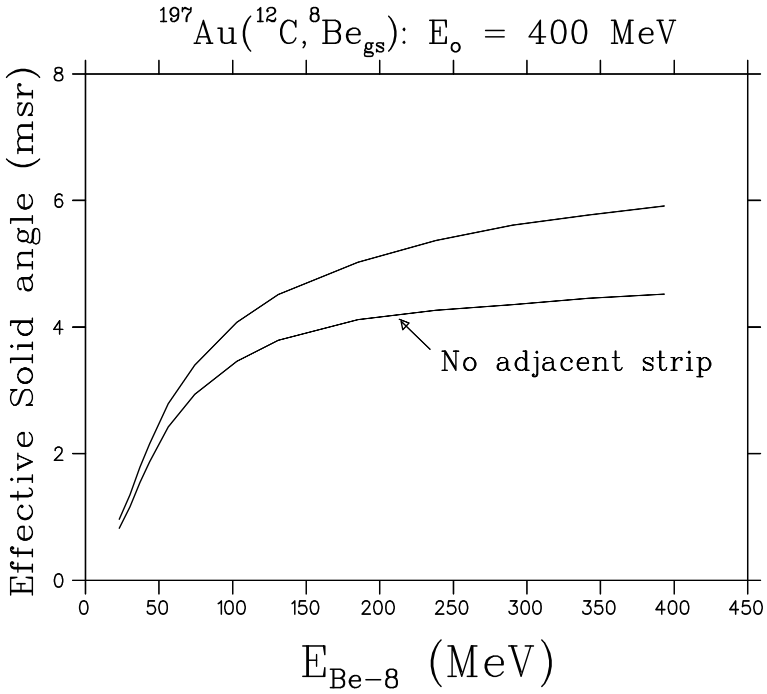

Figure 3.11: Effective solid angle subtended by the ^{8}Be detector telescope versus the ejectile energy for ^{8}Be$_{g.s.}$, with all 16 vertical strips included and also with the adjacent strip hits excluded as shown.

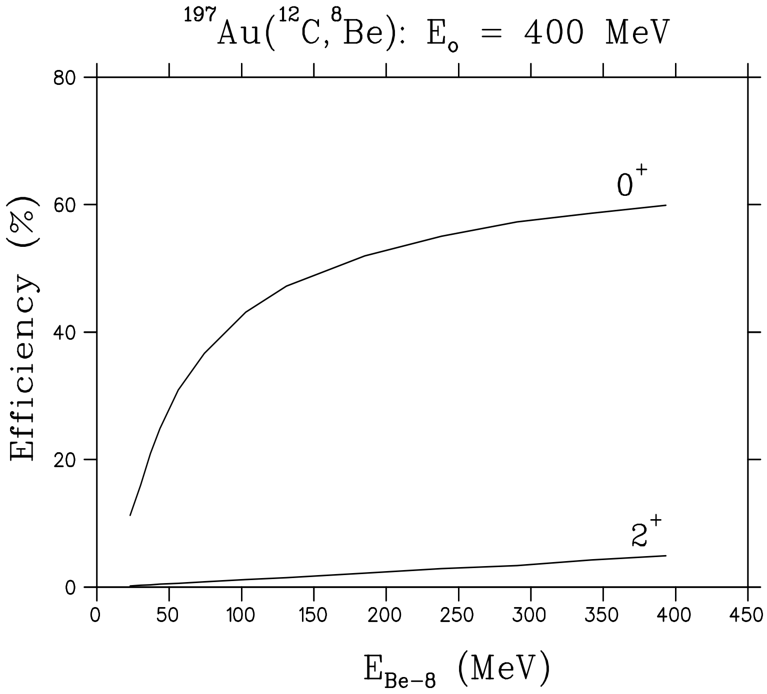

Figure 3.12: The DSSSD efficiency curves for ^{8}Be fragments produced in the ground state (0^+) and the first excited state (2^+).

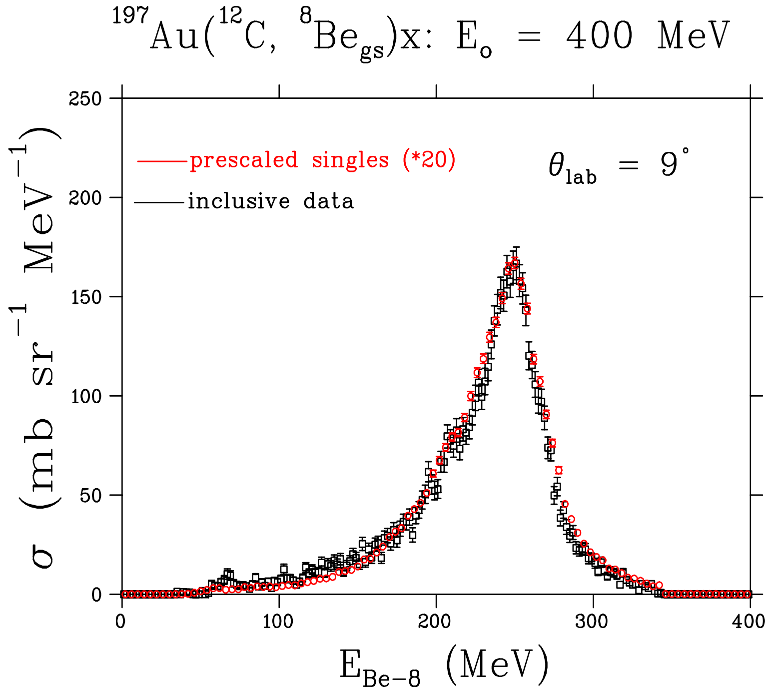

Figure 3.13: Double differential cross sections of the ^{8}Be$_{g.s.}$ fragment spectra for the prescaled singles data (red) normalised to the published inclusive data (black) [Gad01].

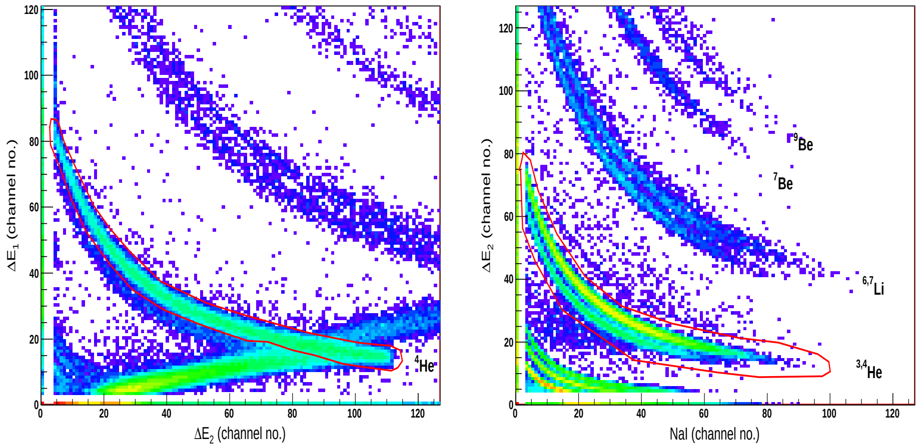

(a)

(b)

Figure 3.14: Typical α-particle PID spectra from the correlation experiment, (a) for ΔE_1 versus ΔE_2, and (b) ΔE_2 versus NaI detectors.

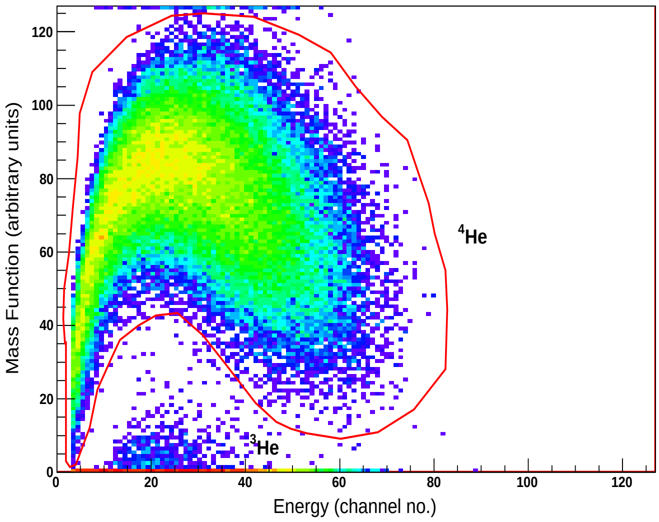

Figure 3.15: Mass function spectrum with the gate set around the α-particle events.

position of the mass function loci and M_o is an offset factor also used to optimise the position of the mass function loci. Fig. 3.15 shows a mass function spectrum with a gate set around α-particle events.

iii Calibration test

The detector calibration test for the α-particle telescope was performed using the pre-scaled singles spectra of the α-particles in a manner similar to the test performed for the ^{8}Be telescope. The α-particle detector was tested by comparing the α-particle prescaled singles cross sections with the published inclusive spectra for different α-particle emission angles [Gad99]. The singles data were scaled down to 20, allowing the scalers to count and record every 20^{th} event on the tape, for this reason the pre-scaled singles data of the α-particles were normalised by multiplying by a factor of 20. Fig. 3.16 shows the comparison between the published data and α-particle singles at $\theta_{lab} = (16°$ and $24°)$.

3.5.2 Two-dimensional energy spectra

In order to extract the coincidence cross-sections of $^8\mathrm{Be}_{g.s.}$ fragments and α particles, two-dimensional energy spectra were generated for all target nuclei for different α-particle emission angles given in Table 3.5. Fig. 3.17 shows a typical two-dimensional spectrum of the sum of kinetic energies of the $^8\mathrm{Be}_{g.s.}$ fragment and α-particle plotted as a function of α-particle energy at an emission angle of $\theta_\alpha = 16°$. These two-dimensional energy spectra are characterised by three distinct regions; namely, a quasi-elastic locus at energies correspond-

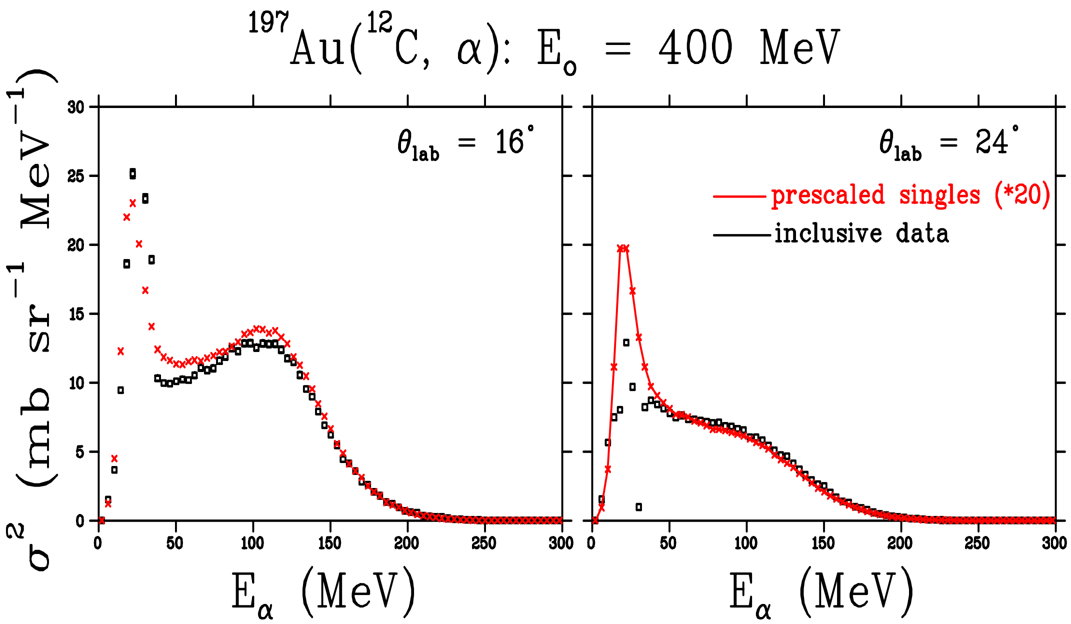

Figure 3.16: Double differential cross sections of the α-particle spectra for the prescaled singles data (red) normalized to the published inclusive data (black) [Gad99].

ing to the beam velocity and a tail of inelastic break-up events extending over the remaining energy region. Also observed was another locus about 30 MeV below the QE locus corresponding to the high energy region of the α-particle at emission angles of $\theta_\alpha = 16°$ to $22°$. The origin of this locus was believed to be due to the interaction of the ^{12}C beam with hydrogen contaminants on the target material. It was also observed that this locus shifted towards lower α-particle emission energies as the α-particle emission angle increases, and eventually disappear at an α-particle emission angle of $\theta_\alpha = 24°$ and larger.

On closer inspection, it was found that the QE events were separated out in two loci at the forward emission angles between $\theta_\alpha = 16°$ and $18°$. These energy distributions in the QE locus were emphasised as seen in the magnified spectrum of the events inside the window shown in Fig. 3.17. The events related to the higher emission energy of the QE locus were also observed to be shifting towards the lower energy distribution as the emission angle increased and disappeared at $\theta_\alpha = 24°$.

Kinematic simulations were performed to investigate the reaction mechanism as well as the break-up channel in ^{12}C which populated these high energy parts of the α-particle energy spectra. The simulations were performed using the Monte Carlo code SimSort which is explained in detail in Chapter 4. The simulations were performed with the same detector geometry as used during the experiments. Different reaction channels were tested in this code in order to populate these energy regions by using a $E_{lab} = 400$ MeV ^{12}C projectile interacting with a hydrogen target. This was also done in backward angles

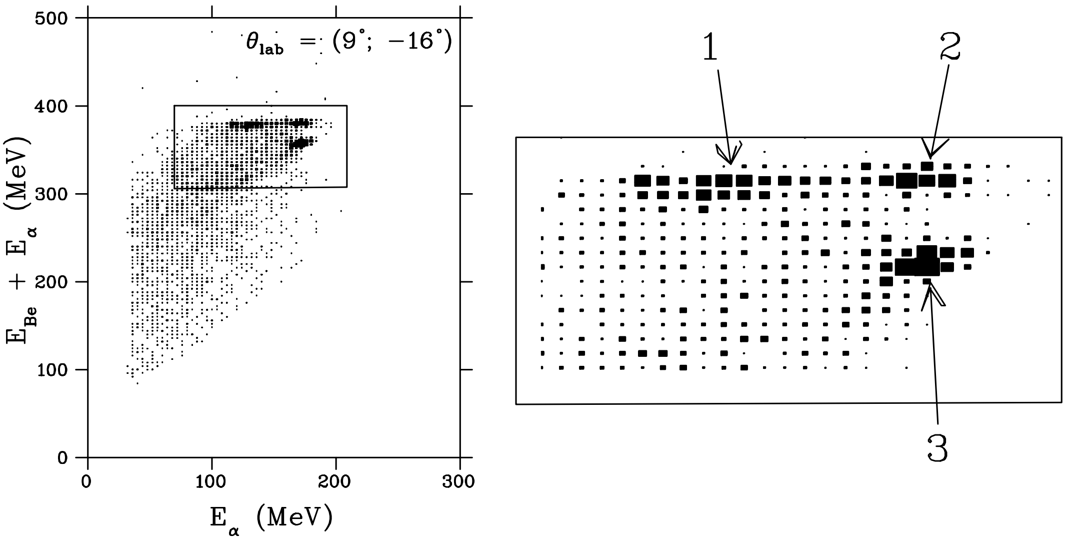

Figure 3.17: Two-dimensional coincidence spectrum of the sum spectra of ^{8}Be$_{g.s.}$ and α-particle energy for the interaction of ^{12}C with ^{12}C at an incident energy of 400 MeV as a function of α-particle energy. A gate used to zoom into the region around the QE locus is shown.

in the centre-of-mass system with the equivalent reaction of ^{12}C(p,α)^{9}B. The reaction mechanism which populated these two regions were found to start with the fusion of the projectile with a hydrogen nucleus and form an excited compound nucleus ^{13}N*, followed by the sequential break-up of the compound nucleus into an α-particle and ^{9}B$_{g.s.}$. Since ^{9}B$_{g.s.}$ is unbound it decays into a proton and ^{8}Be$_{g.s.}$ which again decays into two α-particles. Fig. 3.18 and 3.19 show the comparison between the experimental and SimSort simulations spectra. The experimental cross-sections are obtained from the data measured in the interaction of ^{12}C with (CH$_2$)$_n$. The simulations spectra are populated using the fusion of ^{12}C with the H target at four different α-particle emission angles between $\theta_\alpha = 16°$ to 22°. The locus observed at the highest energy was populated by ^{9}B$_{g.s}$, when the proton is detected together with ^{8}Be$_{g.s.}$, while the locus at the lower energy region was populated when the correlated proton of the ^{9}B fragment missed the detector and only the energy of ^{8}Be$_{g.s.}$ was measured. At an emission angle of $\theta_\alpha = 24°$ and above the interaction of ^{12}C with hydrogen no longer has an effect on the measured coincidence data due to kinematic constraints. These observations are similar to the results observed in the experimental spectra. The SimSort results show that the QE break-up events of ^{12}C in the interaction with hydrogen appear at lower energies around 350 MeV. In the experimental data these events are not clear because of the contribution from the inelastic events.

Fig 3.20 shows the comparison between experimental and simulation spectra where the energy loss in a single strip is plotted against the energy deposited in the NaI stopping detector. These events were extracted by setting

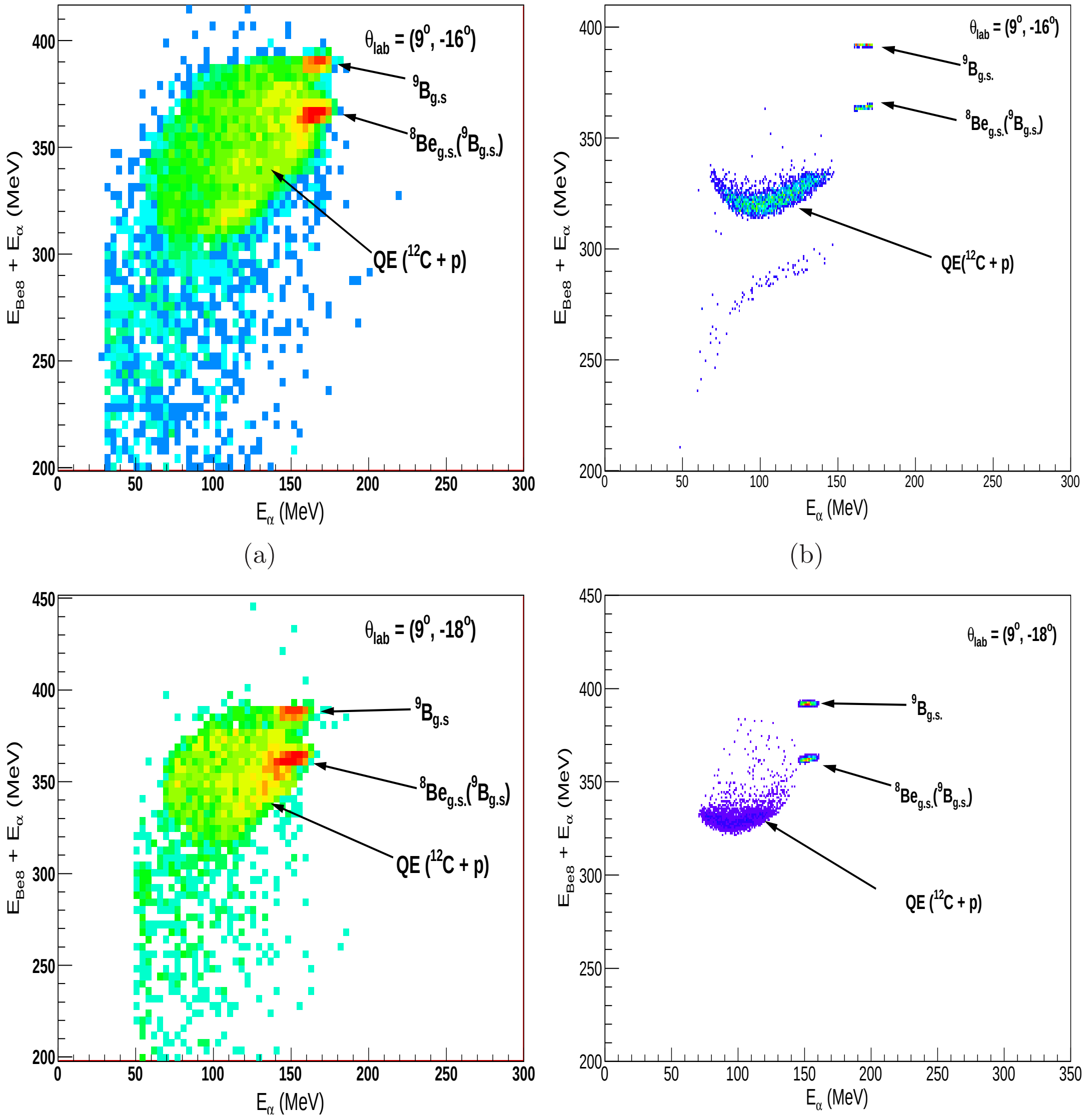

(a) (b)

(c) (d)

Figure 3.18: Two-dimensional coincidence spectra shown at different angle pairs θ_{lab} with $\theta_{8Be} = 9°$ and $\theta_{\alpha} =$ -16° and -18°, respectively, (a) and (c) the experimental spectra in the interaction of ^{12}C with $(CH_2)_n$ target, (b) and (d) SimSort simulation spectra in the interaction of ^{12}C with hydrogen showing events for QE break-up, as well as events from a fusion reaction of ^{12}C with a proton to form ^{13}N followed by sequential break-up into an α-particle and $^{9}B_{g.s.}$ which also break-up into $^{8}Be_{g.s.}$ and a proton.

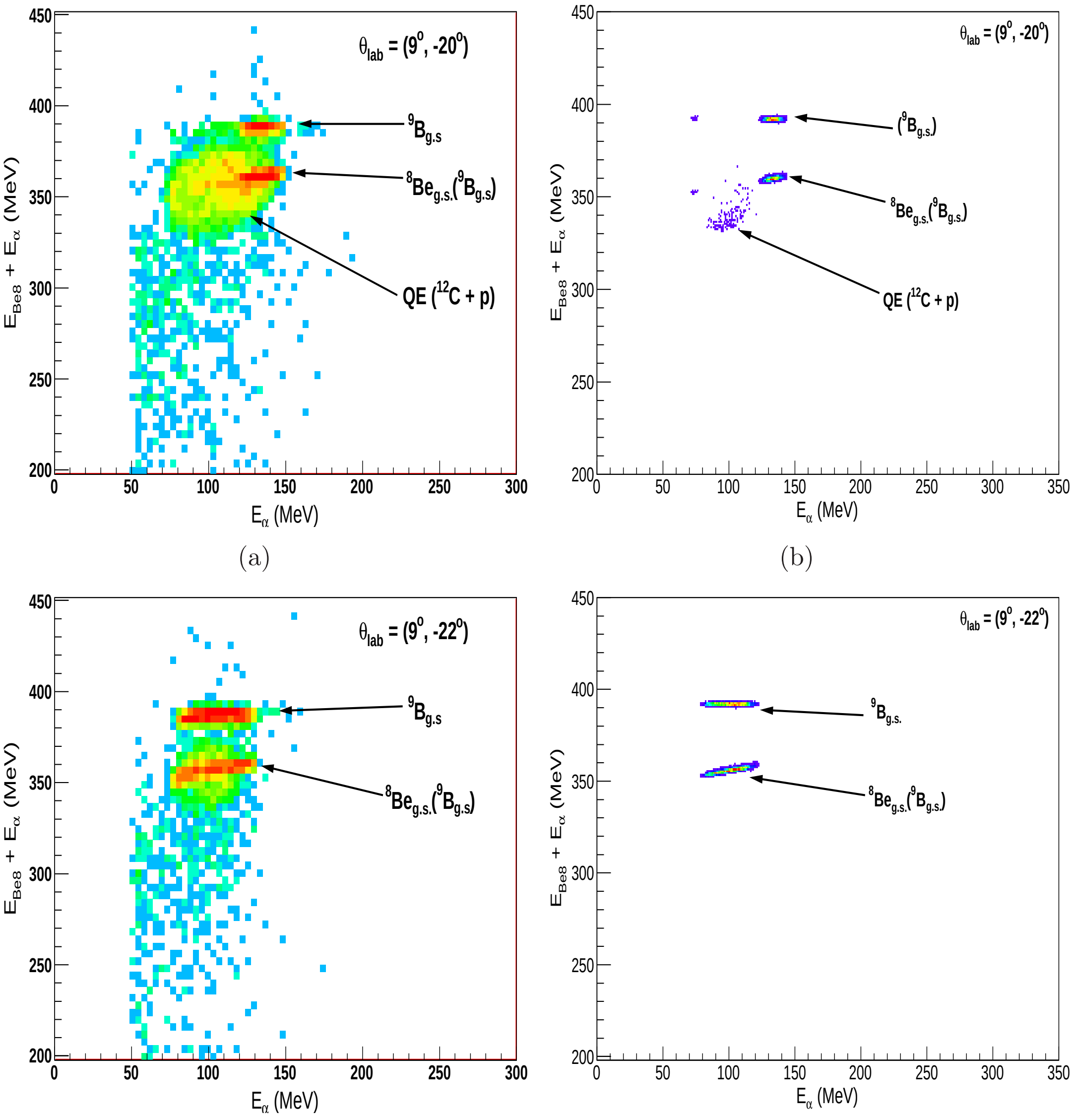

(a) (b)

(c) (d)

Figure 3.19: Two-dimensional coincidence spectra shown at different angle pairs θ_{lab} with $\theta_{8Be} = 9°$ and $\theta_\alpha =$ -20° and -22°, respectively. See caption of Fig. 3.18.

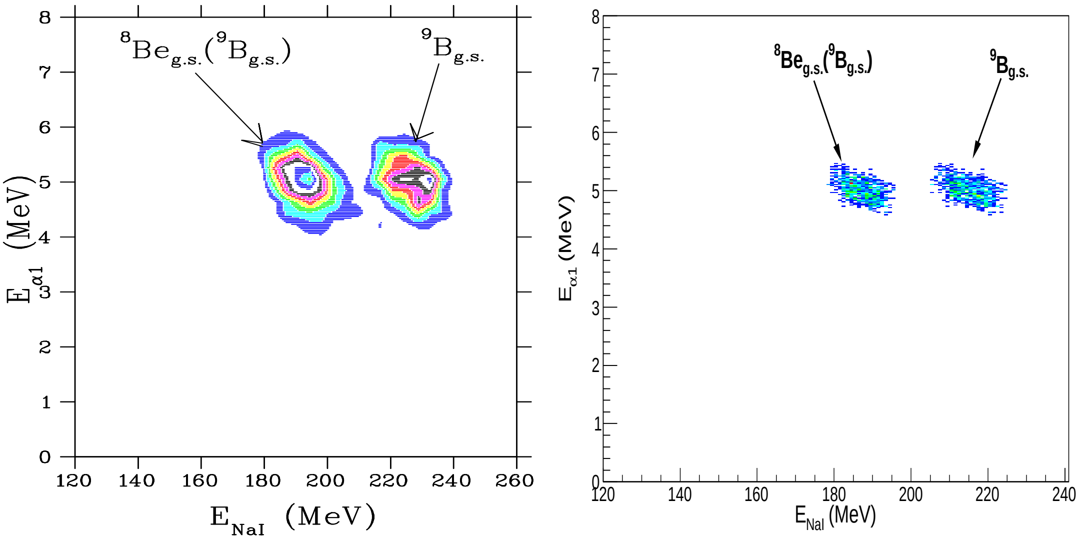

(a) (b)

Figure 3.20: Two-dimensional spectra of the energy deposited in strip no. 8 of the DSSSD plotted against the total energy deposited in the NaI detector for both, (a) the experimental data, and (b) SimSort simulation.

gates around events (2) and (3) on the experimental summed energy spectrum, for every event that populated these two regions a ΔE-E spectrum was plotted. In these measurements the use of DSSSD provided the necessary energy resolution and efficiency to detect unbound fragments such as ^{9}B$_{g.s.}$ and ^{8}Be$_{g.s.}$ in their respective ground states.

Fig. 3.21 shows an angular distribution for the correlation between coincidence α-particles plotted against ^{8}Be$_{g.s.}$ fragments emitted in the interaction of ^{12}C with a hydrogen target. Due to kinematic constraints this angular distribution is limited to an angular range of $\theta_{Be8} = 6°$ to $11°$ for ^{8}Be$_{g.s.}$ fragments, while the α-particles are limited over an angular range between $\theta_\alpha = 14°$ and $22°$. It was also observed in the experimental results that the locus at lower energy is observable over the same α-particle emission angles. In order for the ^{12}C projectile to break-up into the ^{8}Be$_{g.s.}$ and α-particle, an excitation energy sufficient to separate the two fragments to be detected at measured angles is required. The excitation energy that allowed the detection of the ^{8}Be$_{g.s.}$ and α-particle at measured angles ranged between E_{ex} = (15 to 35 MeV). Since the ^{8}Be detector telescope was fixed at $\theta_{Be8} = 9°$, Fig. 3.21(b) shows the excitation energy required by the ^{12}C to break-up into the ^{8}Be$_{g.s.}$ and α-particle in the interaction with the hydrogen target with respect to α-particle emission angle. The pronounced locus marked by the gate in Fig. 3.21(b) shows the minimum excitation energy required in ^{12}C for the emitted fragments to be observed with the detector setup used.

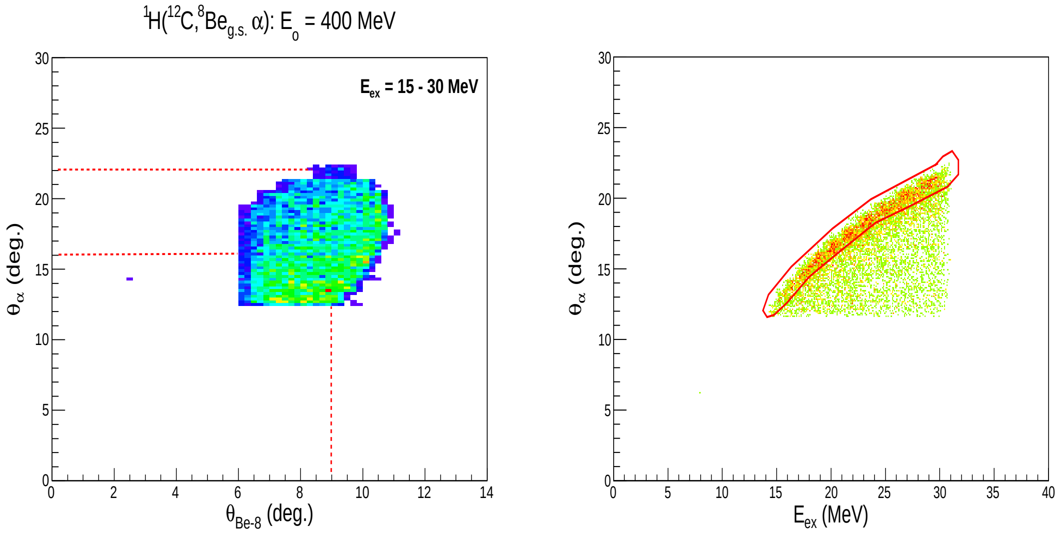

(a) (b)

Figure 3.21: SimSort simulation results showing; (a) Two-dimensional coincidence angular distribution of ^{8}Be$_{g.s}$ against α-particle emission angle in the interaction of ^{12}C with hydrogen target, and (b) the α-particle's emission angle as a function of excitation energy required by the ^{12}C to break-up into the ^{8}Be$_{g.s.}$ and α-particle.

3.5.3 Regions of Interest

Fig. 3.22 shows the two-dimensional summed energy spectra for all measured α-particle emission angles between $\theta_\alpha = 16°$ and 26°. The integrated charge measured by the Current Integrator and used to normalised the cross-section are also presented in table 3.5. The events of QE and inelastic break-up were selected by two respective gates, as indicated in Fig. 3.22, in order to extract the energy spectra of ^{8}Be$_{g.s.}$ and α-particles. Fig. 3.23 shows a typical two-dimensional sum of the ^{8}Be$_{g.s.}$ and α-particles spectrum as function of the ^{8}Be$_{g.s.}$ emission energy, with the events from the QE and inelastic break-up selected by the gates, respectively. The coincident data are presented in three different ways, first the two-dimensional spectra are projected onto the sum of the ^{8}Be$_{g.s.}$ and α-particle energy axis. Also presented are the QE and inelastic energy spectra as a function of the individual α-particles and ^{8}Be$_{g.s.}$ energies, as well as their energy integrated angular distribution. The QE energy spectra were fitted with two Gaussian distributions in order to select the pure QE events without contributions from the break-up of ^{13}N, i.e. ^{9}B$_{g.s.}$. A gate was set during the extraction of inelastic spectra to exclude the events originating from the ^{13}N break-up, i.e. ^{8}Be$_{g.s.}$ with the proton missing the detector.

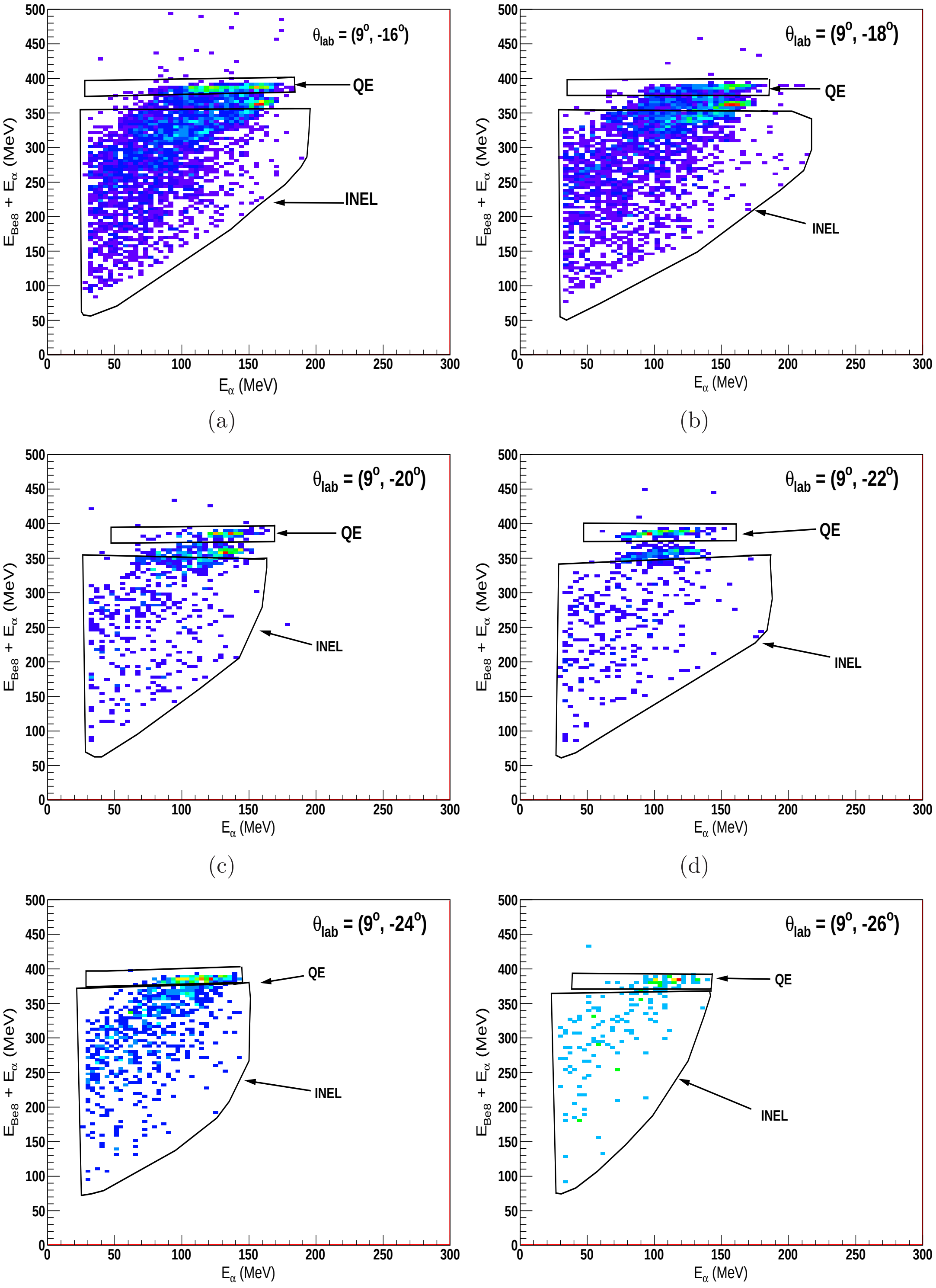

(a) (b)

(c) (d)

(e) (f)

Figure 3.22: Two-dimensional coincidence energy spectra of the sum of kinetic energy of $^{8}Be_{g.s.}$ fragments and the α-particle plotted as a function of α-particle emission energy in the interaction of ^{12}C with ^{93}Nb, for different emission angles. Quasi-elastic (QE) and inelastic (INEL) events are selected by gates excluding the hydrogen contaminants locus.

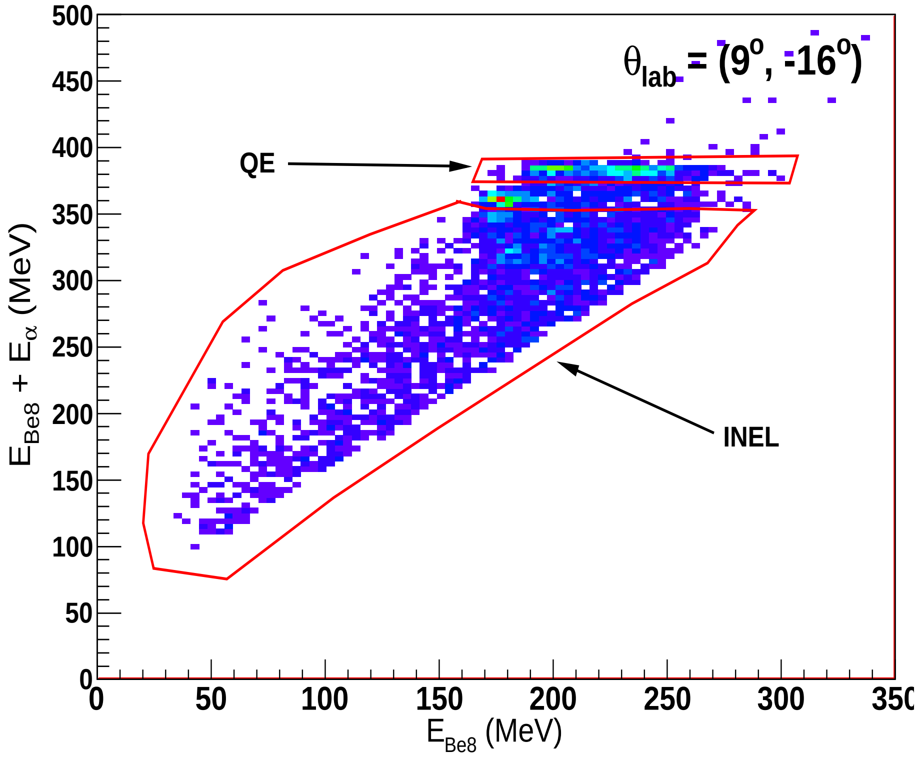

Figure 3.23: Two-dimensional coincidence energy spectrum in the interaction of ^{12}C with ^{12}C as function of ^{8}Be$_{g.s.}$ emission energy.

Table 3.5: A list of integrated charge used for normalisation of cross sections for different targets in the correlation experiment as a function of α-particle emission angle.

	^{197}Au	^{93}Nb	^{12}C
θ_α	charge (nC)	charge (nC)	charge (nC)
16°	174866	82157	14412
18°	77349	165480	17067
20°	30759	95728	3835
22°		118932	3676
24°	100430	111432	19221
26°	82573	182693	

3.5.4 Random Event Subtractions

The random event subtractions were performed by subtracting the random from real coincidences. From a relevant TAC spectrum Fig. 3.7 the random and real coincidences were selected by a gates for each α-particle emission angle. The subtraction of the random coincidences were performed for case where their amount exceeded 5% of the real coincidences. The random coincidence subtraction was only necessary in the interaction of ^{12}C + ^{12}C for the following α-particle emission angles ($\theta_{lab} = 16°$ and $18°$).

3.5.5 Conversion to Coincidence Cross-Sections

After confirmation of the energy calibrations and the background subtractions, the double differential cross sections for both the coincidence and inclusive measurements were extracted. This section explains how the energy spectra were converted into coincidence cross-sections.

The number of counts in each bin were converted to coincidence cross-sections for every energy spectrum. The energy spectra were compressed to 4 and 8 MeV per bin, since the structure of these energy spectra is characterised by a smooth continuum that does not have any narrow peaks. By compressing these spectra, one increases the number of counts in each bin, which reduces the statistical uncertainty in the number of counts. To obtain the coincidence differential cross sections the number of counts in each energy spectrum was multiplied by a conversion factor. The coincidence differential cross sections were obtained as follows:

$$\frac{d^3\sigma}{dE d\Omega^2} = N_c \times \Lambda \tag{3.3}$$

where, N_c is the corrected number of counts per bin in energy spectra. The conversion factor Λ was determined from,

$$\Lambda = \frac{1}{dE d\Omega^2} \frac{e \cos\theta_T A/N}{\lambda_T N_A D} \tag{3.4}$$

where, dE is the energy per bin (MeV), $d\Omega$ is the solid angle in sr, e is the proton charge, D is the correction factor for the electronic dead time and N is the number of projectiles in the beam. ρ is the density of the target given by

$$\rho = \frac{\lambda_T N_A}{\cos\theta_T A} \tag{3.5}$$

where, λ_T is the thickness of the target expressed in mass per unit area, N_A is the Avogadro number, A is the atomic mass of the target nucleus, and θ_T is the angle of the target normal to the beam direction.

3.5.6 Extraction of QE break-up Cross-Sections

The energy integrated angular distributions were extracted in order to study the target dependency of the QE and inelastic break-up mechanism. The energy integrated angular distributions were extracted from the gates set on the two dimensional summed energy spectra for both the QE and inelastic events as shown in Fig. 3.22. In order to obtain the pure QE energy integrated angular distributions without the events from the interaction of projectile with hydrogen contaminations, two Gaussian distributions were fitted on the QE

α-particle energy spectra at emission angles of $\theta_\alpha = 16°$ and $18°$. The events under the first Gaussian distribution were integrated to extract pure QE angular distribution. At $\theta_\alpha = 20°$ and $22°$ the contribution from ^{13}N seen in QE at the most forward θ_α were overlapping with the pure QE events, and could not be corrected by fitting two Gaussian distributions. This behaviour prompted a different approach to correct for the pure QE energy integrated angular distribution: a gate was set around the locus (3), as well as the events in locus (2) shown in Fig. 3.17 to extract the cross-sections as seen in Fig. 3.24. The cross-sections from locus (2) were multiplied by a normalising factor of (1.55 for ^{12}C, 1.3 for ^{93}Nb and 2.0 for ^{197}Au targets) in order to normalise on the cross-sections extracted from locus (3), as seen in Fig. 3.25. These figures show that the cross-sections have similar characteristics when normalised. The information gathered from these results were used to correct for the cross-sections at the emission angle of $\theta_\alpha = 20°$ and $22°$ where the events at higher α-particle emission energy region overlap with the pure QE events. The cross-sections obtained from the events extracted in locus (3) were divided by the above mentioned factors for different target to mimic the events of locus (2) and were subtracted from the pure QE events. Figs. 3.26(c) and 3.26(d) show the corrections made for extracting the pure QE energy integrated angular distribution; the red Gaussian is the sum of the two contributions from the loci (1 and 2) and the green one presents the subtracted events while the cyan represents the pure QE.

The QE cross-sections extracted as function of α-particle energy also reveal two energy distributions at the most forward emission angles of $\theta_\alpha = 16°$ and $18°$. Fig 3.26(a) and 3.26(b) show that the distribution at lower energy peaks around energies corresponding to beam velocity, while the distribution at higher α-particle energies is centred at an energy value that is too high with respect to the corresponding beam velocity. It is also evident from these QE α-particle cross-sections that the high energy distribution shifts towards the lower energy distribution enhancing the cross section at $\theta_\alpha = 20°$ and $22°$.

The QE α-particle energy spectra extracted from the data obtained in the interaction with a $(CH_2)_n$ target also revealed a pronounced peak at higher energies. The distributions at higher energy are also seen to be shifting towards the lower α-particle emission energies as a function of the emission angle. This evidence together with the result obtained from SimSort simulations justify the previous assumptions that the higher energy peak in the α-particle spectra originates from the interaction of the ^{12}C ion with the hydrogen contaminants and forming a compound ^{13}N nucleus that decays via sequential break-up.

3.6 Inclusive IMF Experiment

The offline data analysis of the inclusive IMF measurements were performed with the same COM and EVAL files used during the online data collection.

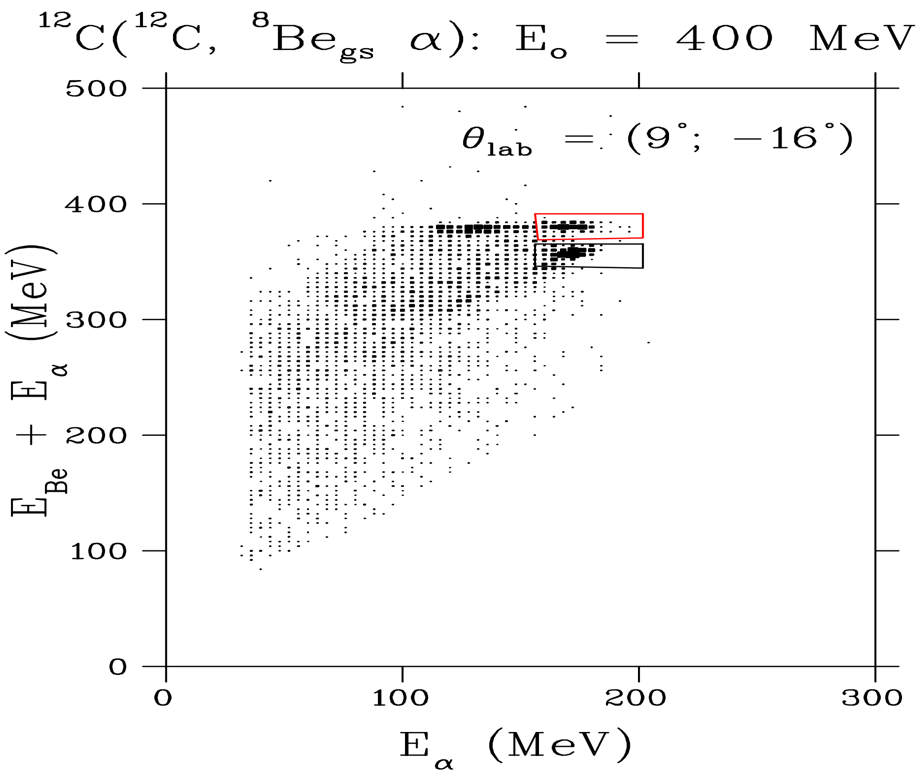

Figure 3.24: Two-dimensional coincidence energy spectrum in the interaction of ^{12}C with ^{12}C, showing two gates set around the lower locus and on the events from ^{12}C + p on the QE locus.

These files were modified in order to accommodate new data areas such as mass functions, energy spectra and the additional gates that were used to select events of interest. The offline energy calibration parameters were also added to the EVAL file. The following subsections discuss how the particles of interest were identified and selected in detail.

3.6.1 Particle Identification

In the case of the inclusive IMF experiment the particle identification as well as isotope separation were obtained by implementing the ΔE-E technique. As mentioned in Chapter 2, two detector telescopes were used to measure the energies of the emitted IMF. The heavier IMFs ($5 \leq Z \leq 10$) were measured with a triple Si detector telescope (T1), while the lighter IMFs ($3 \leq Z \leq 4$) were measured using a telescope (T2) consisting of the Si T2A ΔE-detector followed by the NaI stopping E-detector. Two particle identification (PID) spectra were generated for telescope T1, i.e. T1A versus T1B as well as T1B versus T1C detectors. Fig. 3.27(a) shows a typical two-dimensional PID spectrum measured between T1A-T1B, while 3.27(b) show typical two-dimensional PID spectra for high energy particles measured between T1B-T1C detectors

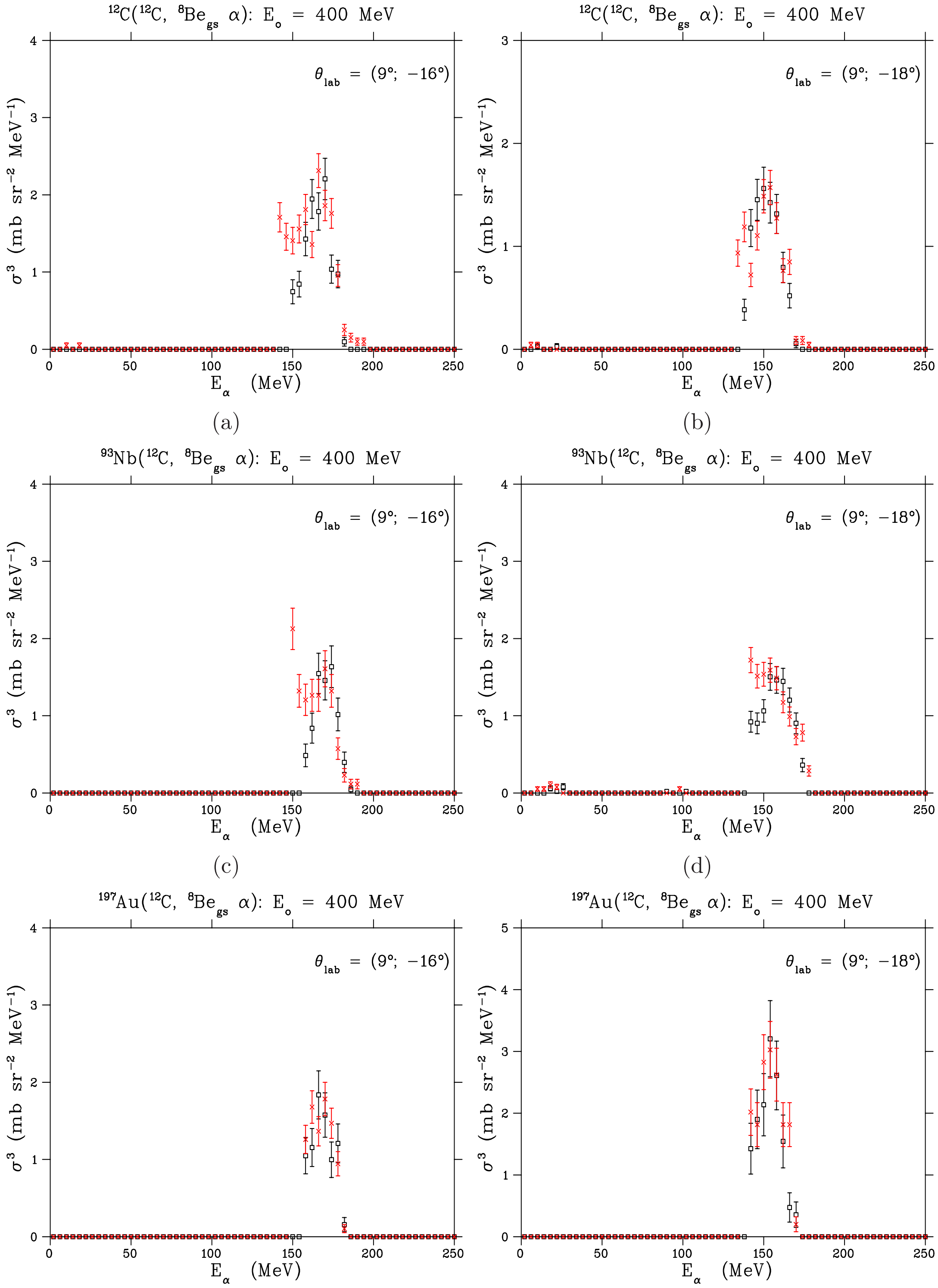

(a) (b)

(c) (d)

(e) (f)

Figure 3.25: Cross-sections extracted from gated events from the hydrogen contamination on the (QE) locus (red) overlaid on the cross-sections extracted from the H peak (black) at an α-particle emission angle of $\theta_{lab} = 16°$ and 18° for different targets, as indicated, that were used for corrections in the extraction of QE energy integrated angular distributions.

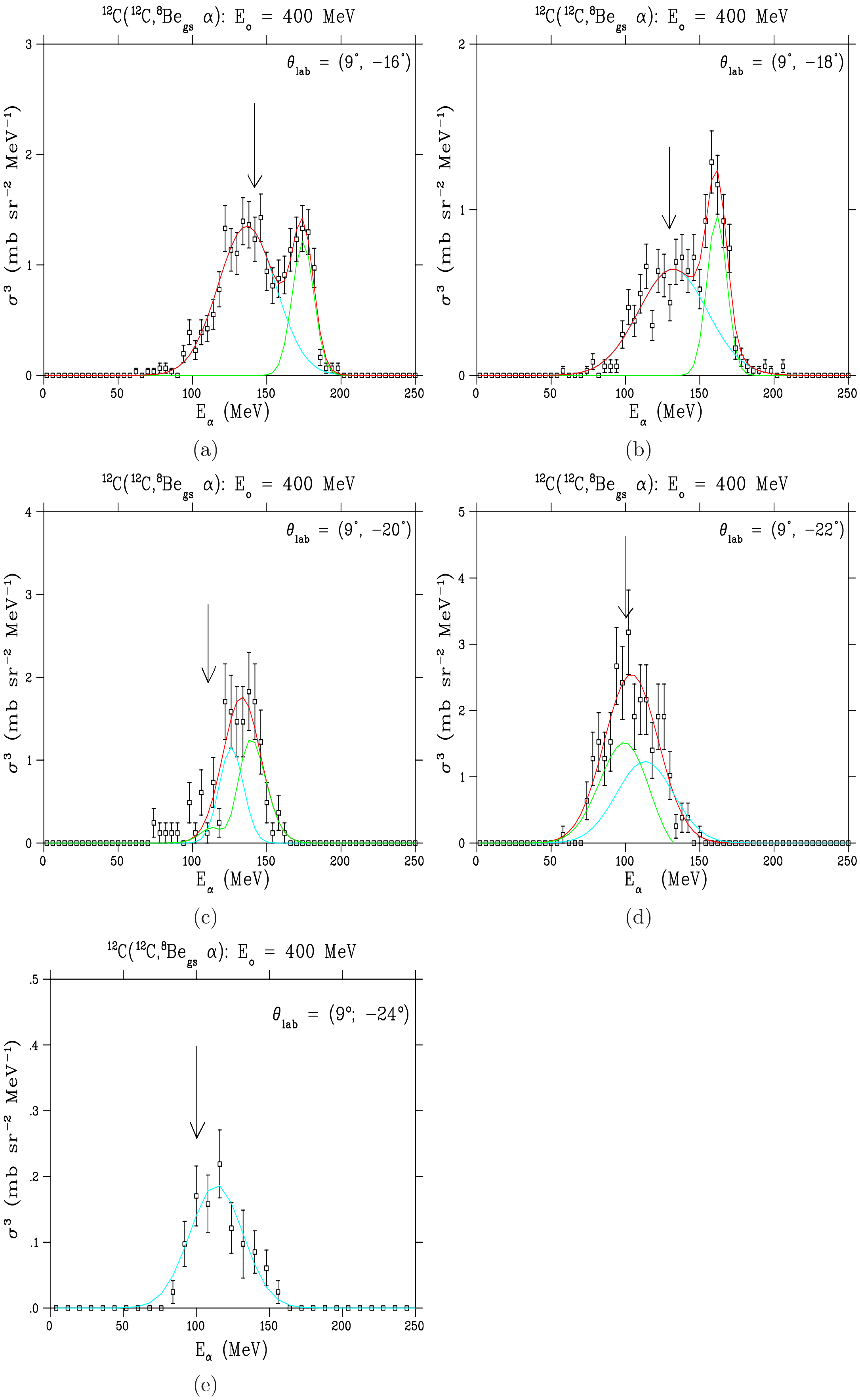

Figure 3.26: Typical QE α-particle energy spectra fitted with the two different Gaussian functions for different α-particle emission angles in the interaction of ^{12}C with ^{12}C, pure QE events (cyan), QE hydrogen contamination events (green) and the sum of the two Gaussian (red), with arrows positioned at the expected energy peak calculated with QUASTA.

Table 3.6: Integrated charge measured with the current integrator in the interaction of ^{16}O with ^{12}C at an incident energy of 235 MeV used to normalise the cross-sections at the corresponding emission angles.

	Integrated charge (nC)	Integrated charge (nC)
Emission angle	IMF ($5 \leq Z \leq 10$)	IMF ($3 \leq Z \leq 4$)
8°	-	118519
10°	159923	154324
12°	144993	150332
15°	283614	128909
20°	609666	344118
30°	462644	462644
40°	344118	609666
50°	154324	159923

with gates set around the different loci ranging from B to Ne isotopes. In order to identify and separate different isotopes of the same element two-dimensional mass functions were generated for events falling inside the gates set on the PID spectra, as discussed in Sec. 3.5.1.2. Fig. 3.28 to 3.29 show two-dimensional mass function spectra used to separate different isotopes with the gates set to extract one dimensional energy spectra. The fold back originating from the events of the particles that punch through the T1C detector were excluded by the gates set to extract the energy spectra as seen in Fig. 3.28(b). For the lighter IMF ($3 \leq Z \leq 4$) a two-dimensional PID spectrum was also generated between T2A and the NaI stopping detector, as shown in Fig. 3.30, with the gates set around the loci of Lithium and Beryllium to extract the mass functions. Fig. 3.31 shows two-dimensional mass function spectra for lighter fragments with the gates set around the different isotopes of Li and Be elements. Table 3.6 presents all the emission angles and integrated charges for the inclusive IMF experiment for all measured fragments.

3.6.2 Energy spectra

The number of counts in the energy spectra of the IMFs were converted to the double differential cross sections as shown in Sec. 3.5.5. These spectra were compressed into 4 MeV/bin in order to increase the statistics and reduce the uncertainties. In the case of telescope (T1), the energy spectra were constructed by adding the energy of events in T1A-T1B with the events in T1B-T1C in the EVAL file to create a complete energy spectrum. Fig. 3.32 shows an energy spectrum of ^{11}C measured with triple detector telescope (T1) in the interaction of ^{12}C with ^{12}C at an incident energy of E_{lab} = 400 MeV, while Fig. 3.33 show the energy spectrum of ^{6}Li measured with telescope T2 in the interaction of ^{16}O with ^{12}C at an incident energy of E_{lab} = 235 MeV. For every energy spectrum the number of counts in each bin were converted to

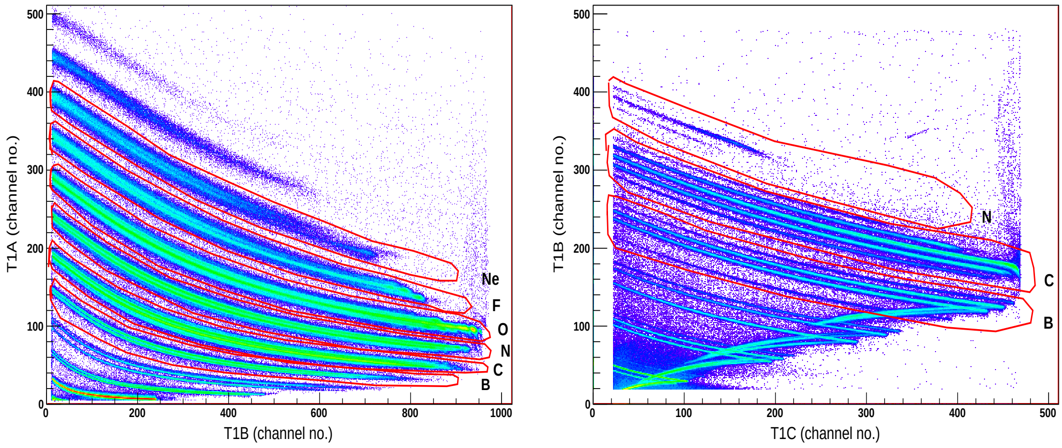

(a) (b)

Figure 3.27: Typical two-dimensional PID spectra for heavier IMFs Z ≥ 5 measured with telescope T1.

double differential cross-sections. The energy spectra were all compressed to 4 MeV per bin since these energy spectra are also characterised by a smooth continuum structure and do not have any narrow peaks.

The inclusive IMFs present full energy spectra extracted only in the interaction of an ^{16}O beam with a ^{12}C target at an incident energy of $E_{lab} = 235$ MeV. In the case of the interaction of a $E_{lab} = 400$ MeV ^{12}C beam with a ^{12}C target, only the angular distributions are presented. The full energy spectra was contaminated by the pile-up events on the particle identification spectra. The angular distributions are presented for energies where the spectra are not affected by the pile-up events. These distributions are plotted as a function of emission angles. The angular distributions extracted for particles measured with detector telescope T1 were selected carefully to avoid energy regions that fall in the dead layer between T1A-T1B and T1B-T1C detectors. The conversion to double differential cross-sections were performed as discussed under the correlation experiments by the following equation:

$$\frac{d^2\sigma}{dEd\Omega} = N_c \times \frac{1}{dEd\Omega}\frac{e\cos\theta_T A/N}{\lambda_T N_A D} \tag{3.6}$$

3.6.3 Background subtractions

The background subtraction in the case of the IMF measurements was performed as follows. In order to obtain the correct number of counts in each energy spectrum, the background had to be subtracted from the energy spectra. The ECR ion source produces ^{12}C and ^{16}O ions with charge states of $+5$ and $+6$ for beam energies of 400 MeV and 235 MeV, respectively. When the beam interacts with the target the remaining electrons are stripped off,

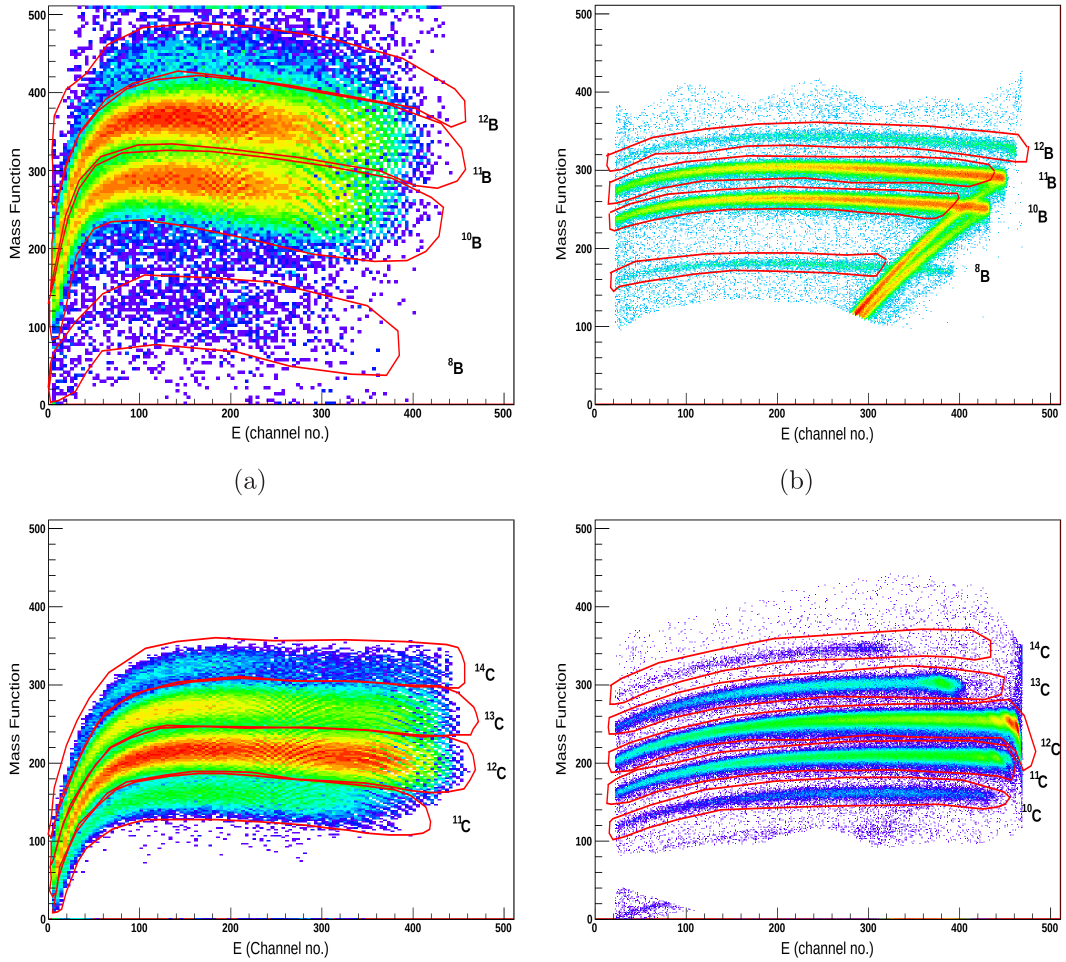

(a) (b)

(c) (d)

Figure 3.28: Mass function spectra generated from selected events in T1A-T1B and T1B-T1C detector sets with gates set around the loci of Boron and Carbon isotopes as shown in the figures.

leaving the ion in the charge state of +6 and +8, respectively, while the charge states with an empty target remain at +5 and +6, respectively. In order to perform the background subtraction correctly the total charge from an empty target should be normalised to that of ^{12}C target and also for the time differences in data taking. The normalisation was performed by multiplying the total charge from the empty target by a factor of 1.2 and 1.33, which are the ratios of the respective charge states. To check if the background subtraction was needed, the empty runs of the corresponding angles were analysed and the energy spectra were examined to check whether they were affected by background contamination. The background subtractions were performed for the forward emission angles between $\theta_{lab} = 8°$ and $15°$ where the background exceeded 10%. From these analyses it was observed that the subtraction of

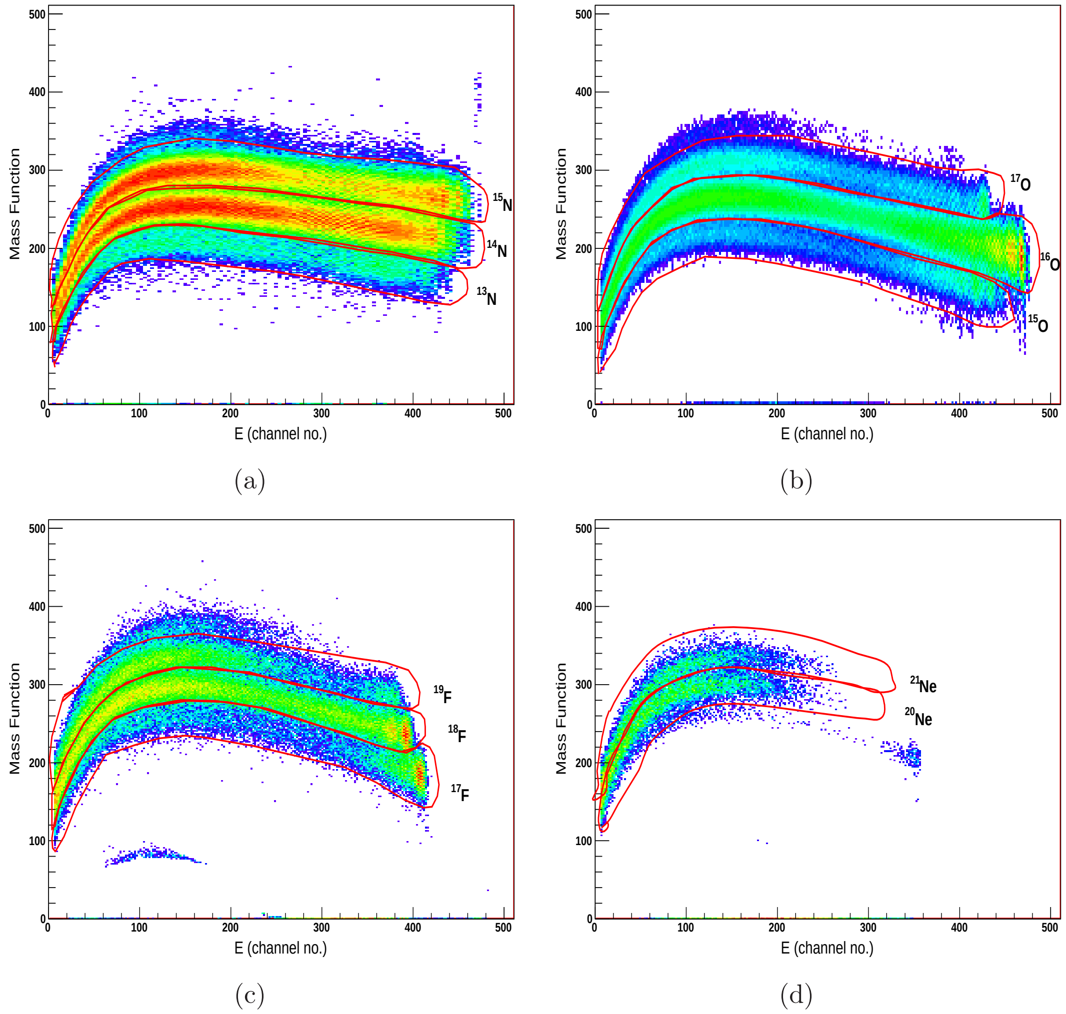

Figure 3.29: Mass function spectra generated for the selected events in T1A-T1B with gates set around the loci of ^{13,14,15}N (a), ^{15,16,17}O (b), ^{17,18,19}F (c), and ^{20,21}Ne (d) as indicated in the figures.

the background contamination was needed only for the most forward emission angles.

3.7 Error analysis

Two types of errors are associated with the experimental results, namely statistical and systematic errors. These errors are related to the methods used to perform the experiments.

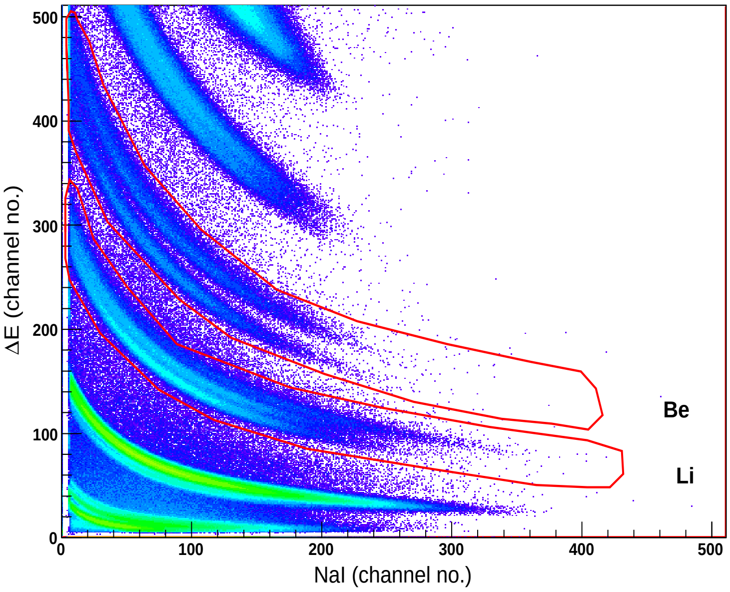

Figure 3.30: A typical two-dimensional PID spectrum of the Si T2A-T2B detectors with gates set around the loci of Li and Be elements.

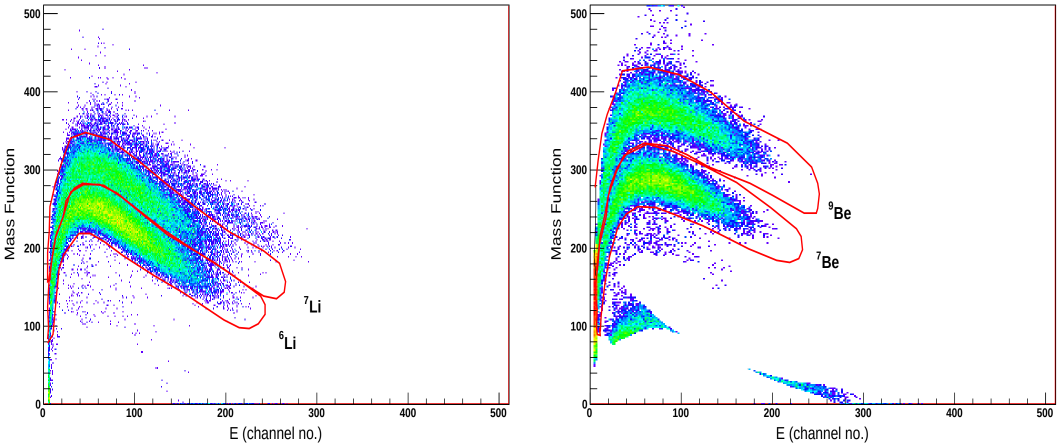

(a)

(b)

Figure 3.31: Mass function spectra with gates set around the loci of ^{6,7}Li (a), ^{7,9}Be (b), as indicated in the figures.

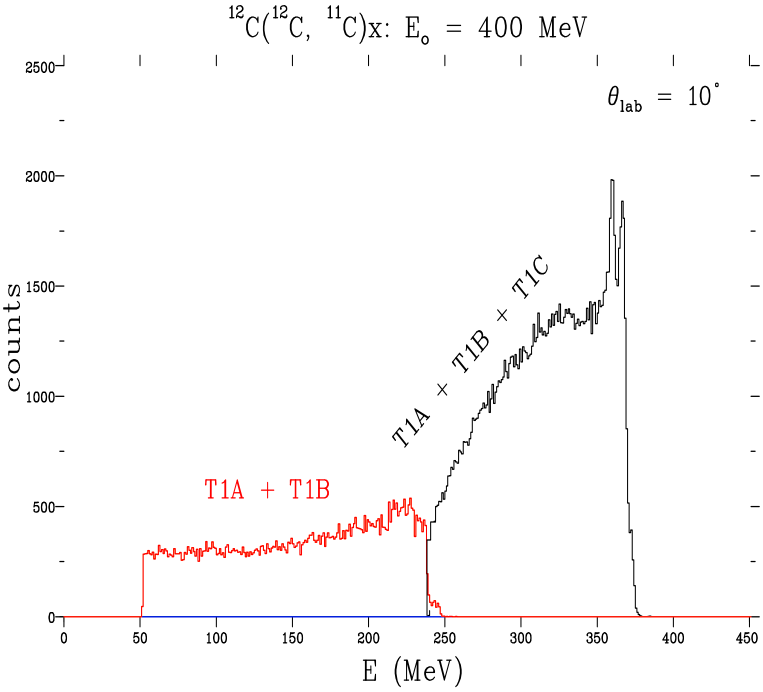

Figure 3.32: A typical ^{11}C energy spectrum extracted in the interaction ^{12}C with ^{12}C at an incident energy of 400 MeV, the red histogram represents detector set T1A-T1B and the black histogram is between T1B-T1C detectors.

3.7.1 Statistical errors

The statistical error is due to the uncertainty in the number of counts per bin. These kinds of errors may arise from the inherent statistical nature of the phenomenon being observed [Leo87]. The statistical error taken from the number of counts N_i is simply the square root of the total number of counts, $\sqrt{N_i}$. The corrected number of counts in a bin is given by $N_i \pm \sqrt{N_i}$. The cross sections were compressed in 4 MeV per bin for both experiments, but for larger emission angles, in the case of the correlation experiment, the cross sections were binned into 8 MeV per bin to increase the counts thereby reducing the statistical uncertainties. The error bars on the data points in the cross sections for both the correlations and inclusive IMFs represent the statistical uncertainties only.

3.7.2 Systematic errors

Systematic errors are classified as the uncertainties caused by the bias of the data [Leo87]. These errors occur due to uncertainties in the measurement of particular instruments used in the experiment, such as detectors, solid angles, energy calibration and the target's thickness. All the uncertainties and their sources are explained in the subsections that follow and are also presented in

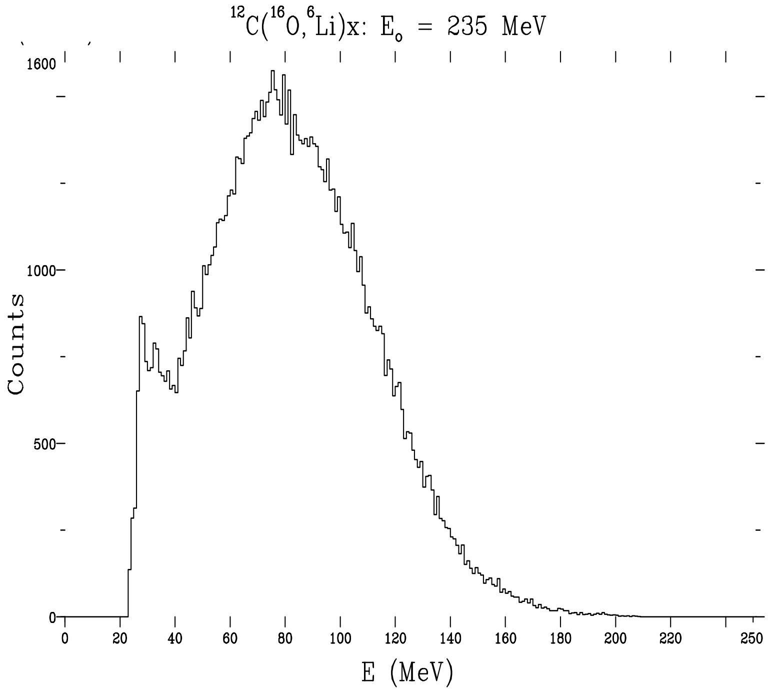

Figure 3.33: A typical ^{6}Li energy spectrum extracted in the interaction ^{16}O with ^{12}C at an incident energy of $E_{lab} = 235$ MeV.

Table 3.7 together with the total uncertainties presented as a percentage.

3.7.2.1 Energy Calibration

The errors in the energy calibrations of the detectors arise from the uncertainties in the identification of channel numbers corresponding to the characteristic α-particle energies from a ^{228}Th source and the elastic scattering peaks of the ion beams. The energy bins might differ slightly with respect to the corresponding expected energy values. The uncertainty in the energy range is about 2 MeV which translates into estimated uncertainties of 4% in the absolute cross sections of both experiments.

3.7.2.2 Target Thickness

The uniformity of the target thickness is an important contribution towards the overall systematic error. Uncertainty in the target thickness was checked by using a ^{228}Th source. The uniformity of the target thickness was examined by illuminating the target foil at different positions and measuring the energy loss of the 8.78 MeV α-particle from a ^{228}Th source in the target material. The variance of the 8.78 MeV peak positions for different positions on the target foils was found to be about 3% for ^{197}Au, 2% for ^{93}Nb, while uncertainty of 5% was quoted for the ^{12}C thickness.

3.7.2.3 Solid Angle

The uncertainty in the solid angle subtended by a detector arises from the uncertainties in measuring the distance from the centre of the target to the centre of the back of the collimators inset, as well as the radii of the collimator insets, and about 2 mm beam spot spread on the centre of the target. The combined error was estimated from the uncertainties in the geometry parameters. These uncertainties in the solid angles were estimated to be about 1%.

3.7.2.4 Particle Identification

In the case of the correlation experiment, uncertainties occur in separating α-particles from ^{3}He and in distinguishing ^{8}Be from ^{4}He by means of a PID gate. The fold back from the Li isotopes crossing over the α-particle events furthermore contributed to the uncertainty in the correlation measurement. The uncertainties from the PID in the correlation experiment was estimated to be about 2%. The uncertainties from PID in the inclusive IMF experiment mainly arose from two-dimensional gating on the PID spectra to separate different elements, and gating on the mass function spectra when selecting the different isotopes. Even though a careful procedure was followed when selecting a specific specie an uncertainty of about 1% was estimated.

3.7.2.5 Subtraction of random coincidences

The uncertainty in the selection of coincidence events arises when selecting true from random coincidences by setting appropriate gates in the TAC spectrum. In the case of the correlation measurement the random coincidence events were subtracted from the true coincidences and the uncertainty for this background subtraction was estimated to be about 2%.

3.7.2.6 Current integrator

In both experiments the uncertainty in the amount of charge collected by the current integrator was estimated to be less than 2%.

3.7.2.7 Electronic dead time

The uncertainty which relates to the electronic dead time was estimated to be less than 2% for both the correlation and inclusive IMF experiments.

Table 3.7: Summary of all uncertainties contributing to systematic errors

System	Correlation experiment (%)	Inclusive IMF experiment (%)
Target thickness		
^{12}C	5	5
^{93}Nb	2	-
^{197}Au	3	-
Energy calibration	4	4
Solid Angle	1	1
Particle identification	2	1
Subtraction of random	2	-
Current integrator	2	2
electronic dead time	2	2
Total Systematic error	6 - 7.6	7.1

Chapter 4

Theoretical Models

4.1 Overview

Theoretical calculations were performed and compared to the data to interpret the experimental energy spectra of both the correlation experiment and the inclusive measurement. The theoretical calculations and simulations for the correlation data were performed with GEANT4 code [Ago03]. GEANT4 is a toolkit for simulating the passage of particles through matter and its areas of application include high energy, nuclear and accelerator physics, as well as studies in medical and space science. The GEANT4 simulation code was developed at CERN and a large number of physical models such as Binary cascade, Pre-compound, Fermi break-up model, etc., are implemented to interpret the reaction mechanisms such as the binary break-up mechanism. The aim of the present simulations was to examine the binary break-up of the ^{12}C projectile into ^{8}Be fragments and α-particles, which were measured in coincidence. Most importantly, it was to interpret the energy distribution spectra of the QE α-particles. The binary break-up of ^{12}C into its constituents ^{8}Be$_{g.s}$ fragments and α-particles was done with GEANT4 simulation by incorporating a detailed description of the experimental setup used during the experiment. The Fermi beak-up model [Fer50] which is incorporated in QBBC and QGS physics lists was applied in GEANT4 to interpret the binary break-up of ^{12}C as described in Sec. 4.2, below.

A Monte Carlo simulation code SimSort [Pap07] was also used to analyse the correlation results. The SimSort code is mainly used to analyse experimental nuclear physics data and also to simulate the kinematic of nuclear reactions. The SimSort code is mainly used with charged particle detectors. This code can recognise any type of telescope with Silicon, ionisation chambers and CsI (Tl) detectors. Until now the SimSort has mainly handled the Silicon detectors such as the Double-Sided Silicon Strip Detector (DSSSD) and the Position-Sided Silicon Strip Detector (PSSSD) in different combinations.

The theoretical calculations of the spectra of the IMFs were performed by using the nuclear transport and Monte Carlo simulation code FLUKA. This code is also used in treatment planning in hadron therapy starting from nucleus-nucleus reaction modelling at low energy to post irradiation computed tomography (CT) based dose calculations and biological effective dose calculations [Par07]. Most of the similar experiments previously performed at iThemba LABS that also investigated the role that different reaction mechanisms play in the production of IMFs were interpreted by means of a theoretical model developed at the University of Milan [Gad99, Gad03, Bec03, För05]. This model has been used to model the interaction of light nuclei such as ^{12}C and ^{16}O with light to heavier target nuclei ranging from ^{12}C to ^{197}Au. The results of these earlier studies showed that this model could be successfully implemented to reproduce energy spectra by incorporating reaction mechanisms such as projectile and target fragmentation and nucleon coalescence through complete and incomplete fusion reactions. The present study of ^{16}O + ^{12}C is also interpreted with this model incorporating different reaction mechanisms. For this study the model was implemented to reproduce the energy spectra of Projectile-Like Fragments (PLF) and heavier fragments. The isotopes that were modelled were ^{15}N, ^{15,16,17}O, ^{17,18,19}F and ^{19,20}Ne. At present, the model used to interpret the above mentioned isotopes is still undergoing modification, with the multi-nucleon transfer from the target to projectile and vice versa still needs to be incorporated. The reaction mechanisms incorporated in the FLUKA model include complete and incomplete fusion reactions and the binary break-up mechanism.

In this chapter, the projectile and target fragmentation, as well as complete and incomplete fusion reaction mechanisms have been revisited for the IMFs calculations. The complete and incomplete reaction mechanisms are interpreted by a set of Boltzmann Master Equations (BMEs) [Cav01], and the theory of the binary break-up mechanisms was described by folding a Local Plain Wave Born Approximation (LPWBA) [Hus81, McV80, Ser47] with the survival probability of the projectile. These two reactions are described in details in the following sections.

4.2 Fermi Break-up

In GEANT4 versions preceding version 8.3, the modelling of quasi-elastic (QE) scattering was not incorporated in the Quark Gluon String (QGS) model [Apo09]. A simple model for QE scattering was added later to the QGS. This was done by adding effects of Fermi motion of the nucleons on the momenta of the two final-state particles. The QE scattering reduces the energy and momentum of the two final-state particles by a small amount and their scattering angle is very forward.

The Fermi break-up mechanism was initially proposed by Enrico Fermi [Fer50] to describe high energy hadronic collisions due to the multiple production of particles. The Fermi break-up model (FBM) was incorporated into the GEANT4 simulation code by the GEANT4 group at CERN [Ago03]. The GEANT4 FBM is capable of predicting final states resulting from the statistical break-up of an excited nucleus with atomic number Z $<$ 17. The Fermi break-up decay is allowed if the total kinetic energy E_{kin} of all fragments of a given channel is greater than zero. The total kinetic energy is thus given by the expression,

$$E_{kin} = U + M(A, Z) - E_c - \sum_{b=1}^{n} (m_b + E^*), \tag{4.1}$$

where U represents the Coulomb interaction energy of the fragments, *M(Z,A)* represents the mass of an excited nucleus, m_b is the mass of the emitted fragment, E^* is the excitation energy of the fragment, and E_c is the Coulomb barrier for the appropriate channel b and is given by,

$$E_c = \frac{3}{5}\frac{e^2}{r_o}(1 + V/V_o)^{-1/3} \cdot \left(Z^2/A^{1/3} - \sum_{b=1}^{n} Z^2/A_b^{1/3} \right), \tag{4.2}$$

where V_o is the volume of the system corresponding to the normal nuclear matter density; the relation $V/V_o = 1$ is normally used.
The total probability for the residual nucleus to break-up into n components in the final state is given by,

$$P(E, n) = (V/\Omega)^{n-1} \cdot \rho_n(E), \tag{4.3}$$

where V is the decay volume of the system, $\Omega = (2\pi\hbar)^3$ is the normalisation volume of the system, $\rho_n(E)$ is the density of the number of final states and can be defined as the product of three factors,

$$\rho_n(E) = M_n(E) \cdot S_n \cdot G_n, \tag{4.4}$$

where $M_n(E)$ is the phase space and is defined as

$$M_n(E) = \int_{-\infty}^{+\infty} \cdots \int_{-\infty}^{+\infty} \delta\left(\sum_{b=1} \boldsymbol{p_b} \right) \delta\left(E - \sum_{b=1}^{n} \sqrt{p^2 + m_b^2} \right) \prod_{b=1}^{n} d^3 p_b, \tag{4.5}$$

where $\boldsymbol{p_b}$ is the momentum of fragment b. The second factor is the spin S_n which gives the number of states with different spin orientations and is given by,

$$S_n = \prod_{b=1}^{n} (2s_b + 1), \tag{4.6}$$

The third one is a permutation factor and is given as

$$G_n = \prod_{j=1}^{k} \frac{1}{n_j!} \tag{4.7}$$

which takes into account the identity of the fragments. The value n_j is the number of components of the j-type particles and k is defined by $n = \sum_{j=1}^{k} n_j$. By substituting for a non-relativistic case in Eq. (4.5), the corresponding functions for the density, the phase space factor, the fragment momentum, and the spin orientation and solving the integral of Eq.(4.5), the probability *P(E,n)* of the nucleus with energy E disassembling into n fragments with masses m_b, where $b = 1, 2, 3, ..., n$ is expressed as

$$P(E,n) = S_n \cdot G_n \cdot \left(\frac{V}{\Omega}\right)^{n-1} \cdot \left(\frac{1}{\sum_{b=1}^{n}} \prod_{b=1}^{n}\right)^{3/2} \cdot \frac{(2\pi)^{3(n-1)/2}}{\Gamma(3(n-1)/2)} \cdot E^{(3n-5)/2}, \tag{4.8}$$

where Γ is the gamma function. The Fermi break-up model has only one free parameter V which is the volume of the decaying nucleus and can be calculated as follows

$$V = 4\pi \cdot R^3/3 = 4\pi \cdot r_o^3 \cdot A/3, \tag{4.9}$$

where, $r_o = 1.4 fm$ may be used.

The GEANT4 code was modified for the correlation study in order to reproduce the experimental set-up. In this code it is assumed that the ^{8}Be breaks-up into its two constituent α-particles. A physics list that incorporates Fermi break-up model was activated to run the GEANT4 code. In order to reconstruct the ^{8}Be fragments, a coincidence between two α-particles measured on the ^{8}Be telescope was searched for and their kinetic energy was summed up. For every coincident on the ^{8}Be telescope, the coincidence between the ^{8}BE and α-particle telescopes was searched and the data were recorded.

4.3 The BME-FLUKA interface for nucleus-nucleus interactions below 100 MeV/n

The processes which may occur during the thermalisation of a composite nucleus created during the complete fusion of the projectile with the target nucleus, or incomplete fusion of fragments with the target nucleus, are simulated by means of a Monte-Carlo event generator. This event generator is able to incorporate the results of the numerical integration of the Boltzmann Master Equations (BMEs) [Cav01, Mai07] as input. The theory of BMEs describe the time evolution of the momentum distribution of the nucleons of the composite nucleus via two-body elastic scattering and particle emissions into the continuum (both single nucleons and clusters such as a light particles or an IMF) [Cav96]. The occupation probabilities at a subsequent time t are evaluated by integrating the set of BMEs given below for a particle which is emitted into the continuum

$$\begin{aligned}\frac{d(n_i g_i)}{dt} &= \sum_{jlm}[\omega^{\pi\pi}_{lm\to ij} g^{\pi}_l n^{\pi}_l g^{\pi}_m n^{\pi}_m (1-n^{\pi}_i)(1-n^{\pi}_j) \\ &\quad -\omega^{\pi\pi}_{ij\to lm} g^{\pi}_i n^{\pi}_i g^{\pi}_j n^{\pi}_j (1-n^{\pi}_l)(1-n^{\pi}_m)] \\ &\quad +\sum_{jlm}[\omega^{\pi\nu}_{lm\to ij} g^{\pi}_l n^{\pi}_l g^{\nu}_m n^{\nu}_m (1-n^{\pi}_i)(1-n^{\nu}_j) \\ &\quad -\omega^{\pi\nu}_{ij\to lm} g^{\pi}_i n^{\pi}_i g^{\nu}_j n^{\nu}_j (1-n^{\pi}_l)(1-n^{\nu}_m)] \\ &\quad -n^{\pi}_i g^{\pi}_i \omega^{\pi}_{i\to i'} g_{i'} \delta(\epsilon^{\pi}_i - \epsilon^{\pi}_F - B^{\pi}_i - \epsilon^{\pi}_{i'}) - \frac{dD^{\pi}_i}{dt},\end{aligned} \tag{4.10}$$

the symbols π and ν represent the proton and neutron, respectively. The quantities g_i are total number of states in bin i, the quantities $\omega_{ij\to lm}$, $\omega_{i\to i'}$ and dD^{π}_i/dt represent the internal transition decay rates, the decay rates for emission of a single proton into the continuum, and a depletion term which accounts for the emission of protons bound in a cluster, respectively. The internal transition rate $\omega_{ij\to lm}$ is given by the following expression:

$$\omega_{ij\to lm} = \frac{1}{2\pi}\int_0^{2\pi} \boldsymbol{\omega_{ij\to lm}} d\phi_j, \tag{4.11}$$

where

$$\boldsymbol{\omega_{ij\to lm}} = \frac{\sigma_{ij}\nu_{ij}\Pi_{ij\to lm}}{V}, \tag{4.12}$$

Here V is the nuclear volume, ν_{ij} is the two interacting nucleons' relative velocity. The indices $\boldsymbol{i, j, l, m}$ stand for momenta p_i, p_j, p_l and p_m. ϕ_j is the azimuthal angle of p_j, taken $\phi_j = 0$. The quantity $\Pi_{ij\rightarrow lm}$ represents the probability of reaching bins l and m if the interacting nucleons have the momenta p_i and p_j belonging to bins i and j, respectively. The decay rates $\omega_{i\rightarrow i'}$ are given by

$$\omega_{i\rightarrow i'} = \frac{\sigma_{inv}\nu_i}{g_i V'}, \tag{4.13}$$

where σ_{inv} is the inverse process cross section and ν_i is the relative velocity between the nucleon and the residual nucleus. When neglecting the nucleus recoil momentum, it coincides with the nucleon velocity with respect to the centre-of-mass system. V' is the laboratory volume which cancels a similar factor appearing in the expression of $g_{i'}$ in equation (4.10). The differential multiplicity of the particles emitted in the time interval dt at an angle θ with energy E' is given by

$$\frac{d^3N'(E', \theta, t)}{dE'd\theta dt} = RN(\epsilon, \theta, t)\frac{\sigma_{inv}\nu'}{V'}\rho(E', \theta), \tag{4.14}$$

and the measured multiplicity spectrum of emitted nucleons is given by

$$\frac{d^2M}{dE'd\Omega} = \int_0^{t'} \frac{1}{2\pi \sin\theta}\frac{d^3N'(E', \theta, t)}{dE'd\theta dt}dt, \tag{4.15}$$

where $N'(E', \theta, t)$ is the occupation probability of the states of the considered particle inside the composite nucleus, E' is the energy of the emitted particle in the continuum, t' is the time taken for the emission of high energy particles, R is the survival factor that takes into account the possible dissolution of the cluster into its constituent nucleons before emission and

$$\rho(E', \theta) = \frac{\sin\theta}{2}\rho E', \tag{4.16}$$

where $\rho(E')$ is the density of the particle states in the continuum. For calculating the multiplicity of the cluster c, one has to evaluate the probability that the momenta (Z_c + N_c) nucleons are correlated in such way as to move together as a cluster with centre-of-mass energy E_c inside the composite nucleus, the direction of which forms an angle θ_c with respect to the beam, $N(\epsilon, \theta, t) \equiv N(E_c, \theta_c, t)$ is given by,

$$N(E_c, \theta_c, t) = \prod_i (n_i^\pi)^{P_i(E_c,\theta_c)Z_c} \cdot \prod_i (n_i^\nu)^{P_i(E_c,\theta_c)N_c}, \tag{4.17}$$

The index i runs over all the bins in which the nucleons constituting the cluster may be found. $P_i(E_c, \theta_c)$ is the fraction of the bin i within the Fermi sphere of the cluster c with radius P_{CF}. Z_c and N_c are the respective numbers of protons and neutrons of cluster c. If Q_c is the Q-value for the cluster emission and $A_c = N_c + Z_c$, then $E_c^{'}$, the continuum energy of the cluster c, is given by

$$E_c^{'} = E_c + Q_c - A_c(\epsilon_F - \epsilon_{FC}), \tag{4.18}$$

where ϵ_F and ϵ_{FC} are the composite nucleus and the cluster Fermi energies, respectively. The depletion term is given by,

$$\frac{dD_i^{\pi}}{dt} = \sum_c \int \int P_i(E_c, \theta_c) \frac{d^3N'(E', \theta, t)}{dE' d\theta dt} dE_c d\theta_c. \tag{4.19}$$

4.4 Binary break-up

The binary fragmentation of the projectile or target nucleus is interpreted under the binary break-up mechanisms. The theory of binary break-up is based on the assumption that projectile or target fragmentation is a peripheral direct reaction occurring in a window of large angular momenta [Lil01, Gad03]. It is assumed that the probability of the projectile surviving break-up decreases exponentially with an increasing energy loss [Gad03]. In the study of the IMF production the spectra of the break-up fragments are evaluated by folding the local plain wave approximation (LPWA) cross-sections with an exponential survival probability [Gad00]. The break-up fragments populate the higher energy region of the spectra and is based on the assumption that before breaking-up the projectile does not suffer a significant energy loss [Gad00, Bec03, Gad03]. In summing up all these assumption the break-up contribution to the spectra is given by

$$\frac{d^2\sigma}{dE' d\Omega}(E_0, E', \theta) = \sigma_{bu} \frac{\int_{E_{l,min}}^{E_0} P(E_l) S(E_0 - E_l, \theta) dE_l}{\int_{E_{l,min}}^{E_0} P(E_l) dE_l}, \tag{4.20}$$

where, σ_{bu} is the angle and energy integrated break-up cross-section, E_0 is the asymptotic kinetic energy of the projectile in the two ions centre-of-mass system, E_l is the energy lost by the projectile before breaking-up, and the function P_l represents the probability of the projectile surviving a break-up or mass transfer reaction and is assumed to decrease exponentially with increasing projectile energy loss, starting from a minimum energy loss $E_{l,m}$ given by

$$P(E_l) = exp[-C(E_l - E_{l,m})]. \tag{4.21}$$

According to the local plain wave Born Approximation (LPWBA) [Ser47, Gad03], the cross-section $\boldsymbol{S}$ for production of a fragment with energy E' at an angle θ with the projectile break-up energy of $E = E_0 - E_l$ is given by

$$S(E, E', \theta) \propto p'p'' \mid \hat{\psi}(\boldsymbol{P}) \mid^2, \tag{4.22}$$

where p' is the linear momentum of the spectator fragment, p'' is the linear momentum of the participant fragment, and $\hat{\psi}$ represent the Fourier transform of the wave function describing the motion of the spectator fragment within the projectile and is given by

$$\hat{\psi}(\boldsymbol{P}) = \frac{1}{(2\pi\hbar)^{3/2}} \int \psi(\boldsymbol{r}) exp[-\frac{i}{\hbar}(\boldsymbol{P} \cdot \boldsymbol{r})] d\boldsymbol{r}. \tag{4.23}$$

By assuming that the participant fragment fuses with the target nucleus, the three momenta $\boldsymbol{p}'$, $\boldsymbol{p}''$ and $\boldsymbol{p}$ are related as follows

$$\boldsymbol{p}' + \boldsymbol{p}'' = \boldsymbol{p}_p, \tag{4.24}$$

where $\boldsymbol{p}_p$ is the projectile momentum at the break-up time in the two ion centre-of-mass system, the spectator fragment internal momentum in the projectile is given by

$$\boldsymbol{p} = \boldsymbol{p}' - (m'/m_P)\boldsymbol{p}_p, \tag{4.25}$$

where m' and m_P are the masses of the spectator fragment and the projectile, respectively.

Chapter 5

Results and Discussion

5.1 Overview

This chapter is dedicated to the presentation of the energy spectra extracted from the data for both the correlation measurements and the inclusive IMF measurements. The data from the correlation measurements are presented for both the quasi-elastic (QE) as well as the inelastic cross-sections. A subset of these data is presented here as energy spectra as well as energy-integrated angular distributions. The complete set of energy spectra is shown in Appendix A.

The inclusive double differential cross sections of the IMFs are presented for both the interaction of E_{lab} = 400 MeV ^{12}C and E_{lab} = 235 MeV ^{16}O beams impinging on the ^{12}C target. The double differential cross-sections of the following isotopes; ^{6,7}Li, ^{7,9}Be, ^{8,10,11}B, ^{11,12,13,14}C, ^{13,14,15}N ^{15,16,17}O, ^{17,18,19}F and ^{20,21}Ne measured in the interaction of ^{16}O with ^{12}C are presented. The angular distributions of the IMFs from ^{12}C on ^{12}C are presented. Results of comparisons between the experimental spectra and the theoretical calculations performed with the FLUKA code [Mai07] are presented for all the fragments with ($7 \leq Z \leq 10$).

5.2 Coincidence cross-sections

The coincidence energy spectra are projected onto the axis of the sum of the kinetic energy of the ^{8}Be$_{g.s.}$ fragment and α-particle. These cross sections are accurate to within a systematic error of approximately 6%, as shown in Table 3.7. These energy spectra consist of two regions of interest, which are shown in Figs. 5.1 to 5.3. The sharp peak that appears at the highest energy, corresponding to the beam velocity, is referred to as the QE peak. Secondly, a tail of inelastic break-up events extend down to the lowest energy part of the spectra. The intensity of the QE peak decreases with an increasing α-particle emission angle. The inelastic events mostly originate from the final-state in-

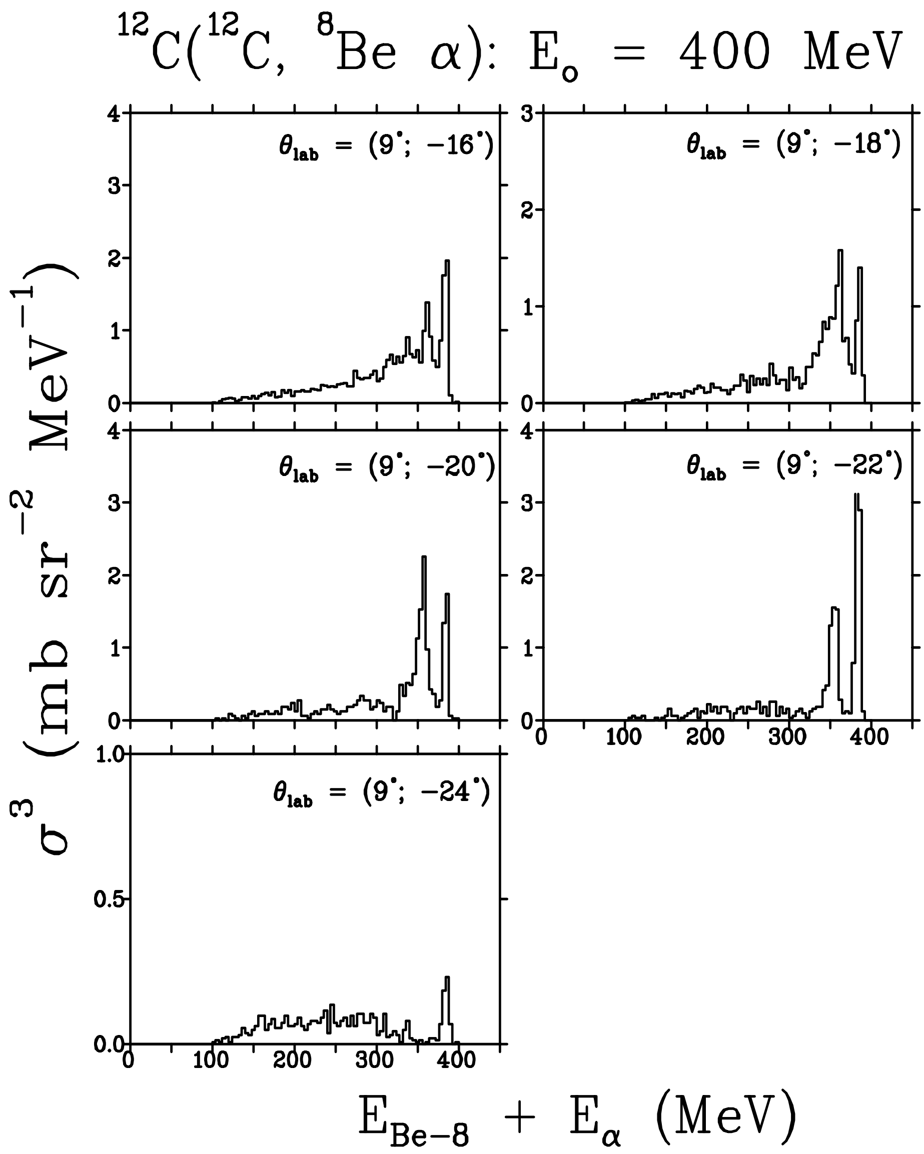

Figure 5.1: Coincidence cross-sections of the sum of the kinetic energy of the correlated ^{8}Be$_{g.s.}$ and α-particle emitted in the interaction of 400 MeV ^{12}C with ^{12}C target as indicated in the figure. The ^{8}Be$_{g.s.}$ fragments were measured at a fixed angle of $\theta_{lab} = 9°$ and α-particles were measured at different emission angles, as indicated. The triple differential cross-sections are plotted with a binning of 4 MeV/bin.

teraction of α-particles with the target nucleus leaving the correlated ^{8}Be in its ground state. Since ^{8}Be$_{g.s.}$ is unbound, it cannot survive the final-state interaction with the target nucleus without breaking up into its two constituent α-particles. Only the final-state interaction between the α-particles and the target nucleus is considered. Also observed is a narrow peak that appears about 30 MeV below the QE peak which vanishes as the α-particle emission

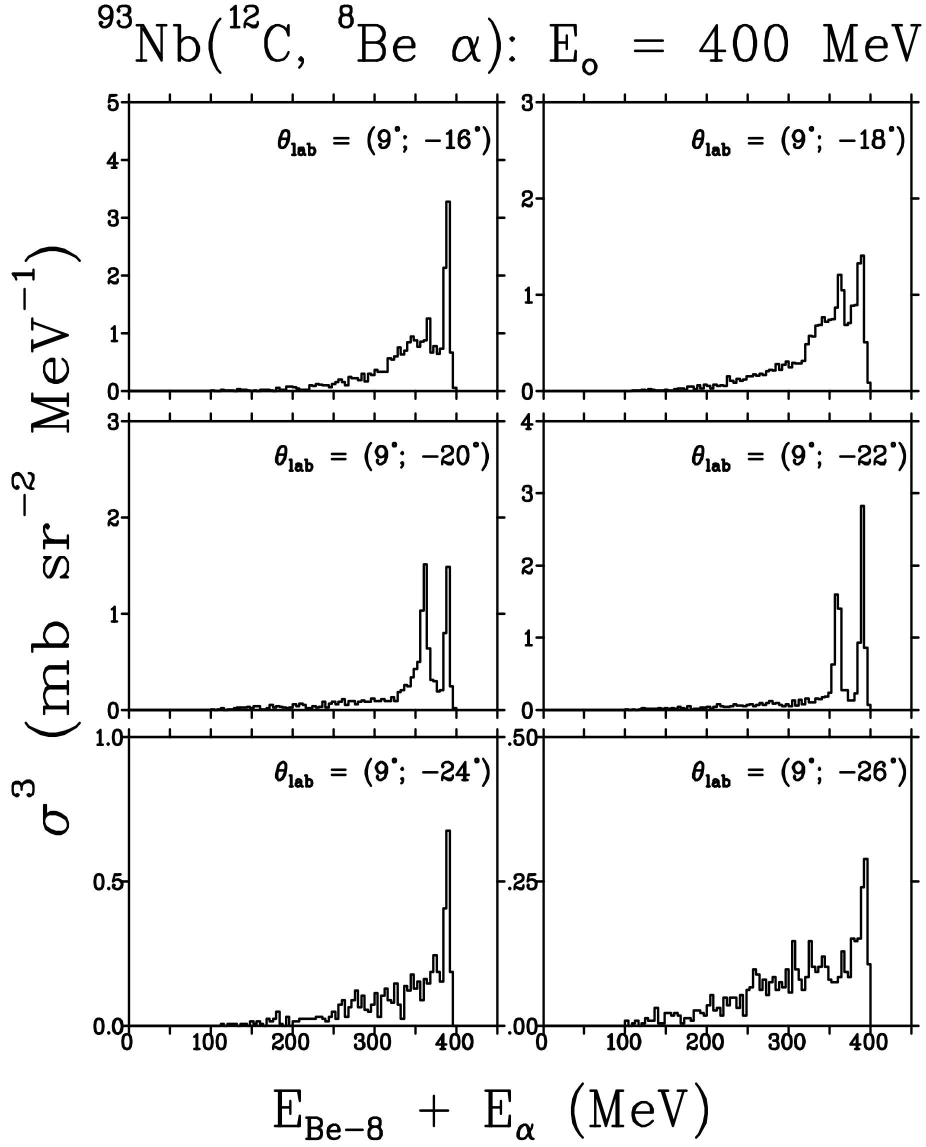

Figure 5.2: Coincidence cross-section in the interaction of ^{12}C with a ^{93}Nb target. See full caption in Fig. 5.1.

angle reaches $\theta_\alpha = 24°$ and larger. For the α-particle emission angles between $\theta_\alpha = 18°$ and 22°, the intensity of the lower energy peak reaches maximum and then decreases again for all the targets as a function of the α-particle emission angle. The origin of this lower energy peak was found to originate from the interaction of ^{12}C with hydrogen contamination on the target foils. The SimSort simulation code was used to model the fusion of ^{12}C with H to form a ^{13}N compound nucleus which decays by sequential break-up into an α-particle and ^{9}B$_{g.s.}$ that decays into a proton and ^{8}Be$_{g.s.}$. A $(CH_2)_n$ target was also used in these measurements to affirm the hypothesis about the peak at low energy around 360 MeV. Fig. 5.4 shows a pronounced intensity of the energy peak around 360 MeV when the ^{12}C beam interacts with the $(CH_2)_n$ target. Since the $(CH_2)_n$ target has two hydrogen nuclei for each C nucleus, the density of the H nucleus is about 14% of the total thickness and the fusion cross-sections are larger. This observation confirms the hypothesis that the peak that appear at energies of 360 MeV originates from the fusion of the ^{12}C projectile that interacts with H to form ^{13}N, which breaks up into an α-particle and $^{9}B_{g.s}$, which breaks up again, into $^{8}Be_{g.s.}$ and a proton. In the case of $^{12}C + ^{12}C$, it is probable that the target could also break-up into ^{8}Be and α-particles, which might contaminate the spectra of the projectile break-up. The detector set-up and the technique used to detect the ^{8}Be are less efficient in measuring $^{8}Be_{g.s.}$ fragments emitted from the ^{12}C target, because the fragments are emitted with lower energy and the separation angle between the constituent α-particles is very large. In this case, one of the α-particles will miss the detector and the coincidence will not be established. In the case of frontal collisions between the projectile and target, the kinematics is the same for both the projectile and target if the projectile breaks up and carries at 0° or if it transfers all its energy to the ^{12}C target and kicks it at 0°.

5.2.1 QE and inelastic energy spectra of ^{8}Be and α-particles

The role played by individual α-particles and ^{8}Be fragments in the QE and inelastic break-up processes is examined by investigating their energy distributions. The QE energy spectra of both α-particles and $^{8}Be_{g.s}$ fragments show narrow energy distributions compared to their corresponding inelastic spectra, as seen as examples in Figs. 5.5 and 5.6, respectively. The complete set of cross-sections is presented in Appendix A, Figs. A.1 to A.6. These cross sections are shown with statistical error bars and are accurate to within a systematic error of approximately 6%, as shown in Table 3.7. The cross-sections of the QE energy spectra of both the $^{8}Be_{g.s.}$ and the α-particle are dominated by the QE break-up mechanism at forward α-particle emission angles. These cross-sections drop as the emission angle becomes larger. The two energy peaks in QE α-particles energy spectra measured at forward emission angles between $\theta_\alpha = 16°$ and 18° could be seen on all the spectra measured with different targets. When the QE α-particle spectrum in the interaction $^{12}C + ^{12}C$ is fitted with Gaussian distribution it has a centroid at 148 MeV. This value of the centroid is too high (about 15 MeV) to be associated with the QE events where the average energy is expected to be closer to the beam velocity (about 133.3 MeV). The centroid position is higher due to the contribution of the events originating from the fusion of ^{12}C with the hydrogen contaminants. Similar results, of QE α-particle cross-sections peaking at energies higher than the corresponding beam velocity when measured in coincidence with projectile-like fragments were also reported in the previous studies [Gon87, Mag98].

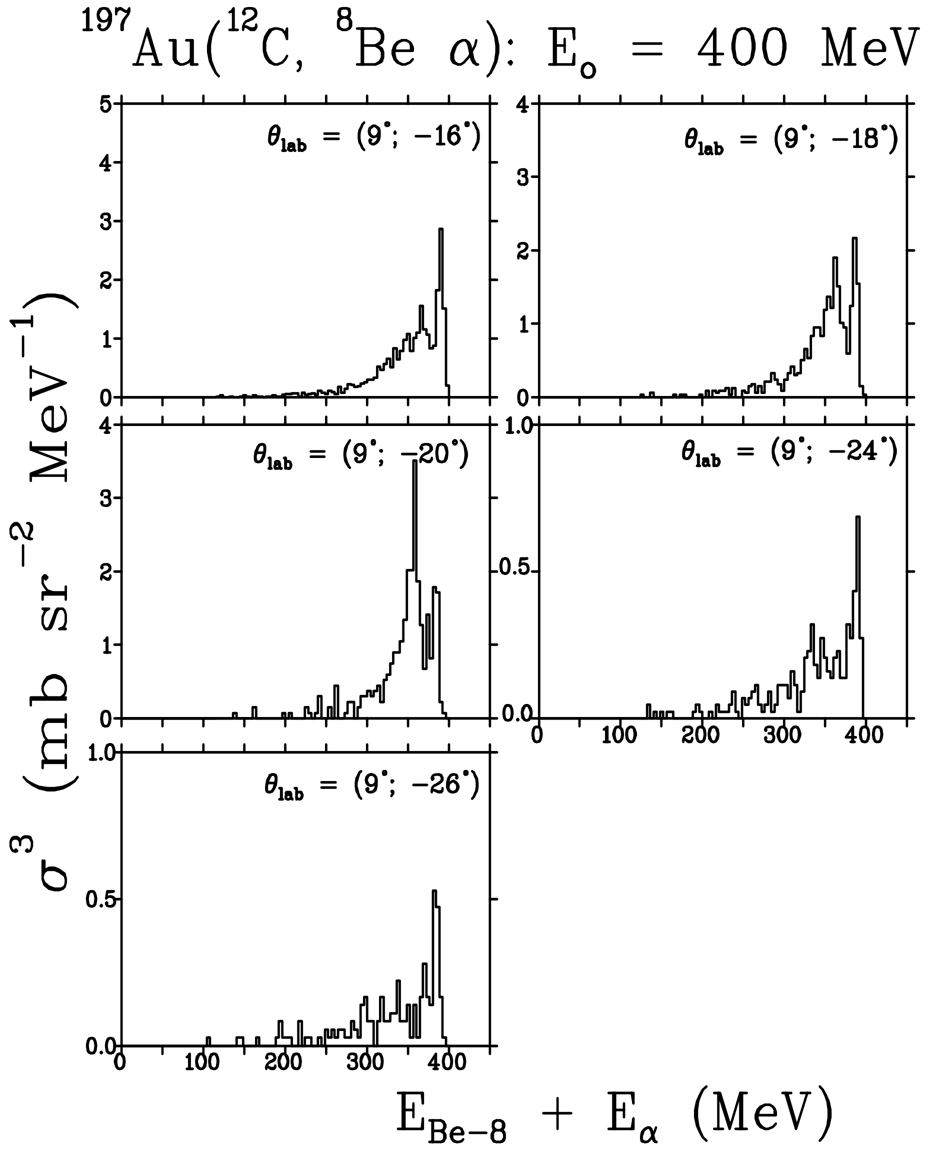

Figure 5.3: Coincidence cross-section in the interaction of ^{12}C with a ^{197}Au target. See full caption in Fig. 5.1.

In order to extract the parameters for the pure QE α-particle energy peak, each energy distribution was deconvoluted with two Gaussian functions for α-particle emission angles between $\theta_\alpha = 16°$ to $22°$, as discussed in Chapter 3. Figs. 5.5 and 5.6 show the individual energy spectra of the coincident QE α-particles and ^{8}Be$_{g.s.}$ fragments, respectively. These cross-sections were extracted from the data measured with different targets and α-particle emission angles of $\theta_\alpha = 16°$ and $24°$ and then fitted with Gaussian distributions. Table 5.1 shows that the width of the QE α-particle spectra is target dependant. The cross-sections measured in the interaction with lighter targets show a broader energy distribution compared to the ones measured with heavier targets. These

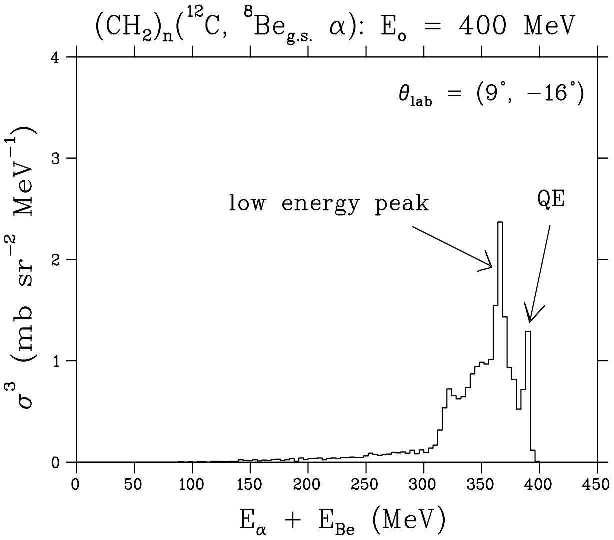

Figure 5.4: Coincidence cross-sections of the sum of the kinetic energy of the correlated ^{8}Be$_{g.s.}$ and α-particle in the interaction of the 400 MeV ^{12}C with (CH$_2$)$_n$ target normalised to the cross-sections obtained with ^{12}C target. The ^{8}Be$_{g.s.}$ fragments were measured at a fixed angle of θ_{lab} = 9°, while the α-particle angle was θ_{lab} = -16°.

broader energy spectra observed in the interaction with a lighter target were due to the high recoil energy of the target nucleus which resulted in a wider energy spread of the QE α-particle spectra. It was also observed that the QE α-particle energy spectra measured in the interaction of the projectile with a ^{197}Au target peaked at energies slightly higher in comparison with the energy distribution of the spectra produced in the interaction with a lighter target, as seen in Table 5.1.

From these spectra it is evident that the energy distribution appearing at the higher energy part of the QE α-particle spectra is more pronounced in the case of lighter target nuclei. Since the events from the interaction of ^{12}C with the hydrogen contaminants affect the high energy part of the QE α-particle spectra, their corresponding events on the QE ^{8}Be$_{g.s.}$ spectra are observed on the lower energy part, as seen in Fig. 5.6. The intensity of the high energy distribution on the QE α-particle spectra at θ_α = 16° and 18° corresponds to the intensity on the peak that appears at the lower energy part of the QE ^{8}Be$_{g.s.}$ energy spectra due to kinematics. The break-up components of the ^{8}Be$_{g.s.}$ fragment shows a narrow peak in the interaction of ^{12}C with the heavier target ^{197}Au compared to the spectra produced in the interaction with lighter targets, as seen in Fig 5.7. This is due to the effect of low recoil energy of the heavier target which produces a sharp peak, while the high recoil energy of the lighter targets cause a wider energy spread. Similar observations were reported in the literature by Gadioli *et al.* [Gad01].

The inelastic break-up events for both the ^{8}Be$_{g.s.}$ fragments and α-particles

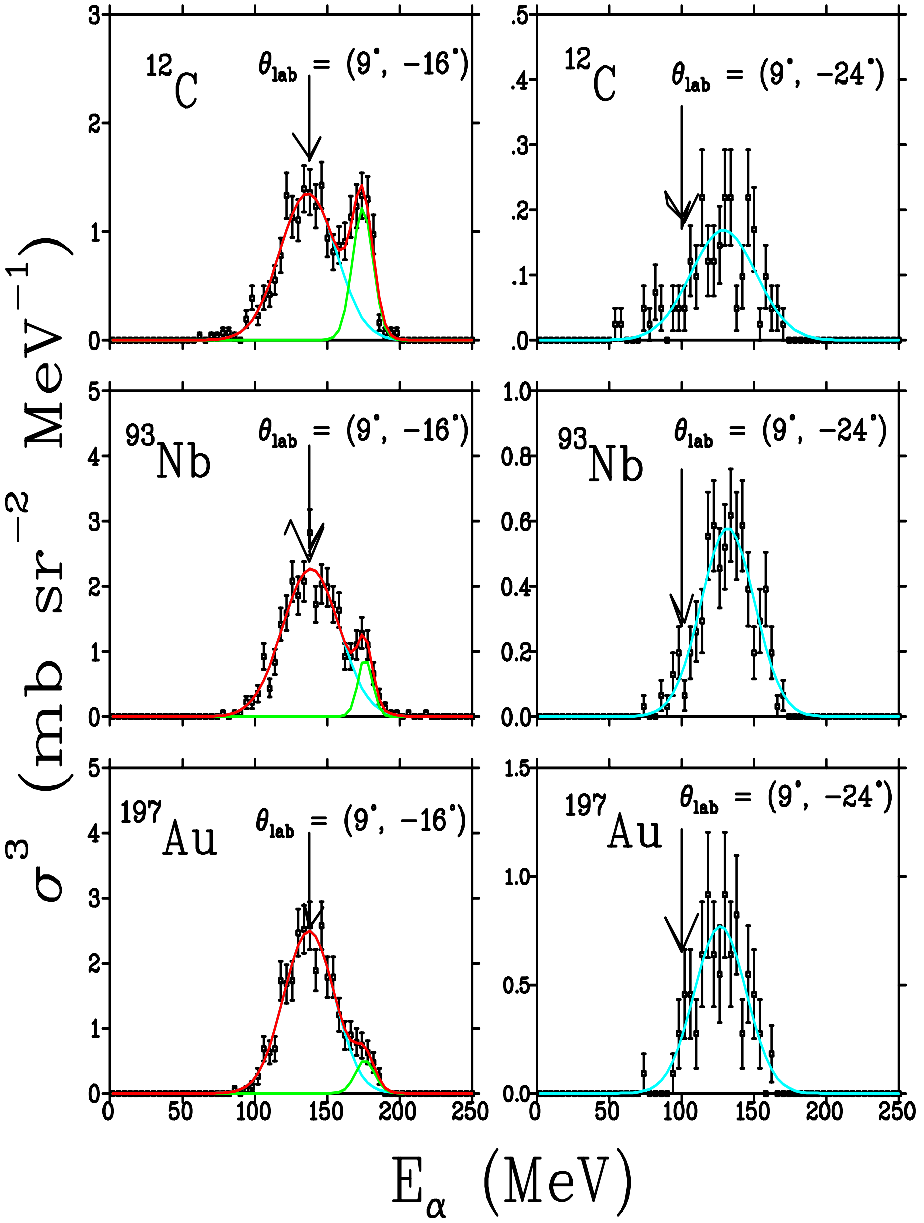

Figure 5.5: Triple differential cross-sections of the QE α-particles fitted with two Gaussians distributions for different targets and emission angles as indicated, showing the pure QE (cyan), the events due to the H contaminants (green) and the sum of the two Gaussians distributions (red). The triple differential cross-sections are plotted with a binning of 4 MeV/bin.

Table 5.1: Parameters of the FWHM and Centroids of α-particle spectra for QE part in the interaction of ^{12}C with ^{12}C, ^{93}Nb and ^{197}Au at different emission angles obtained from the Gaussian fits as explained in Chapter 3.

Target	θ_α	FWHM (MeV)	Centroid (MeV)
^{12}C	16°	44.2	134
	18°	44.2	131
	20°	35.3	126
	22°	38.4	113
	24°	36.3	113
^{93}Nb	16°	39.2	136.5
	18°	40.3	134.1
	20°	36.2	126.3
	22°	38.4	120.6
	24°	37.6	121.4
	26°	34.7	121.8
^{197}Au	16°	34.2	138.3
	18°	30.5	136.1
	20°	29.3	134.5
	24°	34.9	120.3
	26°	32.7	119.6

were extracted from the inelastic gate by excluding the locus originating from the fusion of ^{12}C with hydrogen contaminants. The inelastic coincidence cross-sections of the individual α-particle and $^{8}\mathrm{Be}_{g.s.}$ fragments show a broader energy distribution compared to their corresponding QE cross-sections as seen in Figs. 5.8 and 5.9, as well as in Appendix A in Figs. A.7 to A.12. The contribution from the inelastic events is also observed in the sum of the kinetic energy spectra extending from about 350 MeV to lower energy as shown in Figs. 5.1 to 5.4. These events are mainly produced from a more central collision in which ^{12}C breaks up into its constituent α-particle and $^{8}\mathrm{Be}_{g.s.}$ fragments after losing a substantial amount of its energy. In all these cases, the $^{8}\mathrm{Be}_{g.s.}$ acts as spectator fragment while the α-particle interacts with denser regions of the target nucleus, losing energy through collisions with its nucleons. The α-particle could also be absorbed and re-emitted by the target nucleus with lower energy, while the $^{8}\mathrm{Be}_{g.s.}$ fragment acts as spectator. Since a $^{8}\mathrm{Be}_{g.s.}$ fragment is unbound and cannot survive final-state interactions with the target nucleus without breaking the bond between its constituent α-particles, the $^{8}\mathrm{Be}_{g.s.}$ inelastic events can only originate when the ^{12}C projectile interacts inelastically with the target and eventually decelerates by Coulomb excitation before it breaks up into $^{8}\mathrm{Be}_{g.s.}$ and an α-particle with lower energies. These cross-sections show an unexpected peak at high energies due to the contribution from the QE events originating from the interaction of ^{12}C with hydrogen contaminants. Fig. 5.10(a) and 5.10(b) show the two-dimensional summed

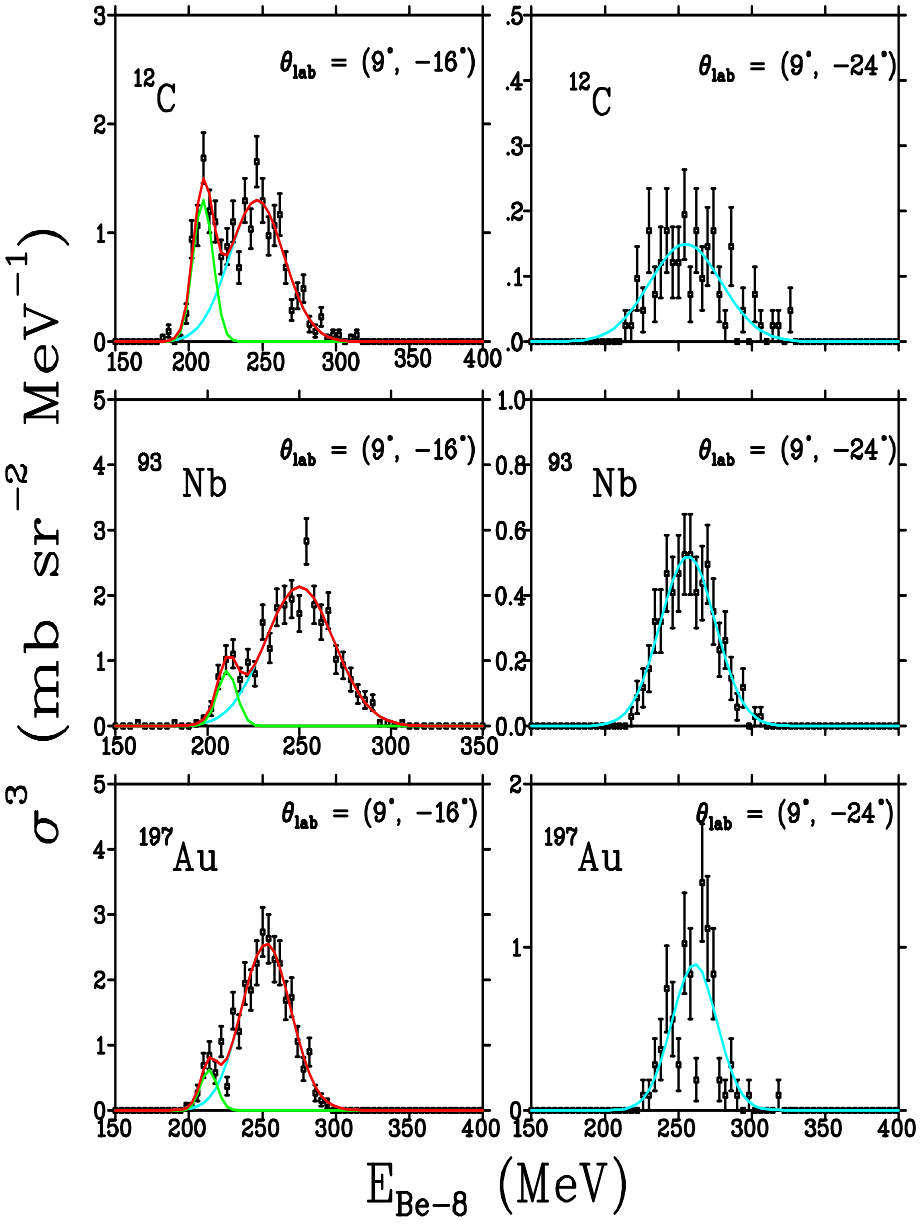

Figure 5.6: Triple differential cross-sections of the QE ^{8}Be$_{g.s.}$ fragments fitted with two Gaussian distributions for different targets and different α-particle emission angles as indicated and explained in the caption of Fig. 5.5. The triple differential cross-sections are plotted with a binning of 4 MeV/bin.

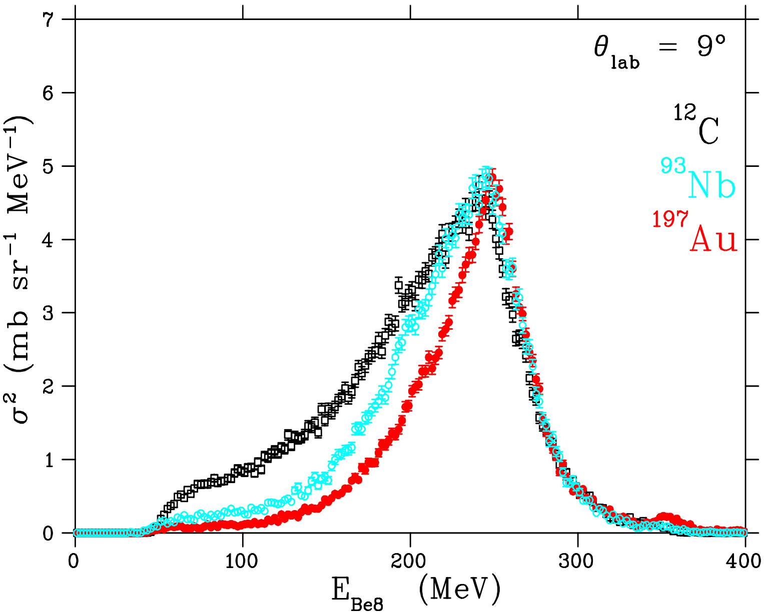

Figure 5.7: Comparison of the double differential cross-sections of the inclusive ^{8}Be$_{g.s.}$ measured in the interactions of ^{12}C with ^{197}Au (red) and ^{93}Nb (cyan) observed by Gadioli *et al.* [Gad01], as well as the spectra of pre-scaled singles of ^{8}Be$_{g.s.}$ in the interaction of ^{12}C with ^{12}C (black) at an incident energy of 400 MeV obtained from the present work.

energy spectra as a function of the energy of α-particles and ^{8}Be$_{g.s.}$ fragments, respectively, with the gate around the QE events originating from the interaction of ^{12}C with hydrogen contaminants. It is clear from these figures that the QE contaminants are spread across almost the entire energy region of the inelastic α-particle spectra, while it only affects a small region of the high energy part of the inelastic ^{8}Be$_{g.s.}$ spectra centred around 200 MeV.

The present correlation data show that a small amount of impurity on the target foils could easily affect the energy spectra compared to the inclusive measurements. This is reported in Chapter 3, concerning the efficiency of the detector when tested using the pre-scaled singles events for both ^{8}Be$_{g.s.}$ and α-particle cross-sections.

5.2.2 QE and Inelastic Energy Integrated Angular Distributions

The target-nucleus influence in the binary break-up of ^{12}C ions into ^{8}Be$_{g.s.}$ fragments and α-particles was also investigated by studying the QE and inelastic angular distributions. These angular distributions were extracted by integrating the curve under both the QE and inelastic cross-sections as discussed in Section 3.5.6. Table 5.2 shows the values of the QE energy integrated angular distribution cross-sections. As discussed in Chapter 3, the events from the

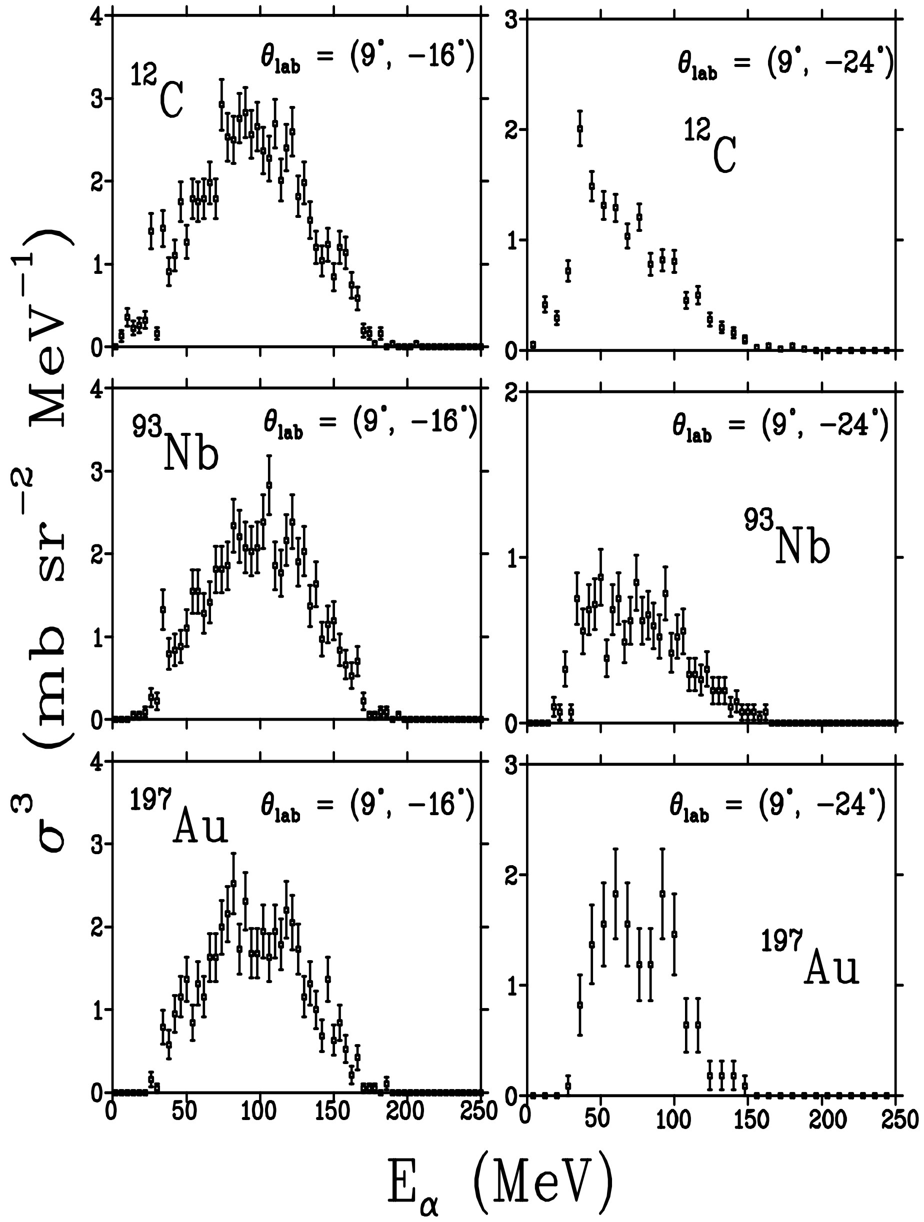

Figure 5.8: Triple differential cross-sections of the inelastic α-particles measured in coincidence with ^{8}Be$_{g.s.}$ in the interaction of ^{12}C with different targets at two different α-particle emission angles as indicated. These cross-sections are compressed into 4 MeV/bin except in the interaction with ^{12}C and ^{197}Au at emission angle $\theta_{lab} = 24°$ where the binning is 8 MeV/bin.

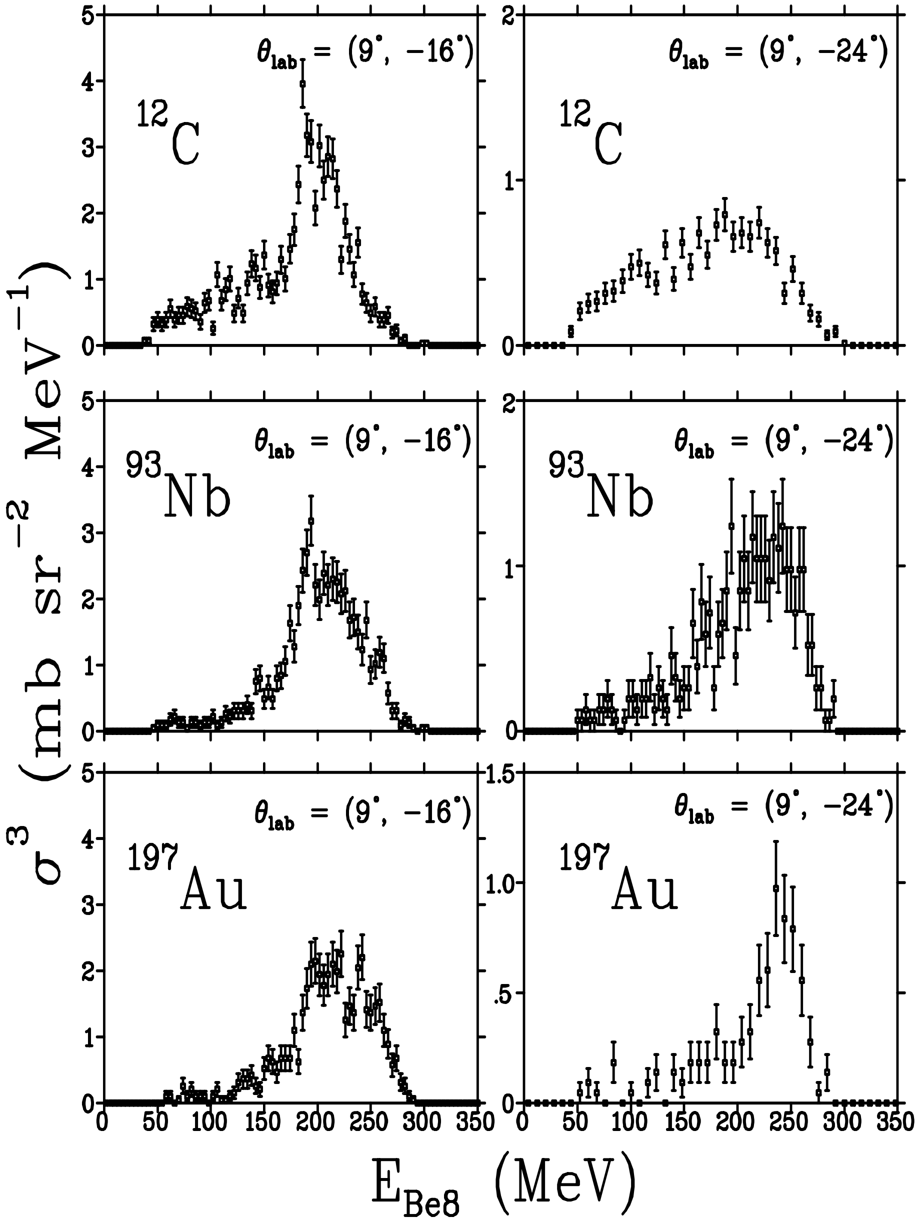

Figure 5.9: Triple differential cross-sections of the inelastic $^{8}Be_{g.s.}$ fragments measured in coincidence with α-particles in the interaction of ^{12}C with different targets at two different α-particle emission angles as indicated. These cross-sections are compressed into 4 MeV/bin except in the interaction with ^{12}C and ^{197}Au at emission angle $\theta_\alpha = 24°$, where the binning is 8 MeV/bin.

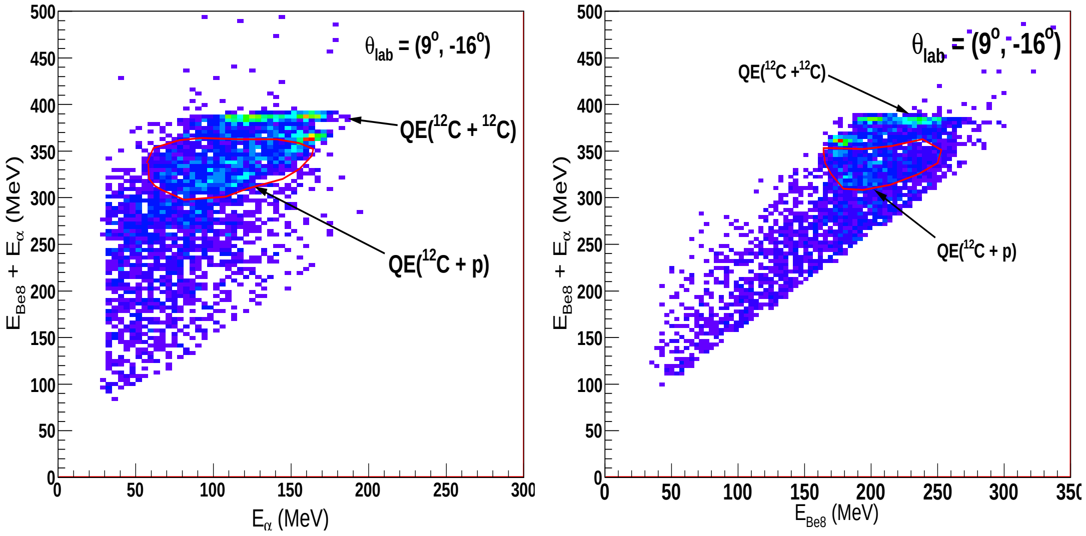

(a) (b)

Figure 5.10: Two dimensional coincidence energy spectra in the interaction of ^{12}C with ^{12}C plotted as a function of (a) α-particle, and (b) ^{8}Be$_{g.s.}$ emission energy with gate showing the QE events originating from the interaction of ^{12}C with hydrogen contamination.

fusion of ^{12}C with hydrogen contaminants were subtracted from the pure QE events before the energy integrated angular distributions were extracted. The QE energy integrated angular distributions are shown in Fig. 5.11. It can be seen that the QE energy integrated angular distributions measured in the interaction of ^{12}C with ^{93}Nb and ^{197}Au show high cross-sections at most forward α-particle emission angles and a steeper decreasing trend as the emission angle becomes larger. In the case of the ^{12}C target, the QE energy integrated angular distribution cross-sections are lower and have a less steep structure as function of emission angle compared to the ^{93}Nb and ^{197}Au target nuclei. These low QE energy integrated cross-sections in the case of light target could be due to the weaker Coulomb interaction between two colliding nuclei. The probability of a longer interaction time with the target nucleus therefore increases, and consequently prompt QE break-up of the projectile becomes less probable. The longer interaction time with the target nucleus can also cause the projectile to lose a substantial amount of energy before breaking, up leading to ^{8}Be$_{g.s.}$ fragments and α-particles with lower energies subsequently populating the inelastic break-up region.

The inelastic energy integrated angular distributions measured with ^{12}C have higher cross-sections compared to the ones measured with ^{93}Nb and ^{197}Au, as shown in Fig. 5.12. This is also due to the weaker Coulomb force which the projectile experiences in the case of the lighter target nucleus. Therefore, as explained earlier, the probability of the projectile having a longer interaction time with the target nucleus increases, which allows the projectile to

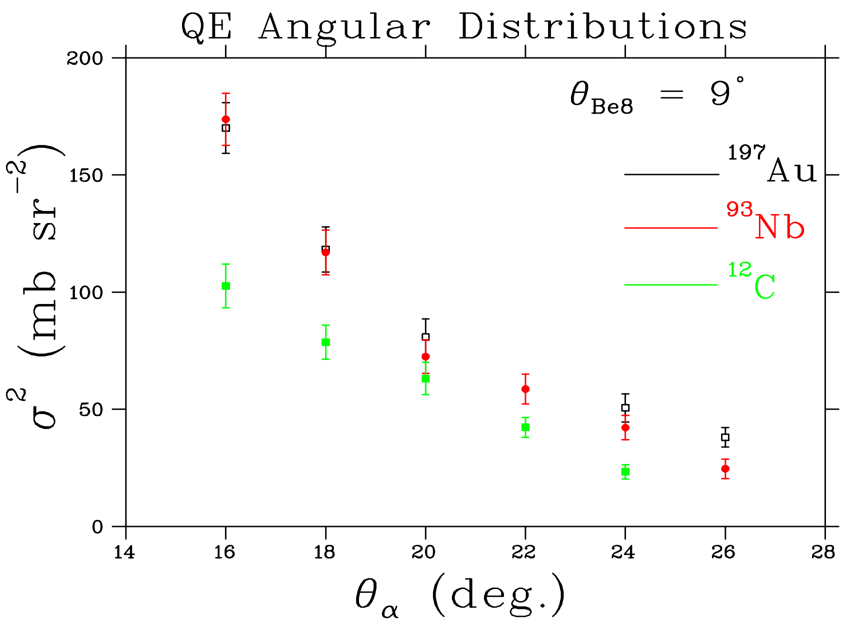

Figure 5.11: The QE energy integrated angular distributions obtained from the interaction of ^{12}C with different target nuclei as indicated.

Table 5.2: Cross-section values of the QE energy integrated angular distributions for events measured in the interaction of ^{12}C with ^{12}C, ^{93}Nb and ^{197}Au at different emission angles

α-particle angle	^{12}C (mb sr^{-2})	^{93}Nb (mb sr^{-2})	^{197}Au (mb sr^{-2})
16°	102 ± 9.3	173 ± 13.1	170 ± 13.8
18°	78 ± 7.2	116 ± 10.5	118 ± 9.6
20°	63 ± 6.8	72 ± 7.2	80 ± 7.8
22°	46 ± 5.2	58 ± 6.3	
24°	23 ± 3.1	42 ± 5.1	50 ± 5.0
26°		24 ± 4.1	38 ± 4.1

lose energy before it breaks up into ^{8}Be and α-particles. These fragments are produced with lower energies and populate the inelastic region. The cross-sections of the inelastic energy integrated angular distributions show smooth decreasing trends in the case of ^{93}Nb and ^{197}Au and a steeper slope in the interaction with the lighter target. The quantitative cross-sections for the inelastic energy integrated angular distributions are shown in Table 5.3. Since the hydrogen contaminant on the ^{12}C target could not be established quantitatively, and no background corrections were made for the inelastic break-up events, only relative energy integrated cross-sections were extracted from the ^{9}B$_{g.s.}$ and ^{8}Be$_{g.s.}$ events which are the decay products of ^{13}N. These relative cross-sections presented in Table 5.4 show an increasing trend as a function of the α-particle emission angle. This trend, although not fully conclusive, could

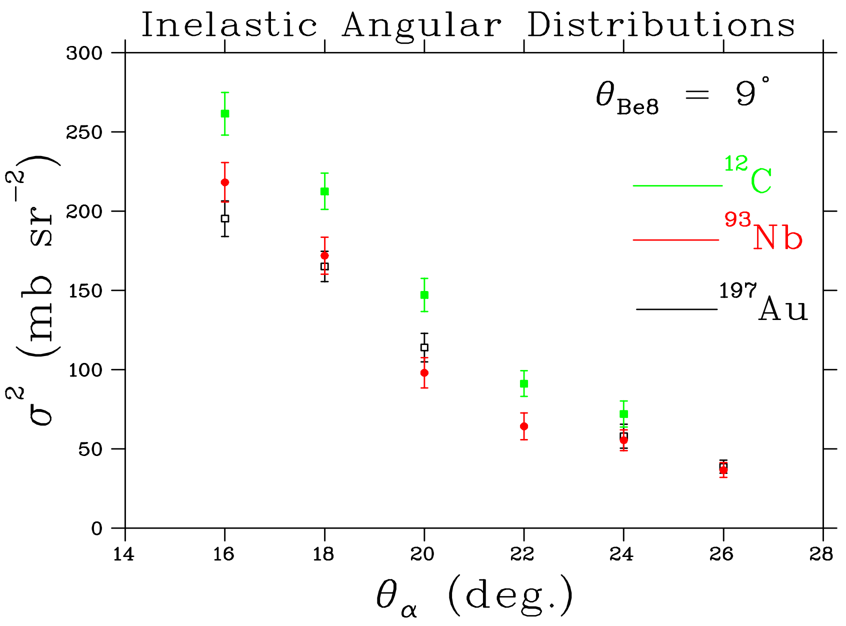

Figure 5.12: Inelastic energy integrated angular distribution obtained from the interaction of ^{12}C with different target nuclei as indicated.

Table 5.3: Cross-section values of the inelastic energy integrated angular distributions for events measured in the interaction of ^{12}C with ^{12}C, ^{93}Nb and ^{197}Au at different emission angles

θ_α	^{12}C (mb sr^{-2})	^{93}Nb (mb sr^{-2})	^{197}Au (mb sr^{-2})
16°	261 ± 13.5	218 ± 12.4	195 ± 11.3
18°	212 ± 11.4	171 ± 11.7	175 ± 10.5
20°	147 ± 10.5	97 ± 9.6	113 ± 9.9
22°	101 ± 9.2	64 ± 7.5	
24°	82 ± 8.3	55 ± 6.6	57 ± 7.6
26°		36 ± 4.6	38 ± 4.1

Table 5.4: Relative cross-section values of the energy integrated angular distributions for events originating from fusion of ^{12}C with hydrogen nuclei to form ^{13}N, which decays into ^{9}B$_{g.s.}$ and α-particle.

θ_α	16°	18°	20°	22°
σ (mb sr^{-2})	68.23 ± 5.38	70.8 ± 6.01	90.7 ± 6.66	133.5 ± 8.77

be an indication of isotropic decay occurring as a result of a fusion-like process between the ^{12}C projectile and the hydrogen nucleus forming the compound nucleus ^{13}N.

5.2.3 GEANT4 and SimSort simulations

The GEANT4 simulations were performed in order to reproduce the α-particle spectra and also to calculate the QE integrated angular distributions for comparison with the experimental results. The GEANT4 simulation code consists of different physics lists incorporating various reaction mechanisms as explained in Chapter 4. When a physics list is called, relevant reaction mechanisms are activated. In this work, two different physics lists that contain the Fermi break-up mechanism were used in order to model the binary break-up of ^{12}C into a ^{8}Be fragments and α-particles. In the GEANT4 code, the Fermi break-up mechanism is incorporated into the Quasi-elastic Binary Break-up (QBBC) and Quark Gluon String (QGS) physics lists [Apo09], which were activated to simulate the coincidence measurements. The detector geometry used during the experiment was also used in the simulations. These physics lists were implemented individually in order to simulate the binary break-up of ^{12}C into ^{8}Be fragments and α-particles measured in coincidence at the most forward α-particle emission angle where the QE cross-sections are at maximum. Figs. 5.13(a) and 5.13(b) show two-dimensional coincidence sum energy spectra obtained in the interaction of ^{12}C with ^{12}C using the QGS and QBBC physics lists, respectively. From these two energy spectra it was evident that the physics lists used for simulations were not able to simulate the QE break-up of the ^{12}C into ^{8}Be$_{g.s.}$ and α-particles. These spectra mainly show the events produced from the inelastic break-up of ^{12}C into ^{8}Be fragments and α-particles. This failure could be due to the fact that most of the physics lists that are used were originally designed to simulate the reaction of light hadrons such as protons and neutrons at high energies of GeV/u and are still under development. Another reason could be that the QE binary break-up of projectiles heavier than protons and neutrons are not yet treated in those physics lists.

The SimSort code was used to simulate the QE spectra in the case where a 400 MeV ^{12}C beam interacts with ^{93}Nb and H targets. These simulations are explained in detail in Section 3.5.2. Figs. 5.14(b) shows two-dimensional simulated QE loci of the sum energies of the correlated ^{8}Be$_{g.s.}$ and α-particles produced in the interaction of ^{12}C with both ^{93}Nb and H targets as indicated, measured at emission angles of θ_{lab} = (9°, -16°), with their corresponding experimental spectrum shown in Fig. 5.14(a). The projection of the QE spectrum onto the sum of the kinetic energy axis is shown in Fig. 5.14(d) obtained from SimSort in the interaction of ^{12}C with both ^{93}Nb and H targets, as indicated, while their corresponding experimental projections are shown in Fig. 5.14(c). The peak at the highest energy corresponds to events produced when the projectile interacts with the ^{93}Nb target, while the peak at the lower energy corresponds to events produced in the fusion between ^{12}C with hydrogen contaminant. In the case of the experimental energy spectrum, the contribution of the QE break-up events from the reaction of ^{12}C with a hydrogen

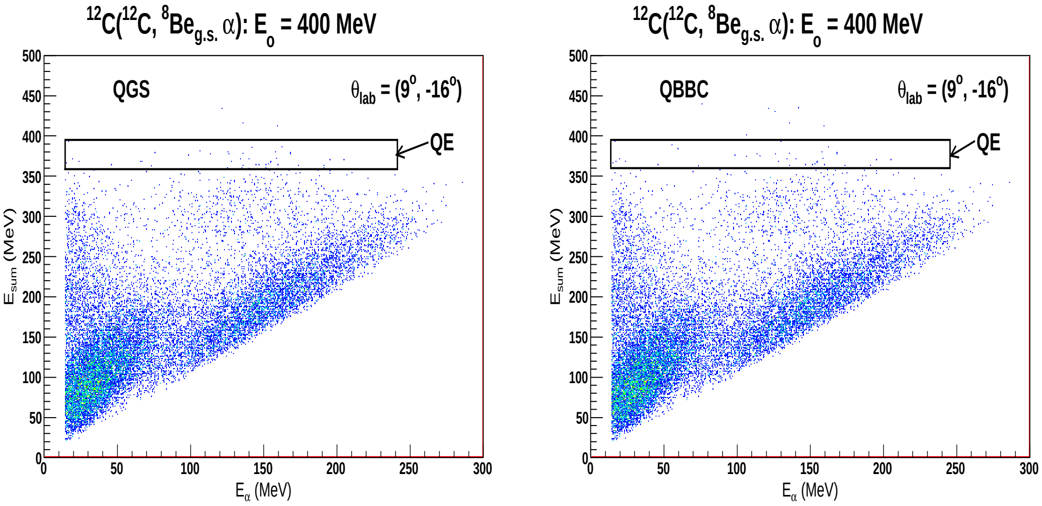

(a) (b)

Figure 5.13: Two-dimensional coincidence energy spectra in the interaction of ^{12}C with ^{12}C obtained from the GEANT4 simulations using different physics lists, namely (a) QGS and (b) QBBC. The gates show where the Quasi-elastic (QE) events should appear.

contaminant are superimposed on the inelastic events from the target. In this case, only the peak originating from the break-up of ^{13}N could be observed clearly. The SimSort simulation spectra are very similar to what is observed in the experimental results whereby the two-dimensional sum energy spectra reveal two loci at the forward α-particle emission angles of $\theta_\alpha = 16^\circ$ to 22°. The peak at lower energy disappears at α-particle emission angles of $\theta_\alpha = 24^\circ$ and larger. These observations provide more evidence indicating that the locus at the lower energy in the coincidence sum energy spectrum results from the fusion between the projectile and hydrogen contaminants on the target foils.

Even though formal theoretical calculations that model the QE break-up of ^{12}C into ^{8}Be$_{g.s.}$ and α-particles are still lacking at this stage, the results obtained with the SimSort simulations affirm the hypothesis that the origins of the peak at the highest energy of the QE α-particle spectra, as well as the distribution observed at energies (about 30 MeV) below the QE in the sum spectra are due to interaction of the projectile with hydrogen contaminants on the target. The SimSort results furthermore show good agreement with the experimental data concerning the angular range in which the events originating from ^{12}C + H could be observed.

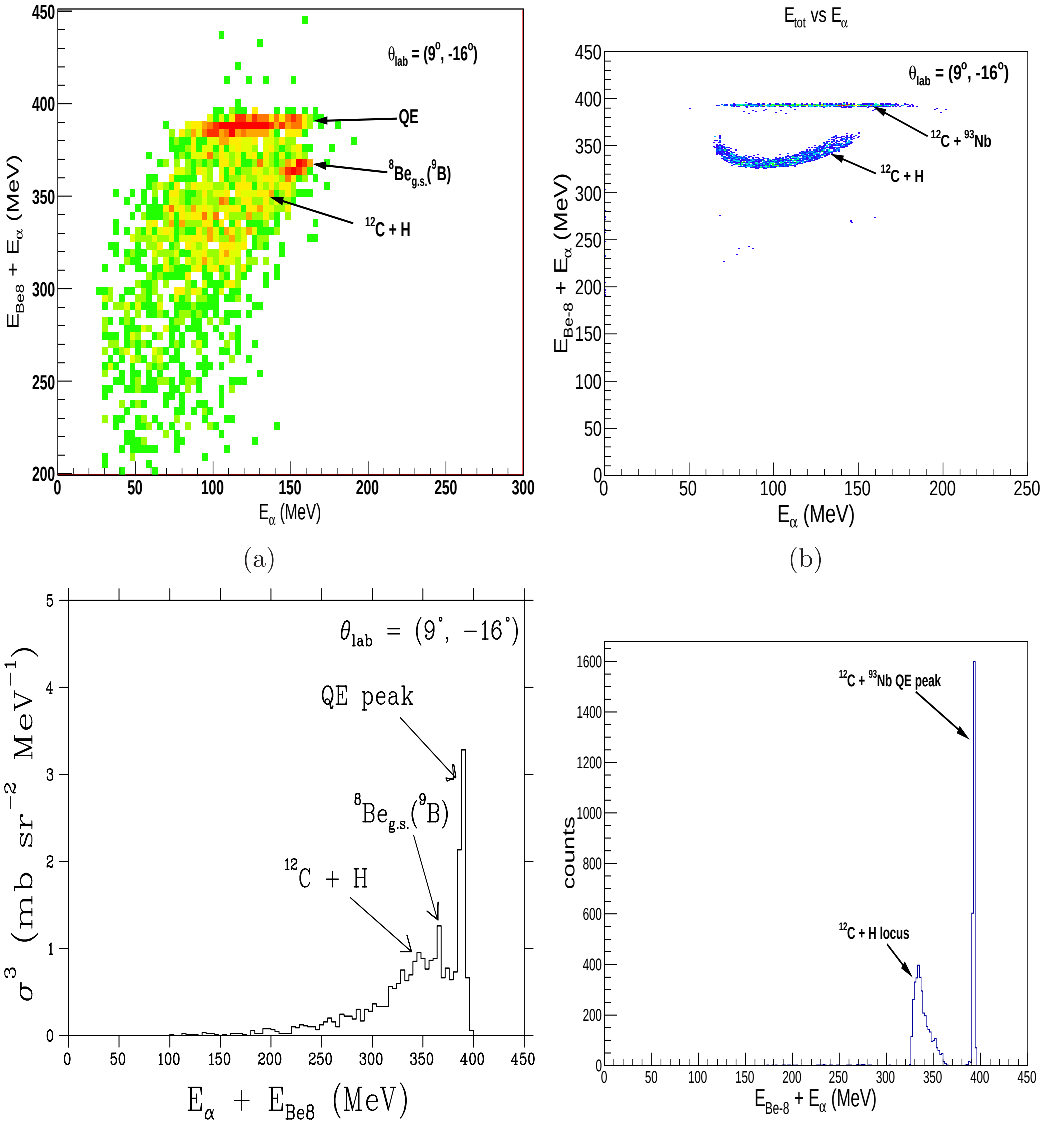

(a) (b)

(c) (d)

Figure 5.14: (a) Experimental two-dimensional coincidence spectrum, and (c) projection onto the axis of the sum of kinetic energy of the QE ^{8}Be$_{g.s.}$ and α-particle spectrum in the interaction of ^{12}C with ^{93}Nb. (b) Two-dimensional spectrum, and (d) projection of the spectrum onto the sum axis in the interaction of ^{12}C with ^{93}Nb and hydrogen targets as indicated, obtained from the SimSort simulations.

5.3 Double Differential Cross Sections of Inclusive measurements

In this section double differential cross sections of IMFs which were produced in the interaction of ^{12}C and ^{16}O with ^{12}C at incident energies of 400 and 235 MeV, respectively, are presented. The light IMFs of Li, Be and B isotopes are presented in section 5.3.1, while section 5.3.2 presents the inclusive energy spectra of the Projectile-Like Fragments (PLF) that range from the Carbon to Neon isotopes.

5.3.1 Inclusive energy spectra of Li, Be and B isotopes

Laboratory double-differential cross-sections of the inclusive spectra of the ^{6,7}Li, ^{7,9}Be and ^{8,10,11}B isotopes are presented as examples in Fig. 5.15, while the complete results are shown in Appendix B in Figs. B.1 to B.3. The cross-sections of ^{6,7}Li and ^{7,9}Be were measured over an angular range between $\theta_{lab} = 8°$ and 50° in the interaction of ^{16}O ions with a ^{12}C target, while B isotopes were measured over an angular range between $\theta_{lab} = 10°$ and 50°. These cross sections are presented with statistical errors given by error bars and are accurate to within a systematic error of approximately 7%, as discussed in Chapter 3, and are shown in Table 3.7. The cross-sections for these light IMFs show similar structural behaviour for all isotopes at lower and intermediate emission energies for all measured emission angles. As the emission angle increases, the cross-sections drop gradually but maintain the same structure for all the isotopes identified. The production of these light IMFs is most likely dominated by reaction mechanisms such as nucleon coalescence, which populates the intermediate energy regions. Similar results from the energy spectra were observed in previous measurements of IMFs in the interaction of ^{12}C with ^{12}C at incident energies of $E_{lab} = 200$ and 400 MeV [Mir08].

Fig. 5.16 shows that these light fragments are produced at different rates. At lower and intermediate energies the production rate for ^{6}Li is higher than for ^{7}Li, while the rate is opposite at higher emission energies. In the case of Be isotopes the production rate for ^{7}Be and ^{9}Be is similar at both lower and intermediate emission energies, while ^{8}B is produced at a rate much smaller than ^{10}B and ^{11}B which are produced at the same rate. Table 5.5 shows the Q-values for different reation channels for the production of light fragments ($3 \leq Z \leq 5$) in the interaction of ^{16}O with ^{12}C. These are the excitation energies required for the reaction to populate a specific channel, which determines the cross-section of that specific fragment. It seems that the lesser the excitation energy required (meaning lesser Q-value) the higher the cross-section for the isotopes is.

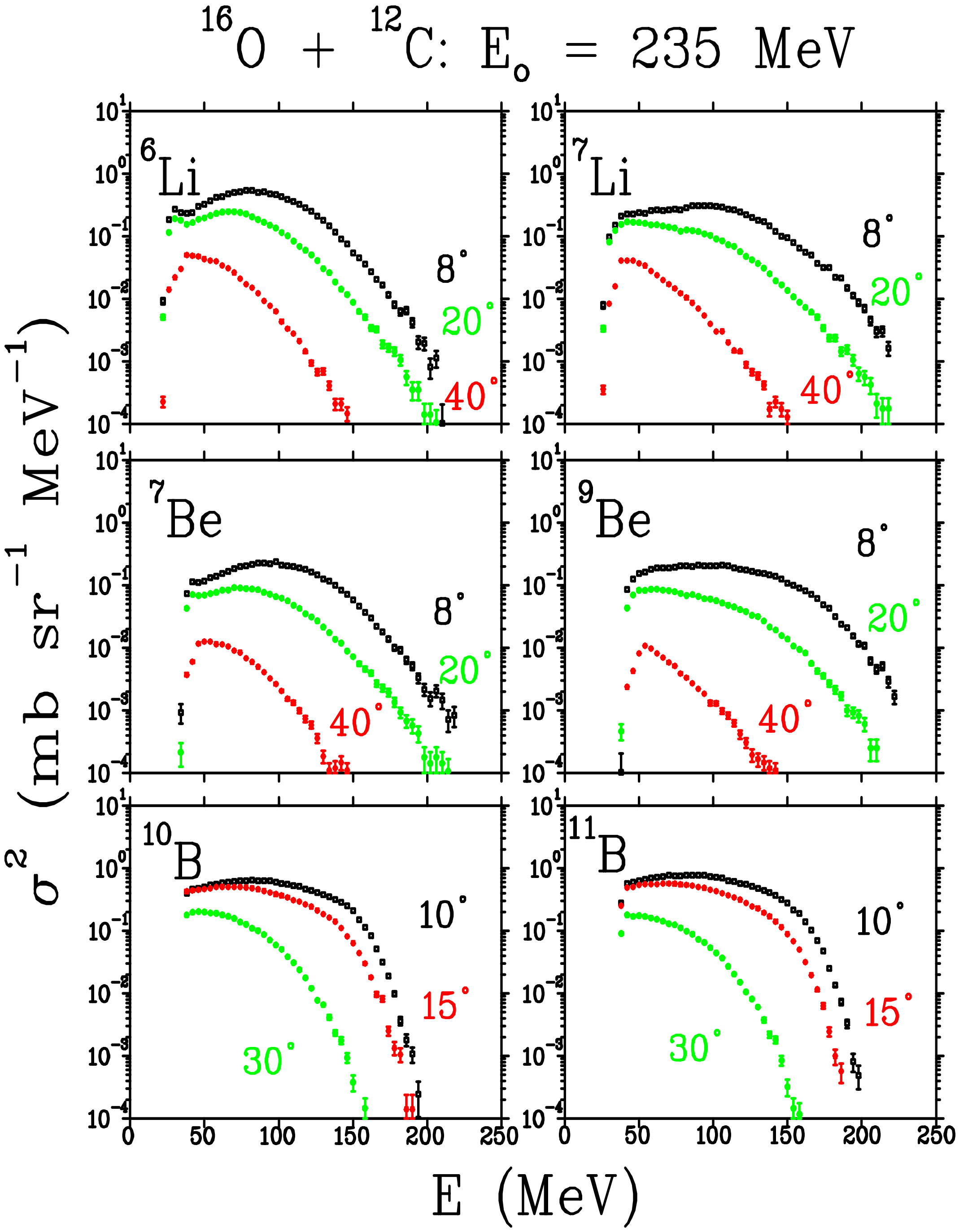

Figure 5.15: Double differential cross sections of ^{6,7}Li, ^{7,9}Be, ^{10,11}B emitted in the interaction of ^{16}O with ^{12}C at an incident energy of $E_{lab} = 235$ MeV at different emission angles, as indicated. The error bars reflect the statistical errors. These cross-sections are binned to 4 MeV/bin.

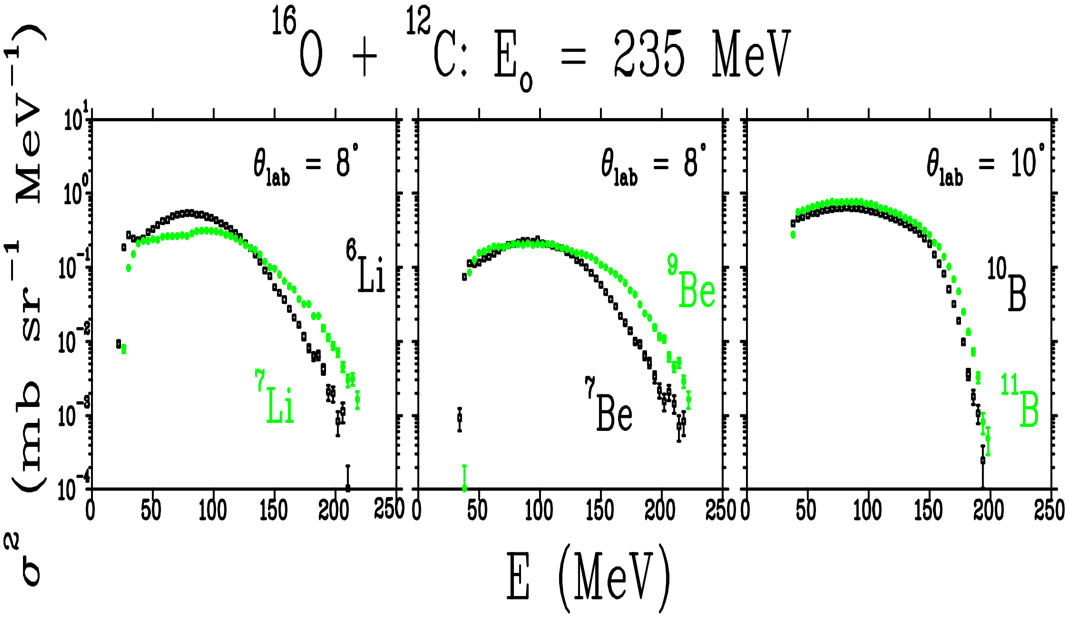

Figure 5.16: Comparison of the rates in which different isotopes of lighter IMFs are emitted in the interaction of ^{16}O with ^{12}C at an incident energy of $E_{lab} = 235$ MeV. The error bars reflect the statistical errors. These cross-sections are binned to 4 MeV/bin.

Table 5.5: Q-values for different break-up channels for IMFs with ($3 \leq Z \leq 5$) in the interaction of ^{16}O with ^{12}C.

Reaction	Q-value (MeV)
^{12}C(^{16}O,^{6}Li)^{22}Na	-13.639
^{12}C(^{16}O,^{7}Li)^{21}Na	-17.457
^{12}C(^{16}O,^{7}Be)^{21}Ne	-14.770
^{12}C(^{16}O,^{9}Be)^{19}Ne	-17.836
^{12}C(^{16}O,^{8}B)^{20}F	-27.640
^{12}C(^{16}O,^{10}B)^{18}F	-17.660
^{12}C(^{16}O,^{11}B)^{17}F	-15.356

5.3.2 Inclusive energy spectra of C, N, O, F and Ne isotopes

Laboratory inclusive double-differential cross-sections of the heavier fragments of C, N, O, F and Ne isotopes are also presented as examples in Fig. 5.17, while the complete results are presented in appendix B in Figs. B.4 to B.8. These cross sections are also presented with statistical errors and are accurate to within a systematic error of approximately 7%. The double differential cross-sections of these heavier fragments show a rather flat distribution at intermediate energies and discrete peaks at high energies at forward emission angles between $\theta_{lab} = 10°$ and $15°$. This is evidence that the production of these heavier IMFs at most forward emission angles is dominated by direct reaction mechanisms such as binary projectile fragmentation and nucleon transfer which dominate the high energy part of these spectra. As the emission angle increases to between $\theta_{lab} = 20°$ and $30°$, the cross sections decrease slightly as a function of emission energy due to the fact that the contributions from mechanisms such as direct reactions (e.g. binary projectile fragmentation) start to fade. These emission angles are dominated by reaction mechanisms such as pre-equilibrium reactions and nucleon coalescence which populate the intermediate energy region. At emission angles larger than $\theta_{lab} = 30°$, the cross-sections drop rapidly and form an exponential decay curve. This is due to the fact that the reaction mechanisms dominating the most forward and intermediate emission angles fade and the production of IMFs is dominated by a nuclear evaporation mechanism which populates the lower emission energy region of the spectra. Table 5.6 shows the Q-values for the break-up channel for the reaction specified in the table.

5.3.3 Angular distributions

Laboratory angular distributions of ^{6,7}Li, ^{7,9}Be, ^{10,12}B, ^{11,12,13,14}C, ^{13,14,15}N and ^{15,16}O isotopes in the interaction of ^{12}C with ^{12}C at an incident of 400 MeV are shown in Figs. 5.18 to 5.20 for three different emission energies. The angular distributions of the lighter fragments of Li and Be isotopes are shown in Fig. 5.18. Fig. 5.19 shows the angular distribution cross-sections of B and C isotopes, while the angular distributions of N and O isotopes are shown in Fig. 5.20. At the lowest emission energy cut of 86 MeV, the angular distribution cross-sections drop slightly with increasing emission angle and exhibit a flat curve. These features show that the reaction mechanism responsible for the emission of these IMFs at the lower energy holds for almost the entire range of measured emission angles. The reaction mechanism that dominates this lower energy region is the nuclear evaporation mechanism. At the intermediate emission energy of 198 MeV, the cross-sections are slightly higher compared to the low energy cut at most forward emission angles, but these cross-sections drop as a function of emission angle. At the intermediate emission energy, the

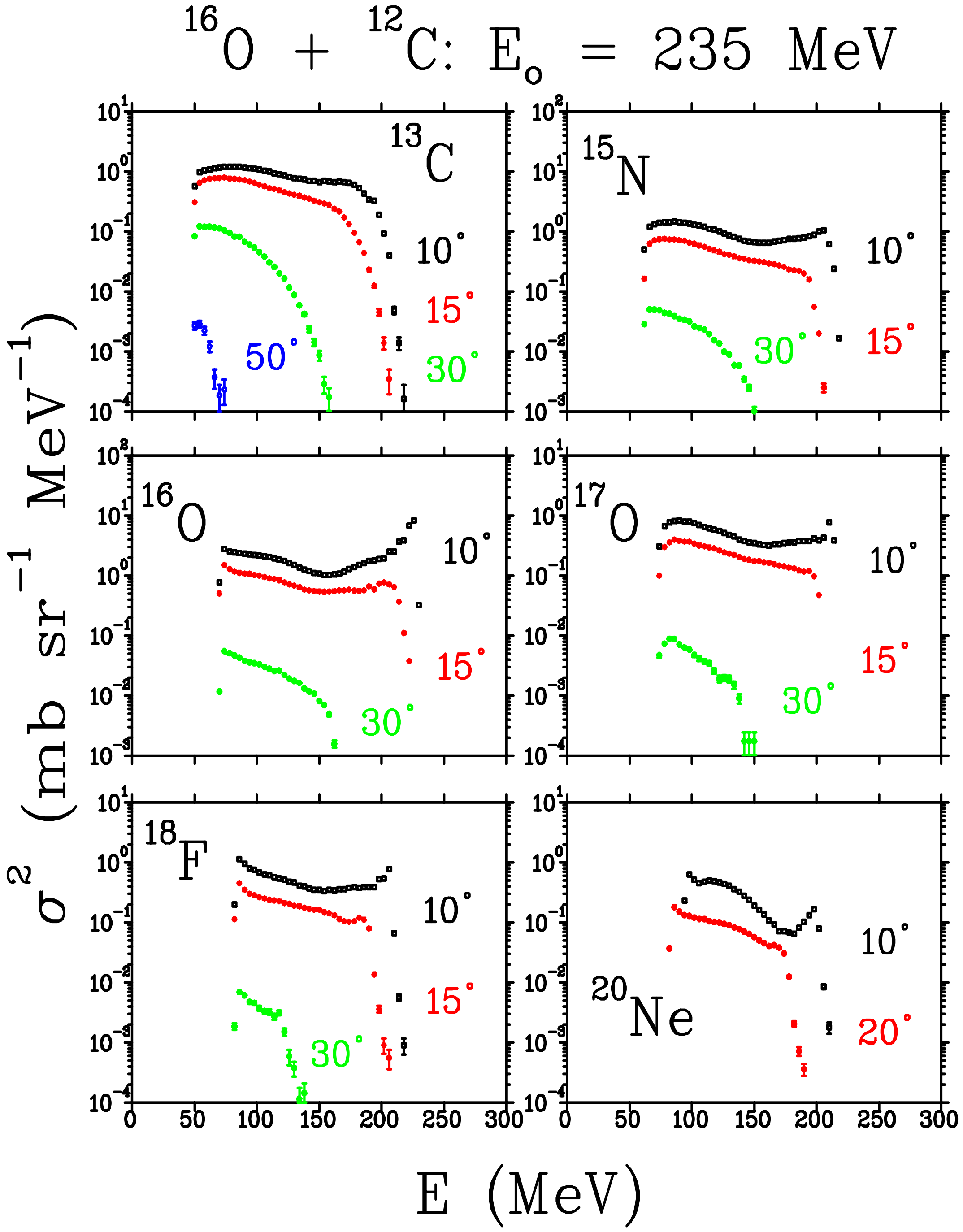

Figure 5.17: Double differential cross sections of ^{13}C, ^{15}N, ^{16}O, ^{17}O, ^{18}F and ^{20}Ne emitted in the interaction of ^{16}O with ^{12}C at an incident energy of $E_{lab} = 235$ MeV at different emission angles as indicated. The error bars reflect the statistical errors. These cross-sections are compressed into 4 MeV/bin.

Table 5.6: Q-values for different break-up channels for IMFs with ($6 \leq Z \leq 10$) in the interaction of ^{16}O with ^{12}C

Reaction	Q-value (MeV)
$^{12}C(^{16}O,^{11}C)^{17}O$	-14.577
$^{12}C(^{16}O,^{13}C)^{15}O$	-10.718
$^{12}C(^{16}O,^{14}C)^{14}O$	-15.765
$^{12}C(^{16}O,^{13}N)^{15}N$	-10.185
$^{12}C(^{16}O,^{14}N)^{14}N$	-10.464

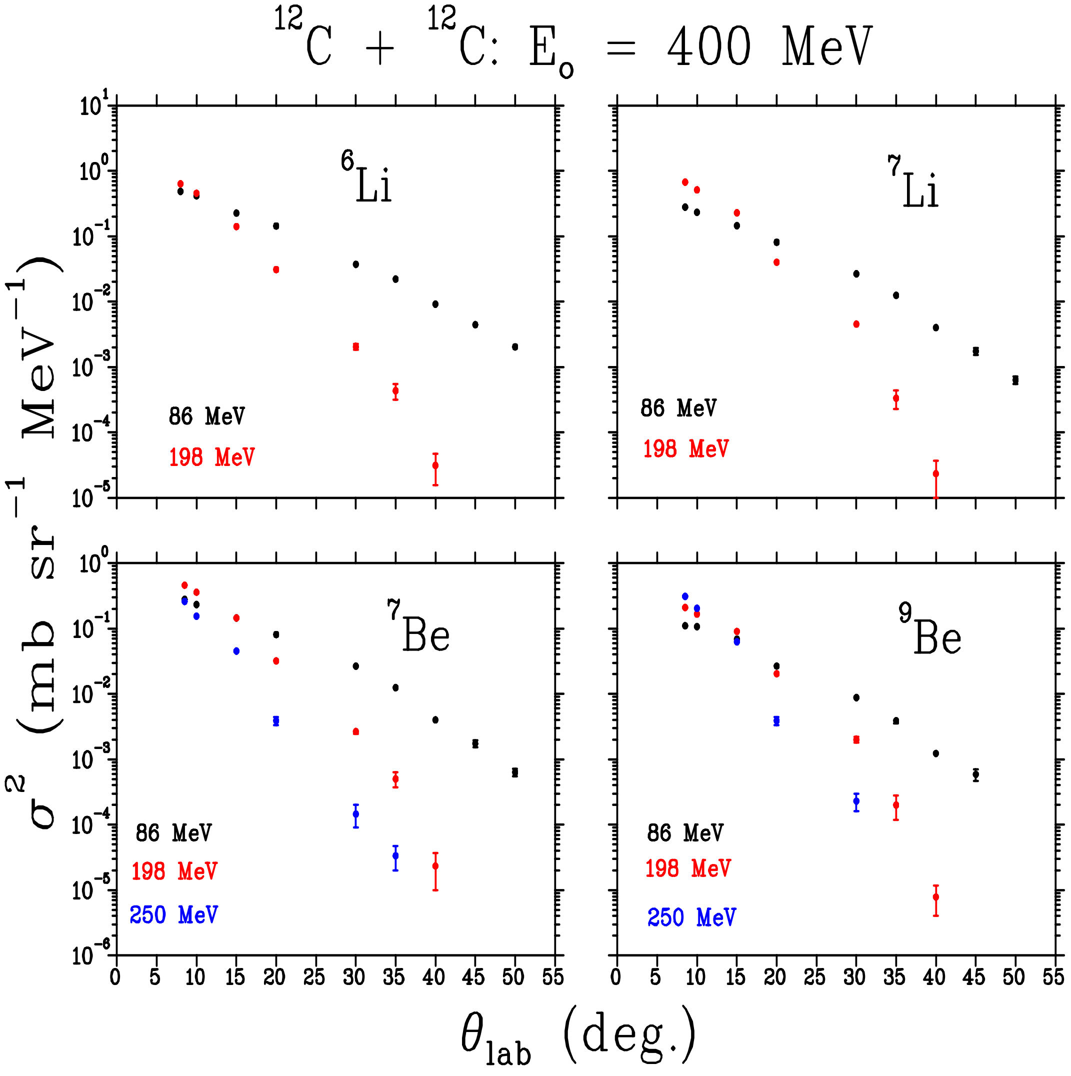

Figure 5.18: Angular distributions of ^{6}Li, ^{7}Li, ^{7}Be and ^{9}Be in the laboratory system in the interaction of ^{12}C with ^{12}C at an incident energy of $E_{lab} = 400$ MeV. The fragments together with their laboratory emission energy cuts are indicated. The error bars reflect the statistical errors.

distributions are dominated by reaction mechanisms such as pre-equilibrium and nucleon coalescence which fade at larger emission angles. At the higher emission energy of 250 MeV and above, the cross-sections dominate the most forward emission angles for all isotopes and then drop-off more rapidly as a function of emission angle, showing an exponential decreasing trend. This behaviour shows that the fragments are produced by direct reaction mechanisms, such as projectile fragmentation and nucleon-transfer reactions which fade rapidly as a function of the emission angle.

5.4 Comparison between Experimental and Theoretical results

The comparison between experimental results and theoretical calculations have been performed for fragments with mass number A = 14 to 21. These calculations were performed for IMFs produced in the interaction of ^{16}O with ^{12}C at an incident energy of $E_{lab} = 235$ MeV at the most forward emission angles ranging between $\theta_{lab} = 10°$ to $15°$. The spectra of the theoretical calculations were obtained by simulating the complete and incomplete fusion with the FLUKA-BME event generator, as described in section 4.3. The theoretical models considered for simulation of the complete and incomplete reaction mechanisms (e.g. nucleon coalescence) were interpreted by a set of BME while the nuclear evaporation was modelled with the Weisskopf-Ewing model, both of which were both incorporated into the FLUKA code. The theory of a binary break-up mechanism was interpreted by assuming that the projectile and target density overlap by folding the Local Plain Wave Born Approximation (LPWBA) with the survival probabilty of the projectile. This model is still under development for the simulations of lighter fragments.

The comparisons between the experimental and theoretical results are shown in Figs. 5.21 to 5.25. The theoretical spectra are not truncated at low emission energies with regard to the low energy thresholds of the detector telescope. Table 5.7 shows the low energy thresholds of the detector telescope (T1) for different isotopes.

Fig. 5.21 presents the comparison between the experimental and theoretical results for ^{14}N (left) and ^{15}N (right) in the interaction of ^{16}O with ^{12}C at an incident energy of $E_{lab} = 235$ MeV. The theoretical cross-sections spectra are represented by red circles and the experimental cross-sections by black squares. The statistical errors of the theoretical and experimental cross-sections are presented with error bars. The comparison of ^{14}N at $\theta_{lab} = 10°$ shows good agreement between the experimental and theoretical cross-sections at low emission energies. The production of these fragments in this energy region is dominated by the nuclear evaporation mechanism. At intermediate emission energies the theoretical cross-sections overestimate the experimental

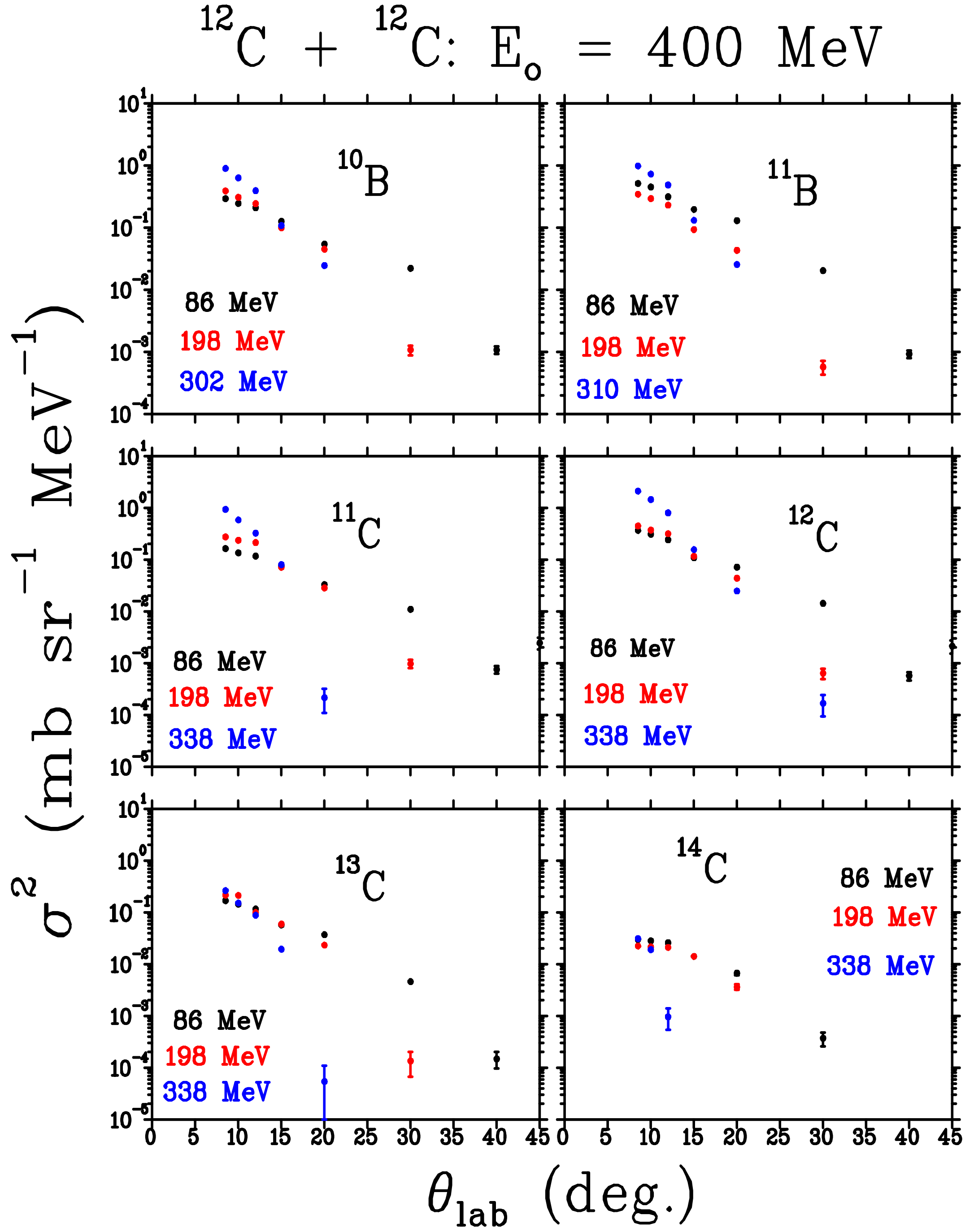

Figure 5.19: Angular distributions of ^{10,11}B and ^{11,12,13,14}C in the laboratory system in the interaction of ^{12}C with ^{12}C at an incident energy of $E_{lab} = 400$ MeV. The fragments are indicated together with their laboratory emission energy cuts. The error bars reflect the statistical errors.

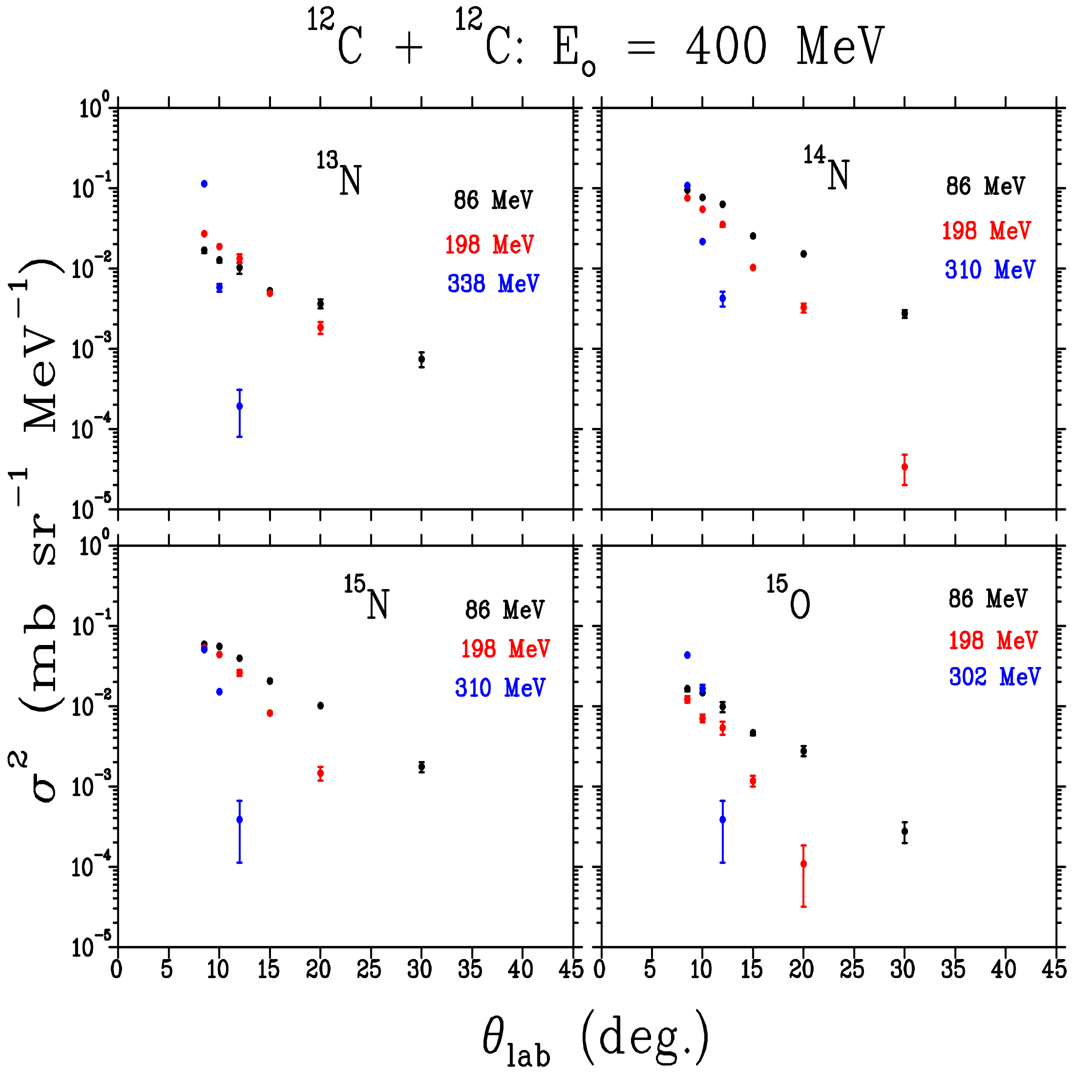

Figure 5.20: Angular distributions of ^{13,14,15}N and ^{15}O in the laboratory system in the interaction of ^{12}C with ^{12}C at an incident energy of E_{lab} = 400 MeV. The fragments are indicated together with their laboratory emission energy cuts. The error bars reflect the statistical errors.

Table 5.7: Low energy thresholds for different isotopes measured with detector telescope (T1) in the interaction of ^{16}O with ^{12}C at an incident energy of $E_{lab} = 235$ MeV.

Isotopes	^{14}N	^{15}N	^{15}O	^{17}O	^{17}F	^{18}F	^{19}F	^{20}Ne	^{21}Ne
E threshold (MeV)	60	62	70	74	82	84	86	94	98

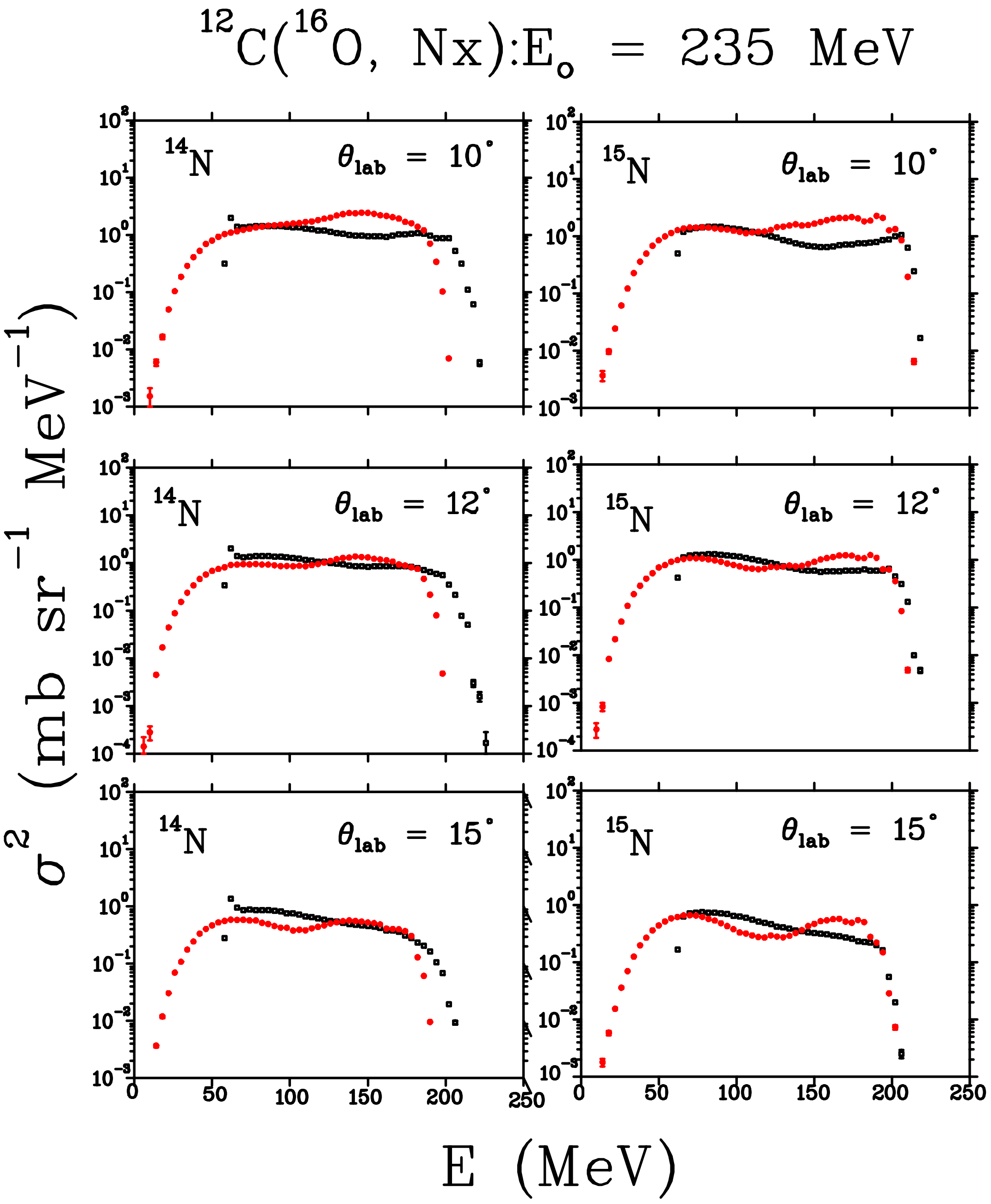

Figure 5.21: Comparisons between experimental data (black squares) and theoretical calculations (red circles) of double differential cross sections of ^{14}N (left) and ^{15}N (right) at different emission angles, as indicated in the figure. These cross-sections are presented with their statistical error bars.

cross-sections and drop-off rapidly at about 16 MeV below the high energy peak of the experimental distribution. This unexpected drop-off of the theoretical cross-sections in the high energy region is caused by the failure of the model to interpret multi-nucleon transfer from the projectile to the target. As the emission angle increases to $\theta_{lab} = 12°$ and 15°, the theoretical cross-sections slightly underestimate the experimental cross-sections at lower emission energies but show good agreement at intermediate emission energies. On the other hand, the comparison for ^{15}N shows similar behaviour to ^{14}N at $\theta_{lab} = 10°$ in the lower energy region, but at $\theta_{lab} = 12°$ and 15° the theoretical cross-sections overestimate the experimental cross-sections at the intermediate emission energies. At high emission energies of ^{15}N, fragments the comparison shows a good agreement between the experimental and theoretical cross-sections. The high energy part of these spectra is dominated by reaction mechanisms such as nucleon-transfer, i.e. the transfer of one proton from ^{16}O to the target nucleus and binary break-up of the projectile to form ^{15}N and a proton.

Fig. 5.22 shows the comparison between the experimental and theoretical cross-sections of ^{15}O (left) and ^{17}O (right) presented at different emission angles, as indicated. At low emission energies both the experimental distributions of ^{15}O and ^{17}O show very good agreement with the theoretical cross-sections. At intermediate emission energies the theoretical cross-sections of ^{15}O overestimate the experimental cross-sections; nonetheless, these spectra show good agreement between experimental and theoretical distributions at high emission energies. The theoretical cross-sections of ^{17}O show an unexpected dip in the intermediate emission energy region. This unexpected dip could be due to the omission of a nucleon coalescence mechanism in the model interpretation of the formation of fragments with atomic mass of A = 17. At high emission energies, the comparison between experimental and theoretical cross-sections again show reasonable agreement. The high energy part of ^{15}O is dominated by the transfer of a neutron from ^{16}O (projectile) to the target and ^{15}O is emitted as spectator fragment, and is detected with high energy, while the transfer of a neutron from the target nucleus to the projectile feeds the high energy part of the energy distribution of ^{17}O.

The comparisons between experimental and theoretical cross-sections of F isotopes are plotted in Figs. 5.23 and 5.24. Fig. 5.23 shows the comparison for ^{17}F (left) and ^{18}F (right), while the comparisons for ^{19}F are presented in Fig. 5.24. In the low emission energy region, the theoretical cross-sections of ^{17}F overestimate the experimental cross-sections for all emission angles presented. The intermediate emission energy region of these spectra exhibits a similar dip to that observed in the theoretical spectra of ^{17}O in Fig. 5.22. At higher emission energies the theoretical spectra show reasonable agreement with the experimental cross-sections. In this energy region the production of ^{17}F is dominated by the transfer of one proton from the ^{12}C target nucleus to the ^{16}O projectile. On the other hand, the low energy region of the theoretical cross-sections of ^{18}F shows good agreement with the experimental spectra at

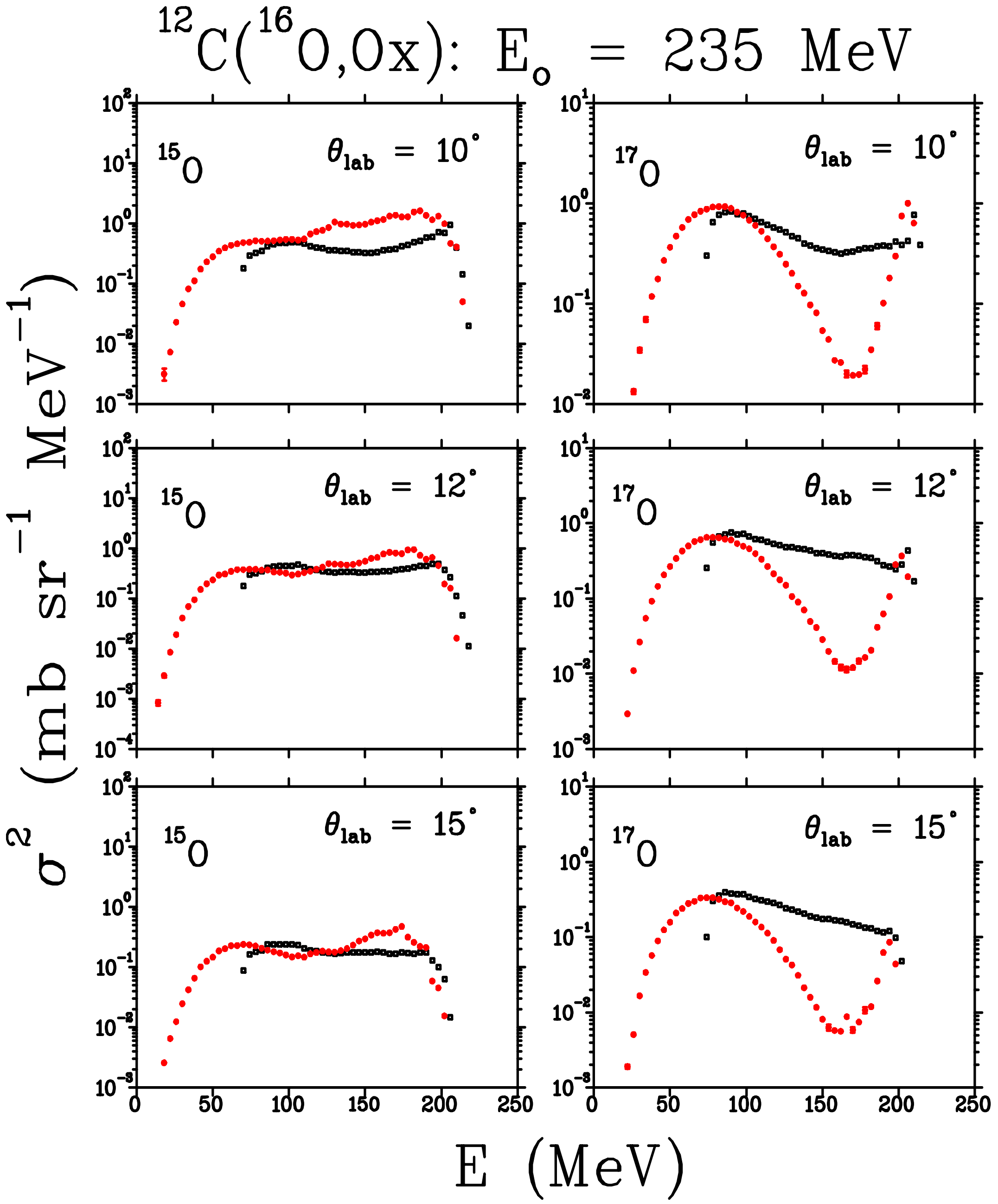

Figure 5.22: Comparisons between experimental data (black squares) and theoretical calculations (red circles) of double differential cross sections of ^{15}O (left) and ^{17}O (right) at different emission angles, as indicated in the figure. These cross-sections are presented with their statistical error bars.

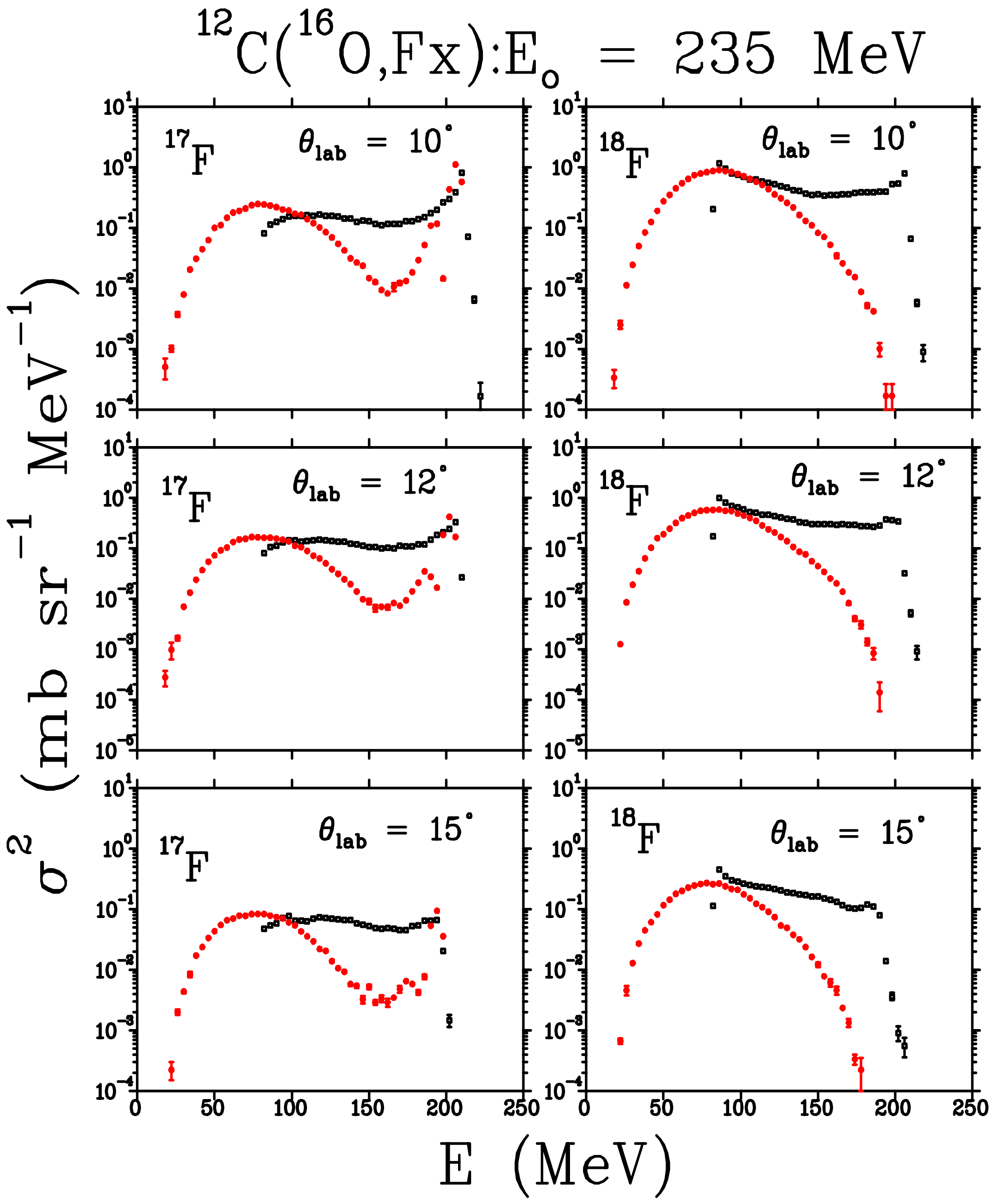

Figure 5.23: Comparisons between experimental data (black squares) and theoretical calculations (red circles) of double differential cross sections of ^{17}F (left) and ^{18}F (right) at different emission angles, as indicated in the figure. These cross-sections are presented with their statistical error bars.

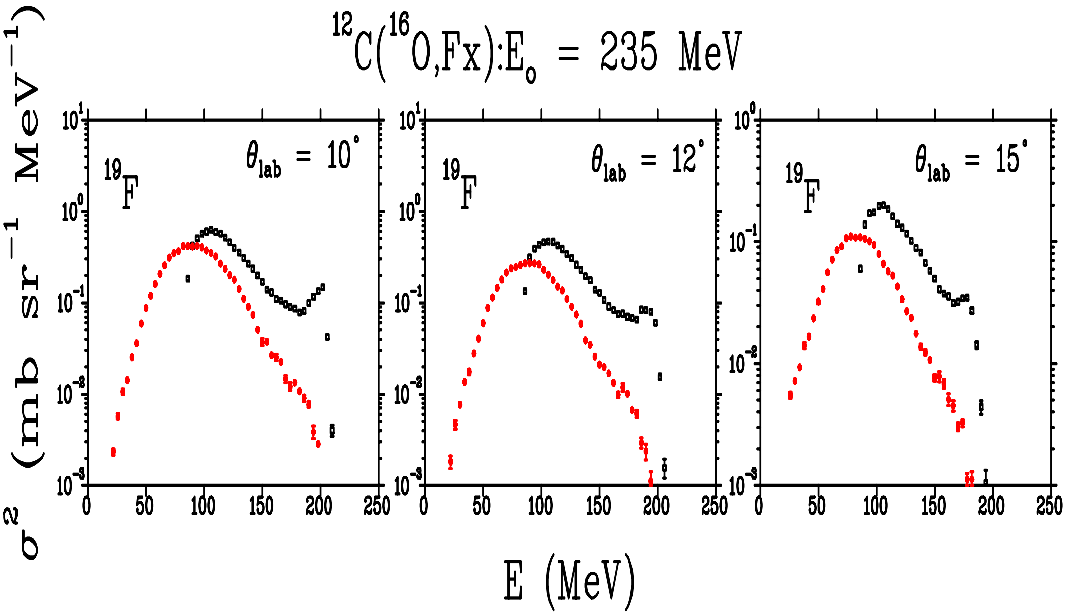

Figure 5.24: Comparisons between experimental data (black squares) and the theoretical calculations (red circles) of double differential cross sections of ^{19}F at different emission angles, as indicated in the figure. These cross-sections are presented with their statistical error bars.

an emission angle of $\theta_{lab} = 10°$. As the emission angle increases to $\theta_{lab} = 12°$ and 15°, the theoretical cross-sections slightly underestimate the experimental spectra at low emission energies. At high emission energies, the theoretical cross-sections drop off rapidly and show huge disagreement with the experimental spectra. This sudden drop-off is due to the failure of the model to predict multi-nucleon transfer from the target nucleus to the projectile to form ^{18}F. A similar failure was observed in the formation of ^{14}N, as shown in Fig. 5.21. In the case of ^{19}F, the theoretical spectra underestimate the experimental cross-sections at all emission angles and energies presented. Nevertheless, these spectra exhibit similar trends at low and intermediate emission energies, except at high emission energies where the theoretical cross-sections drop off rapidly due to the failure of the model to reproduce multi-nucleon transfer, as explained earlier.

Fig. 5.25 presents the comparison between theoretical and experimental distributions of ^{20}Ne (left) and ^{21}Ne (right) for different emission angles, as indicated. At low emission energies, the theoretical cross-sections overestimate the experimental spectra for both ^{20}Ne and ^{21}Ne. At high and intermediate emission energies, the theoretical cross-sections drop off rapidly due to the inability of the model again to reproduce multi-nucleon transfer. At high emission energies, the theoretical energy spectra underestimate the experimental cross-sections at all emission angles for both ^{20}Ne and ^{21}Ne.

This model needs further improvements to accommodate the simulation

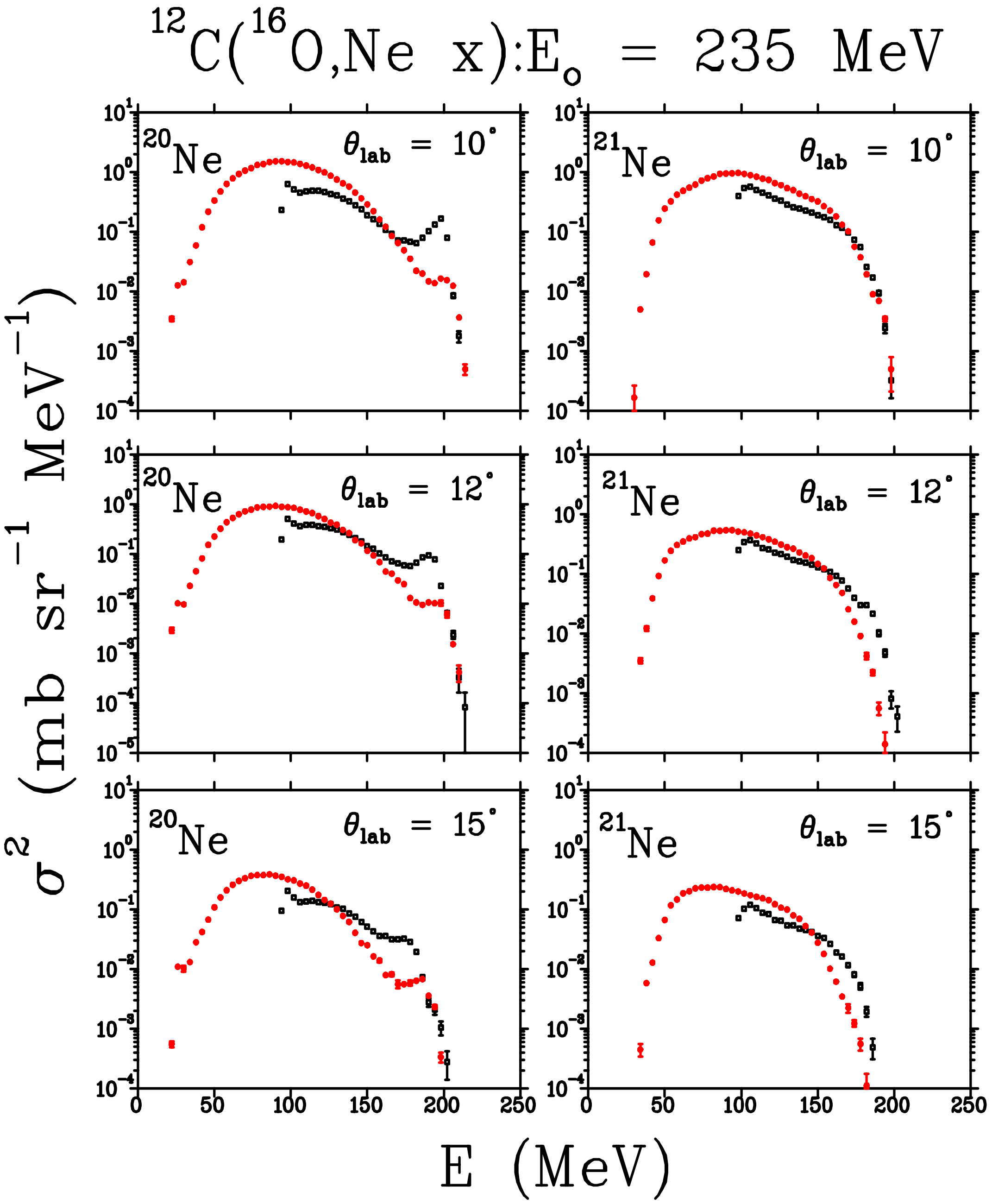

Figure 5.25: Comparisons between experimental data (black squares) and theoretical calculations (red circles) of double differential cross sections of ^{20}Ne (left) and ^{21}Ne (right) at different emission angles, as indicated in the figure. These cross-sections are presented with their statistical error bars.

of fragments lighter than both the projectile and the target nucleus. It was also evident that this model predicts contributions from one nucleon transfer better than when it is used to interpret the spectra making use of multi-nucleon transfer processes as observed in Figs. 5.21 and 5.23. The spectra produced from multi-nucleon transfer need to be improved further in order to simulate the experimental data correctly. This model also failed to correctly interpret the intermediate energies for fragments with mass number (A = 17) for both ^{17}O and ^{17}F as observed in Figs. 5.22 and 5.23. Despite the above mentioned weaknesses, the FLUKA code models the low energy part of the spectra where the nuclear evaporation mechanism dominates relatively well, as well as the intermediate emission energies that are dominated by nucleon coalescence and pre-equilibrium mechanisms for all simulated fragments. The high energy part of the energy distribution of the fragments, produced via single nucleon transfer, also shows good agreement between the model and experimental spectra.

Chapter 6

Summary and Conclusion

Two sets of experiments were performed in order to complete this study. The aim of the first experiment was to ascertain the difference between quasi-elastic (QE) and inelastic fragmentation of the projectile at an incident energy of E_{lab} = 33 MeV/u, and also to investigate the origin of a previously unexplained ^{12}C break-up contribution observed in a coincidence experiment.

The second experiment was performed for further study of the underlying reaction mechanisms involved in the production and emission of Intermediate Mass Fragments (IMFs) in the interaction of a E_{lab} = 400 MeV ^{12}C and a E_{lab} = 235 MeV ^{16}O beams with a ^{12}C target.

The standard ΔE-E technique was implemented for particle identification and isotope separation for both correlation and IMFs measurements. Two detector telescopes were used in each experiments to measure the energy spectra of the emitted fragments.

6.1 Correlation Measurements

In the correlation experiment the difference between QE and inelastic fragmentation was studied by measuring in coincidence the correlation of ^{8}Be$_{g.s.}$ and α-particles induced by E_{lab} = 400 MeV ^{12}C ions interacting with light to heavy mass nuclei (A = 12 to 197). Another aim was to investigate the difference between the inclusive spectra of ^{8}Be$_{g.s.}$ measured in the interaction of ^{12}C with ^{59}Co and ^{93}Nb and the spectra measured in the interaction with ^{197}Au target, as observed in existing inclusive data [Gad01]. The correlation between ^{8}Be$_{g.s.}$ and α-particles was chosen for this study due to its exclusive signature. This channel was chosen because the detector technique that was used allows good separation between the ^{8}Be$_{g.s.}$ at the 0^+ state and the first excited state, whereas other channels such as two ^{6}Li or ^{9}Be and ^{3}He are contaminated by different excited states. The DSSSD detector and the technique used for the ^{8}Be detector telescope is more efficient in detecting ^{8}Be at the 0^+ state than at the first excited state. The data analysis is simplified by the fact that a $^{8}\text{Be}_{g.s.}$ fragment is unbound and cannot survive a final-state interaction without breaking up into its two constituent α-particles, therefore, only the inelastic collision between the α-particle and the target nucleus has to be considered. In order to disentangle the difference between the QE and inelastic fragmentation, and also to investigate the appearance of the unexpected energy peak 30 MeV below the QE contribution, coincidence data were obtained in the interaction of ^{12}C with ^{12}C, ^{93}Nb and ^{197}Au at an incident energy of $E_{lab} = 400$ MeV. A $(\text{CH}_2)_n$ target was also included to study the effect of an excess of hydrogen in the target.

It had previously been observed that the energy spectra of α-particles measured in coincidence with projectile-like fragments peak at an energy which is about 15% higher than the corresponding beam velocity. To further address this anomalous behaviour in the energy spectra of the coincident α-particle, results obtained in the present correlation measurements could provide a possible explanation for this long standing and open issue in the field [Fuc94, Gon87].

The present correlation measurements were carried out with two detector telescopes. While the ^{8}Be fragments were measured with a detector telescope consisting of a DSSSD ΔE followed by a NaI stopping detector; the α-particles were measured on the opposite side of the beam axis with a triple detector telescope consisting of two SSB detectors followed by a NaI stopping detector. The ^{8}Be detector set-up enabled the exclusion of the break-up events of $^{8}\text{Be}_{g.s.}$ emitted from the ^{12}C target, because the detectors were less efficient in detecting lower energy ^{8}Be fragments, due to the large separation angle between its constituent α-particles. In such a case one of the α-particles would miss the detector and the coincidence would not be established.

The gated QE α-particle energy spectra were found to have two peaks at the forward α-particle emission angles of $\theta_\alpha = 16°$ and $18°$. The first energy peak had a centroid at emission energies corresponding to the beam velocity, while the other energy distribution had its centroid at about 15% higher energies relative to the beam velocity. The distributions which peaked at the higher energy were found to be more dominant in the interaction with the ^{12}C target. The results obtained with the SimSort simulation code revealed that the distribution at these higher energies originated from the fusion between projectile and hydrogen contaminants on the target foil. All QE α-particle and $^{8}\text{Be}_{g.s.}$ cross-sections were fitted with Gaussians in order to determine their width and energy peak as a function of target mass, and also to extract the energy integrated angular distributions. The individual QE cross-sections of $^{8}\text{Be}_{g.s.}$ fragments and α-particles measured in the interaction of the projectile with the ^{12}C target showed a broader energy distribution and peaked at slightly lower energies compared to the spectra measured in the interaction with the heavier target nuclei. This was due to the low recoil energy among interacting nuclei. These observations were also made with regards to the widths of the $^{8}\text{Be}_{g.s.}$ break-up distributions in the existing inclusive spectra measured in the interaction of ^{12}C with ^{59}Co, ^{93}Nb and ^{197}Au. In these spectra it was observed that the width of the break-up distribution for the ^{8}Be$_{g.s.}$ fragments was the narrowest for the ^{197}Au target [Gad01].

The projections of the two-dimensional spectra onto the sum of the kinetic energy of the coincident ^{8}Be$_{g.s.}$ and α-particles show that the production of these particles is dominated by the QE break-up mechanism at the most forward emission angles for all targets. These projected sum energy spectra are dominated by a strong QE peak at the highest emission energy part corresponding to the beam velocity, and a tail of inelastic events extending down to the lower part of the energy spectra. The events that populate the inelastic part of the correlation spectra mainly originate from the interaction of α-particles with the target nucleus. Since it is unlikely that the ^{8}Be$_{g.s.}$ fragments would survive any final-state interactions with the residual target nucleus, the inelastic break-up events of ^{8}Be$_{g.s.}$ are mainly produced when the ^{12}C interacts with the target nucleus and loses a substantial part of its kinetic energy before it breaks up into a ^{8}Be$_{g.s.}$ fragment and α-particle. Events that form the locus which appears about 30 MeV below the QE locus were found to originate from a possible fusion between ^{12}C with a hydrogen contaminant on the target foils to form an excited ^{13}N* compound nucleus which decayed via a sequential break-up mechanism. The excited ^{13}N nucleus decays into an α-particle and ^{9}B$_{g.s.}$, which, since it is unbound, decays into a proton and an unbound ^{8}Be$_{g.s.}$, which decays again, into two α-particles. The distribution of the high energy part of the QE locus is due to the effect of the proton that is detected and adds to the ^{8}Be$_{g.s.}$ total energy, while the locus at lower energy is populated when the proton misses the detector and only the ^{8}Be$_{g.s.}$ energy is measured. The SimSort results confirmed the results observed from the experimental data obtained in the reaction of ^{12}C with $(\mathrm{CH}_2)_n$. The summed energy spectra extracted in this specific case showed that the locus at the lower energy below QE, and the peak at higher energy on the QE locus were more pronounced than the pure QE energy peak. These results prove that the locus at lower energies was indeed produced in the interaction of ^{12}C with a hydrogen contaminant on the target foils. The QE events originating from the interaction of ^{12}C with a hydrogen contaminant affect the inelastic cross-sections. These events affect the higher energy part of inelastic ^{8}Be$_{g.s.}$ spectra and are spread across the whole energy range of the inelastic α-particle spectra.

The QE and inelastic energy integrated angular distributions show that the binary break-up of the projectile is target dependent. In the case of ^{197}Au and ^{93}Nb, targets the QE energy integrated angular distributions are much larger and decrease rapidly as a function of emission angle, while the distributions in the case of a ^{12}C target show a more steady decrease in the angular distributions. The inelastic energy integrated angular distributions cross-sections show an opposite structural behaviour compared to the QE energy integrated angular distributions. The energy integrated angular distributions of events originating from a fusion process with a proton to form ^{13}N show an increasing trend as a function of θ_{α}. This observation confirms that the process is not the nucleon transfer but a fusion process which dominates at larger emission angles. The cross-sections for the nucleon transfer mechanism decrease rapidly as a function of emission angle.

Due to the good energy resolution and efficiency of the detector system the events originating from the QE break-up mechanism were well separated from the events emitted by the inelastic break-up mechanism. It was also observed that the role of H contamination of the target cannot be neglected in these types of coincidence experiments. It is therefore essential to correct for the H contaminant before interpreting the coincidence data.

The GEANT4 code was used in order to simulate the correlation results, more especially to model the QE α-particle energy spectra, as well as the QE energy integrated angular distributions. A model for QE scattering has been added to the Quark-Gluon String (QGS) model used in GEANT4. This was done by adding effects of Fermi motion of nucleons to the momenta of the emitted particles. In this study, the GEANT4 code was unable to reproduce the QE locus which is well pronounced in the experimental results.

The SimSort code was also used to simulate the QE break-up in the interaction of ^{12}C with a ^{93}Nb as well as a hydrogen target. These results show that the QE locus extracted in the interaction of ^{12}C with a hydrogen target appears about 30 MeV below the locus observed in the interaction with a ^{93}Nb target.

The present study of the binary break-up of ^{12}C into ^{8}Be$_{g.s.}$ and α-particles provided more information about the role played by the QE and inelastic break-up mechanisms. At these energies above 10 MeV/u it is important to consider the role that is played by both QE and inelastic break-up of the projectile when studying the reaction mechanisms responsible for the production of light particles and IMFs. The QE break-up plays an important role in the most forward emission angles for particles emitted with higher energies corresponding to the beam velocity, while the inelastic break-up mechanisms play an important role in the production of particles emitted at intermediate and lower energies with respect to the beam velocity.

Although enough experimental evidence has been acquired about the role played by the QE and inelastic break-up mechanism in this study, formal theoretical support is still needed to interpret these results.

6.2 Inclusive measurements

The second experiment was concerned with the study of the underlying reaction mechanisms governing the production of IMFs in the interaction of light nuclei ($6 \leq Z \leq 8$). The production of IMFs was investigated by measuring full energy spectra of Li, Be, B, C, N, O, F and Ne isotopes in the interaction of a $E_{lab} = 400$ MeV ^{12}C and a $E_{lab} = 235$ MeV ^{16}O ion beam with a ^{12}C target at different emission angles ranging from $\theta_{lab} = 8°$ to $50°$.

The light fragments of Li and Be were measured with a detector telescope consisting of a SSB ΔE detector followed by a NaI stopping detector, while the other fragments ranging from the B to the Ne isotopes were measured on the opposite side of the beam with a triple SSB detector telescope.

The results of the IMF measurements were divided into two categories, the light fragments ($3 \leq \mathrm{Z} \leq 5$) and the heavier fragments ($6 \leq \mathrm{Z} \leq 10$). The angular distribution cross-sections of the IMFs were extracted at different emission energy cuts from the data measured in the interaction of ^{12}C with ^{12}C at an incident energy of E_{lab} = 400 MeV. The angular distribution cross-sections of the IMFs extracted at a lower emission energy of 86 MeV show a rather flat distribution which drops slightly as a function of emission angle and is almost isotropic. These features reveal that the reaction mechanism involved in the production of IMFs at lower energies with respect to the beam holds for almost all the emission angles, such as the nuclear evaporation mechanism. At the intermediate emission energy of 198 MeV, the cross-sections are higher at most forward angles and drop off rapidly with increasing emission angles. The angular distribution cross-sections extracted at a higher emission energy of 250 MeV and above dominate the most forward emission angles and drop off rapidly as a function of emission angle. These IMFs with high energies compared to beam velocity are mainly produced by direct reaction mechanisms such as binary break-up of the projectile which dominates the most forward emission angles.

The production and emission of the light fragments measured in the interaction of ^{16}O with ^{12}C at an incident energy of E_{lab} = 235 MeV seem to dominate the intermediate emission energy region of the spectra. The cross-sections are lower at the low emission energies and increase as a function of emission energy reaching a maximum at intermediate energies. At higher emission energies, the cross-sections drop off rapidly. The production of these light fragments is dominated by reaction mechanisms such as nucleon coalescence through complete and incomplete fusion of the projectile with the target nucleus which dominate the intermediate energy region. These results show that these IMFs can be produced via a direct break-up mechanism followed by the incomplete fusion of one of the fragments with the target nucleus initiating nucleon coalescence with the emission of fragments in the pre-equilibrium energy region. The probability of producing these fragments as evaporation residue is far less compared to production through nucleon coalescence and pre-equilibrium reaction.

The energy spectra of the heavier IMFs ($6 \leq \mathrm{Z} \leq 10$) have a flat distribution in the low and intermediate energy region at most forward emission angles. These spectra show a discrete peak at the highest emission energy at the most forward emission angles which is populated by a nucleon transfer reaction. As the emission angle increases ($\theta_{lab} \geq 30°$), these cross-sections drop rapidly as a function of emission energy and angle. The production of these IMFs is dominated by direct reaction mechanisms such as nucleon transfer and binary break-up at the most forward emission angles. At larger emission angles the production is dominated by a peak at the Coulomb barrier and decreases rapidly with increasing emission energies. These changes in the structural behaviour of the cross-sections suggest a transition in reaction mechanisms from direct reaction mechanisms such nucleon transfer at a higher energy, to nucleon coalescence and eventually to an evaporation mechanism which dominates the production at lower emission energies.

The Monte Carlo code FLUKA was used in the present study to perform theoretical calculations for the heavier IMFs ($7 \leq Z \leq 10$). The theoretical calculations following the complete and incomplete fusion reactions, e.g. nucleon coalescence, were performed with a set of BME which was incorporated into the FLUKA code, while the theory of a binary break-up mechanism was interpreted by folding the LPWBA with an exponential survival probability of the projectile. The theory of the binary break-up was investigated by assuming that the projectile and target densities overlap. The calculated cross-sections show an agreement with the experimental energy spectra for all simulated fragments at a lower emission energy. At higher emission energies, the theoretical results fail to reproduce the experimental results, especially for fragments produced by multi-nucleon transfer from the projectile or target nuclei. The FLUKA code is under continuous development in order to accommodate the interpretation of all the IMFs which are produced especialy in the incident energy regime of 10 to 100 MeV/u. These improvements will include the ability to model the multi-nucleon transfer from the projectile to the target nucleus, as well as the binary break-up of the projectile into two light nuclei. The failure to reproduce the intermediate energy region of the energy spectra of the fragments with mass number ($A = 17$) still needs to be investigated further.

The studies of reaction mechanisms are still of great interest to investigate the reactions induced by ions on nuclei of biological tissue, as well as the study of the production of positron emitters such as ^{11}C, ^{13}N, ^{15}O and ^{18}F which are used to visualise the beam during tumour irradiations. The bombarding energy used during irradiation with ^{12}C ions is in the range of GeV, which is very high compared to the energy used in these studies. As the ^{12}C ions enter the body, they scatter off human tissue and lose their kinetic energy until they come to a halt by depositing the largest dose at the end of the path. The beam energies used in the present study apply to the final part of interaction between ^{12}C with tissue, which occurs close to or in the Bragg-peak region.

The break-up of ^{12}C and ^{16}O could also contribute to the study of cosmic ray spallation, which is believed to be responsible for the generation of all or almost all of ^{3}He and the elements of lithium, beryllium and boron in the solar system [Van98, Sch03]. This process results from the impact of cosmic rays against the interstellar medium, fragmenting carbon, nitrogen and oxygen nuclei present in the cosmic rays.

The results of the present study will play an important part by adding to the much needed experimental data to further investigate the theory that will enable the interpretation of reaction mechanisms involved in the production of IMFs at incident energies between 14 and 33.3 MeV/u. At these energies a known transition occurs, from more collective processes at lower incident energies (< 10 MeV/u) to more direct processes at higher energies, in the reaction mechanisms responsible for the production of IMFs [Fuc94, Mag98].

The results obtained from both the coincidence and inclusive IMF experiments have shown that the binary break-up at these energies plays a dominant role in the direct emission of particles at the most forward angles, with energies corresponding to the beam velocity. Furthermore, it is shown that both QE and inelastic break-up can be seen as "doorway" mechanisms leading to an excited compound system through other processes like complete or incomplete fusion between the projectile and the target or between their fragments. The different de-excitation processes of this compound system yields particles with different emission energies. The present results have provided not only insights into some of the reaction mechanisms, but at the same time are posing challenges to the development of theoretical models.

6.3 Outlook

Further studies to investigate the fusion cross-section between the ^{12}C projectile with a proton to form an excited ^{13}N* compound nucleus could be of great interest. From the present estimates, as given by relative break-up cross-sections, the fusion cross-section in this case seems to be even larger considering the amount of hydrogen contaminant on the target foils. Since 80% of a human body is water (H_2O), the study of this fusion reaction between the ^{12}C projectile and hydrogen nuclei could further play an important role in tumour irradiations with energetic ^{12}C ions. Carbon ions have distinct advantages relative to both photons and protons, because they deliver a higher dose to the tumours, with less effect on the surrounding tissue [Chu10]. The large fusion cross-sections of ^{12}C with protons could also play a role during tumour irradiation and add to the dose distributed to healthy tissues.

Appendix A

Correlation Cross-sections

A.1 Overview

The quasi-elastic (QE) and inelastic energy spectra of the coincidence α-particle and $^{8}\mathrm{Be}_{g.s.}$ fragments are presented below. These cross-sections are plotted with their statistical error bars and are within the systematic errors of (6 - 7.5 %). The QE α-particle energy spectra produced in the interaction of ^{12}C with ^{12}C, ^{93}Nb and ^{197}Au are presented in Figs. A.1 to A.3, respectively, while their correlated $^{8}\mathrm{Be}_{g.s.}$ fragments energy spectra are presented in Figs. A.4 to A.6. These cross-sections were binned into 4 MeV/bin and 8 MeV/bin as indicated in the captions in order to increase the statistics. The inelastic α-particles were also measured in coincidence with their correlated $^{8}\mathrm{Be}_{g.s.}$ fragments from the above reactions. The inelastic energy spectra of α-particle are shown in Figs. A.7 to A.9, and their correlated $^{8}\mathrm{Be}_{g.s}$ fragments are presented in Figs. A.10 to A.12. These results are explained in details in Chapter 5.

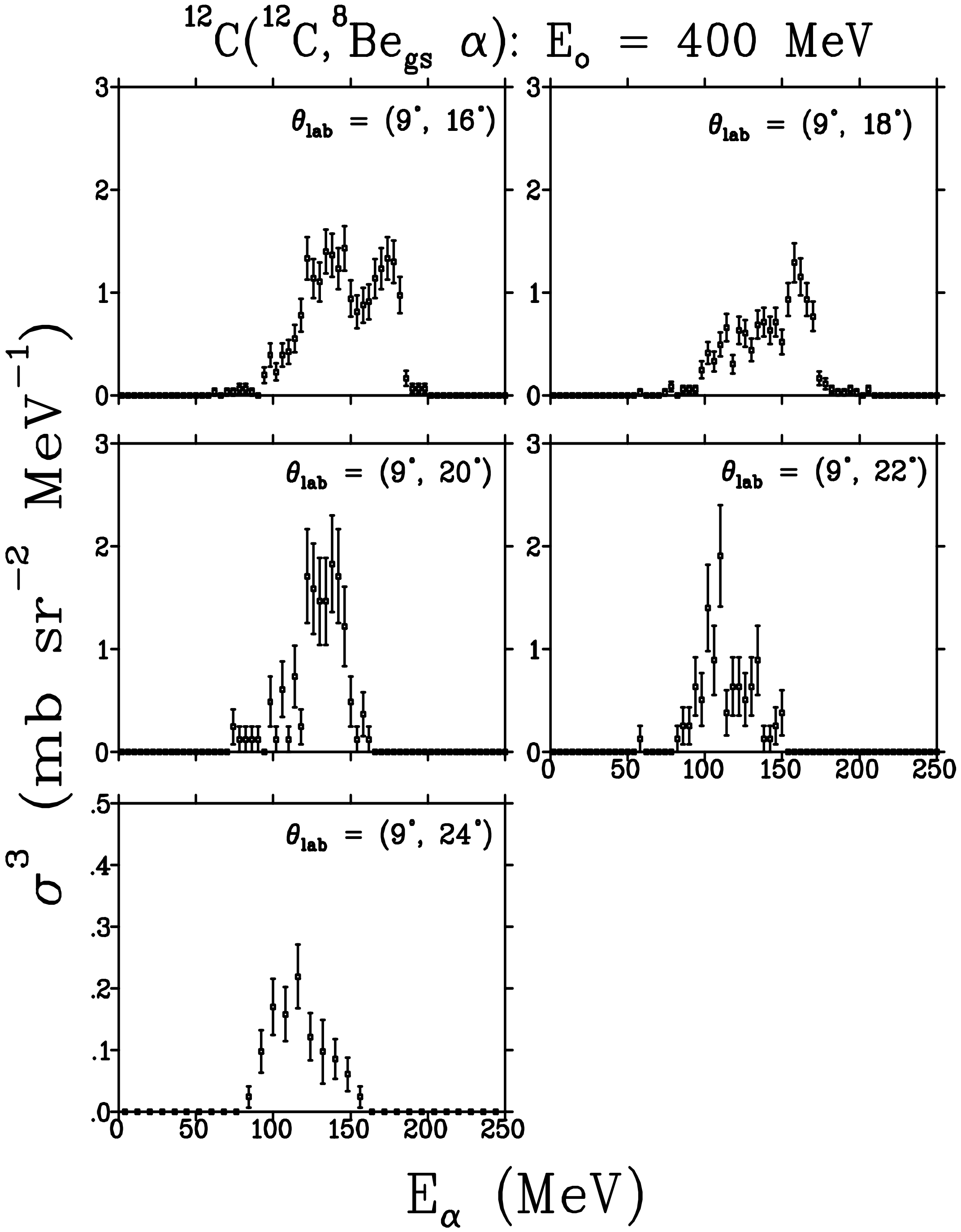

Figure A.1: Cross-sections of the QE α-particles measured in coincidence with $^{8}Be_{g.s.}$ fragments in the interaction of ^{12}C with ^{12}C at an incident energy of 400 MeV for different emission angles, as indicated. These cross-sections are compressed into 4 MeV/bin except at an emission angle $\theta_{lab} = 24°$ for which the width is 8 MeV/bin.

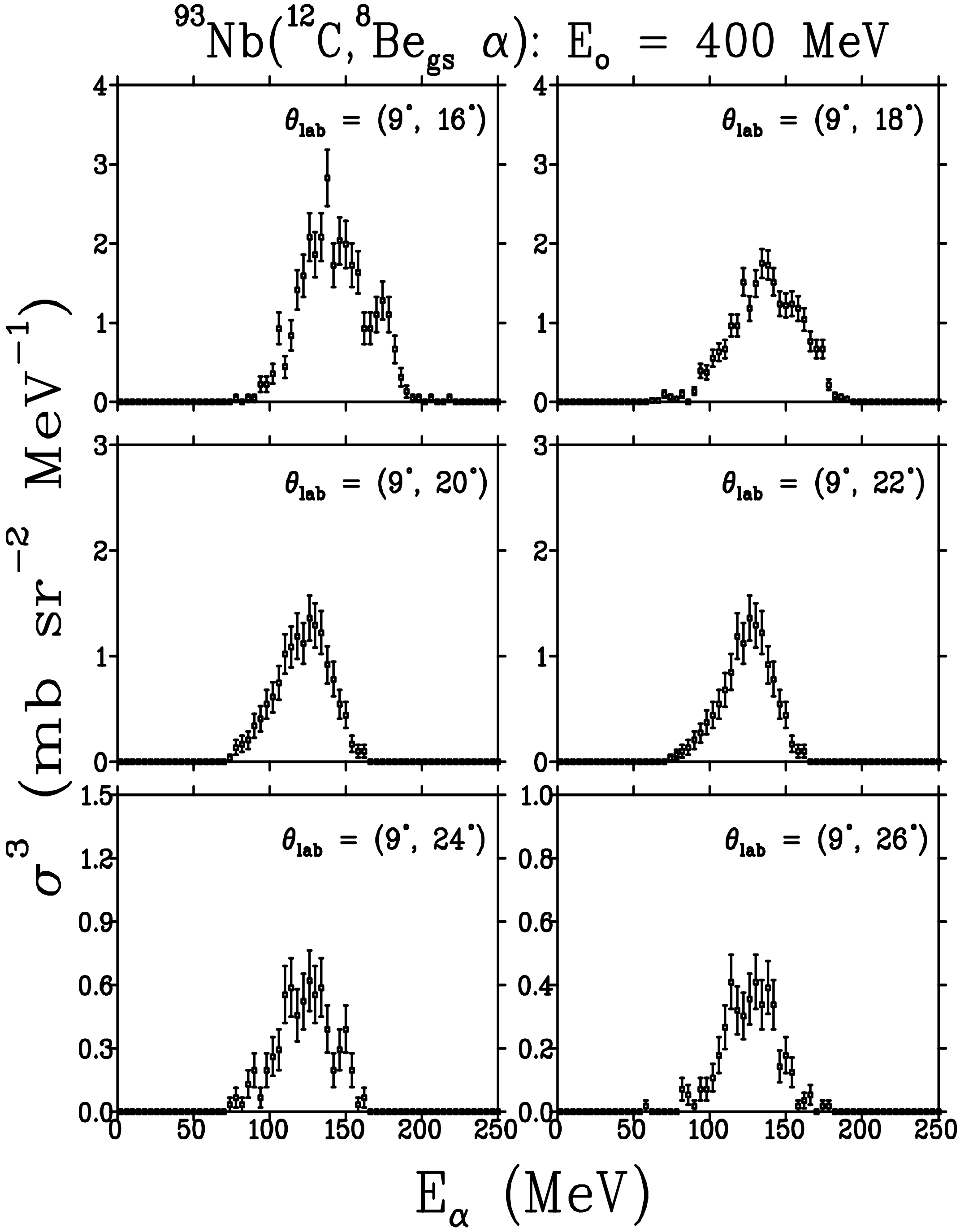

Figure A.2: Cross-sections of the QE α-particles measured in coincidence with ^{8}Be$_{g.s.}$ fragments in the interaction of ^{12}C with ^{93}Nb at an incident energy of 400 MeV for different emission angles, as indicated. These cross-sections are compressed into 4 MeV/bin for all emission angles.

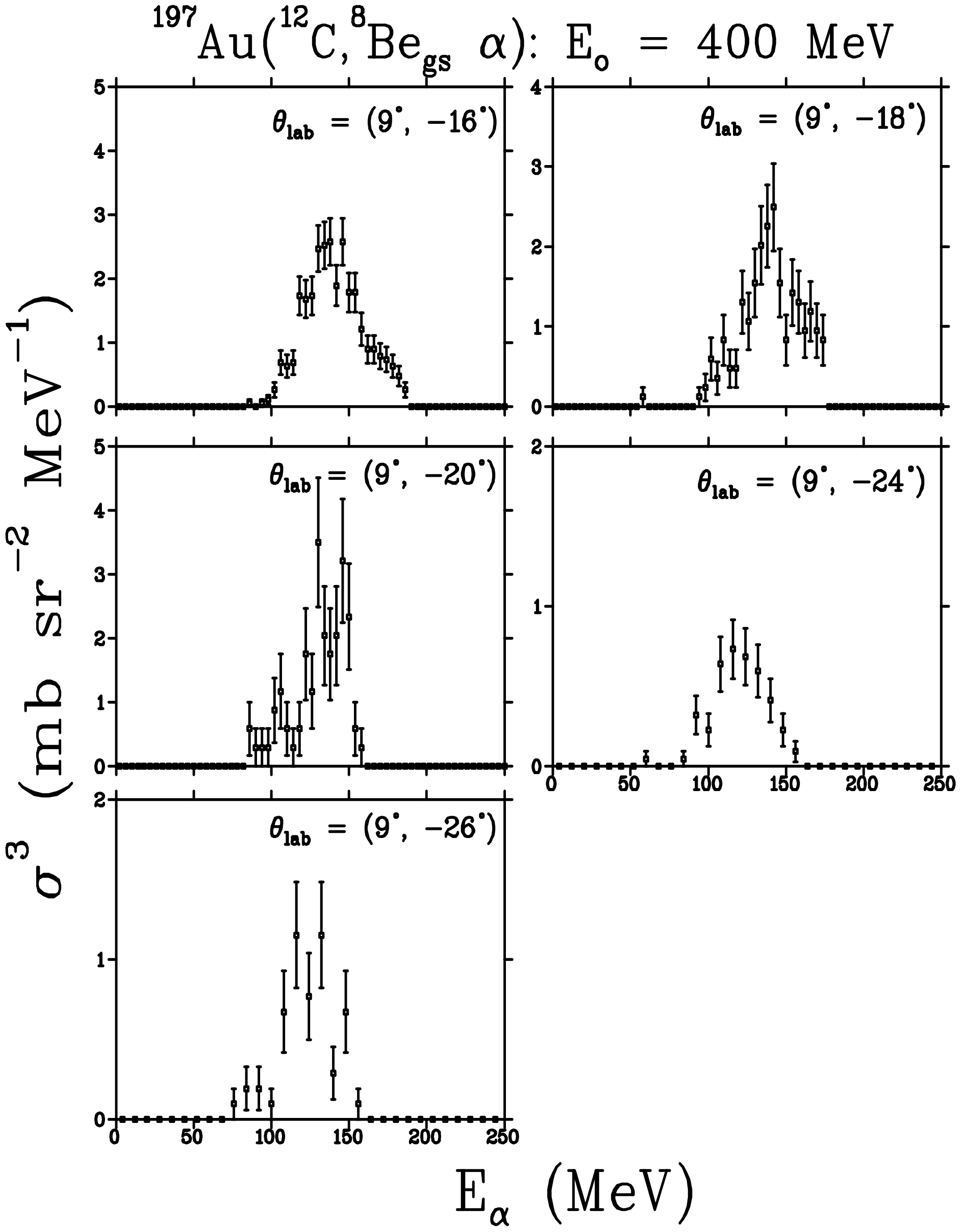

Figure A.3: Cross-sections of the QE α-particles measured in coincidence with ^{8}Be$_{g.s.}$ fragments in the interaction of ^{12}C with ^{197}Au at an incident energy of 400 MeV for different emission angles, as indicated. These cross-sections are compressed into 4 MeV/bin except at the emission angles of ($\theta_\alpha = 24°$ and $26°$) for which the width is 8 MeV/bin.

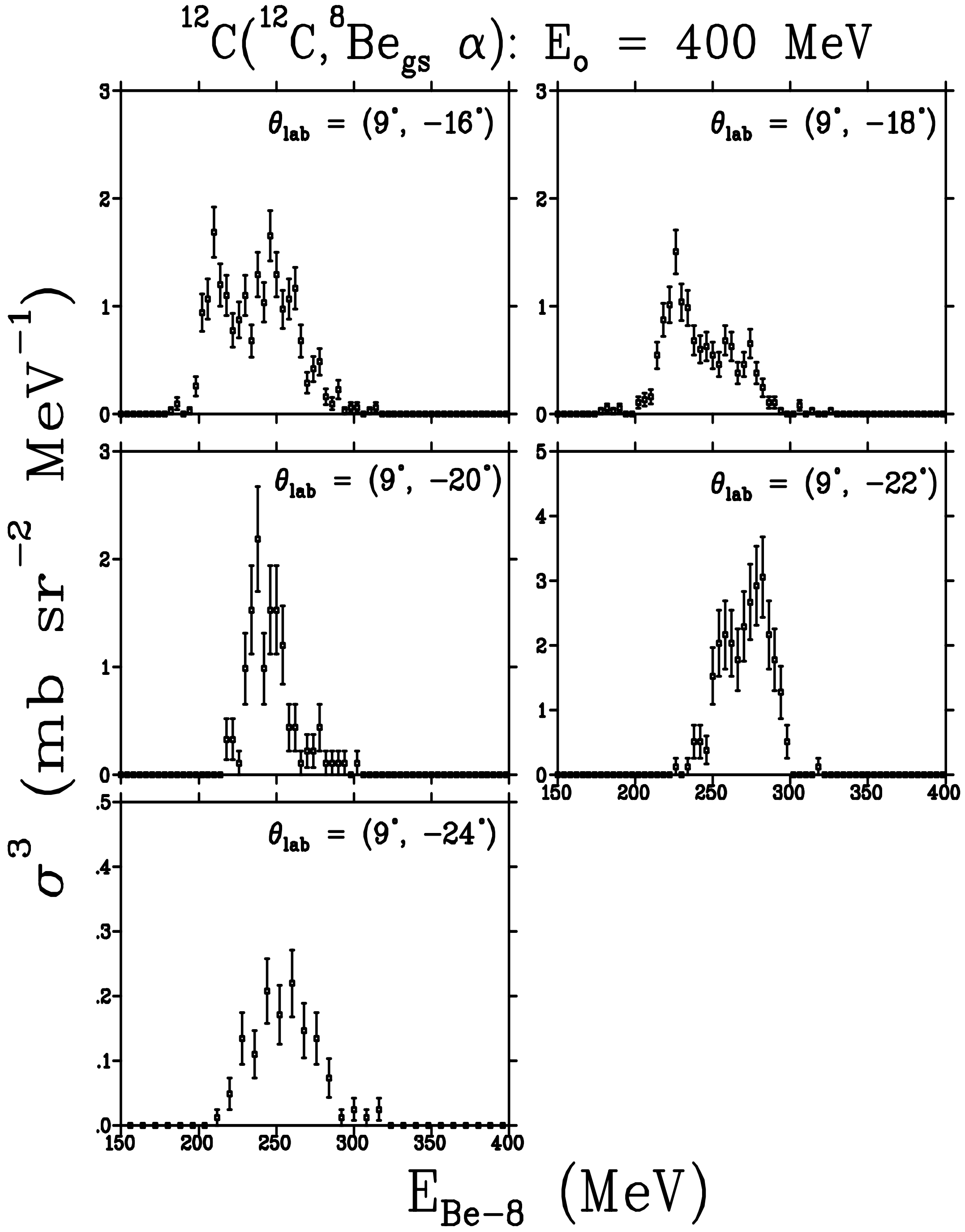

Figure A.4: Cross-sections of the QE $^{8}Be_{g.s.}$ fragments measured incoincidence with α-particles in the interaction of ^{12}C with ^{12}C at an incident energy of 400 MeV for different α-particle emission angles as indicated. These cross-sections are compressed into 4 MeV/bin except at an emission angle of ($\theta_\alpha = 24°$) for which the width is 8 MeV/bin.

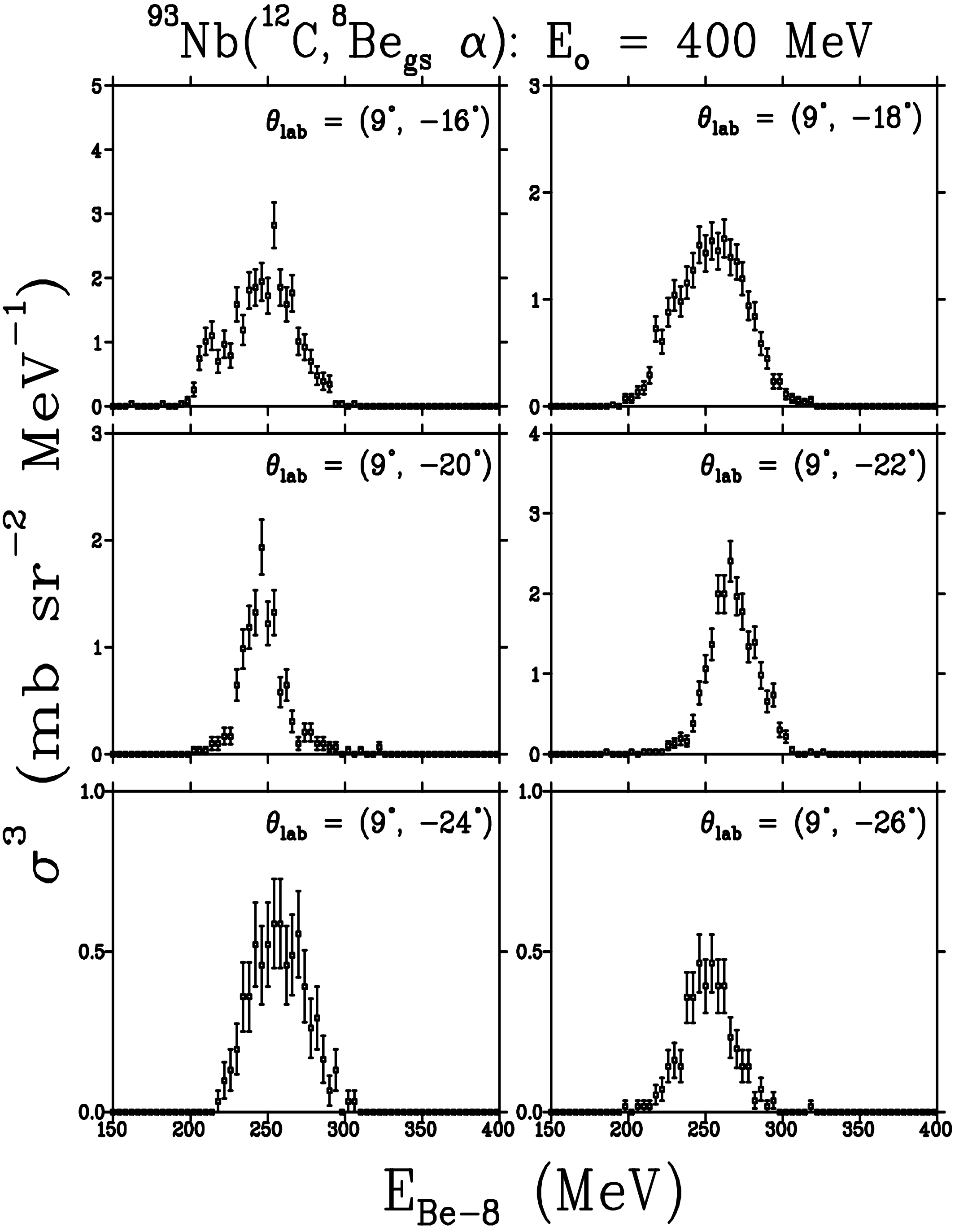

Figure A.5: Cross-sections of the QE ^{8}Be$_{g.s.}$ fragments measured incoincidence with α-particles in the interaction of ^{12}C with ^{93}Nb at an incident energy of 400 MeV for different α-particle emission angles, as indicated. These cross-sections are compressed into 4 MeV/bin.

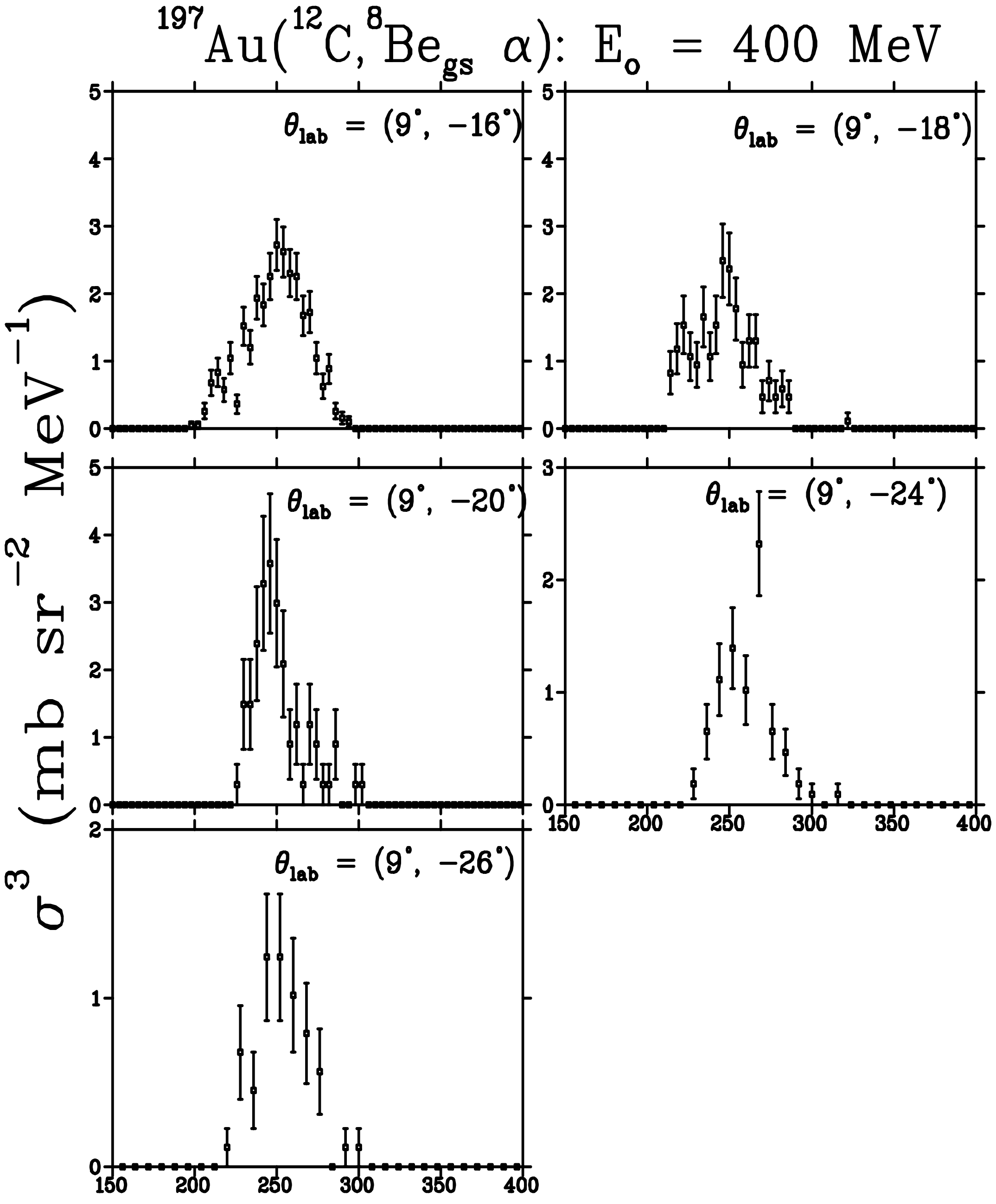

Figure A.6: Cross-sections of the QE ^{8}Be$_{g.s.}$ fragments measured incoincidence with α-particles in the interaction of ^{12}C with ^{197}Au at an incident energy of 400 MeV for different α-particle emission angles, as indicated. These cross-sections are compressed into 4 MeV/bin except at the emission angles of ($\theta_\alpha = 24°$ and $26°$) for which the width is 8 MeV/bin.

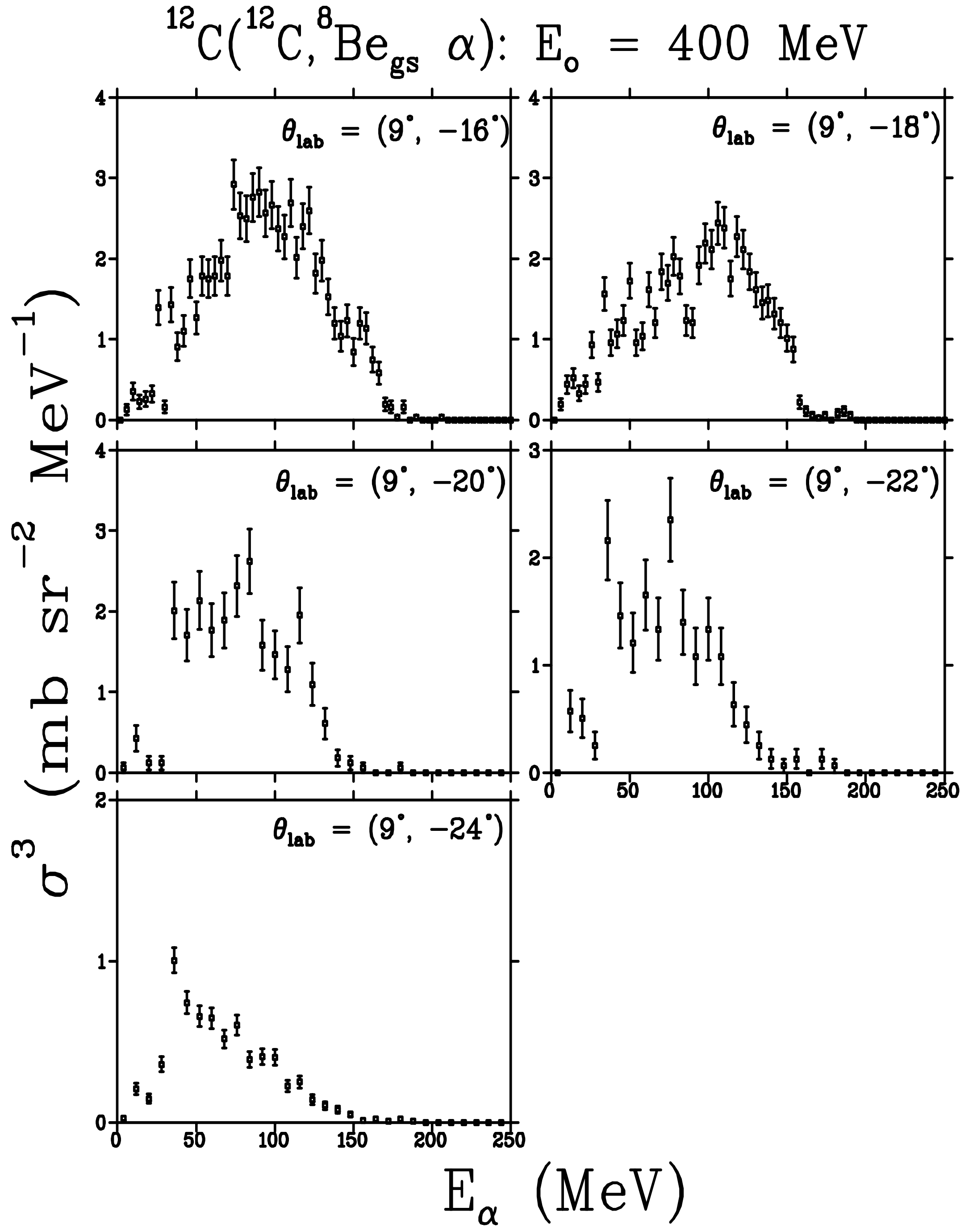

Figure A.7: Cross-sections of the inelastic α-particles measured in coincidence with ^{8}Be$_{g.s.}$ fragments in the interaction of ^{12}C with ^{12}C at an incident energy of 400 MeV for different emission angles, as indicated. These cross-sections are compressed into 4 MeV/bin except at an emission angle of ($\theta_\alpha = 24°$) for which the width is 8 MeV/bin.

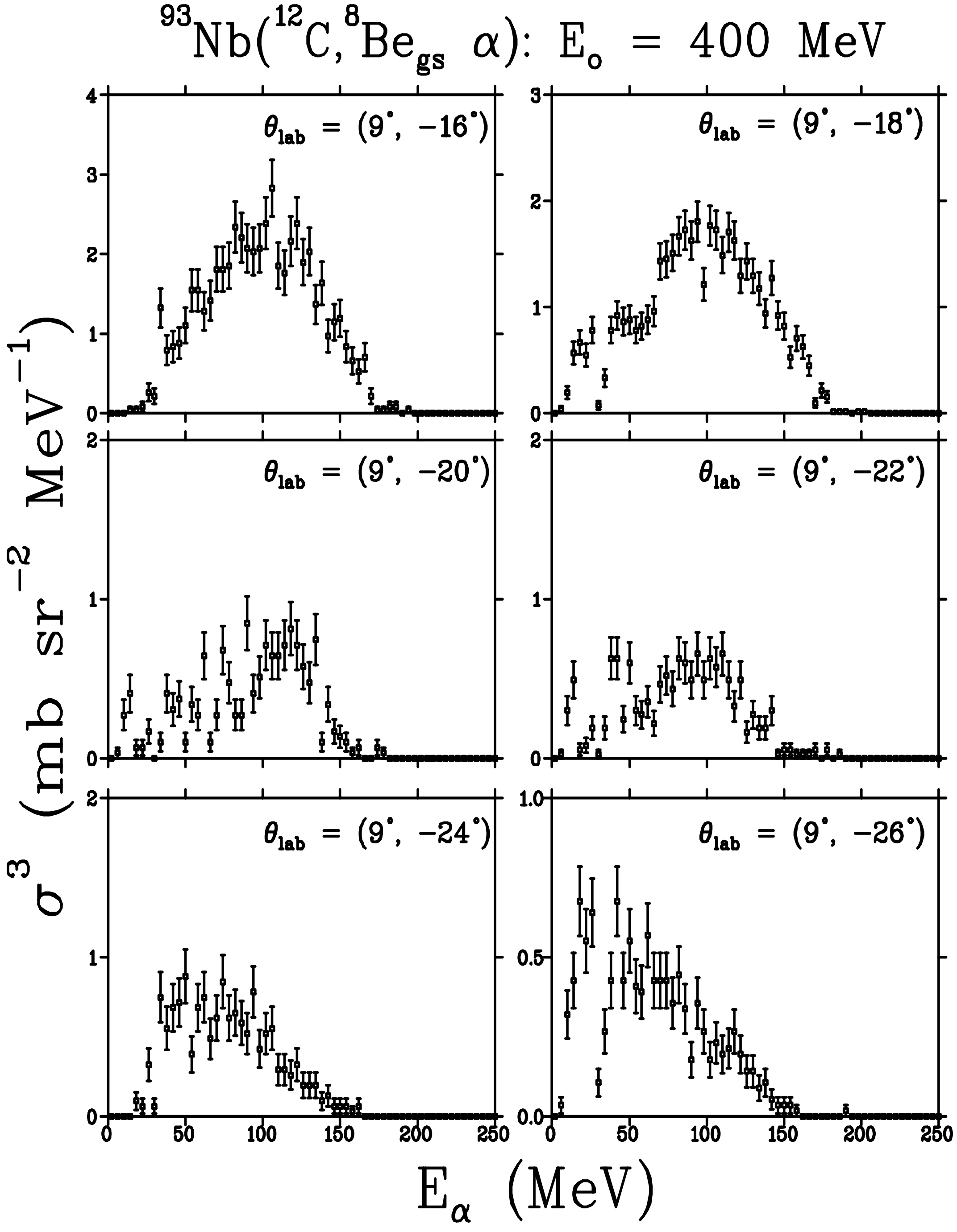

Figure A.8: Cross-sections of the inelastic α-particles measured in coincidence with ^{8}Be$_{g.s.}$ fragments in the interaction of ^{12}C with ^{93}Nb at an incident energy of 400 MeV for different emission angles, as indicated. These cross-sections are compressed into 4 MeV/bin.

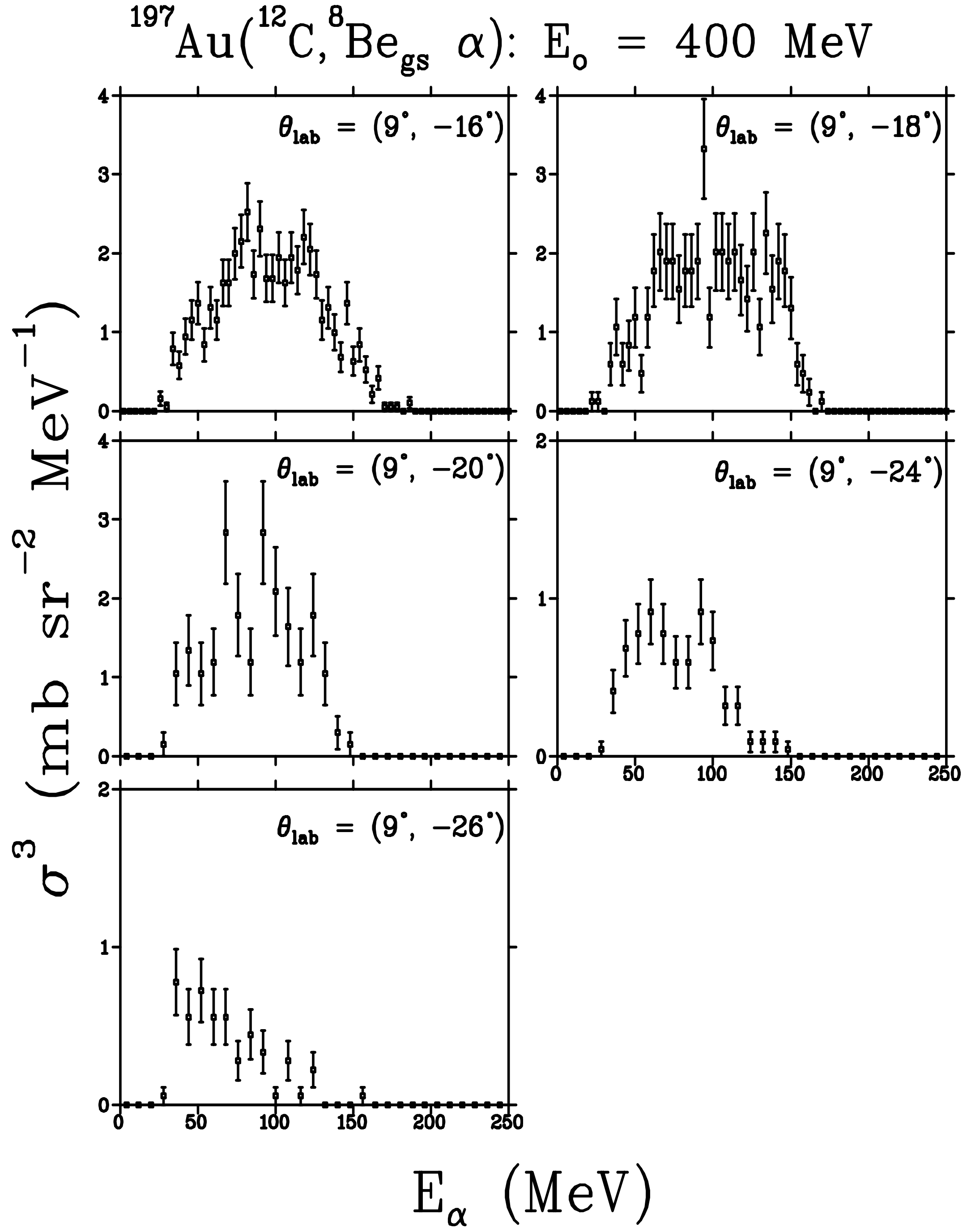

Figure A.9: Cross-sections of the inelastic α-particles measured in coincidence with ^{8}Be$_{g.s.}$ fragments in the interaction of ^{12}C with ^{197}Au at an incident energy of 400 MeV for different emission angles, as indicated. These cross-sections are compressed into 4 MeV/bin except at the emission angles of ($\theta_\alpha = 20$ °, 24° and 26°) for which the width is 8 MeV/bin.

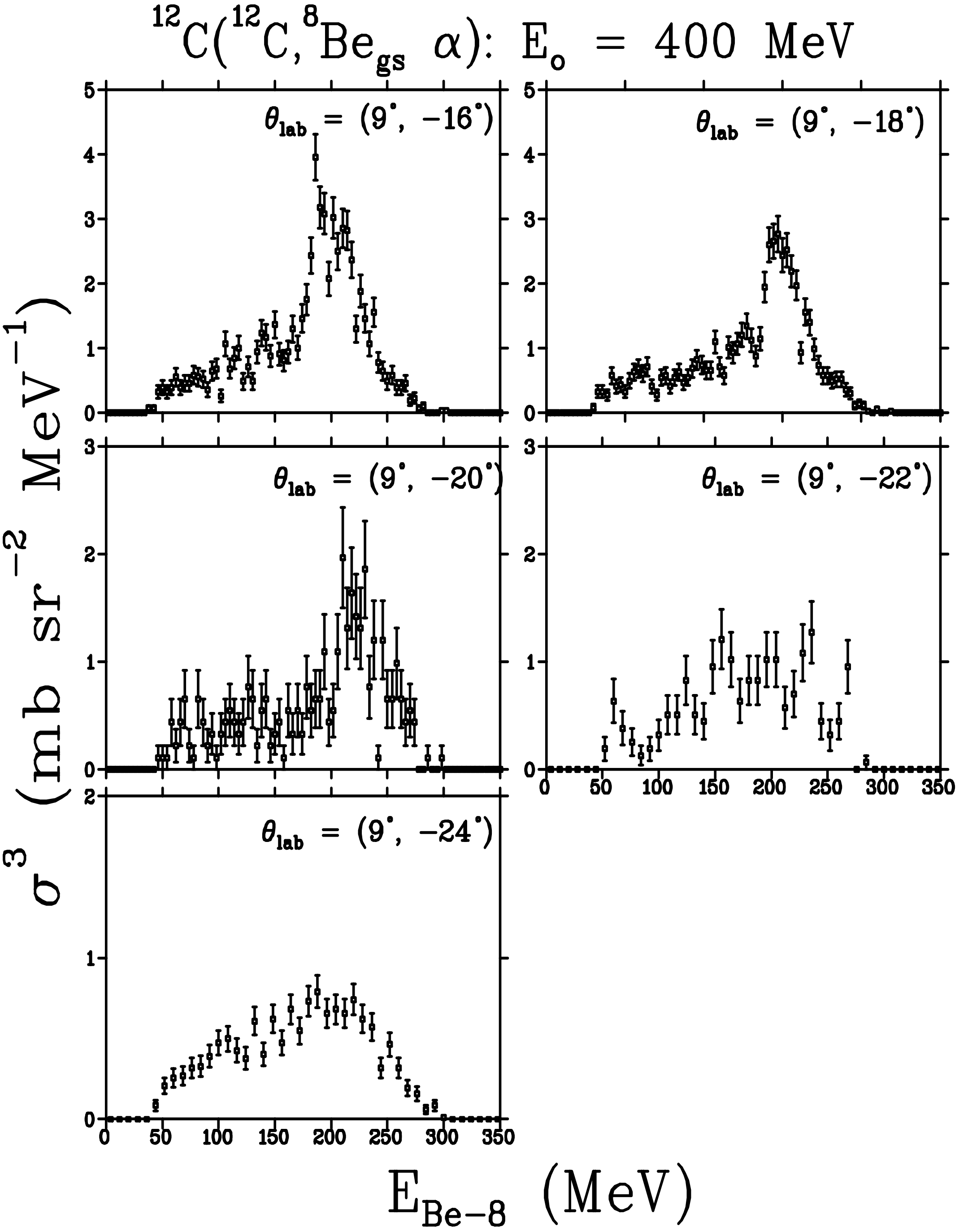

Figure A.10: Cross-sections of the inelastic $^{8}Be_{g.s.}$ fragments measured in coincidence with α-particles in the interaction of ^{12}C with ^{12}C at an incident energy of 400 MeV for different α-particle emission angles, as indicated. These cross-sections are compressed into 4 MeV/bin except at the emission angles of ($\theta_\alpha = 22°$ and $24°$) for which the width is 8 MeV/bin.

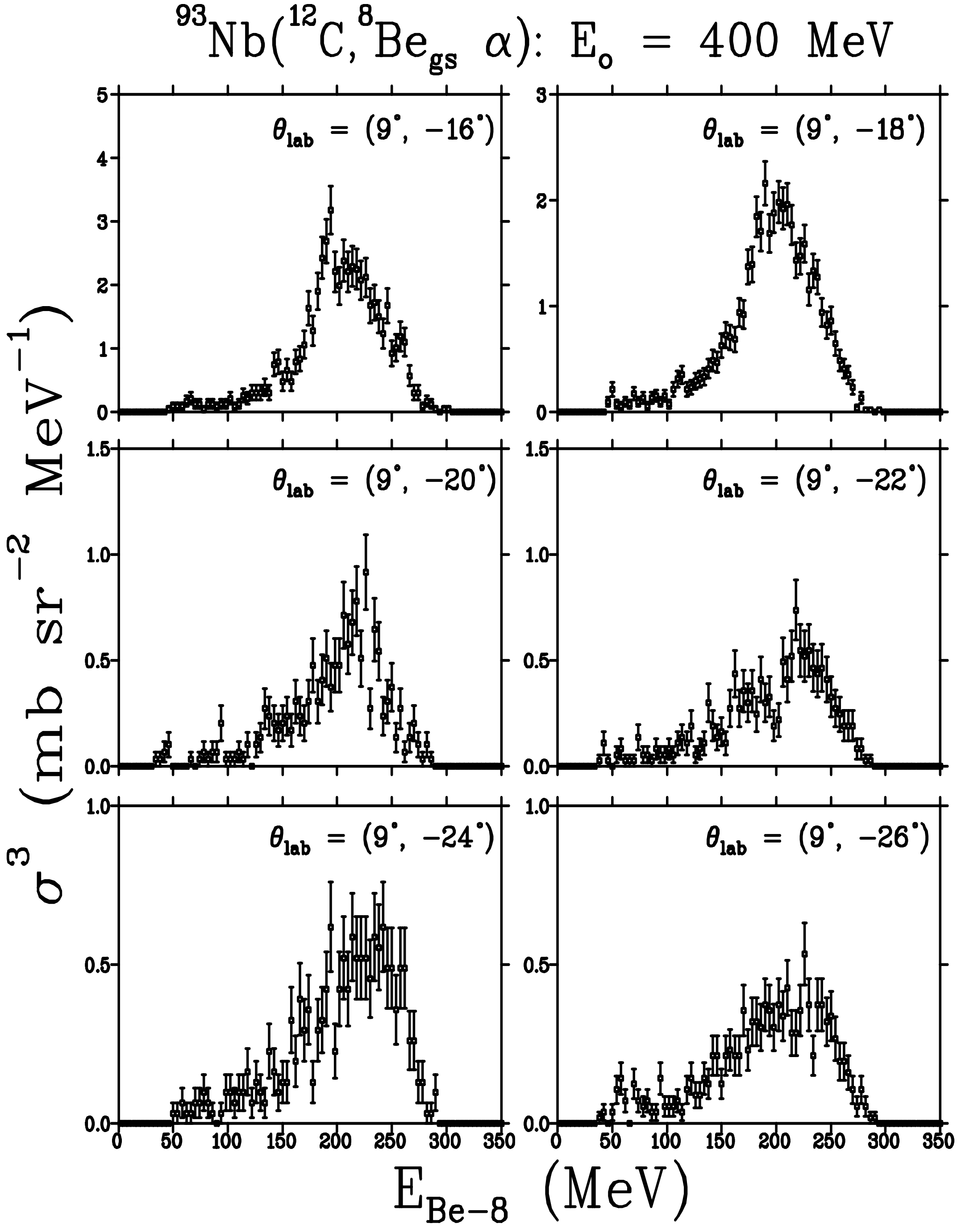

Figure A.11: Cross-sections of the inelastic ^{8}Be$_{g.s.}$ fragments measured in coincidence with α-particles in the interaction of ^{12}C with ^{93}Nb at an incident energy of 400 MeV for different α-particle emission angles, as indicated. These cross-sections are compressed into 4 MeV/bin.

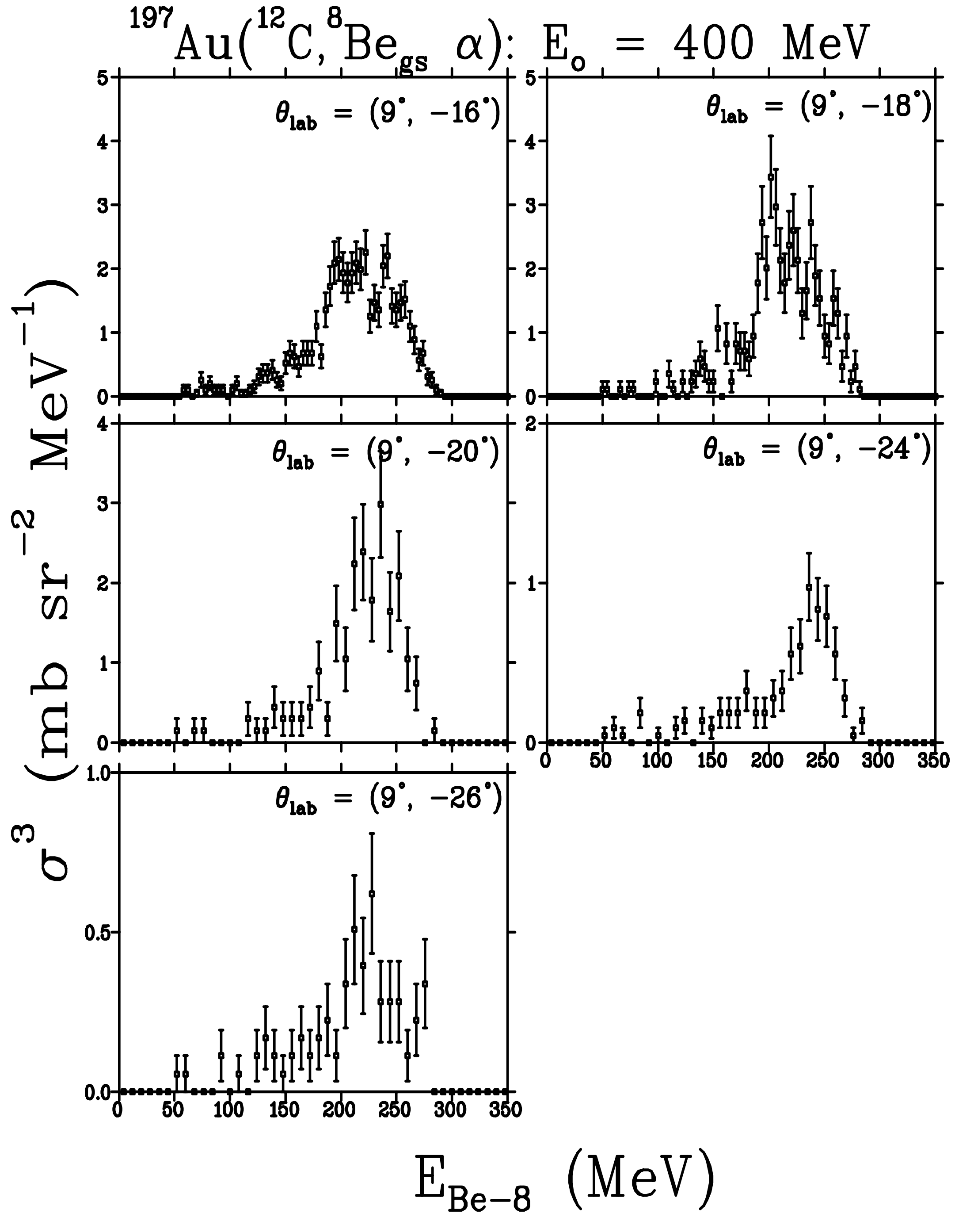

Figure A.12: Cross-sections of the inelastic ^{8}Be$_{g.s.}$ fragments measured in coincidence with α-particles in the interaction of ^{12}C with ^{197}Au at an incident energy of 400 MeV for different α-particle emission angles, as indicated. These cross-sections are compressed into 4 MeV/bin except at the emission angles of ($\theta_\alpha = 20$ °, 24° and 26°) for which the width is 8 MeV/bin.

Appendix B

IMF Cross-sections

B.1 Double differential cross-sections

The double differential cross-sections of IMFs emitted in the interaction of a 235 MeV ^{16}O beam with a ^{12}C target are presented in Figs. B.1 to B.8. These cross-sections are plotted with their statistical error bars and are within a systematic error of 7.1 %. The double differential cross-sections were binned into 4 MeV/bin in order to increase the statistics. The cross-sections of the light fragments ranging from Li to B isotopes peak at an intermediate emission energy region and drop as a function of emission energy for all isotopes. Their distributions have a similar shape for all emission angles, which suggests that they are produced by a similar reaction mechanism such as nucleon coalescence. On the other hand, the cross-sections for the projectile-like fragments (PLF) peak at a higher emission energy at the most forward angle and drop significantly with increasing emission angle. The enhancement of the spectra at high emission energies at most forward emission angles shows that the emission of projectile-like fragments is dominated by direct reaction mechanisms such as nucleon transfer and binary fragmentations. At larger angles, the energy spectra of the projectile-like fragments follow an almost exponential decay. This behaviour suggests that the production of PLF at larger emission angles is dominated by nuclear evaporation mechanisms which dominates the low emission energy part of the spectra.

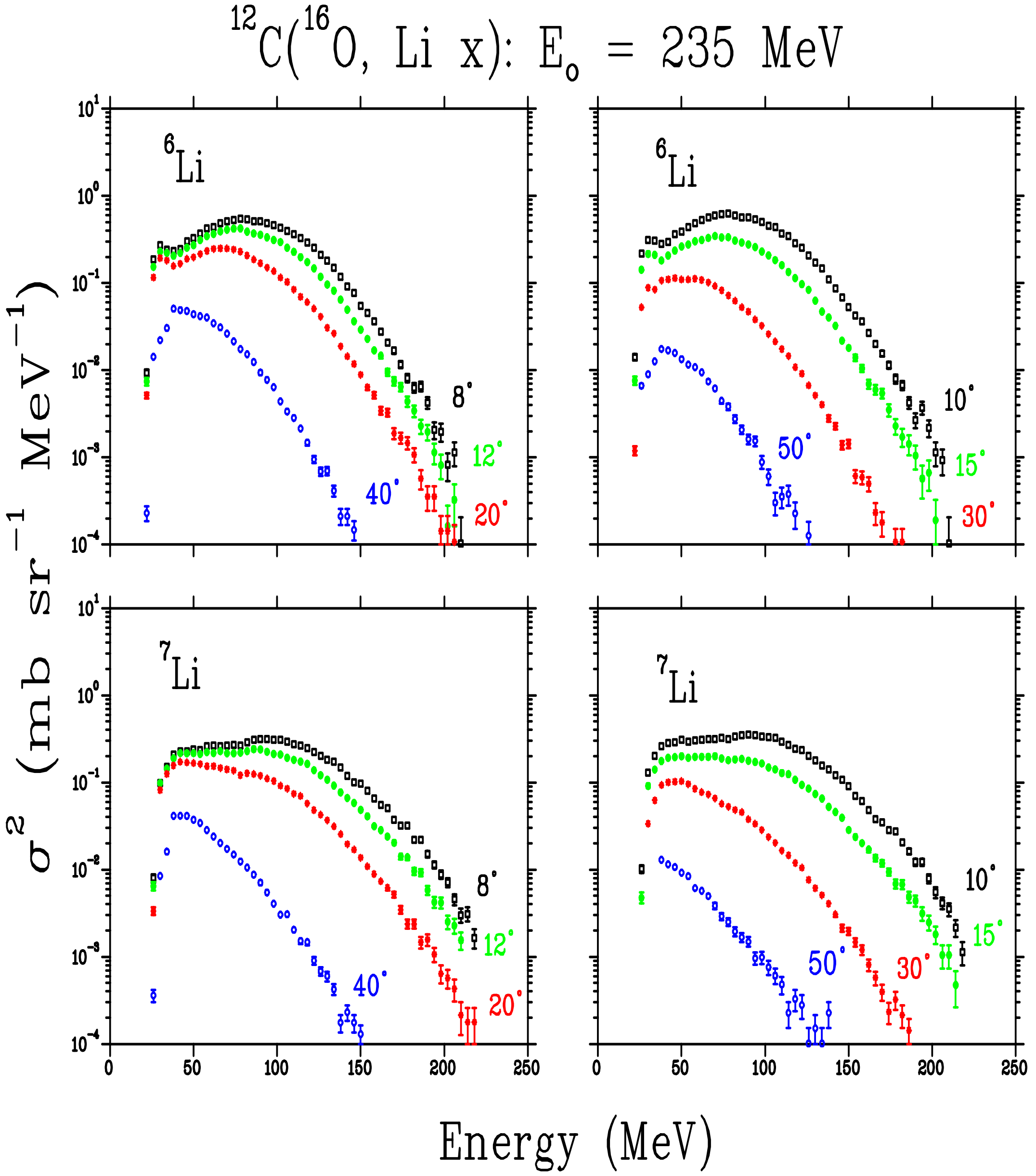

Figure B.1: Double differential cross sections of ^{6}Li and ^{7}Li emitted in the interaction of ^{16}O with ^{12}C at an incident energy of 235 MeV at different emission angles as indicated. The error bars reflect the statistical errors. These cross-sections are binned into 4 MeV/bin.

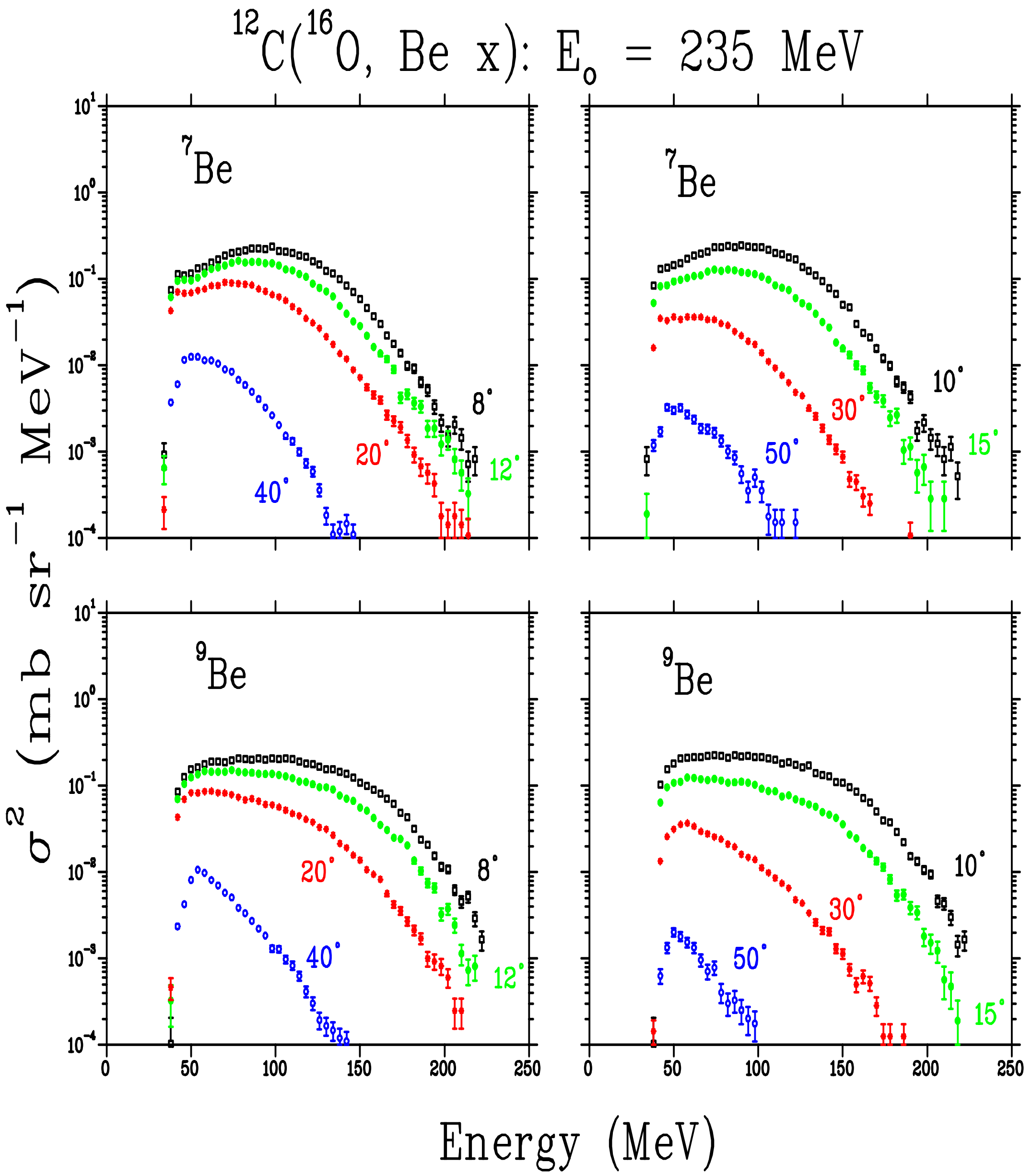

Figure B.2: Double differential cross sections of ^{7}Be and ^{9}Be emitted in the interaction of ^{16}O with ^{12}C at an incident energy of 235 MeV at different emission angles as indicated. The error bars reflect the statistical errors. These cross-sections are binned into 4 MeV/bin.

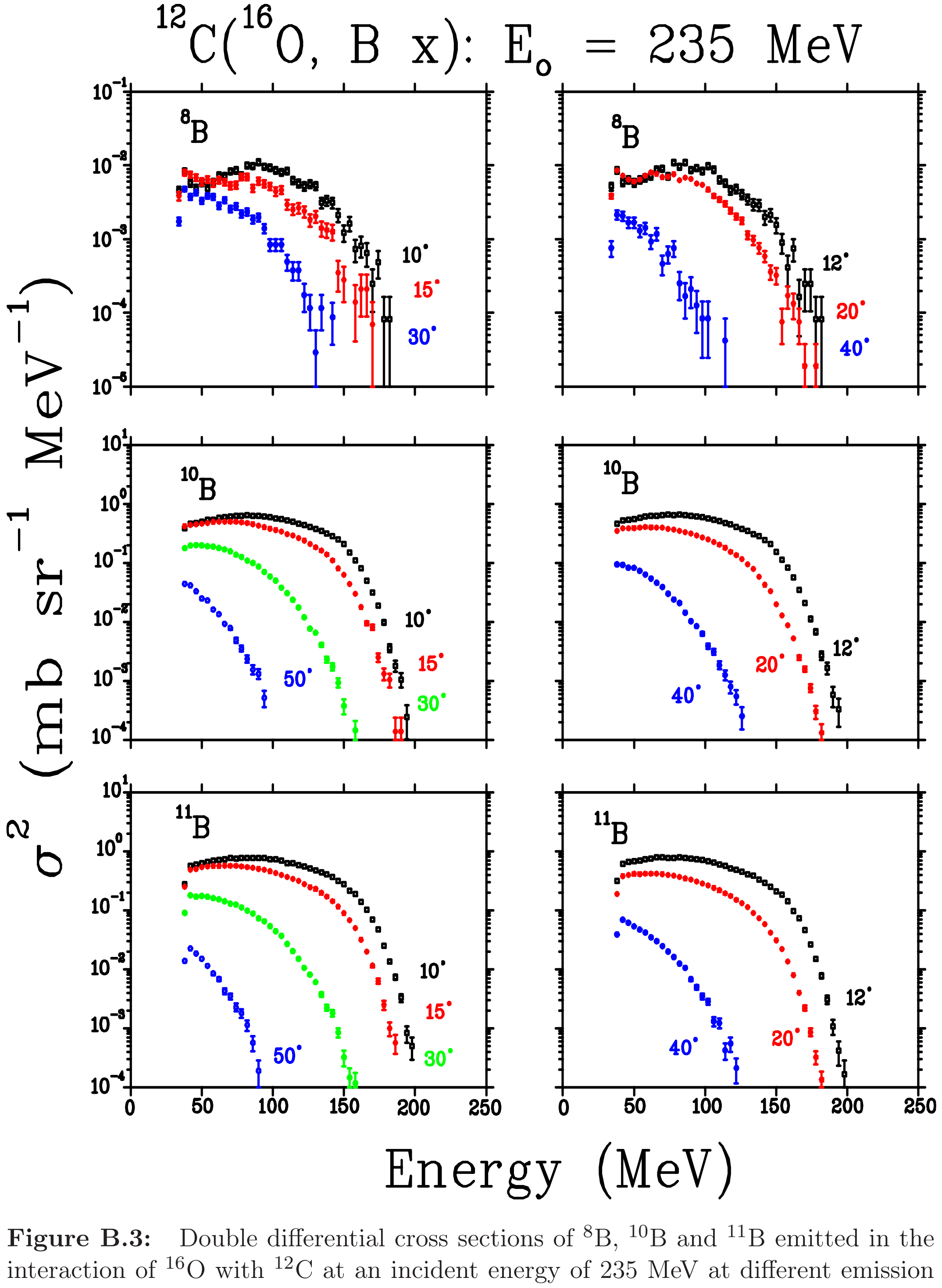

Figure B.3: Double differential cross sections of ^{8}B, ^{10}B and ^{11}B emitted in the interaction of ^{16}O with ^{12}C at an incident energy of 235 MeV at different emission angles as indicated. The error bars reflect the statistical errors. These cross-sections are binned into 4 MeV/bin.

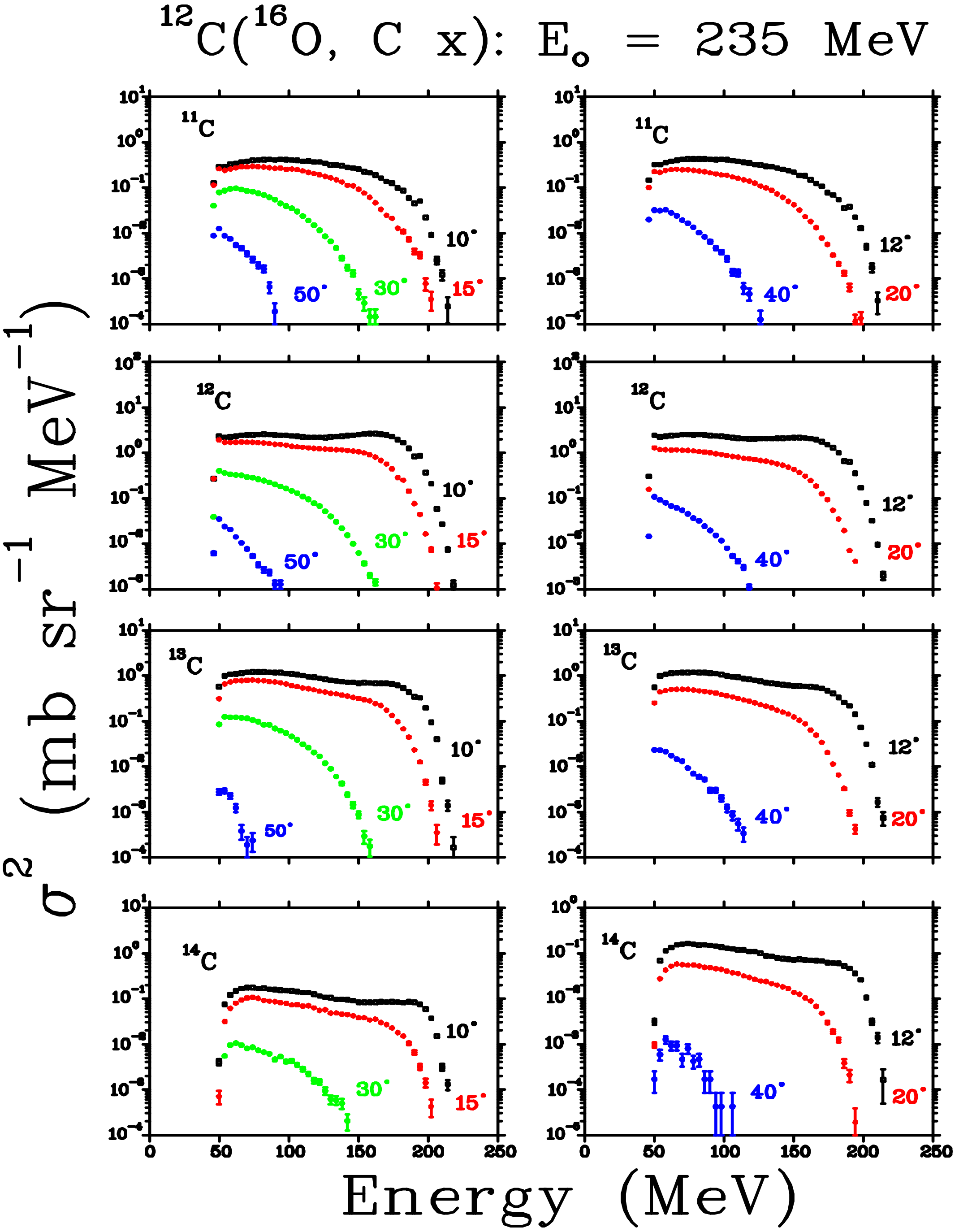

Figure B.4: Double differential cross sections of ^{11}C, ^{12}C, ^{13}C and ^{14}C emitted in the interaction of ^{16}O with ^{12}C at an incident energy of 235 MeV at different emission angles as indicated. The error bars reflect the statistical errors. These cross-sections are binned into 4 MeV/bin.

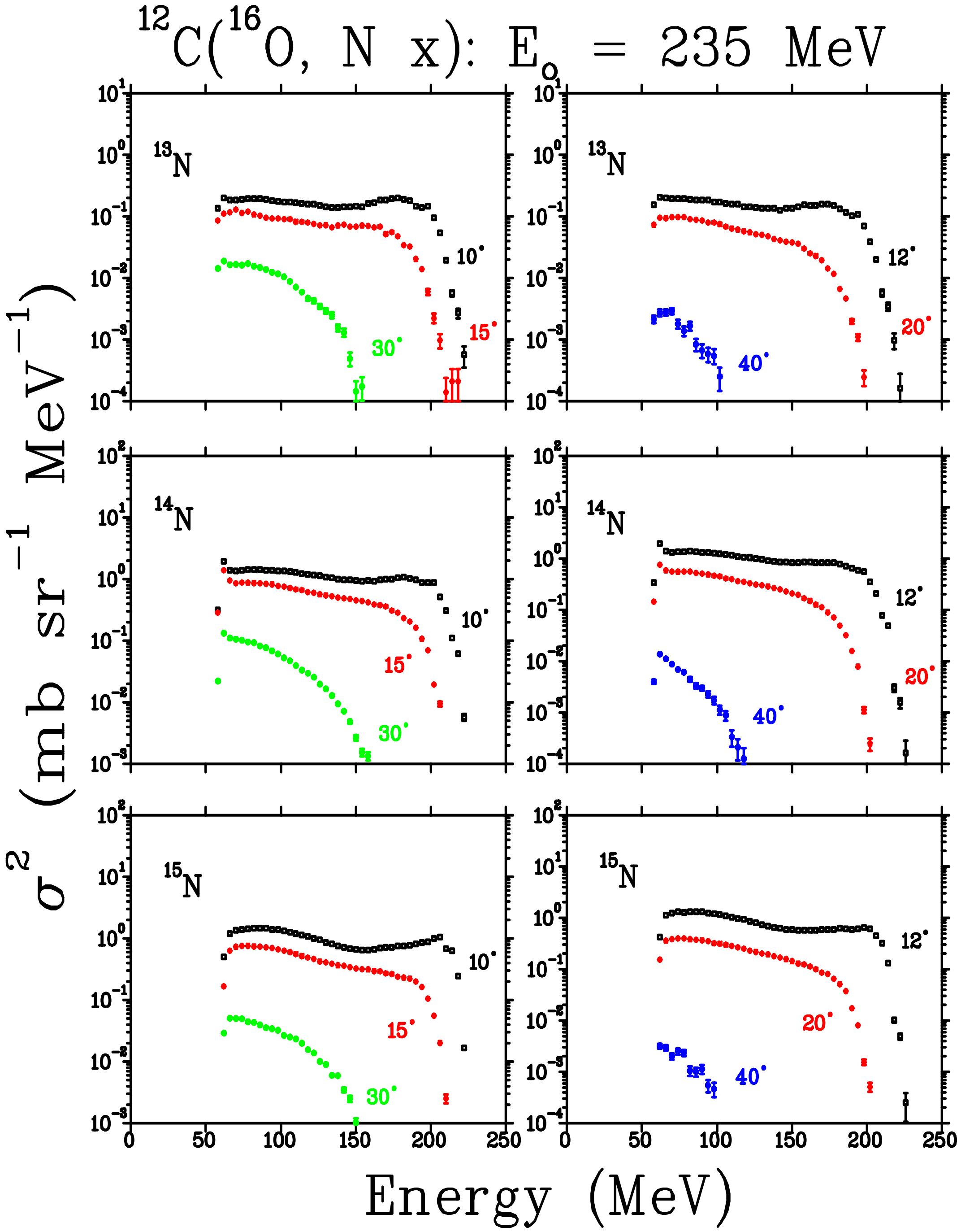

Figure B.5: Double differential cross sections of ^{13}N, ^{14}N and ^{15}N emitted in the interaction of ^{16}O with ^{12}C at an incident energy of E = 235 MeV at different emission angles as indicated. The error bars reflect the statistical errors. These cross-sections are binned into 4 MeV/bin.

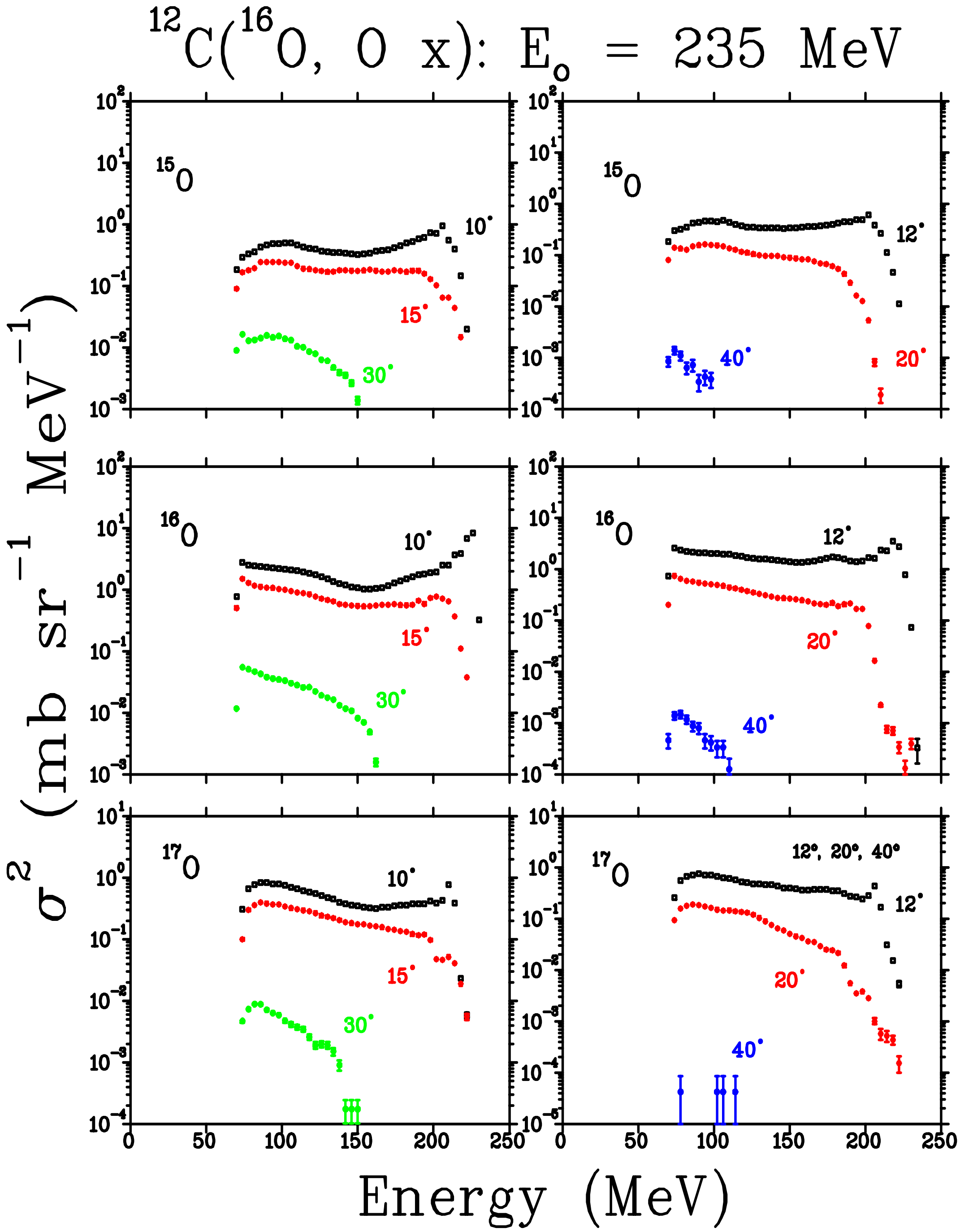

Figure B.6: Double differential cross sections of ^{15}O, ^{16}O and ^{17}O emitted in the interaction of ^{16}O with ^{12}C at an incident energy of $E = 235$ MeV at different emission angles as indicated. The error bars reflect the statistical errors.

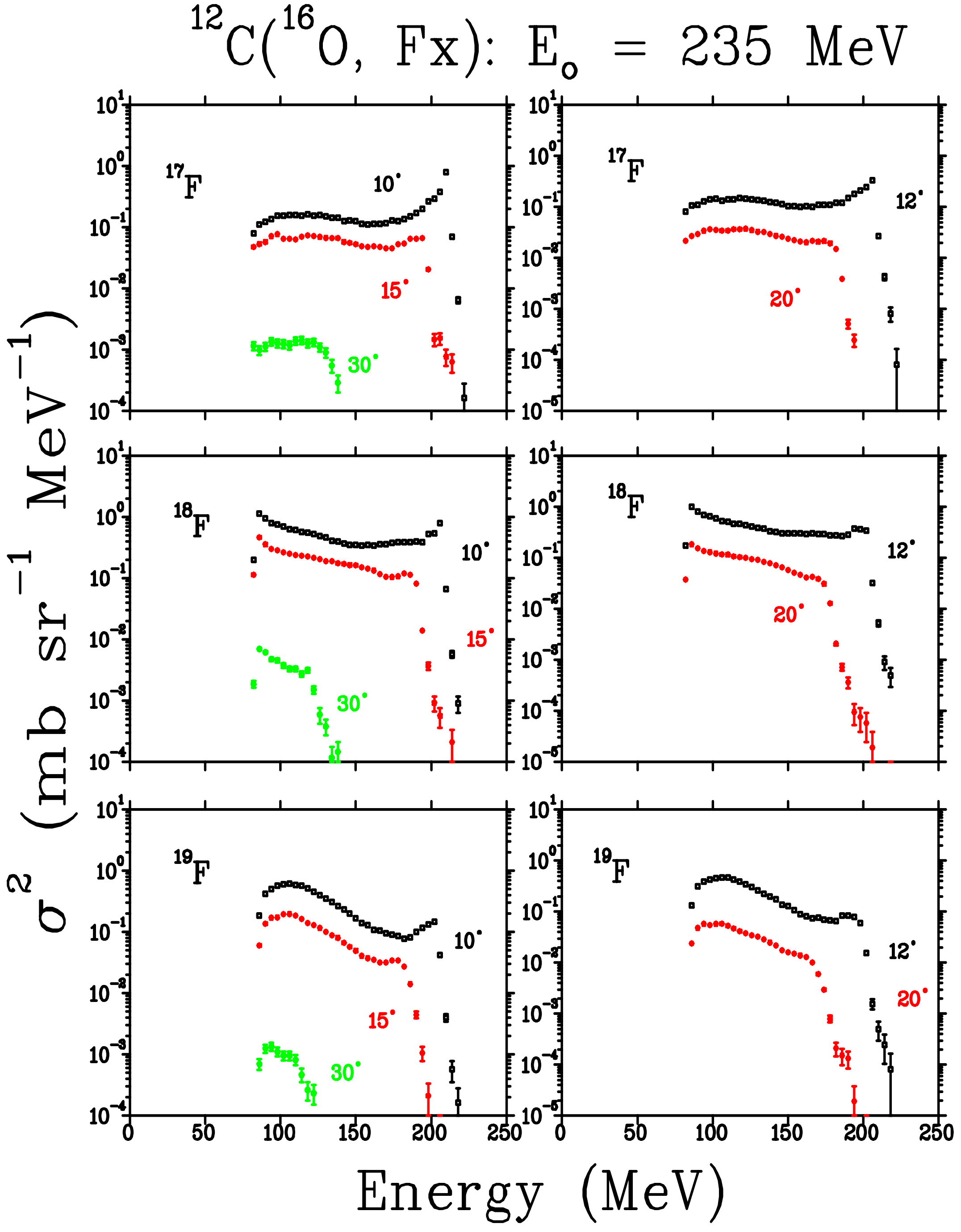

Figure B.7: Double differential cross sections of ^{17}F, ^{18}F and ^{19}F emitted in the interaction of ^{16}O with ^{12}C at an incident energy of 235 MeV at different emission angles as indicated. The error bars reflect the statistical errors. These cross-sections are compressed into 4 MeV/bin.

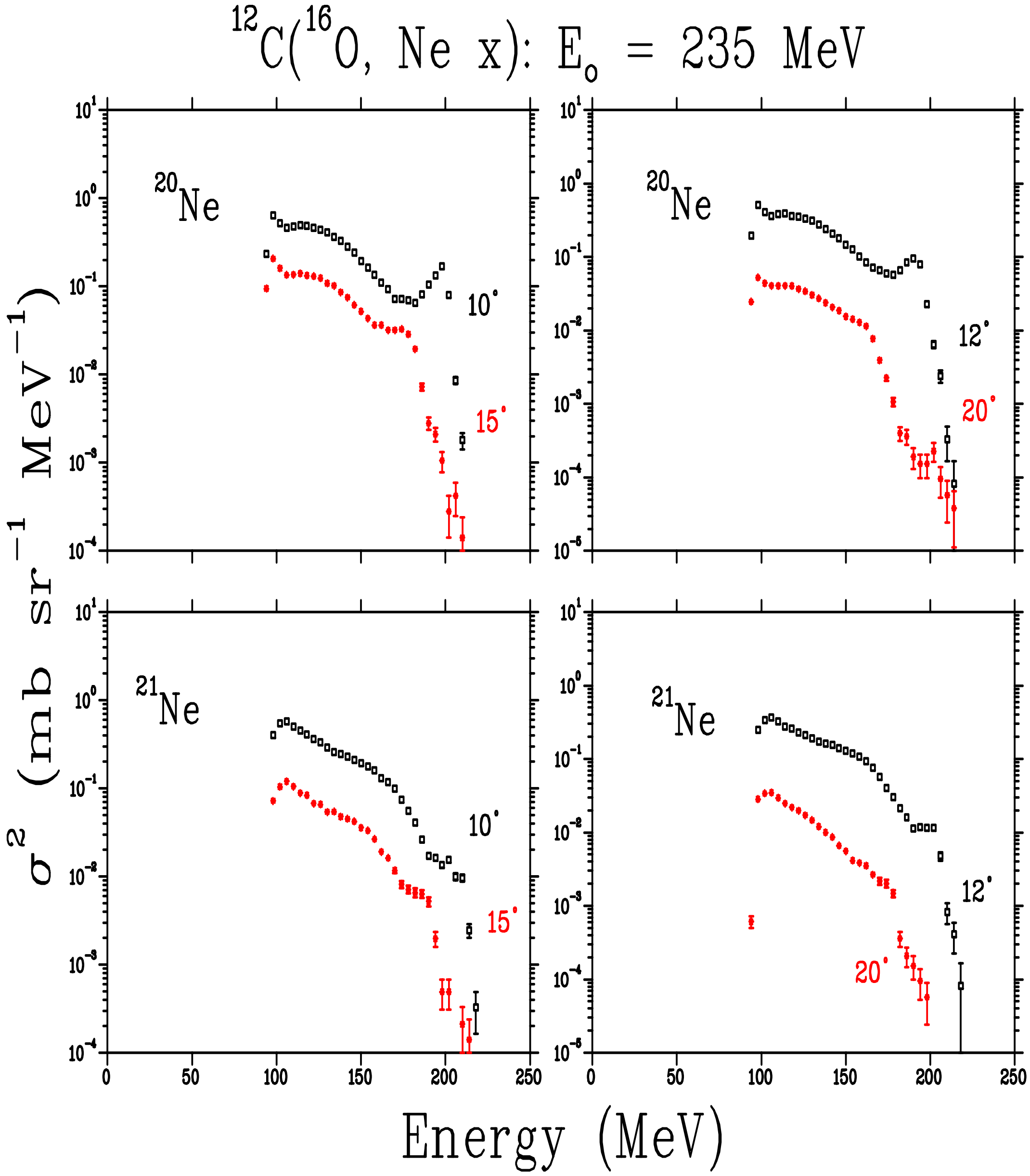

Figure B.8: Double differential cross sections of ^{20}Ne and ^{21}Ne emitted in the interaction of ^{16}O with ^{12}C at an incident energy of 235 MeV at different emission angles as indicated. The error bars reflect the statistical errors. These cross-sections are compressed into 4 MeV/bin.

List of References

[Ada72] H. L. Adair, Nuclear Instrument and Methods, **102** (1972) 599-610.

[Ago03] S. Agostinelli *et al.*, Nuclear Instruments and Methods in Physics Research Section A: Accelerators, Spectrometers, Detectors and Associated Equipment, **Vol. 506** (2003) 250-303.

[Apo09] J. Apostolakis, G. Folger, V. Grichine, A. Heikkinen, A. Howard, V. Ivanchenko, P. Kaitaniemi, T. Koi, M. Kosov, J. M. Quesada, A. Ribon, V. Uzhinskiy, and D. Wright, Journal of Physics: Conference series 160 (2009) 012073.

[Ara03] K. Arai, P. Descouvemont, D. Baye, and W. N. Catford, Physical Review C **68**, 014310 (2003).

[Awe81] T. C. Awes, G. Poggy, C. K. Gelbke, B. B. Back, B. G. Glagola, H. Breuer, and V. E. Viola, Phys. Rev. C **24** (1981) 89.

[Awe82] T. C. Awes, S. Saini, G. Poggi, C. K. Gelbke, D. Cha, R. Legrain, and G. D. Westfall, Phys. Lett. C **25** (1982) 2361.

[Bar09] F. C. Barker, Physical Review C **79**, 017302 (2009).

[Bas05] M. S. Basunia, E. B. Norman, H. A. Shuqart, A. R. Smith, M. J. Dolinski, and B. J. Quiter, Phys. Rev. C **71**, 035801 (2005).

[Bas91] R. Bassini, C. Boiano, S. Brambilla, I. Iori, M. Maletesta, and A. Moroni, Nuclear Instruments and Methods in Physics Research **A 305** (1991) 449-452.

[Bec03] B. Becker, F. Albertini, E. Gadioli, G.F. Steyn, M. Cavinato, S.H. Connel, A. A. Cowley, E. Fabrici, S.V. Förtsch, E.Gadioli Erba, J.J. Lawrie, and E. Sideras Haddad, Eur. Phys. J. **A 18** (2003) 639-644.

[Bel93] E. Belmont-Moreno, A. Menchaca-Rocha, and K. Michaelian, Nuclear Instrument and Methods in Physics Research A **332** (1993) 202-205.

[Bou87] R. Bougault, D. Horn, C. B. Chitwood, D. J. Fields, C. K. Gelbke, D. R. Klesch, W. G. Lynch, M. B. Tsang, and K. Kwiatkowski, Physical Review C, Vol. **36** No. 2 (1987) 830-833.

[Bue78] M. Buenerd, D. Lebrun, J. Chauvin, Y. Gaillard, J.M. Loiseaux, P. Martin, G. Perrin, and P. de Saintignon, Phys. Rev. Lett. **40** (1978) 1482

[Cav96] M. Cavinato, E. Fabrici, E. Gadioli, E. Gadioli Erba, M. Galmarini, and A. Gritti, Z. Phys. **A 347** (1996) 471.

[Cav98] M. Cavinato, E. Fabrici, E. Gadioli, E. Gadioli Erba, and E. Risi, Nuclear Physics **A 643**, (1998) 15-29.

[Cav01] M. Cavinato, E. Fabrici, E. Gadioli, E. Gadioli Erba, and G. Riva, Nuclear Physics **A 679**, (2001) 753-764.

[Cer92] I. Cervesato, M. Cavinato, E. Fabrici, E. Gadioli, E. Gadioli Erba, and M. Galmarini, Phys. Rev. C **45** (1992) 2369.

[Che80] Vianney Kuo-Chuan Cheng, KINMAT: A Nuclear Reaction Kinematics Program, Institute of Nuclear Energy Research (1980).

[Chi86] C. B. Chitwood, T. C. Awes, R. L. Ferguson, D. J. Fields, C. K. Gelbke, D. R. Klesch, W. G. Lynch, F. E. Obenshain, F. Plasil, R. L. Robinson, M. B. Tsang, and G. R. Young, Physical Review C, Vol. **34** (1986) 858.

[Chu10] W. T. Chu, Relativistic Ion Beams for Treating Human Cancer, Proceedings of IPAC' 10, Kyoto Japan, (2010) 21-25.

[Eng04] W. Enghardt, P. Crespo, F. Fiedler, R. Hinz, K. Parodi, J. Pawelke, F. Pönisch, Charged hadron tumour therapy monitoring by means of PET, Nucl. Instrum. Methods Phys. Rev. **A 525** (2004) 284.

[Fat85] M. Fatyga, M. Blann, C. B. Chitwood, D. J. Fields, C. K. Gelbke, K. Kwaitkowski, W. G. Lynch, J. Pochodzolla, M. B. Tsang, V. and E. Viola, Physical Review Letters, Vol. **55** (1985) 1376.

[Fer50] E. Fermi, Progress of Theoretical Physics **5** (1950) 1570.

[Fil09] D. Filges, and F. Goldenbaum, Handbook of Spallation Research, Theory, Experiments and application (2009).

[För05] S.V. Förtsch, F. Cerutti, P. Colleoni, E. Gadioli, A. Mairani, G.F. Steyn, J. J. Lawrie, F. D. Smit, S. H. Connell, R. W. Fearick, T. Thovhogi, H. Machner, F. Goldenbaum, and K. Pysz, AIP Conference Proceedings, **Vol. 769**, (2005) 1642-1645.

[För07] S. V. Förtsch, F. Cerutti, P. Colleoni, E. Gadioli, E. Gadioli Erba, A. Mairani, G. F. Steyn, J. J. Lawrie, F. D. Smit, S. H. Connell, R. W. Fearick, and T. Thovhogi, Nucl. Phys. **A 797** (2007) 1-32.

[För10] S. V. Förtsch, G.F. Steyn, E.Gadioli, R. Bassini, E.Z. Buthelezi, F. Cerutti, S.H. Connell, A.A. Cowley, H. Fujita, J. Mabiala, A. Mairani, J Mira, R. Neveling, P. Papka, and F.D. Smit, 12th International Conference on Nuclear Reaction Mechanisms, CERN proceedings, (2010) 545.

[Fuc94] H. Fuchs and K. Möhring, Rep. Prog. Phys. **57**, (1994) 231-324.

[Gad92] E. Gadioli and P.E. Hodgson. Pre-Eqiulibrium Nuclear Reactions (Oxford Clarendon Press, 1992).

[Gad99] E. Gadioli, M. Cavinato, E. Fabrici, E. Gadioli Erba, C. Birattari, I. Mica, S. Solia G. F. Steyn, S.V. Förtsch, , J. J. Lawrie, F. M. Nortier, T. G. Stevens, S. H. Connell, J. P. F. Sellschop, and A. A. Cowley, Nuclear Phys. **A 654**, (1999) 523-540.

[Gad00] E. Gadioli, M. Cavinato, E. Fabrici, E. Gadioli Erba, R. Bassini, C. Barattari, S. Crippa, G.F. Steyn, S.V. Förtsch, J.J. Lawrie, F.M. Nortier, S.H. Connell, E. Sideras Haddad, J.P.F. Sellschop, and A.A. Cowley, Eur. Phys. J. **A 8** (2000) 373-376.

[Gad01] E. Gadioli, G. F. Steyn, C. Birattari, M. Cavinato, S. H. Connell, A. A. Cowley. E. Fabrici, S. V. Förtsch, E. Gadioli-Erba, J. J. Lawrie, F. M. Nortier, J. P. F. Sellschop, and E. S. Haddad, Eur. Phys. J. **A 11** (2001) 161-173.

[Gad02] E. Gadioli, G. F. Steyn, C. Birattari, C. Catarinaro, M. Cavinato, S. H. Connell, A. A. Cowley, E. Fabrici, S.V. Förtsch, E. Gadioli Erba, J. J. Lawrie, J. P. F. Sellschop and E. Sideras Haddad, Nuclear Physics **A 708** (2002) 391-412.

[Gad03] E. Gadioli, G. F. Steyn, F. Albertini, C. Birattari, M. Cavinato, S. H. Connell, A. A. Cowley, E. Fabrici, S.V. Förtsch, E. Gadioli Erba, J. J. Lawrie, M. Pigni, J. P. F. Sellschop and E. Sideras Haddad, Eur. Phys. J. **A 17** (2003) 195-212.

[Gel87] Claus-Konrad Gelbke and David H. Boal, Progress in Particle and Nuclear Physics, Vol. **19** (1987) 33.

[Gol78] A. S. Goldhaber and H. H. Heckman, Annual Review of Nuclear Science, **28** (1978) 161.

[Gon01] Gönnenwein, A. M. Gagarski, P. Jesinger, M. Mutterer, V. Nesvishevsky, G. A. Petrov, W. H. Trzaska, and O. Zimmer, Proceedings of the International Workshop Fission Dynamics of Atomic Clusters and Nuclei, (2001) 232-247.

[Gon87] P. L. Gonthier, B. Bouma, P. Harper, R. Ramaker, D.A. Cebra, Z.M Koenig, D. Fox, and G.D. Westfall, Phys. Rev. C **35** (1987) 1946.

[Gro90] D. H. E. Gross, Reports on Progress in Physics, Vol. **53** (1990) 605.

[Har99] M. Harada, Y. Watanabe, A. Yamamoto, S. Yoshioko, K. Sato, T. Nakashima, H. Ijiri, H. Yoshida, Y. Ouzumi, N. Koori, S. Meigo, O. Iwamoto, T. Fukahiro, and S. Chiba, Journal Of Nuclear Science and Technology, Vol **36**, No. 4 (1999) 313 - 325.

[Ho80] H. Ho, P. Gonthier, M. N. Namboodiri,, J. B. Natowitz, L. Adler, S. Simon, K. Hagel, R. Terry and A. Khodai, Physics Letters, **98B** (1980) 51-54.

[Ho83] H. Ho, P. Gonthier, J.C. Adloff, D. Disdier, G. Y. Fan, A. Kamili, W. Kühn, A. Pfoh, V. Rauch, G. Rudolf, L. Schad, F. Scheibling, A. Strazzeri, R. Wolski, and J. P. Wurm, Physical Review C **27** (1983) 584.

[Hod97] P. E. Hodgson, E. Gadioli, and E. Gadioli-Erba, Introductory Nuclear Physics, Oxford Science Publications (1997).

[Hom82] H. Homeyer, M. Bürgel, M. Clover, Ch. Engelhaaf, H. Fuchs, A. Gamp, D. Kovar, and W. Rauch, Physical Review C, Vol **26** (1982) 1335.

[Hus81] M.S Hussein, K. W. McVoy, and D. Saloner, Physics Letters **98B, no. 3** (1981) 162-165.

[Jip84] P. Jipsen, ELOSS, A Program for Calculating the Ranges of Ions in Matter, National Accelerator Center (1984) (Unpublished).

[Kha83] A. E. M. Khairozzaman, Astrophysics and Space Science, Volume 95, Issue **1** (1983) 179-186.

[Lar94] Y. Larochelle, L. Beaulieu, B. Djerroud, D. Doré, P. Gendron, E. Jalbert, J. Pouliot, R. Roy, M. Samri, and S. Pierre, Nucl. Instr. and Meth. **A 348** (1994) 167-172.

[Leo87] W. R. Leo, Techniques for Nuclear and Particle Physics Experiments, (1987).

[Lil01] J. Lilley, Nuclear Physics Principles and Applications, Wiley and Sons (2001).

[Lyn82] U. Lynen, H. Ho, W. Kühn, D. Pelte, U. Winkler, W. F. J. Müller, Y. T. Chu, P. Doll, A. Gobbi, K, Hildenbrand, A. Olmi, H.Sann, H.Stelzer, R.Bock, H. Löhner, R. Glasow and R. Santo, Nuclear Physics **A387** (1982) 129.

[Mac92] E. W. Macdonald, A. C. Shotter, D. Branford, J. Rahighi, T. Davinson, N. J. Davis, Y. El Mohri, and J. Yorkston, Nucl. Instr. and Meth. **A 317** (1992) 498-505.

[Mag98] A. Magiera, J. Hebenstreit, L. Jarczyk, B. Kamys, A. Strzalkowski, and B. Styezen, Phys. Rev. C **57**, (1998) 749-763.

[Mai07] A. Mairani, PhD thesis, Unpublished (2007).

[McV80] K. W. McVoy and C. Nemes, Z. Phys. **A295** (1980) 177.

[Met04] W. A. Metwally, R. P Gardner, and C. W. Mayo, Nuclear Instruments and Methods in Physics Research Section B: Beam Interaction with Materials and Atoms, **Vol. 213** (2004) 394-399.

[Mic93] K. Michaelian, A. Menchaca-Rocha, and E. Belmont-Moreno, Nuclear Instruments and Methods in Physics Research **A 334**, (1993) 457-460.

[Mic94] K. Michaelian and A. Menchasa-Rocha, Phys. Rev. **B 49** (1994) 15550.

[Mir08] J. P. Mira, MSc. Thesis, University of Western Cape, Unpublished (2008).

[Mit85] W. Mittig, A. Cunsolo, A. Foti, J. P. Wieleczko, F. Auger, B. Berthier, J. M. Pascaud, J. Quebert, and E. Plagnol, Physics Letters **154B** (1985) 259.

[Mud05] L. J. Mudau, F. Cerutti, E. Gadioli, A. Mairani, S. V. Fortsch, E. Z. Buthelezi, G. F. Steyn, S. H. Connell, J. J. Lawrie, R. Neveling, F. D. Smit, and E. Sideras-Haddad, Nucl. Phys. **A 761** (2005) 190-199.

[Mur10] S. Murray, MSc. Thesis, Unpublished (2010).

[Ogu11] R. Ogul, A. S. Botvina, U. Atav, N. Buyukcizmeci, I. N. Mishustin, P. Adrich, T. Aumann, C. O. Bacri, T. Barczyk, R. Bassini, S. Bianchin, C. Boiano, A. Boudard, J. Brzychczyk, A. Chbihi, J. Cibor, B. Czech, M. De Napoli, J.É. Ducret, H. Emling, J. D. Frankland,

M. Hellström, D. Henzlova, G. Immé, I. Iori, H. Johansson, K. Kezzar, A. Lafriakh, A. Le Févre, E. Le Gentil, Y. Leifels, J. Lühning,1 J. Lukasik, W. G. Lynch, U. Lynen, Z. Majka, M. Mocko, W. F. J. Müller, A. Mykulyak, H. Orth, A. N. Otte, R. Palit, P. Pawlowski, A. Pullia, G. Raciti, E. Rapisarda, H. Sann, C. Schwarz, C. Sfienti, H. Simon, K. Sümmerer, W. Trautmann, M. B. Tsang, G. Verde, C. Volant, M. Wallace, H. Weick, J. Wiechula, A. Wieloch, and B. Zwiegliński, Physical Review C **83** (2011) 024608.

[Ort113] Ortec 113 preamplifier manual, www.ortec-online.com.

[Pap07] P. Papka *et al.*, Physical Review C **75**, 045803 (2007).

[Par07] K. Parodi, A. Ferrari, F. Sommerer, and H. Paganetti, Physics in Medicine and Biology, **52** (2007) 3369-3387.

[Pil96] J. V. Pilcher, The NAC MBD to VME Conversion Guide (1996).

[Pön04] F. Pönisch, K. Parodi, B. G. Hasch, and W. Enghardt, Phys. Med. Biol, **49** (2004) 5217-5232.

[Qua] Quasta, A three body kinematics computer code developed at iThemba LABS, unpublished.

[Rae84] W. D. M. Rae and R. K. Bhowmik, Nuclear Physics **A 420**, Issue 2 (1984 320-350.

[Ric90] J. Richert and P. Wagner, Nuclear Physics **A 517** (1990) 399-412.

[Sch03] R. Schlickeiser, Cosmic and Astrophysics (2003).

[Sch70] F. Schmittroth, A. A. Colestaneh, and W. Tobocman, Physical Review C, Vol. **1 no. 2** (1970) 377.

[Sch84] W. U. Schröder and J. R. Huizenga, Damped Nuclear Reactions, Treatise on Heavy-Ion Science, Plenum Press, D. Allan Bromley, ed. Volume 2 (1984) 113-726.

[Sch92] C. Schwarz, H. Fuchs, H. Homeyer, K. Mohring, T. Schimdt, A. Siwek, A. Sourell, W. Terlau, and A. Budzanowski, Physics Letters B **279** (1992) 223-227.

[Ser47] R. Serber, Phys. Rev. **72**, (1947) 1008.

[Sha04] Manoj Kumar Sharma, Unnati, B. K. Sharma, B. P. Singh, H. D. Bhardwaj, Rakesh Kumar, K. S. Golda, and R. Prasad, Phys. Rev. C **70**, 044606 (2004)

[Sho81] A. C. Shotter, A. N. Bice, J. M. Wouters, W. D. Rae, and J. Cerny, Physical Review Letters, Vol. **46** (1981) 12.

[Sin11] P. P. Singh, A. Yadav, V. R. Sharma, D. P. Singh, U. Gupta, M. K. Sharma, R. Kumar, K. S. Golda, R. P. Singh, S. Muralithar, B. P. Singh, R. K. Bhowmik, and R. Prasad, Journal of Physics: Conference Series **282** (2011) 012019.

[Sin68] J. J. Singh and E. Rind, NASA TECHNICAL NOTES, high energy proton damage in Silicon Surface Barrier detectors (1968)

[Ste05] G.F. Steyn, S.V. Förtsch, J.J. Lawrie, R. Bassini, E. Gadioli, C. Barattari, and S.H. Connell, Nuclear Instruments and Methods in Phys. Research, **A 538** (2005) 559-573.

[Str90] D. W. Stracener, D. G. Sarantites, L. G. Sobotka, J. Elson, J. T. Hood, Z. Majka, V. Abenante, and A. Chbihi, Nucl. Instr. and Meth. **A 294** (1990) 485.

[Sui10] H. Suit, T. DeLaney, S. Goldberg, H. Paganetti, B. Clasie, L. Gerweck, A. Niemierko, E. Hall, J. Flanz, J. Hallmann, and A. Trofimov, Radiotherapy and Oncology, **95** (2010) 3 - 22.

[Jan96] TABLECURVE 2D automated Curve Fitting & Equation Discovery, Jandel Scientific, San Rafael, CA, 1996.

[Tur09] T. J. Turner and L. Miller, arXiv:0912.3479 [astro-ph.HE]

[Tyk95] R. Tykva and J. Sabol, Low-level Environmental Radioactivity: Sources and Evaluation (1995).

[Van98] E. Vangioni-Flam and M. Cassé, Proceedings of the Rencontres de l'Observatoire, (1998) 77-85.

[Wei37] V. F. Weisskopf, Statistics and Nuclear Reaction, Phys. Rev., **52**, (1937) 295-303.